Multiscale, data-driven and nonlocal modeling of granular materials

Thesis by
Konstantinos Karapiperis

In Partial Fulfillment of the Requirements for the
Degree of
Doctor of Philosophy

CALIFORNIA INSTITUTE OF TECHNOLOGY
Pasadena, California

2020
Defended December 17, 2020

Konstantinos Karapiperis
ORCID: 0000-0002-6796-8900

ACKNOWLEDGEMENTS

First, I would like to express my sincere gratitude to my advisor Prof. José E. Andrade for his consistent guidance and support as I was freely following my scientific curiosity. He has been a truly excellent mentor, and has shown me not only how to approach scientific endeavor, but also how to communicate efficiently and plan strategically.

I greatly appreciate Prof. Michael Ortiz, Prof. Ares Rosakis, and Prof. Nadia Lapusta for their willingness to serve on my committee. I have particularly enjoyed our technical discussions on solid mechanics with Prof. Ortiz and Prof. Rosakis, and have benefited greatly from their help and valuable advice.

To everyone that I had the pleasure to work closely together at Caltech (Mr. John Harmon, Dr. Reid Kawamoto, Dr. Liuchi Li, Dr. Jason Marshall, Dr. Siavash Monfared, and Mr. Rob Macedo), at Grenoble Univ. (Prof. Cino Viggiani, Dr. Eddy Ando), at EC Nantes (Prof. Laurent Stainier) and at NGI (Dr. HP Jostad and Dr. Khoa Huynh), I extend my deepest appreciation.

I would also like to thank the Fred L. Hartley Foundation for supporting me through the Hartley fellowship during the period 2018-2019.

Further, I would like to thank Prof. Yiannis Dafalias and Prof. Natarajan Sukumar, my guarantors at UC Davis for recommending me for this PhD, as well as my original guarantors and academic mentors at NTUA (Prof. Nikos Gerolymos, Prof. George Gazetas and Prof. Manolis Papadrakakis).

The administrative staff at MCE and, particularly, Jenni Campbell have been very helpful and supportive during my PhD, and for that I remain grateful.

Special thanks go to my friends at Caltech and back home. I am thankful for the memories that we have shared and have shaped me as a human being.

To my wife, Christina, I feel grateful for having you in my life, for your support and sacrifices, and for spending countless hours on a plane to California during the last five years.

Lastly, I would like to dedicate this work to my sister Myrto, my mother Kostoula, and my father Dennis. Words cannot do justice to the amount of love and support that I have received during the last 30 years. Simply put, this accomplishment would not have been possible without them.

ABSTRACT

Granular materials are ubiquitous in both nature and technology. They play a key role in many applications ranging from storing food and energy to building reusable habitats and soft robots. Yet, predicting the continuum mechanical response of granular materials continues to present extraordinary challenges, despite the apparently simple laws that govern particle-scale interactions. This is largely due to the complex history dependence arising from the continuous rearrangement of their internal structure, and the nonlocality emerging from their self-organization. There is clearly an urge to develop methods that adequately address these two aspects, while bridging the long-standing divide between the grain- and the continuum scale.

This dissertation introduces novel theoretical and computational approaches for behavior prediction in granular solids. To begin with, we develop a framework for investigating their incremental behavior from the perspective of plasticity theory. It relies on systematically probing, through level-set discrete element calculations, the response of granular assemblies from the same initial state to multiple directions is stress space. We then extract the state- and history-dependent elasticity and plastic flow, and investigate the evolution of pertinent internal variables. We specifically study assemblies of sand particles characterized by X-ray computed tomography, as well as morphologically simpler counterparts of the same systems. Naturally arising from this investigation is the concept of a granular genome. Next, inspired by the abundance of generated high-fidelity micromechanical data, we develop an alternative data-driven approach for behavior prediction. This new multiscale modeling paradigm completely bypasses the need to define a constitutive law. Instead, the problem is directly formulated on a material data set, generated by grain-scale calculations, while pertinent constraints and conservation laws are enforced. We particularly focus on the sampling of the mechanical phase space, and develop two methods for parametrizing material history, one thermodynamically motivated and one statistically inspired. In the remainder of the thesis, we direct our attention to the understanding and modeling of nonlocality. We base our investigation on data derived from a discrete element simulation of a sample of sand subjected to triaxial compression and undergoing shear banding. By representing the granular system as a complex network,

we study the self-organized and cooperative evolution of topology, kinematics and kinetics within the shear band. We specifically characterize the evolution of fundamental topological structures called force cycles, and propose a novel order parameter for the system, the minimal cycle coefficient. We find that this coefficient governs the stability of force chains, which succumb to buckling as they grow beyond a characteristic maximum length. We also analyze the statistics of nonaffine kinematics, which involve rotational and vortical particle motion. Finally, inspired by these findings, we extend the previously introduced data-driven paradigm to include nonaffine kinematics within a weakly nonlocal micropolar continuum description. By formulating the problem on a phase space augmented by higher-order kinematics and their conjugate kinetics, we bypass for the first time the need to define an internal length scale, which is instead discovered from the data. By carrying out a data-driven prediction of shear banding, we find that this nonlocal extension of the framework resolves the ill-posedness inherent to the classical continuum description. Finally, by comparing with available experimental data on the same problem, we are able to validate our theoretical developments.

PUBLISHED CONTENT AND CONTRIBUTIONS

- D. Bhattacharya, R. Kawamoto, K. Karapiperis, J.E. Andrade and A. Prashant (2020). "Mechanical behaviour of granular media in flexible boundary plane strain conditions: Experiment and level-set discrete element modelling". In: *Acta Geotechnica* (2020), pp. 1861-1133. DOI: https://doi.org/10.1007/s11440-020-00996-8
  This work was a collaborative effort for which each author made substantial contributions in all aspects.

- K. Karapiperis, J. Marshall, and J. E. Andrade. "Reduced gravity effects on the strength of granular matter: DEM simulations versus experiments". In: *Journal of Geotechnical and Geoenvironmental Engineering* 146 (2020), p. 06020005. DOI: https://doi.org/10.1061/(ASCE)GT.1943-5606.0002232.
  This work was a collaborative effort for which each author made substantial contributions in all aspects.

- K. Karapiperis, J. Harmon, E. Ando, G. Viggiani, and J. E. Andrade. "Investigating the incremental behavior of granular materials with the level-set discrete element method". In: *Journal of the Mechanics and Physics of Solids* 144 (2020), p. 104103. DOI: https://doi.org/10.1016/j.jmps.2020.104103.
  This work was a collaborative effort for which each author made substantial contributions in all aspects.

- J. Harmon, K. Karapiperis, L. Li, S. Moreland, and J. E. Andrade. "Modeling connected granular materials: Particle bonding within the level set discrete element method". In: *Computer Methods in Applied Mechanics and Engineering* 373 (2021), p. 113486. DOI: https://doi.org/10.1016/j.cma.2020.113486.
  This work was a collaborative effort for which each author made substantial contributions in all aspects.

- K. Karapiperis and J. E. Andrade. "Nonlocality in granular complex networks: Linking topology, kinematics and forces". In: *Extreme Mechanics Letters* 42 (2020), p. 101041. DOI: https://doi.org/10.1016/j.eml.2020.101041.
  This work was a collaborative effort for which each author made substantial contributions in all aspects.

- K. Karapiperis, L. Stainier, M. Ortiz, and J. E. Andrade. "Data-Driven multiscale modeling in mechanics". In: *Journal of the Mechanics and Physics of Solids* (2020), p. 104239. DOI: https://doi.org/10.1016/j.jmps.2020.104239.

This work was a collaborative effort for which each author made substantial contributions in all aspects.

- K. Karapiperis, M. Ortiz, and J. E. Andrade. "Data-Driven nonlocal mechanics". (in preparation).
  This work was a collaborative effort for which each author made substantial contributions in all aspects.

TABLE OF CONTENTS

LIST OF ILLUSTRATIONS

LIST OF TABLES

Chapter 1

INTRODUCTION

1.1 Objective

This dissertation focuses on the mechanics of granular materials composed of arbitrarily shaped, rigid, cohesionless, and frictional particles. Within this scope, the objective is to develop novel theoretical and computational methodologies for predicting material response, by linking micromechanical information to macroscopic behavior. This includes:

- developing a high-fidelity discrete element framework for probing the incremental continuum behavior, from the perspective of plasticity theory, as a function of particle properties, configurational state, and past history;
- establishing an alternative multiscale Data-Driven modeling paradigm, in which material data are gleaned from discrete element computations;
- developing a complex network-based approach for probing nonlocal material behavior specifically focusing on failure by shear banding;
- extending the Data-Driven modeling paradigm to weak nonlocality by accounting for higher-order kinematics.

1.2 Approach

We shall confine our investigation to dry athermal granular materials, meaning collections of particles interacting via frictional forces within a medium of negligible viscosity such as air. Particles are considered large enough such that adhesive forces (e.g Van der Waals forces) are negligible. Further, we restrict our study to the quasistatic flow of such materials, close to jamming [220]. This is known as the granular solid regime, as opposed to the granular liquid or gas regime [147], and is highly relevant to many scientific and technological applications. These include the design of soft robotics [42], cushioning and protective equipment [116], aleatory jammed architectures [171], packing of food and pills [35], and, even, space exploration [166] (Fig. 1.1).

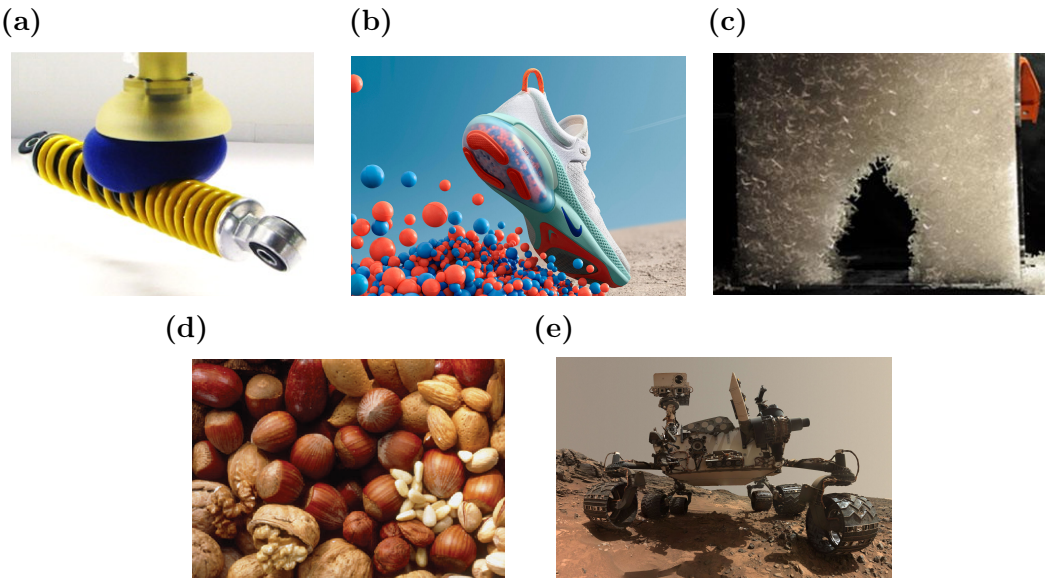

Figure 1.1: Applications of granular solids: a) Universal robotic gripper composed of particles encased in a flexible membrane (Source: reprinted from [42]). b) Bead-filled commercial shoe sole (Source: `https://news.nike.com/`). c) Freestanding architectures composed of topologically entangled z-shaped particles (Source: reprinted from [240]). d) Food as a granular material e) Interaction of a rover wheel with Martian regolith (Source: NASA-JPL).

Granular solids exhibit an intriguing range of complex continuum behavior [277, 124]. Their incremental stress-strain response is a function of their current state [48], which is, in turn, a manifestation of the morphology of the constituent particles and their interaction, in the presence of confining stress. We shall refer to these grain-scale morphological and interaction properties as the granular genome or 'DNA'. To accommodate changing boundary conditions, granular materials continuously rearrange their internal state, which gives rise to rich history-dependent behavior [297, 204]. The conventional approach for modeling such material behavior relies on constitutive laws formulated in the context of plasticity [318, 79]. However, these laws often rely on postulates and internal variables that are not micromechanically justified [332, 366], and are agnostic to the granular 'DNA', despite clear evidence of its importance [169]. Additionally, they tend to oversimplify, if not disregard, nonlocal effects that govern material failure. We seek to address these shortcomings by developing novel methods that accurately account for i) history-, state-, and constituent-dependence of the local stress-strain response, and ii) nonlocal effects accompanying material failure. To do so, we employ a four-pronged approach (Fig. 1.2).

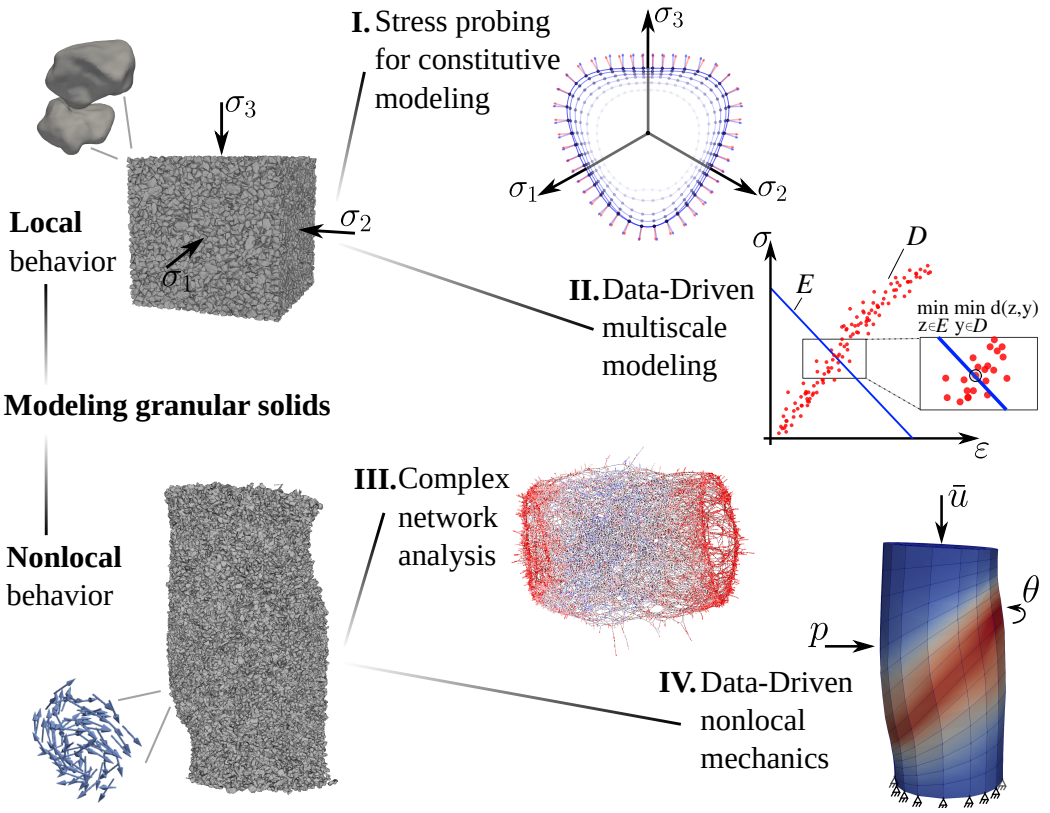

Figure 1.2: Overview of the four-pronged approach for behavior prediction in granular solids: I) Stress probing for identifying the incremental stress-strain response. II) Data-Driven multiscale modeling framework. III) Complex-network based description of nonlocal behavior. IV) Nonlocal extension of the Data-Driven framework.

In the first part of the thesis, we systematically study the incremental behavior of granular solids to motivate a new generation of micromechanically-inspired constitutive laws. To this end, we develop a framework designed to systematically probe the local incremental response of granular assemblies from the same initial state to multiple directions is stress space, in a process- termed stress probing. We rely on the recently developed Level-Set Discrete Element Method (LS-DEM) [170], which is able to resolve the interaction between particles of arbitrary 'DNA', and we control the expression of that 'DNA' to a particular state through simulated packing protocols. By analyzing stress probes carried out on different stress planes, we extract the reversible and elastic response, quantify the irregular and nonassociative nature of the flow rule, map the yield surface, and investigate work hardening and fabric evolution, all of the above as a function of granular morphology, state and history. Such a

detailed investigation has not been possible with previous numerical methods [48, 115, 189] or physical experiments [303].

In the second part of the thesis, inspired by the abundance of generated high-fidelity micromechanical data, we develop an alternative Data-Driven approach for predicting material response, which completely bypasses the need to define a constitutive law. Earlier methods based on machine learning [121, 237] are not thermodynamically consistent, rely on hidden representations devoid of physical meaning, and have uncontrolled extrapolative properties. By contrast, the proposed framework is thermodynamically sound and makes eminent physical sense. This new paradigm is based on the Data-Driven formulation of mechanics [172], which we appropriately extend to a multiscale setting. We particularly focus on optimally sampling the mechanical phase space through micromechanical (LS-DEM) calculations, and also develop two methods for parametrizing material history, one thermodynamically motivated and universal, and one statistically motivated and tailored to granular materials. Comparison with available experiments based on X-ray computed tomography are carried out to validate the developments. This concludes the modeling of the local history-dependent behavior undertaken in the first two parts of the thesis.

In the third part of the thesis, we direct our attention to understanding and modeling nonlocality arising from the self-organization of granular materials during failure. We particularly focus on establishing links between the topological, kinematical, and force signature of shear banding, a prototypical failure mode governed by nonlocal effects. This is made possible through a complex network analysis of a simulated sample of angular sand undergoing triaxial compression and failing by strain localization. We characterize the stability of two mesoscale topological structures, force cycles and force chains, and analyze the statistics of nonaffine kinematics. These aspects have not yet been addressed in three-dimensional or non-idealized systems. We conclude this part by analyzing the implications of our findings to strongly and weakly nonlocal continuum theories.

In the final part of the thesis, inspired by the observations of nonaffine higher-order kinematics governing the behavior during shear banding, we extend the Data-Driven paradigm to include such kinematics within a micropolar framework. The latter represents the prototypical example of a weakly nonlocal continuum, while other types of continua in this taxonomy can be addressed

in the same fashion. By formulating the problem on a phase space augmented by higher-order kinematics and their conjugate kinetics, we bypass the need to define an internal length scale, which is instead discovered from the data. In fact, with the incorporation of a novel distance measure, the framework becomes entirely parameter-free and exhibits improved error convergence properties compared to its predecessor. Among other applications, we investigate the physics-based regularization of the triaxial compression shear banding problem addressed above.

1.3 Organization of the thesis

Chapter 2 provides the necessary background on the fundamentals of granular mechanics, and reviews the state-of-the-art in modeling of the quasistatic flow of granular materials. It also serves to set the notation to be followed throughout this thesis.

Chapter 3 describes the stress probing framework for studying the incremental stress-strain response of granular materials, and establishes the notion of a granular 'DNA'. The main results regarding elasticity and reversibility, yielding and plastic flow, fabric evolution, as well as the influence of morphology and state are presented and detailed.

Chapter 4 presents the local multiscale Data-Driven framework for general materials focusing on the parametrization of material history, and the optimal sampling of the mechanical state space. After a general introduction of the theory, the scope of the framework is then restricted to granular materials, and appropriately validated against experiments.

Chapter 5 concerns the complex network analysis of nonlocality. We discuss the representation of a granular system undergoing shear banding as a network or graph, and, on that basis, we study the cooperative evolution of topology, kinematics, and forces.

Chapter 6 deals with the weakly nonlocal extension of the local Data-Driven paradigm, especially focusing on the micropolar continuum, in accordance with the observations of nonaffine kinematics in the previous chapter. Once again, the theory is presented first in all generality before being restricted to granular materials and validated against experiments.

Chapter 7 concludes with the main findings and provides a future outlook.

Chapter 2

BACKGROUND

2.1 Fundamentals of granular material behavior

Granular materials exhibit a wide range of complex nonlinear behavior, undergoing a transition between three distinct states of matter (Fig. 2.1). In the quasistatic regime, they behave as solids that can withstand significant shear stresses through a dense network of force chains [207, 55, 88, 220]. Their incremental stress-strain response depends on their microstructural state, which encodes the complete history of their past deformation [277]. To model this regime, physicists and engineers have predominantly relied on continuum analysis, specifically frictional rate-independent plasticity [297, 318, 353, 244, 79], as well as multiscale analysis [18, 230, 249, 369].

Subject to increased shearing rate, granular materials undergo a transition to an unusual non-Newtonian liquid regime [147, 52]. This state is characterized by complex rate-dependence arising from pronounced particle velocity fluctuations [76]. Researchers have been developing continuum rheological laws [315, 229, 160, 321, 114, 275, 19] in an ongoing effort to capture this regime.

Upon further increase of the rate of imposed shear, granular materials undergo a second transition to a gas regime, where particles interact primarily through inelastic collisions. Modeling of this state is largely based on kinetic theory, originally introduced for classical gases [65], which is appropriately extended by considering dissipative colisions and granular temperature [53, 317, 152, 216, 316, 368, 52].

Despite century-long research on granular materials [277], understanding and predicting granular material behavior in any of these regimes continues to be extremely challenging, and calls for a new generation of modeling paradigms. In the following, we will briefly review the modeling of the quasistatic (solid) regime of granular matter, which is of immediate interest to this study.

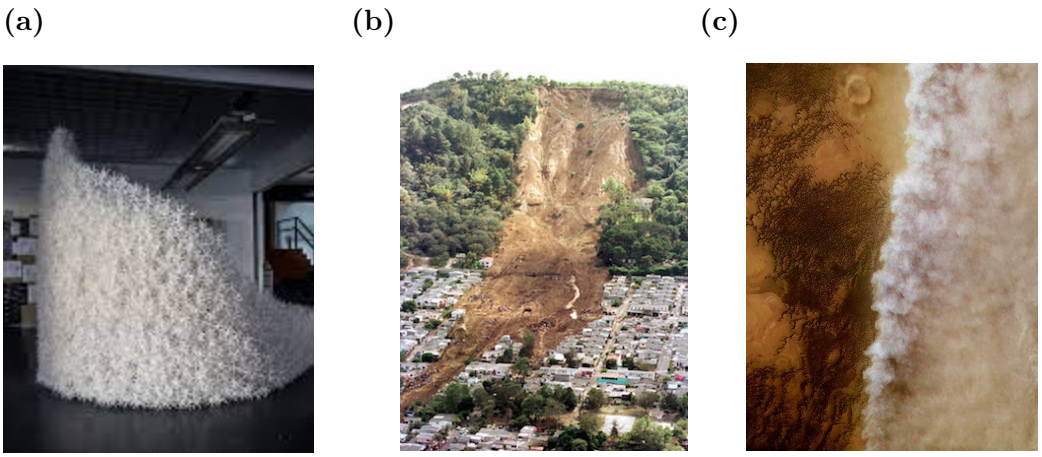

Figure 2.1: Granular matter as a solid, liquid, and gas: a) Jammed entangled architectures (ICD Stuttgart ActLab). b) Landslide in El Salvador (USGS). c) Sand storm on Mars (European Space Agency).

2.2 Continuum modeling of granular materials

Before delving into the major developments in continuum modeling of granular materials in the quasistatic regime, we shall first briefly review the basic framework of continuum mechanics of simple solids.

2.2.1 Brief summary of continuum mechanics

Kinematics

Presented here is a summary of the theory of continuum mechanics from a Lagrangian perspective. It sets the basic framework, while establishing the notation used throughout the thesis. Consider a simple body occupying a domain $\mathcal{B}$ in a reference configuration, and subjected to a deformation mapping φ to a deformed configuration $\varphi(\mathcal{B})$. The motion of a material point $\mathbf{X}$ of the body is given by $\mathbf{x} = \varphi(\mathbf{X}, t)$. Assuming differentiability of φ, one can obtain the deformation gradient $\mathbf{F}$:

$$F_{ij}(\mathbf{X}, t) = \frac{\partial \varphi_i}{\partial X_j}(\mathbf{X}, t). \tag{2.1}$$

The linearization of $\mathbf{F}$ around the reference configuration leads to the usual symmetric strain tensor:

$$\varepsilon_{ij} = \frac{1}{2}(u_{i,j} + u_{j,i}) \tag{2.2}$$

where $\mathbf{u}(\mathbf{x})$ denotes the displacement field.

Principle of virtual work

Under body forces $\mathbf{b}(\mathbf{x})$ and tractions $\bar{\mathbf{t}}(\mathbf{x})$ prescribed over $\partial\mathcal{B}_N$, the principle of virtual work reads:

$$\int_{\mathcal{B}} \left(\sigma_{ij}\eta_{i,j} - \rho b_i \eta_i\right) - \int_{\partial\mathcal{B}_N} \bar{t}_i \eta_i dS = 0 \tag{2.3}$$

for all admissible displacement fields η, resulting in the equilibrium equations:

$$\sigma_{ij,j} + \rho b_i = 0 \tag{2.4}$$

$$\sigma_{ij} n_j = \bar{t}_i \quad \text{on } \partial\mathcal{B}_N \tag{2.5}$$

where $\boldsymbol{\sigma}(\mathbf{x})$ is the Cauchy stress tensor field.

2.2.2 Constitutive modeling for simple continua

The constitutive description of material behavior provides a closure to Eqs. 2.2-2.4, by postulating an analytical relation between stress and strain. The principles constraining such a relation are furnished primarily by the first and second law of thermodynamics, and secondarily by a set of well-established observations about granular materials.

The first and second law of thermodynamics

The first thermodynamic principle furnishes the existence of an extensive quantity U termed the internal energy density, which increases with mechanical work and heat source density s, but decreases with heat flux $\mathbf{h}$. In its local form it reads:

$$\rho\dot{U} = \sigma_{ij}\dot{\varepsilon}_{ij} + \rho s - h_{k,k}. \tag{2.6}$$

The second thermodynamic principle introduces the concept of entropy production, and is equivalently furnished by the Clausius-Duhem inequality:

$$\rho\dot{\eta} - \frac{\rho s}{T} + \frac{h_{k,k}}{T} \geq 0 \tag{2.7}$$

where η is the entropy density, and T the temperature.
In the absence of significant thermal dissipation as in the systems discussed in this work, the above relations can be combined to yield the reduced Clausius-Planck inequality:

$$\rho\dot{\eta}T - \rho\dot{U} + \sigma_{ij}\dot{\varepsilon}_{ij} \geq 0. \tag{2.8}$$

Beyond the above thermodynamic constraints, we review two additional constraints for constitutive models of granular materials, namely critical state theory and the stress-dilatancy relation.

Critical state

Perhaps the most important feature of the behavior of granular materials is the extended memory of their past deformation. Under general loading paths, the internal structure of granular materials evolves while retaining the memory of their initial state. Yet, early experiments revealed the existence of an ultimate state [297, 318, 34], at which the memory of their initial state is fully lost. The Critical State Theory (CST), inspired by these experiments, suggests a unique relation between the deviatoric stress $q = \sqrt{3/2} s_{ij} s_{ij}$ (where $s_{ij} = \sigma_{ij} + p\delta_{ij}$), the mean pressure p and the void ratio e defined as:

$$q = \mu_{cs} p \tag{2.9}$$

$$e = e(p, p_i) \tag{2.10}$$

where μ_{cs} is the critical state friction coefficient and $e(p, p_i)$ is a well-defined function of the mean pressure and a characteristic strength p_i related to a specific material. Upon continued shear deformation at that state, particulate materials remain at constant stress and constant volume. Traditional CST assumed that, at critical state, any initial form of fabric (particle/contact orientation) has disappeared, rendering the microstructure isotropic. Yet, microstructural studies [251, 252, 280, 201] have revealed a particular fabric formation at critical state. As a result, the so-called Anisotropic Critical State Theory (ACST) [204] has recently been established, which sets the additional requirement for attainment of critical state that an appropriately defined fabric tensor $\mathbf{F}$ converges to a critical state value $\mathbf{F}_c$. We will discuss such fabric tensors later in Section 2.3.2.

Stress-dilatancy relation

Another fundamental aspect of granular material behavior is the relation between shear-induced volume change (dilatancy) and the mobilized friction, typically termed the stress-dilatancy relation. Simple considerations of the total work W performed by shear and dilation during simple shear deformation

led to the formulation of a stress-dilatancy relation [334, 302]. Specifically, letting ε_v and ε_q be the volumetric and shear strain, one easily obtains an expression for the mobilized friction angle η:

$$\mu = \frac{q}{p} = -\frac{\dot{\varepsilon}_v}{\dot{\varepsilon}_q} + \frac{\sigma_{ij}\dot{\varepsilon}_{ij}}{p\dot{\varepsilon}_q}. \tag{2.11}$$

For constant shear rate, mean pressure, and rate of work, this relation establishes that the mobilized friction angle emerges from two mechanisms. The first mechanism relates to the geometric constraints on particles due to shear induced dilatancy $D = -\frac{\dot{\varepsilon}_v}{\dot{\varepsilon}_q}$ and has a linear contribution. On the other hand, the second term is typically constant, and represents the mobilized friction $\mu_{cs} = \frac{\dot{W}}{p\dot{\varepsilon}_q}$, at the state of zero dilatancy i.e. the critical state. Variations of the relation have also been proposed [37, 205], which however retain the fundamental implications for constitutive modeling.

To illustrate the above concepts and demonstrate some more of the intricacies in the behavior of granular materials, let us consider the response of a dense specimen under drained triaxial compression and that of a loose specimen under undrained (constant-volume) triaxial compression (Fig. 2.2). A dense sample will typically exhibit an initially contractive response which then transitions to a dilative response, in a process termed phase transformation. This leads to a peak in the shear stress followed by softening before collapsing to critical state. On the other hand, loose samples may not experience this transition. Instead, they experience a dramatic decrease in strength (liquefaction), due to their tendency but inability to contract.

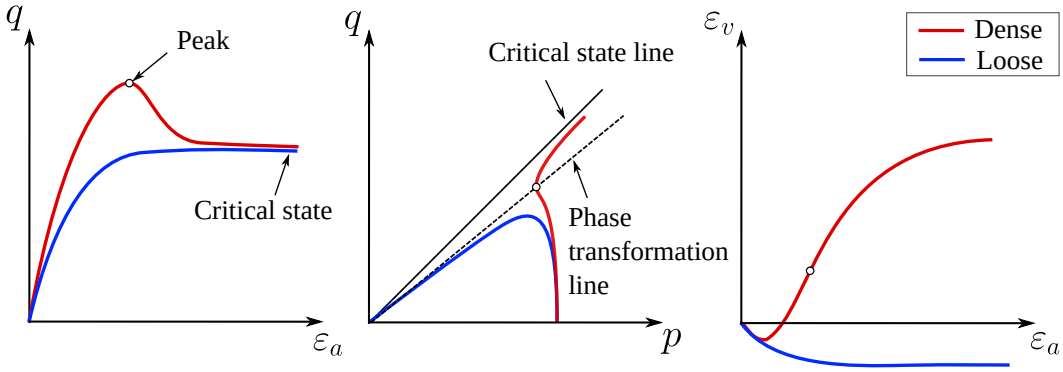

Figure 2.2: Response of dense (red lines) and loose (blue lines) specimen subject to triaxial compression.

Now that we have reviewed the essential constraints underlying the continuum modeling of granular solids, we delve into a more detailed analysis of different

families of available approaches. The vast majority of them rely on plasticity theory taking several different forms.

Hyperelastoplasticity

Hyperelastoplasticity encompasses the internal variable formalism for rate independent material behavior. Within this formalism, it is typical to assume, under athermal conditions, a free energy density of the form $\mathcal{A} = \mathcal{A}(\varepsilon_{ij}, q_{ij})$ where q_{ij} is an appropriately defined internal variable, encapsulating history effects. Using standard thermodynamics arguments, one obtains the equilibrium relations:

$$\sigma_{ij} = \rho \frac{\partial \mathcal{A}}{\partial \varepsilon^e_{ij}} \qquad \chi_{ij} = -\rho \frac{\partial \mathcal{A}}{\partial q_{ij}} \tag{2.12}$$

where χ_{ij} is a generalized stress-like kinetic quantity conjugate to the internal variable. Any irreversible dissipative processes are tied to the evolution of the internal variable. To describe the latter, a dissipation potential $d = d(\chi_{ij}(\varepsilon_{ij}, q_{ij}), \dot{q}_{ij})$ is introduced. The yield surface f emerges as the Legendre transform of the dissipation potential, and the flow rule/internal variable evolution law emerges as a generalized normality rule [140]:

$$f = \chi_{ij}\dot{q}_{ij} - d = 0 \qquad \dot{q}_{ij} = \lambda \frac{\partial f}{\partial \chi_{ij}}. \tag{2.13}$$

The yield function and plastic flow emerge from the dissipation potential, instead of being imposed [74], thereby ensuring thermodynamic consistency.

Classical elastoplasticity

Classical elastoplasticity is a more practical application of plasticity which overcomes the modeling difficulties in describing complex material response in terms of potentials [83], at the expense of not satisfying thermodynamic consistency a priori. This framework defines the incremental material response by postulating an additive decomposition of strain into elastic and plastic components, an elasticity tensor $\mathbb{C}^e_{ijkl}$, a yield surface $f(\sigma_{ij}, q_{ij})$, and a plastic potential $g(\sigma_{ij}, q_{ij})$, all resulting in a closed set of equations:

$$\dot{\sigma}_{ij} = \mathbb{C}^e_{ijkl}\dot{\varepsilon}^e_{kl} \qquad \varepsilon_{ij} = \varepsilon^e_{ij} + \varepsilon^p_{ij} \tag{2.14}$$

$$f(\sigma_{ij}, q_{ij}) = 0 \qquad \dot{\epsilon}^p_{ij} = \dot{\lambda}\frac{\partial g}{\partial \sigma_{ij}} \qquad q_{ij} = q_{ij}(\epsilon^p_{ij}) \tag{2.15}$$

where λ represents an appropriately defined Lagrange multiplier.
Many such theories have so far been developed that are able to predict many essential features of granular material behavior, including pressure-dependent and fabric-dependent elasticity, nonassociativity [193] and noncoaxiality (non-coincidence of the principal axes of stress and plastic strain rate tensors), shear-induced anisotropy [299, 300, 117, 132, 184], phase transformation [145], critical state consistency [149, 17, 79]. Steps towards the extension of classical plasticity have been taken with the introduction of multiple surfaces, as in the bounding surface plasticity paradigm [223, 79, 204, 118], or corners of surfaces as in the vertex based elastoplasticity model [67].

Hypoplasticity and incrementally nonlinear theories

The breakdown of some of the postulates introduced by the aforementioned paradigms, such as the regularity of the flow rule [48], has led to the development of a family of incrementally nonlinear theories. Characteristic examples include hypoplasticity [179, 335, 377, 378] and generalized plasticity [267]. These theories do not explicitly depend on a yield function or a plastic potential nor do they require the additive decomposition of strain. The constitutive relations typically take the general form [81, 332]:

$$\dot{\sigma}_{ij} = \mathbb{D}_{ijkl}\big(\sigma_{ij}, \frac{\dot{\varepsilon}_{ij}}{\|\dot{\varepsilon}_{ij}\|}, q_{ij}\big)\, \dot{\varepsilon}_{ij} \tag{2.16}$$

where $\mathbb{D}$ is a directionally variable elastoplastic tensor.

A nice classification of all the above theories can be achieved in terms of the unifying concept of tensorial zones [130, 81]. Standard elastoplastic models are considered bilinear and incorporate two tensorial zones corresponding to loading and unloading [82], while incrementally nonlinear theories incorporate a continuous dependence of the constitutive relation to the loading direction [370, 84, 124].

Microstructural plasticity models

A separate family of constitutive models represents the continuum behavior as the average of an appropriately defined set of micro-systems, such as a contact network [61, 153, 206, 243, 329, 244, 64, 248, 365, 119] or a family of slip systems or microplanes [382, 186]. These theories attempt to bypass the need for continuum-scale postulates by upscaling a lower-order description of

each micro-system through statistical homogenization. The fundamental principles are the projection (localization) of macroscopic strain to microscopic kinematics (contact/slip plane kinematics), the use of contact scale constitutive laws towards a force distribution, and finally the homogenization of forces towards the macroscopic stress response. Characteristic examples include the microdirectional model [248], which draws similarities from earlier statistical models [243, 244], which in turn can be considered as a generalization of the double-sliding model [158, 226]. The fundamental challenge of this family of methods is the construction of a realistic *nonaffine* strain projection (localization) operator, which is an ill-posed problem. We refer to [266] for a relevant review.

2.2.3 Instabilities

Granular materials are notoriously prone to instabilities in the form of localized [354, 146, 87] or diffuse [85] failure modes. This has fundamental implications regarding the non-uniqueness of the material response in the post-instability regime [290, 36]. Especially the emergence of shear bands is tied to the mathematical concept of loss of ellipticity of the governing equation. The usual criterion for continuum localized instability in the form of a shear band is the loss of positiveness of the eigenvalues of the acoustic tensor [221, 290], in the framework of bifurcation theory [304]:

$$\det n_{ij} C_{ijkl} n_{kl} = 0 \tag{2.17}$$

where $\mathbf{n}$ denotes the unit normal of the unstable direction. Another instability criterion concerns the loss of positiveness of the second-order work [85, 247], also known as Hill's material instability criterion [138], which states:

$$d^2 W = \dot{\sigma}_{ij} \dot{\varepsilon}_{ij} > 0. \tag{2.18}$$

This criterion examines both the stress and strain paths, and has been shown to generalize all other known criteria [80]. From a thermodynamic perspective, it is the loss of convexity of the dissipation potentials that leads to material instability.

It is well established that simple continua fail to capture the post-localized response, which instead calls for generalized or nonlocal theories [154]. The latter effect a regularization of the problem by introducing an appropriate length scale.

2.2.4 Nonlocal modeling

Evidence of nonlocality

In the standard continuum description discussed so far, a solid body is decomposed into a set of infinitesimal material points, whose constitutive behavior is independent from one another except via the exchange of linear momentum, energy, and entropy. Nonlocality is the deviation from this idealized description, and is a manifestation of the internal microstructure of a material [154, 155]. Perhaps the most studied aspect of nonlocality in granular materials is the one related to shear banding. The pioneering experiments in [296, 239] first established the width of a shear band in granular materials at 8-10 particle diameters. Additional evidence of nonlocality is furnished by the formation of force chains [211, 282, 283, 238] and force communities [122] of characteristic correlation length [219, 328], or the correlated nonaffine movement of particle clusters [278, 274, 327] leading to vortices of characteristic sizes [269, 293]. These phenomena are associated with shear banding, with studies showing the development of vortices inside an incipient shear band, which in turn [343] induce force chain buckling [254, 345, 344]. Nonlocality also manifests itself in several other forms, e.g. in nozzle jamming of silos [384] and thickness-dependent repose angles in surface flows [273]. Studies suggest that nonlocal effects are influenced and potentially enhanced by irregular particle shapes [114].

A plethora of nonlocal theories have been developed that introduce a length scale in an effort to capture these phenomena. These largely fall under two main categories, strongly nonlocal and weakly nonlocal theories [294]. Strongly nonlocal theories typically rely on an integral formulation [182, 33] or a constitutive equation that is itself a PDE [7, 353, 161]. On the other hand, weakly nonlocal theories, also known as gradient or generalized continuum theories, enrich the constitutive description with gradients of local kinematic variables. Due to the presence of these gradients, the response at a material point depends on the response at a neighborhood of that point (Fig. 2.3).

As a general rule, many of these theories have been succesful in regularizing the ill-posed local problem, but have not enjoyed general acceptance due to their complex formulation or the lack of a sound micromechanical basis. Only recently, the hypotheses inherent to some of these formulations have been supported by micromechanics, through advanced homogenization techniques

[94, 93, 29, 341, 210], kinematic models [343], and direct micromechanical descriptions of order parameters [374].

Strongly nonlocal theories

The majority of strongly nonlocal theories rely on a constitutive equation that is itself a PDE, instead of an ODE, as in local theories. This PDE models the diffusion of an internal variable (e.g. plastic strain) or an additional field variable (e.g. granular fluidity, order parameter, spot concentration, STZ density) that represents the density g of a rearrangement event. It typically takes the form of a Helmholtz-type differential equation:

$$g - \ell \nabla^2 g = g^{loc} \tag{2.19}$$

where ℓ is the length scale and g^{loc} is the density g under the assumption of locality. As a result, the length scale is identified as the characteristic length scale of this diffusion process driven by the correlated motion of the material neighborhood. These theories have been used to describe the unjamming transition during shear banding or the related transition between the solid and liquid granular flow regimes. We briefly review the major developments below.

One of the first theories of this family was developed in the context of gradient plasticity, which introduces the Laplacian of the plastic shear strain in the

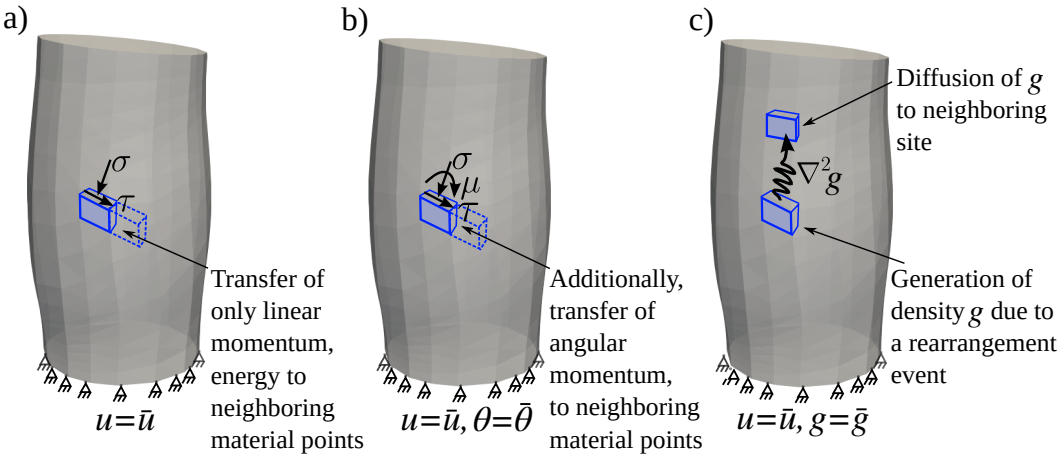

Figure 2.3: Modeling of granular solids: a) The classical (local) Cauchy continuum, b) the weakly nonlocal continuum, exemplified by the micropolar description, and c) the strongly nonlocal continuum characterized by the diffusion of the density of a local event (e.g. force fluctuation, temperature).

yield function and flow rule [7, 353, 8]. In a different study, related to the granular solid-fluid transition [21], a fluidization model was developed, which is based on an additive decomposition of the stress tensor into a solid and fluid part. The authors suggested that the order parameter defined as the ratio between the two parts is governed by a Ginzburg-Landau equation of the above type. A similar nonlocal model that is based on the self-activation processes driven by velocity fluctuations was developed in [275]. In this model, granular temperature or stress fluctuations may trigger a rearrangement of the grains somewhere else. The nonlocal granular fluidity model of [161] is also similar to the fluidization model and postulates the existence of a granular fluidity field, which represents an inverse viscosity and enters the flow rule, again via a similar diffusion equation. For a review of the concept of fluidity, the reader is referred to [159, 40]. Finally, the Shear Transformation Zone (STZ) theory was first developed in the general context of amorphous solids [222, 107] and then applied to granular flow [106]. According to this theory, there exist regions of characteristic size (STZs) that are susceptible to localized failure under shear. In the context of granular materials, STZs are typically assumed as two-state systems (jammed/flow state). The STZ theory also relies on the diffusion of the granular temperature to drive these rearrangements, thereby introducing an effective length scale for this process.

Weakly nonlocal theories (Generalized continua)

The most general description of weak nonlocality is furnished by the micromorphic continuum [101, 99], according to which, each material point in a macroscopic body is itself considered a continuum at an appropriate scale of observation, and is subject to its own microdeformation. The theory effectively endows the material point with a director triad which, under the action of a microdeformation, is mapped to its deformed configuration. This mathematical assumption introduces additional degrees of freedom to each material point beyond the translational ones present in the standard Cauchy continuum. The properties (degrees of freedom) of the microdeformation induce a hierarchy in the class of generalized continua [120, 113].

By restricting the microdeformation to an independent rigid microrotation, one obtains the micropolar continuum [75, 98]. This results in a total of six degrees of freedom for each material point, three translational ones and three

rotational ones. A particular variation of the micropolar continuum, where the microrotation is prescribed to be the same as the macroscopic rotation, is known as the indeterminate couple-stress theory [347, 177]. Similarly, restricting the microdeformation to the macroscopic deformation gradient, gives rise to strain-gradient (or second-grade) theory [233, 111, 110]. The common characteristic of these higher-order theories is the induced asymmetry of the stress tensor and the presence of additional kinetics furnished by the couple stress, in the case of micropolar theory, and the double-stress in the case of strain gradient theory, that are conjugate to the microdeformation gradient. These thermodynamic quantities are subject to their own balance equations. We refer to [113] for a relevant review.

Several of the above formulations and their kinematical assumptions have been explored in modeling granular materials. Perhaps the first breakthrough was the observation that rotational and vortical motion is a major dissipation mechanism in these materials [255, 253, 28] and affects macroscopic strength [330]. This inspired the use of micropolar theory, in the context of plasticity, for modeling shear banding [239, 336, 12]. On the other hand, the restricted micropolar (couple-stress) assumption has so far not been validated by micromechanical studies. In another set of elaborate experiments [187], it was shown that strain gradients also affect the response of granular materials, and that a simple strain gradient model can predict the spacing of microbands in some cases. Such strain-gradient models have also been obtained by upscaling micromechanics-based descriptions [59]. Finally, researchers have modelled granular materials as micromorphic continua [287]. Although micromorphic theory is rich enough to capture the full range of behavior of granular materials, it has not been rigorously proven that such a complex kinematic assumption is indeed necessary.

2.3 Discrete modeling of granular materials

A major breakthrough in the understanding of granular materials was enabled by the development of methods for particle-scale modeling and simulation. These include the widely used Discrete Element Method (DEM) [78], which we review below, as well as its non-regularized version, termed Non-Smooth Contact Dynamics (CD) [235, 148].

2.3.1 Discrete Element Method (DEM)

DEM was proposed by [78] and resolves the kinematics of rigid but locally compressible particles whose interaction is modeled by spring and dashpot systems. Essential ingredients of DEM include the representation of particle morphology, the representation and detection of contact between particles, and the contact laws. In the original formulation, particles are represented as spheres. Each contact point c of each particle is characterized by a unit vector $\mathbf{n}$, which in turn describes the orientation of the normal contact force $\mathbf{f}_n^c$ (Fig. 2.4 a)). Typically, either a nonlinear (Hertzian) or a linear (Hookean) contact is assumed, that is capped by Coulomb friction. Assuming the latter, the interparticle contact forces associated with a contact c is given by:

$$\mathbf{f}^c = \mathbf{f}_n^c + \mathbf{f}_t^c \qquad \mathbf{f}_n^c = k_n \delta \mathbf{n} \qquad \mathbf{f}_t^c = -\frac{\Delta \mathbf{s}}{\|\Delta \mathbf{s}\|} \min(k_t \|\Delta \mathbf{s}\|, \mu \|\mathbf{f}_n^c\|)$$

where k_n (k_t) is the normal (tangential) Hookean stiffness, related to the elastic properties of the individual particles, δ_n is the interparticle penetration (local contact deformation), $\Delta \mathbf{s}$ is the accumulated tangential contact displacement, and μ is the friction coefficient.

Once all contacts have been detected, and the total forces $\mathbf{f}_i$ and moments $\mathbf{m}_i$ acting on each particle i have been computed, the particle dynamics are updated through Newton's equations of motion:

$$m_i \frac{d\mathbf{v}_i}{dt} + C\mathbf{v}_i = \mathbf{f}_i + m_i \mathbf{g} \tag{2.20}$$

$$I_i \frac{d\boldsymbol{\omega}_i}{dt} = \mathbf{m}_i \tag{2.21}$$

where $m_i, \mathbf{v}_i, \boldsymbol{\omega}_i$ is the mass, velocity, and angular velocity of the particle i, respectively, while C represents a global damping parameter. The equations are usually integrated explicitly with a time step dependent on the spring stiffness and particle mass [78]. In fact, the time increment needs to be small enough to resolve the period in which particle collision occurs. After the new contacts are established, the process is repeated.

DEM has been succesfully applied to study critical state mechanics, shear localization [77, 27], yielding [338], stress-dilatancy relations [125], incremental granular behavior [28, 48], grain crushing [66, 133], and many other aspects of granular material behavior.

Variations of DEM

Since its inception, the main criticism against DEM has been its inability to capture complex shapes. To tackle this limitation, several variants of DEM have been introduced that can model non-spherical particles. Polyhedral DEM [242] is able to capture the interaction between arbitrary convex polytopes. The multi-sphere method [250] uses clumping of spheres to represent shape. Super-quadrics [272] extend the ability to detect contact to a wider variety of shapes albeit at a higher computational cost. The same is true for the so-called potential particles [263]. In the Level-Set Discrete Element Method [170], the geometry of particles is defined by an implicit level set function, whose value represents the distance from the particle surface. The method represents the most versatile DEM framework to-date.

2.3.2 Granular texture

In this section, we briefly review the most common descriptors of the arrangement of granular assemblies. These descriptors often furnish internal variables adopted within continuum theories.

Packing density and coordination number

It is widely accepted that the most important factor determing the mechanical response of a granular assembly is its packing density, or equivalently, its packing fraction or void ratio. Early studies established a correlation between the packing fraction and the coordination number Z [252]. The latter admits several definitions [188, 338], the simplest of which being the mean number of contacts per particle:

$$Z = \frac{2N_c}{N} \tag{2.22}$$

where N_c is the total number of contacts and N the total number of particles in the assembly. When Z is below a critical value Z_c, then the assembly is at a so-called isostatic state [137]. The critical coordination number Z_c is also the prototypical microstructural signature of the jamming transition [281]. A treatment of isostaticity within rigidity theory and its consequences in instabilities are given in [236], while connections between isostaticity and critical state are drawn in [300, 183].

Fabric

Beyond the isotropic description of packing furnished by the packing fraction, the second most important descriptor of granular texture is the orientational arrangement of the constituent particles, generally termed fabric [251]. Several descriptions of fabric have been suggested in the literature [257, 311, 201], each relying on the definition of a unit vector $\mathbf{n}$ describing the direction of a certain microstructural property [313, 164] such as the particle major axis, branch vectors, contact normal. Denoting as $E(\mathbf{n})$ the orientational density function of these microstructural quantities, we have $\int_\Omega P(\mathbf{n})d\Omega = 1$, and $P(\mathbf{n}) = P(-\mathbf{n})$ due to the lack of intrinsic parity. A second order approximation of $E(\mathbf{n})$ gives rise to the usual (second-order) fabric tensor [256]:

$$\mathbf{F} = \int_\Omega E(\mathbf{n})\mathbf{n} \otimes \mathbf{n}\, d\Omega \tag{2.23}$$

or, in the usual discrete notation:

$$\mathbf{F} = \frac{1}{N}\sum_{k=1}^{N} \mathbf{n}^k \otimes \mathbf{n}^k \tag{2.24}$$

where N is the total number of contact points, in the case where $\mathbf{n}$ describes the contact normals.

Several studies have shown that second order expansions can well approximate both the orientational distribution of contact normals, as well as those of normal and tangential contact forces [299]. The principal direction of contact forces generally coincides with the principal stress axis, while the principal direction of the contact normal fabric evolves in the presence of shear [153, 47] such that it also aligns with the principal stress (and strain rate) axis [349, 201, 204]. This holds true in other types of fabric tensors e.g. those concerning the orientation of elongated particles [38]. Fabric anisotropy is also intimately related to the onset of yielding, and has been successfully used as an internal variable within continuum plasticity theory [301, 281, 377, 204].

Network analysis

The coordination number and fabric are only a few examples of a far more general tool for modeling granular systems, namely network analysis [265], whose objective is the topological characterization of these systems. The most common network description of a granular system is one furnished by a graph with

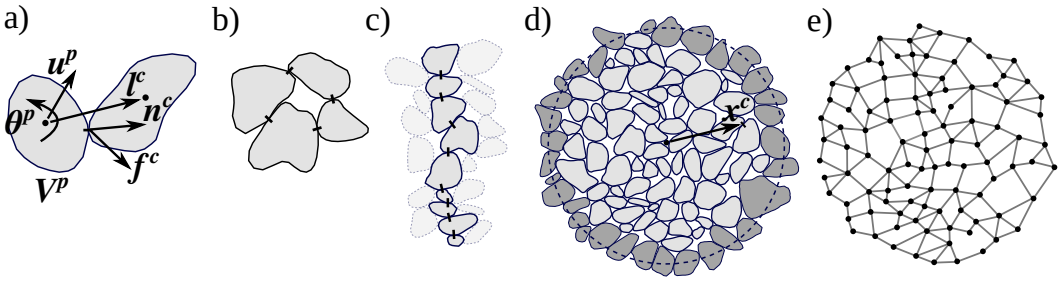

Figure 2.4: Modeling discrete systems: a) Interparticle contact. b) Force cycle. c) Force chain. d) Representantive assembly. e) Graph representation of the assembly.

grains serving as nodes and contacts between grains serving as edges (Fig. 2.4 e)). Binary graphs account for the mere presence of a contact, while weighted graphs additionally account for the level of interparticle force. The contact graph described above can also be complemented by the void graph, giving rise to a dual description, often referred as a Satake-graph [313]. Graph theoretic and complex network approaches to granular assemblies have been considered in many studies [312, 314, 188, 361, 342]. Within network analysis, the concept of degree distribution has generalized the notion of a coordination number [22], and provided a measure of heterogeneity in granular systems. Studies of the weighted (force) network have established several statistical properties such as the distribution of contact forces [219, 209, 282] as well as relations with bulk properties [299, 31, 258]. Complex networks analysis has also focused on different centrality and clustering measures and their correlation with failure nucleation [361]. Other studies have focused on identifying stable and unstable mesoscale structures [314, 26, 188, 285, 213, 323, 342]. Finally, a plethora of studies have focused on the identification of communities [270, 30, 342]. Of these communities, two distinct families have monopolized the interest, quasi-linear filamentary clusters, termed force chains [270] (Fig. 2.4 c)) and closed loop clusters, termed force cycles [342] (Fig. 2.4 b)). We elaborate on these two patterns in the following sections.

Force chains

The study of force chains has long attracted the interest of researchers [89, 55, 282, 270]. Photoelasticity and related techniques, as well as DEM have provided the most popular force chain detection techniques [89, 209, 282, 142,

270]. Before their detection, the presence of force chains was anticipated by inspecting the distribution of contact forces in an assembly. Force chains comprise the strong network that sustains any applied shear stress, while the complementary weak network primarily contributes to the mean pressure [279]. The two networks have fundamentally different characteristics, with the forces in the strong network (above average) exhibiting an exponential decay, and the forces in the weak network (below average) exhibiting a power law decay. The study of force chains have also given rise to several models explaining the observed heterogeneities [238, 276], including a hyperbolic description of granular systems [39] (as opposed to the usual elliptic nature of continuum mechanics). According to this description, the stress propagates along characteristic directions, which are the experimentally observed force chains in granular configurations. Force chains have been shown to align with maximum compressive principal stresses [219] and are prone to buckling instability [342]. The length of force chains was first studied in [270], and later in [305] in relation to their coordination number, in [339] in relation to their confined buckling, and in [379] with respect to their aging properties.

Force cycles

On the other hand, force cycles refer to the arrangement of particle contacts in a closed loop [314, 26, 188, 342, 184] (Fig. 2.4 b)), and have not received as much attention as force chains. Cycle size distributions have been analyzed in [213, 346] in relation to their stability. In [342], the authors studied the evolution of these cycles up to the onset of shear banding and found that three-cycles provide the necessary lateral confinement for force chains. This complemented earlier results of studies on the importance of cycles for the stability of tilted granular packings [323]. Finally, the fabric and stress-strain characteristics of these cycles have been investigated in [184, 246, 245, 51].

2.3.3 Homogenization

Stress

The average macroscopic stress in an assembly of granular particles (Fig. 2.4 d)) is defined as [20]:

$$\bar{\boldsymbol{\sigma}} = \frac{1}{\Omega} \sum_{p=1}^{N_p} \Omega_p \bar{\boldsymbol{\sigma}}^p \tag{2.25}$$

where N_p is the number of particles in the assembly, and $\bar{\boldsymbol{\sigma}}^p$ is the average stress in particle p obtained as:

$$\bar{\boldsymbol{\sigma}}^p = \frac{1}{\Omega_p} \sum_{c=1}^{N_c^p} \mathrm{sym}\left(\mathbf{f}^c \otimes \mathbf{x}^c\right) \tag{2.26}$$

where $\mathbf{x}^c$ is the vector defined from the origin to the point of application of the contact force $\mathbf{f}^c$ at the contact point c (Fig. 2.4), with a total number of contact points N_c^p in a particle p.

Combining the two expressions and after some simple manipulations, one obtains the following compact expression [68] for the average stress:

$$\bar{\boldsymbol{\sigma}} = \frac{1}{\Omega} \sum_{c=1}^{N_c} \mathrm{sym}\left(\mathbf{f}^c \otimes \mathbf{l}^c\right) \tag{2.27}$$

where $\mathbf{l}^c$ is the so-called branch vector connecting the centroids of two particles in contact, and N_c is the total number of contacts in the assembly. Note that this interpretation of a stress tensor corresponds to a simple solid, where the symmetry of $\boldsymbol{\sigma}$ is required to ensure moment equilibrium.

Strain

The homogenized description of strain is not as straightforward, and no widely accepted formulation exists. Instead, several formulations have been proposed [26, 185, 135], an evaluation of which may be found in [91]. According to the equivalent continuum formulation [26]:

$$\bar{\boldsymbol{\epsilon}} = \frac{1}{V} \sum_{e} \mathbf{u}^e \otimes \mathbf{d}^e \tag{2.28}$$

where e represents edges of tetrahedra forming a Delaunay tesselation of the assembly and $\mathbf{d}^e$ is the complementary area vector of the edge $e(p,q)$, defined as:

$$\mathbf{d}^e = \frac{1}{12}\sum_{t=1}^{T_e}(\mathbf{b}^{q_t} - \mathbf{b}^{p_t}) \tag{2.29}$$

with the summation being over all T_e tetrahedra sharing the edge $e(p,q)$.

2.3.4 Higher-order homogenization

Homogenization of discrete kinetics towards stresses and couple stresses has been attempted from different perspectives. There is currently no overall consensus regarding the form of the homogenized couple stress or its uniqueness. In this section, we present the main three approaches in the literature, Hashin's principle approach [94], the principle of virtual work approach [29, 60], and finally, the coarse graining approach [128].

The Hashin's principle approach

Assuming rigid particle and point contact forces, and invoking equilibrium and scale separation arguments (Hashin's principle), Ehlers et al. [94] was able to recover the stress in a form similar to that of [68]:

$$\langle \sigma_{ij} \rangle = \frac{1}{V}\sum_{c\in\partial\mathcal{R}} f_i^c x_j^{p(c)} \tag{2.30}$$

and obtain an expression for the couple stress:

$$\langle m_{ij} \rangle = \frac{1}{V}\int_{\partial\mathcal{R}} m_i x_j ds = \frac{1}{V}\sum_{c\in\partial\mathcal{R}} \epsilon_{ikl} l_k^c f_l^c x_j^{p(c)}. \tag{2.31}$$

In the above expressions, $\mathbf{x}^{p(c)}$ denotes the position of the center of the particle on the RVE boundary corresponding to contact c (Fig. 2.4). The authors were able to show that couple stresses can naturally arise from the eccentricity of contact forces, and not necessarily from the existence of contact moments.

The principle of virtual work approach

A different strategy for deriving micropolar and, generally, gradient kinetics, was laid out in [29] (and later [64]). The authors first obtain expressions for the discrete (grain-scale) virtual work and the equivalent continuum virtual work. By equating the two, they were able to obtain the following expressions for stress and couple stress:

$$\langle \sigma_{ij} \rangle = \frac{1}{V} \sum_{c \in \partial \mathcal{R}} f_i^c x_j^{p(c)} = \frac{1}{V} \sum_{c \in \mathcal{R}} f_i^c l_j^c \tag{2.32}$$

$$\begin{aligned} \langle m_{ij} \rangle + \epsilon_{ikl} \langle \Sigma_{jkl} \rangle &= \frac{1}{V} \sum_{c \in \partial \mathcal{R}} \left[\epsilon_{ijk} (x_j^c - x_j^{p(c)}) f_k^c + m_i^c \right] x_j^{p(c)} \\ &= \frac{1}{V} \sum_{c \in \mathcal{R}} \left[\epsilon_{ikl} f_l^c \left(l_j^c x_k^c - J_{jk}^c \right) + m_i^c l_j^c \right] \end{aligned} \tag{2.33}$$

where:

$$l_j^c = x_j^m - x_j^n \tag{2.34}$$

$$J_{jk}^c = x_j^m x_k^m - x_j^n x_k^n, \quad c \in \mathcal{R} \tag{2.35}$$

where x_i is measured with respect to the RVE centroid. Note that this approach cannot yield separable expressions in terms of the couple stress $\mathbf{m}$ and the stress moment $\boldsymbol{\Sigma} = \mathbf{x} \otimes \boldsymbol{\sigma}$.

The coarse-graining approach

More recently, Goldhirsch [128] approached the issue of homogenization in micropolar continua using coarse-graining. The latter approach relies on the spatial averaging of grain scale dynamics, while assumptions include point contacts and convex rigid particles. Imposing conservation of linear momentum and taking the quasistatic limit, one obtains the average (coarse-grained) stress in body-integral form:

$$\langle \sigma_{ij} \rangle = \frac{1}{V} \sum_{c \in V} f_i^c l_j^c. \tag{2.36}$$

Analogously, conservation of angular momentum yields the coarse-grained couple stress:

$$\langle m_{ij} \rangle = \frac{1}{2V} \sum_{c \in V} \epsilon_{ikl} x_k^c f_l^c l_j^c. \tag{2.37}$$

2.4 Multiscale modeling of granular materials

The complicated phenomenology of constitutive behavior, and, at the same time, the developments in discrete mechanics and homogenization have paved the way for the application of multiscale modeling. Multiscale methods are typically thermodynamically consistent (satisfying micro-macro energy balance) and do not require complex calibration procedures. This is because these methods obtain information from a lower scale material description, which is inherently given in terms of fewer system parameters. Two major families can be distinguished, hierarchical and concurrent methods.

2.4.1 Hierarchical methods

Hierachical models rely on the assumption of scale separation, in order to introduce a Representative Volume Element (RVE) in the form of a granular assembly (Fig. 2.5 a)). Micromechanical and statistical considerations determine the size of the RVE, which must be significantly smaller than the characteristic dimension of the macroscopic boundary value problem. A well-defined RVE is one that undergoes homogeneous deformation under the influence of a uniform boundary stress, and lacks sharp gradients over its width. The issue of scale separation and its existence or lack thereof has been discussed in several studies [127, 126, 305, 123]. In [305], it was shown that a reasonable continuum representation can be obtained at the level of the velocity correlation length. The observation of stress plateaus over a range of scales at the linear regime also imply some degree of scale separation [126].

Assuming that scale separation holds, the balance equations are then solved in the RVE, subject to appropriate boundary conditions (BCs), usually by means of DEM [78] or its variants. It has been shown that affine displacement BCs render the RVE problem stiff, while the opposite effect is obtained for stress-based BCs. Periodic BCs are widely considered as optimal [230], although the so-called minimal kinematic BCs are also a promising alternative [228]. Particular boundary conditions have also been developed specifically for localization studies [144, 197, 70]. In any case, BCs are required to satisfy the thermodynamic constraints furnished by the Hill-Mandel condition, which, in the case of infinitesimal kinematics, reads:

$$\langle \sigma_{ij} \varepsilon_{ij} \rangle = \langle \sigma_{ij} \rangle \langle \varepsilon_{ij} \rangle. \tag{2.38}$$

Once the RVE problem is solved, the next step is the application of an upscaling procedure to the continuum level, where the continuum balance equations are solved, for example, using FEM. This upscaling is typically furnished by statistical homogenization [251, 68, 227, 313, 50, 95]. Hierarchical two-scale models for general elastoplastic heterogeneous materials were initiated in [337, 231, 180]. In the context of granular materials, two-scale (DEM-FEM) models for granular materials in the quasistatic regime was proposed by [230, 249] and later by [131]. A different hierarchical approach was developed in [18], where the upscaling procedure involves computing the effective frictional angle and dilation angle of the granular assembly and passing that information to a simple macroscopic plasticity model. The implicit assumption in that approach is that of isotropy.

Conventional homogenization techniques, developed in the context of simple continua, only allow for first-order RVE deformation modes. In contrast, the extension of these techniques to weakly nonlocal or generalized continua additionally account for microstructural (e.g. gradient) effects [112, 181, 93, 202, 203]. These extended schemes have been shown to relax the requirement for separation of scales [198]. Most studies have focused on developing homogenization and two-scale schemes for micropolar continua (e.g. [93]), in which case the Hill-Mandel condition is appropriately extended to [112, 202].

$$\langle \sigma_{ij}\varepsilon_{ij} + \mu_{ij}\kappa_{ij} \rangle = \langle \sigma_{ij} \rangle \langle \varepsilon_{ij} \rangle + \langle \mu_{ij} \rangle \langle \kappa_{ij} \rangle \tag{2.39}$$

2.4.2 Concurrent methods

Concurrent methods do not rely on scale separation, and do not assume the existence of an RVE. Instead, these methods seek the solution of a boundary value problem at both the continuum and the grain scales simultaneously and use techniques such as handshake domains to exchange information between the two scales (Fig. 2.5 b)). The developments relevant to granular materials have been inspired by earlier developments in molecular dynamics [331, 32]. In [369], researchers developed a methodology that assumes both a continuum and a discrete domain with a partial overlap and utilizes the Arlequin method for the reconciliation/coupling of the two scales. Particle displacements are split into a fine and coarse scale part, with the latter being forced to equal the continuum solution. Similar overlapping domain methods have been developed in [348, 371].

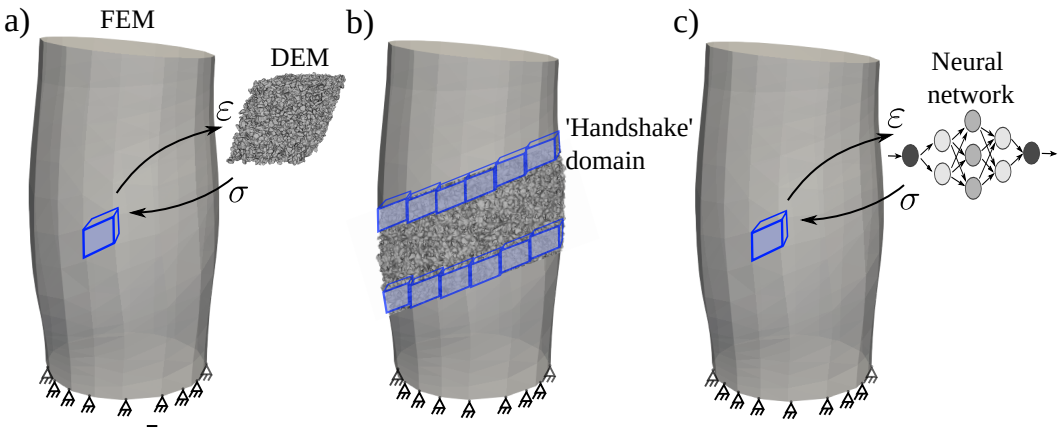

Figure 2.5: Multiscale modeling of granular solids: a) Hierarchical modeling b) Concurrent modeling c) Machine learning-based modeling.

2.5 Machine learning-based modeling of granular materials

In light of the many challenges encountered in the modeling of granular materials via continuum, discrete and multiscale methods, promising modeling alternatives have surfaced in the form of machine learning and data-driven techniques. These are driven by the increasing abundance of experimental and high fidelity DEM data and the rapid progress in data science. The first machine learning studies relied on standard feed-forward neural networks (NN) trained with experimental data in order to predict the general mechanical behavior of materials [121]. This technique, along with support vector machines, were quickly adapted to the modeling of granular materials, replacing conventional constitutive models [268, 175]. Capabilities for modeling complex history-dependent behavior were enhanced with the use of recurrent [380, 295], and particularly Long Short-Term Memory (LSTM) neural networks [373]. Multiscale methods, where upscaling is furnished by means of deep learning, have been developed in [367, 237] (Fig. 2.5 c)). In all of the above methods, machine learning models trained with experimental or high-fidelity micromechanical simulation data are used as surrogates for constitutive laws. Only very recently some of the developed techniques feature appealing properties such as built-in invariance and thermodynamic consistency. In another set of studies, machine learning techniques have been developed to predict specific features of the micromechanical state. Stick slip events in sheared granular materials were predicted using decision trees in [289], while in [134], local rearrangement events in amorphous packings of ellipses were characterized using support vector machines.

Chapter 3

INVESTIGATING THE INCREMENTAL BEHAVIOR OF GRANULAR MATERIALS WITH *IN-SILICO* EXPERIMENTS

K. Karapiperis, J. Harmon, E. Ando, G. Viggiani and J. E. Andrade. Investigating the incremental behavior of granular materials with the level-set discrete element method. *Journal of the Mechanics and Physics of Solids* 144 (2020), p. 104103.

Abstract

A computational framework is presented for high-fidelity virtual (in-silico) experiments on granular materials. By building on i) the accurate mathematical representation of particle morphology and contact interaction, ii) the full control of the initial state of the assembly, and iii) the discrete element simulation of arbitrary stress paths, the proposed framework overcomes important limitations associated with conventional experiments and simulations. The framework is utilized to investigate the incremental response of sand through stress probing experiments, focusing on key aspects such as elasticity and reversibility, yielding and plastic flow, as well as hardening and fabric evolution. It is shown that reversible strain envelopes are contained within elastic envelopes during axisymmetric loading, the yield locus follows approximately the Lade-Duncan criterion, and the plastic flow rule exhibits complex nonassociativity and minor irregularity. Hardening processes are delineated by examining the stored plastic work and the fabric evolution in the strong and weak networks. Special attention is given to isolating in turn the effect of particle shape and interparticle friction on the macroscopic response. Interestingly, idealization of particle shape preserves qualitatively most aspects of material behavior, but proves quantitatively inadequate especially in anisotropic stress states. The results point to the importance of accurately resolving particle-scale interactions, that allows macroscopic behavior to emerge free from spurious micromechanical artifacts present in an idealized setting.

3.1 Introduction

The continuum response of a granular assembly is encoded in the evolving kinematics of particles, driven by frictional forces at discrete interparticle contacts. Decoding this response experimentally is fraught with difficulties mainly in extracting interparticle forces, and creating reproducible conditions. The Discrete Element Method (DEM) [78] has provided a numerical framework that overcomes these difficulties, but at the same time introduces new limitations, due to the idealization of granular shape or the incorporation of questionable rolling dissipation [6]. Recently, a pivotal advancement that overcomes these limitations has been achieved through the level-set characterization of the morphology of individual grains using X-ray Computed Tomography (XRCT) [356], and its utilization within the Level-Set DEM (LS-DEM) framework [170]. Even more recently, significant steps have been made in validating the method [169, 200, 166], thus paving the way for a systematic investigation of granular behavior through high-fidelity virtual experiments.

The cornerstone of experiments on granular matter is stress probing, which relies on achieving multiple incremental stress paths originating from an identical initial state. Physical stress probing experiments are extremely hard to conduct, which explains the scarcity of relevant studies [13, 303]. On the other hand, numerical stress probing via conventional DEM (e.g. [28, 48, 332, 366]) has served as an effective platform for the investigation of constitutive behavior in a qualitative sense. The first DEM stress probing experiments were conducted by Bardet [28] using disks. Later, Calvetti and coworkers carried out similar experiments with spheres, and used them to examine the importance of preloading [48], inspect the underlying micromechanics [49], and assess different classes of continuum theories [332]. In several occasions (e.g. when probing from a preloaded state), they identified deviations from classical plasticity in the form of a nonregular flow rule, which was interpreted as evidence of thorough incremental nonlinearity (e.g. hypoplasticity) [333]. This was in line with later observations in [366, 189]. The influence of triaxiality on the regularity of the flow rule was investigated in [366], while the effect of the rotation of principal stresses was discussed in [115]. A critical element in analyzing results of numerical (or virtual) stress probing experiments is the decomposition between elastic and plastic strains. These have been typically extracted either by unloading to the initial state [28], or by carrying out ad-

ditional simulations where dissipative mechanisms are inhibited [48, 49, 332]. Wan and Pinheiro [366] have suggested that the two approaches are equivalent. On the other hand, Kuhn and Daouadji [190] observed that the two approaches produce different decompositions, and examined the relevant implications within the context of a thermodynamical framework, complementing an earlier discussion in [73]. With the exception of a 2D polygon study in [10], all the aforementioned studies involve highly idealized particle shapes (disks or spheres).

The first objective of this paper is to introduce a new paradigm of virtual experiments building on the recent development of LS-DEM (Section 2). The framework incorporates an unprecedentedly accurate representation of particle morphology and interaction, which jointly define a type of granular genome or 'DNA'. By controlling the expression of that 'DNA' to a desired configurational state — a process intractable with preexisting techniques — and evolving that state by imposing arbitrary stress paths, the proposed framework is established. In Section 3, the framework is utilized to systematically investigate the incremental response of an angular sand through multiple stress probing experiments. In a first set of axisymmetric experiments, the elastic-plastic and reversible-irreversible decompositions of strain are investigated, and the properties of plastic flow are discussed as functions of the current state and its history. We, then, shed light on the micromechanical processes driving dissipation, hardening and fabric evolution, and briefly examine the relevant role of fluctuations. Subsequent experiments focus on isolating the effect of interparticle friction and particle morphology, and assessing the effect

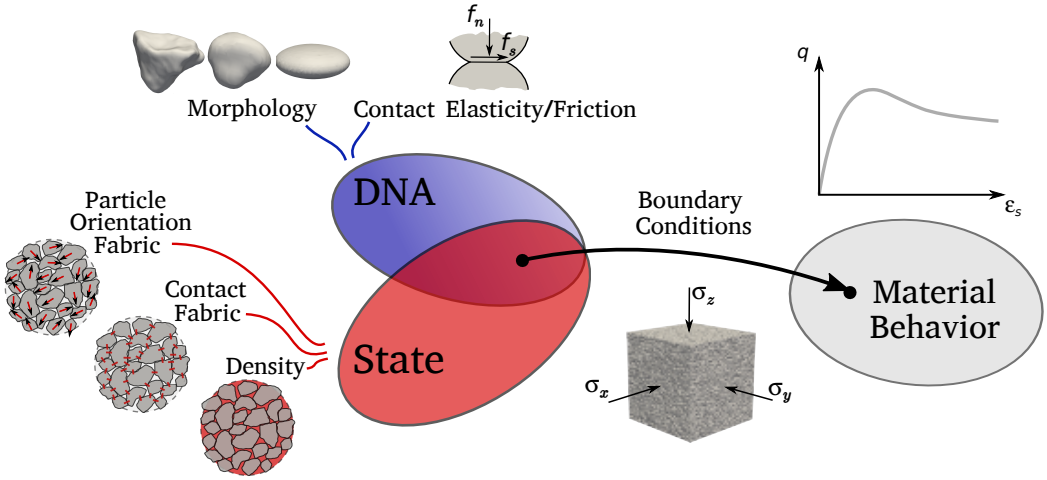

Figure 3.1: The concept of granular 'DNA' within virtual experiments.

of the common spherical idealization. In a final set of deviatoric experiments, we map the entire yield surface in 3D principal space and quantify the nonassociativity of the flow rule as a function of the mean stress and Lode angle. A discussion of the main findings and the future potential of virtual experiments, in Section 4, concludes this paper.

3.2 *In-silico* experiments

Physical experiments of granular materials suffer from poor reproducibility and limited control of initial and boundary conditions. They also inherently lack the ability to measure interparticle forces, a key ingredient in understanding the constitutive behavior. The proposed virtual experimentation framework effectively bypasses these limitations by relying on a) the accurate mathematical description of particle morphology and interaction, b) the control of the initial state of the assembly, and c) the enforcement of boundary conditions following an experimental protocol.

3.2.1 Particle morphology and interaction

The mathematical representation of particle geometry is achieved through mathematical objects termed level sets [170]. Given a local (particle) coordinate system, the value of a level set function $\phi(\mathbf{x})$ is the signed distance from a point $\mathbf{x}$ to the grain's surface, described by the zero-level set $\{\mathbf{x} \,|\, \phi(\mathbf{x}) = 0\}$. Such functions may either be constructed using standard level set operations [262] or extracted directly from XRCT images using level set imaging techniques [356], given the increased resolution of modern 3D XRCT technology [15, 69]. An example of extracting a level set of an angular sand grain is given in Fig. 3.2. From a collection of grain morphologies, a distribution of geometrical properties spanning multiple scales (e.g. sphericity, roundness) may be obtained. Finally, this distribution can be sampled to produce granular clones of similar morphology [44].

The granular 'DNA' can be described by these morphological distributions, complemented by interparticle contact laws and associated grain-scale material properties. A general description of interparticle contact is furnished by thermodynamics; for a discrete contact point c, one can consider a Gibbs energy $G^c(\mathbf{f}^c, \mathbf{q}^c, \theta)$ as a function of the contact force $\mathbf{f}^c$, the temperature θ and an internal variable $\mathbf{q}^c$ related to dissipative events (sliding displacement/con-

tact damage), and an associated contact dissipation potential ψ^c, in analogy to continuum thermodynamics [381, 260, 259]. Presented in Appendix 3.A is a simple formalism, from which various contact laws may be derived. Note that the material properties on which they rely (e.g. interparticle friction, contact stiffness) may now be directly measured at the grain-scale by means of compressive [71], shearing [56, 319] and multidirectional [241] tribological experiments conducted between individual particles.

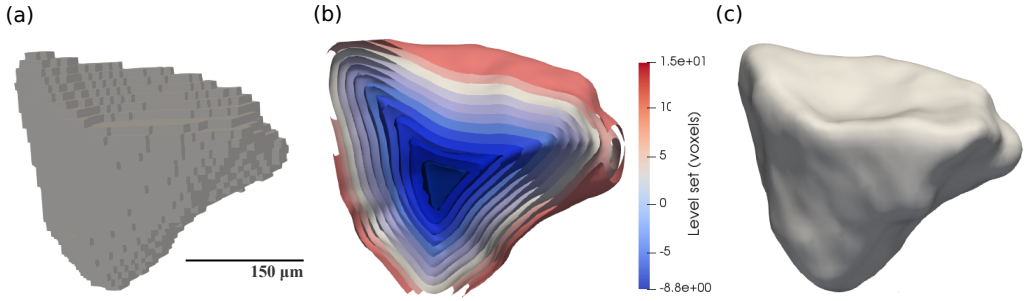

Figure 3.2: Particle morphology characterization: a) Hostun sand grain segmented from XRCT, b) slice of grain level set (blue: interior, red: exterior), and c) particle surface.

3.2.2 Control of initial state

Once the granular 'DNA' is fully characterized, the next step is to control its expression to a configurational state, that includes initial stress, density, and contact-/particle orientation-fabric. The state may be either obtained using imaging techniques in an *in-situ* XRCT experiment [169], or, more generally, it may be generated by simulating a preparation protocol designed to target particular state properties. The latter relies on simulating particle interaction, through a level-set based discrete element framework, termed LS-DEM [170]. Similarly to the original DEM formulation [78], LS-DEM resolves the kinematics of grains whose interaction is governed by contact mechanics, but at the same time is able to represent realistic grain shape. At each time step and contact point, the contact force $\mathbf{f}^c$ is computed based on the interaction law, and contributes to a moment $\mathbf{m}^c$ about the particle's center of mass. Given the inertial properties of the particle, its kinematics are updated using an appropriate time integration scheme of Newton's equations of motion. For a detailed explanation of the LS-DEM framework, the interested reader is referred to [170].

Fig. 3.3 shows an example preparation protocol using LS-DEM, where grains are being pluviated from an orifice into a cubical container. By controlling the height and supply rate of pluviation, as well as the orientation of the container, a desired packing fraction and fabric may be achieved. Importantly, the complete description of fabric involves not only on the orientational distribution of contacts — the most common way of quantifying fabric to date [263] - but also on the distribution of particle orientations or voids, which is intractable with conventional methods (e.g. DEM). We refer to Section 3.3.1 for an example of fabric quantification within the proposed framework.

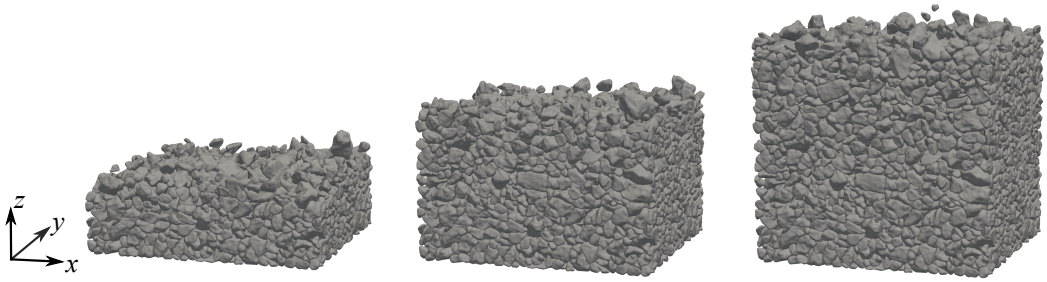

Figure 3.3: Stages of virtual pluviation of a sample of Hostun sand.

3.2.3 Testing protocol

The power of virtual experiments is fully exploited in the testing phase, since they enable the exact replication of any generated initial state and the enforcement of arbitrary mixed boundary conditions. For example, true triaxial conditions (Section 3.3.9) can be easily established without the need for complicated experimental design [286]. Before enforcing such conditions and embarking on a systematic exploration of stress space, it is necessary to establish confidence in the method within conventional stress paths. Indeed, LS-DEM has recently been validated against physical triaxial compression [169] and shear experiments [200], where parameters were directly computed from particle material properties and the initial state was replicated using level-set imaging. The method was able to capture quantitatively the macroscopic (stress-strain), mesoscopic (spatiotemporal prediction of onset and evolution of a shear band and its kinematics), and particle-scale response (contact-normal and force distribution, and friction mobilization).

3.3 Stress probing

3.3.1 Setup

This section details the virtual experiment setup used to investigate the incremental response of an angular sand. The model consists of 15625 virtual Hostun sand grains[1], whose morphology has been extracted from μ-XRCT data (Section 3.2.1). The grain interaction follows a Hookean elastic – Coulomb frictional law (Appendix 3.A), with the relevant properties given in Table 3.1. To accelerate the approach to equilibrium, contact damping with a coefficient of restitution of 0.6 is introduced in the interaction law. Additional experiments verified that the results were insensitive to the choice of coefficient of restitution, under a sufficiently low dimensionless inertial number ($I \leq 10^{-3}$). We employ LS-DEM to simulate both specimen preparation and stress probing. Via dry pluviation, we construct a dense cubical assembly of virtual Hostun sand particles (Fig. 3.4) of relative density $D_r = 85\%$ and corresponding void ratio $e = 0.55$. To calculate the relative density, the minimum and maximum void ratios were first estimated based on the following protocols. The densest state was reached by pluviating particles into a container under gravity, and subsequently subjecting the container to vertical sinusoidal vibration at 60 Hz under constant vertical load, until the void ratio plateaued to a value $e_{min} = 0.51$. This method is similar to that described in the ASTM standards [24, 63]. Accordingly, the loosest state was obtained by pluviation from zero height [350, 23], followed by compression to the same vertical load for consistency with the dense measurement, resulting in a void ratio $e_{max} = 0.74$.

Parameter	Value	Units
Density (ρ)	2500	Kg/m^3
Normal stiffness (k_n)	$3 \cdot 10^4$	N/m
Shear stiffness (k_t)	$2.7 \cdot 10^4$	N/m
Friction coefficient (μ)	0.4	-
Coefficient of restitution (c)	0.6	-

Table 3.1: Particle properties used in the virtual experiments.

After pluviation, each specimen is isotropically consolidated to state A by applying a uniform confining pressure of $p_A = 50$ kPa. Note that the sign convention of solid mechanics (compression negative) is adopted here, and we

[1]Increasing sample sizes were used to ensure that the size of the unit cell is representative (see Appendix 3.B).

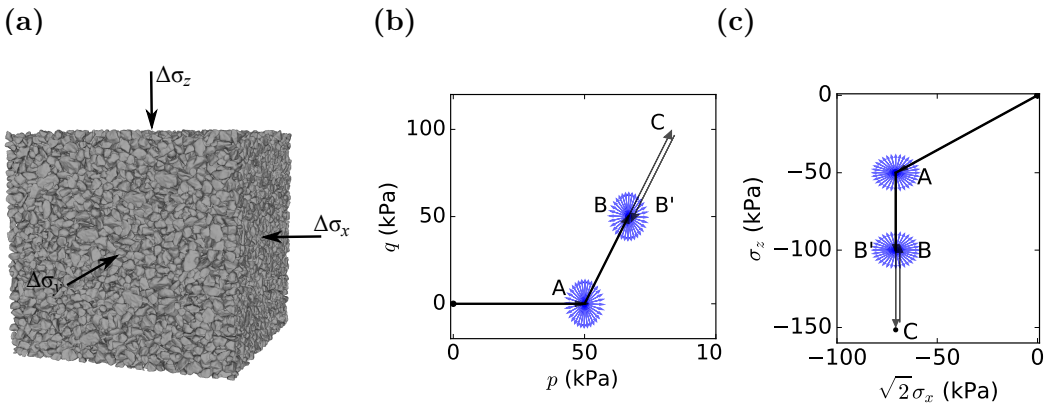

Figure 3.4: Specimen subjected to a loading protocol: a) Virtual specimen of Hostun sand under three dimensional stress conditions. b) Imposed stress states and probing protocol in p-q plane. c) Same in the Rendulic plane.

define $p = -1/3\,\mathrm{tr}\boldsymbol{\sigma}$, $q = \sqrt{3/2\,\boldsymbol{s}:\boldsymbol{s}}$ where $\boldsymbol{s} = \boldsymbol{\sigma} + p\boldsymbol{I}$. The confining pressure is applied using numerical servocontrol to adjust the displacement of the surrounding walls, which are modelled as smooth frictionless elements[2]. This ensures that the principal axes of stress and strain are coincident with the axes of the cube (Fig. 3.4 a)) [48]. Afterwards a drained triaxial compression along the z-direction is imposed at constant lateral stress $\sigma_X = \sigma_Y$ until an anisotropic state B ($q_B = 50$ kPa), termed the *virgin* state, is reached. Finally, the samples are subjected to further drained triaxial compression to state C ($q_C = 100$ kPa), and unloaded to produce the *preloaded* state B' ($q_{B'} = 50$ kPa). The packing and history at states A, B, and B' are stored and cloned [10], since each will serve as the initial condition of a subsequent axisymmetric stress probing protocol (Fig. 3.4 b, c)). The latter consists of 32 axisymmetric probes, uniformly distributed in the Rendulic angle $\alpha_{\Delta\boldsymbol{\sigma}} = \arctan(\Delta\sigma_z/\sqrt{2}\Delta\sigma_x) \in [0°, 360°)$, each with a Euclidean norm of 5 kPa (Fig. 3.5 a)). Characteristic probes include: isotropic (IE), triaxial (TE), and deviatoric (DE) extension, as well as isotropic (IC), triaxial (TC), and deviatoric (DC) compression. The stress states and probing magnitudes/angles were chosen such that the effect of anisotropy and history is adequately captured while minimizing computational demands.

Before analyzing the stress probing response, we quantify the state of the sample beyond the isotropic measure of relative density discussed above. To this

[2]An alternative way to impose the stress state is through periodic boundary conditions. This is avoided in this study since it imposes constraints on the sample preparation procedure, which in this particular case is non-periodic.

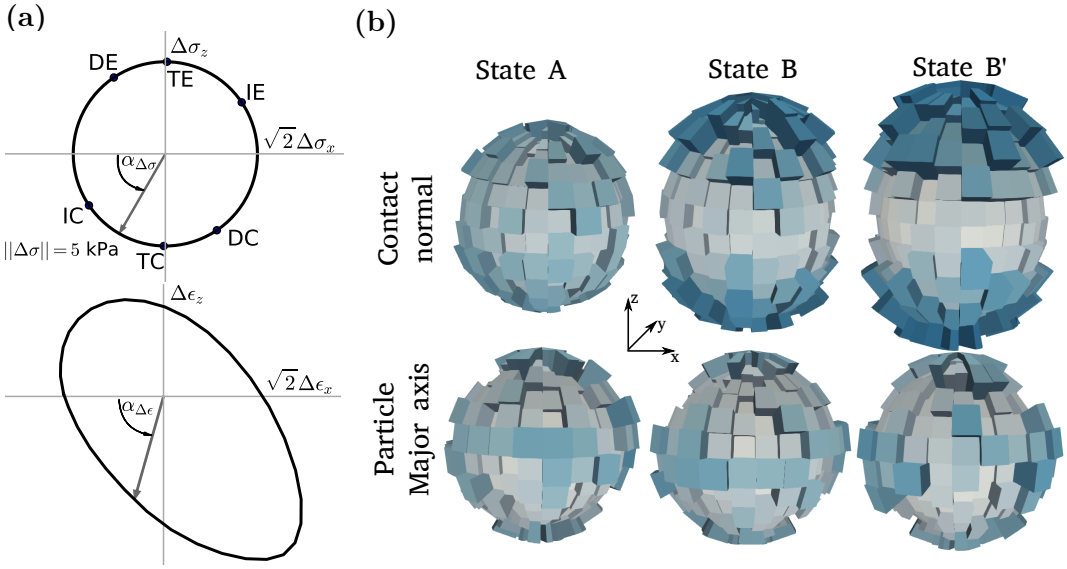

Figure 3.5: Stress, strain and fabric during probing: a) Top: Stress probing paths form a circle in the Rendulic plane of stress increments. Marked characteristic paths: isotropic (IE), triaxial (TE), and deviatoric (DE) extension, isotropic (IC), triaxial (TC), and deviatoric (DC) compression. Bottom: Sketch of the strain response in the Rendulic plane of strain increments. b) Contact-normal and major particle axis orientation fabric at states A, B, and B'.

end, Figure 3.5 b) shows the orientation histograms for the contact-normals and major particle orientation axes at each state. The sample exhibits initially (state A) only a slight vertical fabric anisotropy, which becomes increasingly pronounced at the anisotropic states B and B'. On the other hand, the particle orientation fabric remains approximately isotropic throughout the experiment.

3.3.2 Scope

In the remaining sections, we will focus on gaining insight into i) the strain response due to stress probing, mathematically summarized as $d\boldsymbol{\epsilon} = \mathcal{S}(\boldsymbol{\sigma}, \boldsymbol{\eta}, \mathbf{q}) : d\boldsymbol{\sigma}$, where $\boldsymbol{\eta}$ is the stress probing direction, and $\mathbf{q}$ is some representation of the internal state, and ii) the evolution of the internal state due to probing, succinctly given as $d\mathbf{q} = \mathcal{H}(\boldsymbol{\sigma}, \boldsymbol{\eta}, \mathbf{q}) : d\boldsymbol{\sigma}$.

3.3.3 Strain response

Fig. 3.6 a) shows two decompositions of the strain response considered in this study. In order to define the *elastic-plastic* strain decomposition, we follow

the work of Bardet [28], where the plastic strain is identified as the residual strain upon unloading to a reference stress state. The elastic strain is, then, recovered by subtracting the residual from the total strain. On the other hand, the *reversible-irreversible* decomposition partitions the strain into that arising from reversible and irreversible grain-scale mechanisms. The reversible response is furnished by an additional set of stress probing experiments in which frictional dissipation (slip) has been inhibited [48]. The irreversible component follows by subtracting the reversible from the total strain response.

As illustrated schematically in Fig. 3.6 b), the *elastic-plastic* and the *reversible-irreversible* decompositions may only coincide in a perfectly *crystalline* arrangement. Indeed, in that case, the applied loading induces an affine deformation of the contacts, which is exactly reversed upon unloading. On the contrary, during loading of an *amorphous* assembly, fluctuations are known to develop [292], leading to some contacts behaving elastically, and others sliding variably. Upon unloading, the contact deformations are not exactly reversed, as shown in Appendix 3.C. This results in an altered configuration, and, hence, the divergence between elastic and reversible response. Macroscopically, this divergence manifests itself as elastic-plastic coupling [141, 73, 190].

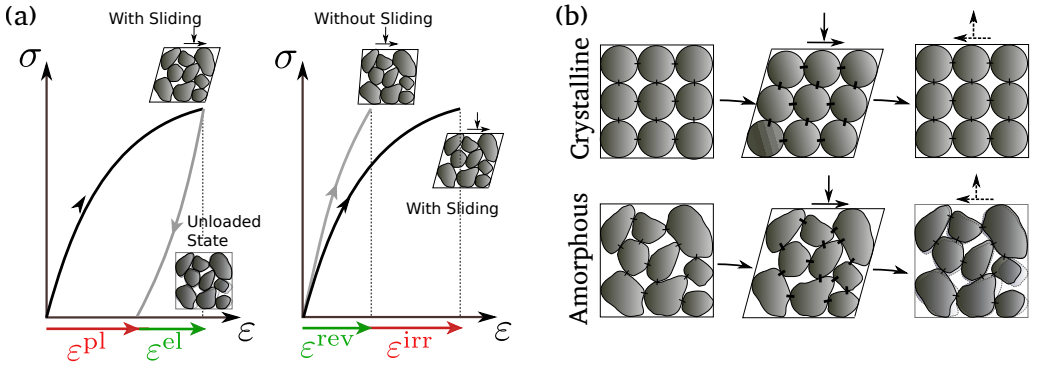

Figure 3.6: Elasticity versus reversibility of the material response: a) Elastic-plastic (left) and reversible-irreversible strain decomposition (right). b) Incremental response of a crystalline vs an amorphous assembly upon a loading-unloading cycle.

Elastic-plastic strain decomposition

Figs. 3.7, 3.8, and 3.9 show the total, elastic, and plastic strain response envelopes [130] obtained in this manner for stress probes originating at states A, B, and B' respectively. The plot insets show the stress-strain response

for specific probes, revealing different amounts of hysteresis depending on the probing direction. A few observations can be made:

- To a first approximation, the total strain envelope at state A is given by an ellipse, while the same envelopes at states B and B' are given by two sections of ellipses, one in the direction of deviatoric compression (DC) and another in the direction of deviatoric extension (DE).
- The elastic envelopes form ellipses, which, for anisotropic states (B, B'), are coincident with the corresponding total strain envelopes in the direction of previous loading history, essentially corresponding to stress reversal (DE and DC respectively).
- The elastic envelopes are approximately centered at the origin of the Rendulic plane. Non-centricity is more pronounced in anisotropic states.
- An approximately unique plastic strain increment direction is observed, which is distinct for each state, suggesting incremental bilinearity [48]. Yet, closer inspection reveals some degree of deviation in the form of angle dependence for all states. Particularly, at state A, this deviation could be attributed to the presence of a minor vertical fabric.
- The principal axes of the total, elastic, and plastic envelopes are non-coaxial. This is related to the nonassociativity of the plastic flow rule which is quantified for all three states in Fig. 3.10. The latter shows the average orientation of the normal to the implied yield surface (intepreted as the locus of stress states corresponding to the same norm of plastic strain rate) and the orientation of the normal to the plastic potential (i.e. the average orientation of the plastic strain rate). Their difference is a measure of the nonassociativity of the flow, which appears to be most pronounced in the anisotropic state B.
- By comparing the elastic envelopes at the three states (Fig. 3.11), we observe an increase in elastic stiffness, and the development of elastic anisotropy at states B and B', compared to state A. The elastic response in each state is quantified by fitting linear elastic isotropic and transversely isotropic envelopes, as described in Appendix 3.D. The relevant parameters are tabulated in Table 3.2.

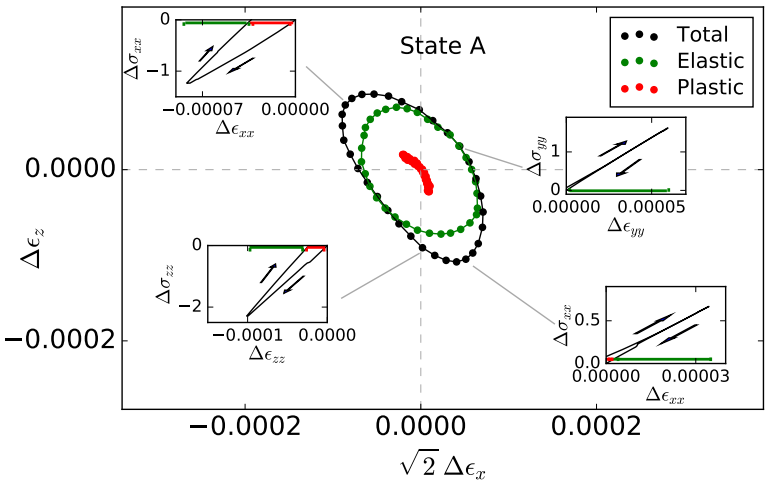

Figure 3.7: Total (black), elastic (green), and plastic (red) strain response envelopes for the dense specimen at *isotropic state A*. Insets: Loading/Unloading stress-strain curves.

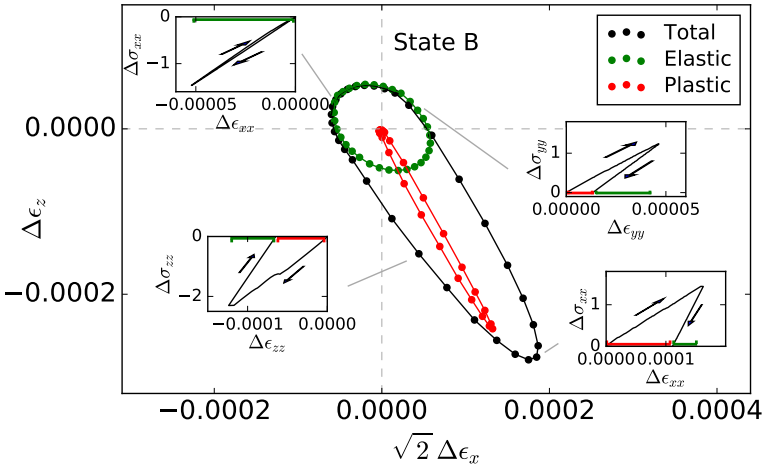

Figure 3.8: Total (black), elastic (green), and plastic (red) strain response envelopes for the dense specimen at *virgin state B*. Insets: Loading/Unloading stress-strain curves.

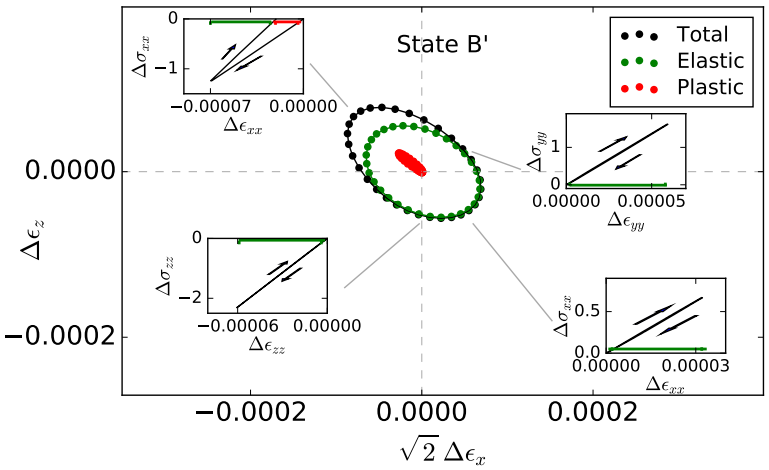

Figure 3.9: Total (black), elastic (green), and plastic (red) strain response envelopes for the dense specimen at *preloaded state B′*. Insets: Loading/Unloading stress-strain curves.

Model	Parameter	A	B	B'
Isotropic Elastic	E (MPa)	**34.1**	45.1	41.2
	ν	**0.149**	0.113	0.106
Transversely Isotropic Elastic	E_x (MPa)	34.2	**13.2**	**14.6**
	E_z (MPa)	34.1	**48.2**	**45.8**
	ν_x	0.151	**0.698**	**0.616**
	ν_{zx}	0.147	**0.146**	**0.154**

Table 3.2: Fitted parameters for isotropic and transversely isotropic elasticity.

Reversible-irreversible strain decomposition

Fig. 3.12 shows, for all states, the reversible, irreversible, and total strain response envelopes obtained via inhibited-dissipation experiments. We observe that:

- Reversible strain envelopes form ellipses that are very similar yet slightly smaller than the elastic ones. They are generally contained within the elastic envelopes.

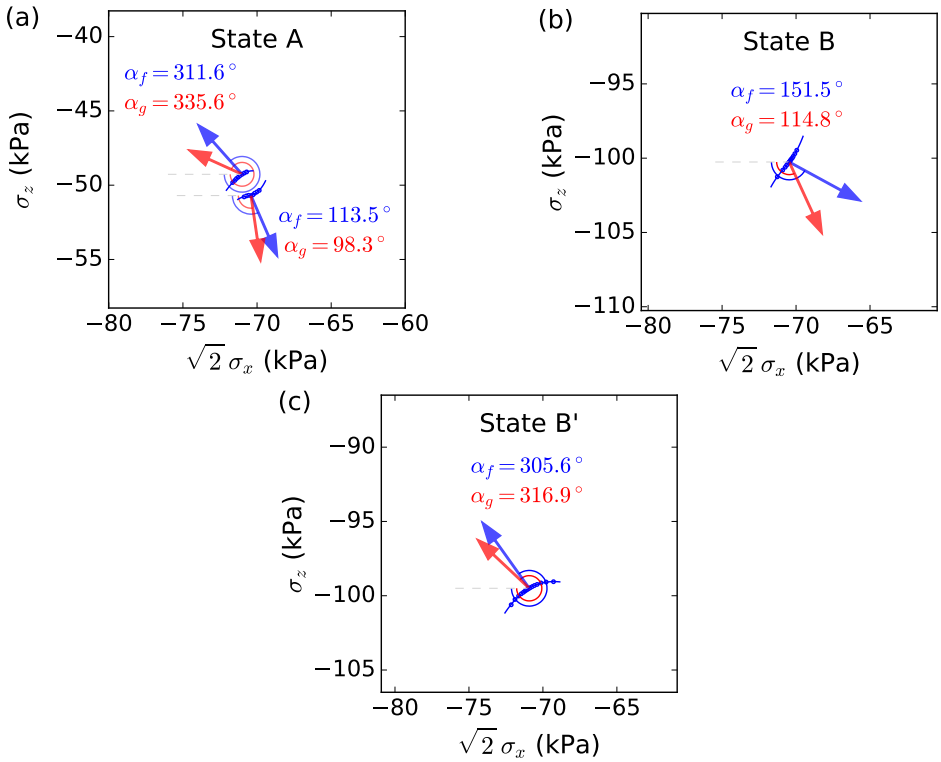

Figure 3.10: Average orientation of yield surface normals (blue) and plastic potential normals (red) in the Rendulic stress plane for a) the isotropic state A, b) the anisotropic state B, and c) the preloaded state B'. Blue dots represent the trace of the yield surface.

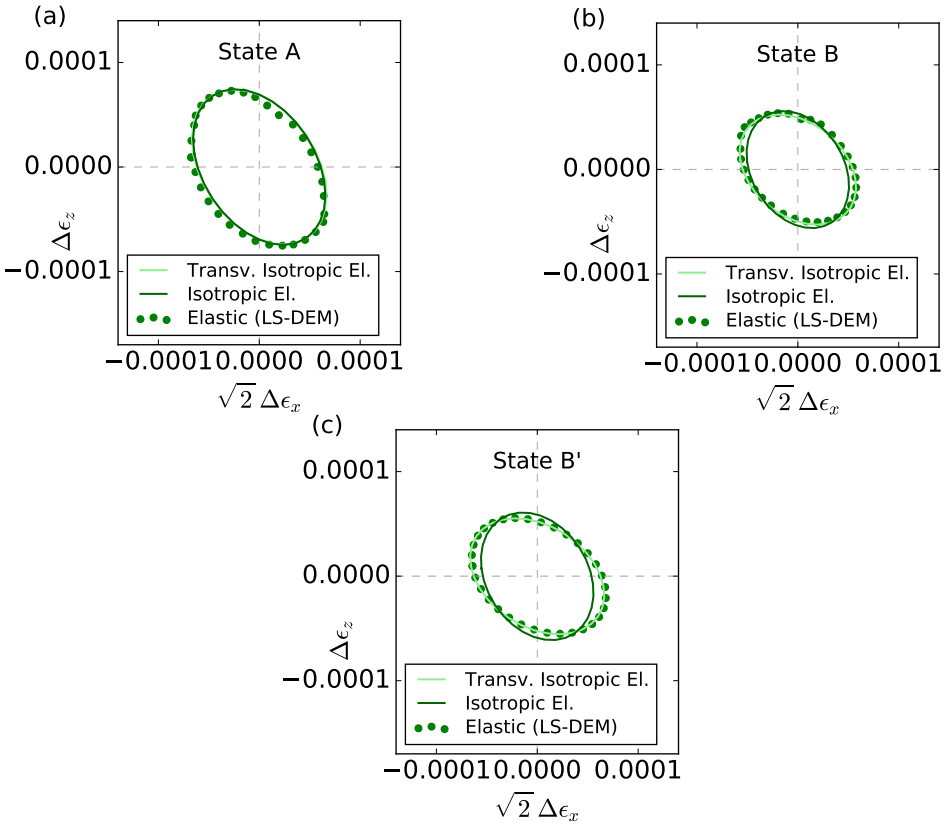

Figure 3.11: Elastic envelopes obtained from the virtual experiments compared to the fitted linear elastic isotropic and transversely isotropic envelopes for a) the isotropic state A, b) the anisotropic state B, and c) the preloaded state B'.

- The difference between elastic and reversible strain, which can be identified as a coupled strain [190], is most pronounced along the directions of (DC) and (DE).
- Irreversible strains generally arise for almost all Rendulic angles, with the exception of isotropic compression (IE) and isotropic extension (IE). The direction of the irreversible strain rate is only weakly dependent on the probing angle, which defines a slightly irregular flow rule [366].
- For any given state, irreversible and plastic strain increment directions generally coincide.
- Preloading leads to a stiffness increase along the (DC) direction, evidenced by the corresponding reduction in total strain. As a result, total and irreversible strain envelopes become more symmetric at B' compared to B.

Remark: In extracting the reversible response through such numerical experiments, one needs to ensure that no irreversible changes occur in the contact topology (creation and extinction of contacts). However, this condition cannot be guaranteed *a priori* by only inhibiting interparticle dissipation (slip). Our approach is to accept that some minor topological changes will occur, and then quantify the extent of these topological changes on the response *a posteriori*. To do so, we consider the stress increment during a probe [67]:

$$\Delta\boldsymbol{\sigma} = \boldsymbol{\sigma}' - \boldsymbol{\sigma} = \sum_{c\in\mathcal{C}'} \mathbf{f}'_c \otimes \mathbf{l}'_c - \sum_{c\in\mathcal{C}} \mathbf{f}_c \otimes \mathbf{l}_c \tag{3.1}$$

where $\mathbf{f}_c, \mathbf{l}_c$ denote the force and branch vectors at the initial configuration, and $\mathbf{f}'_c, \mathbf{l}'_c$ denote those at the configuration after probing. The sets $\mathcal{C}, \mathcal{C}'$ represent the sets of contacts at the two configurations. We can rewrite Eq. 3.1 to obtain the following decomposition:

$$\Delta\boldsymbol{\sigma} = \sum_{c\in\mathcal{C}\cap\mathcal{C}'} (\mathbf{f}'_c \otimes \mathbf{l}'_c - \mathbf{f}_c \otimes \mathbf{l}_c) + \sum_{c\in\mathcal{C}'\setminus\mathcal{C}} \mathbf{f}'_c \otimes \mathbf{l}'_c - \sum_{c\in\mathcal{C}\setminus\mathcal{C}'} \mathbf{f}_c \otimes \mathbf{l}_c \tag{3.2}$$

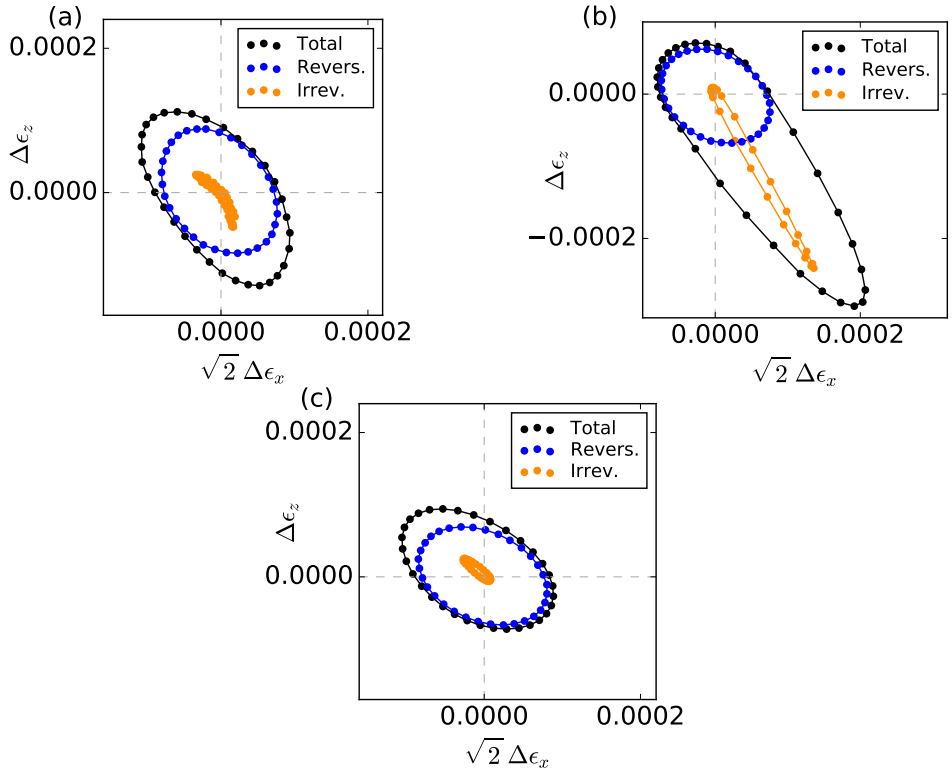

Figure 3.12: Total (black), reversible (blue), and irreversible (orange) strain response envelopes in the Rendulic stress plane for a) the isotropic state A, b) the anisotropic state B, and c) the preloaded state B'.

where the first term arises from two reversible mechanisms: i) the change in interparticle forces under fixed topology and ii) the change in fabric due to dissipation-free particle rolling. The second and third terms are due to the change in topology via creation and loss of contacts, respectively, and represent irreversible mechanisms. We find that these last two terms consistently contribute less than 5% to the stress increment. Hence, we conclude that this approach yields a good (slighty overestimated) approximation of the reversible response.

In Appendix 3.E, two additional strategies for the estimation of the reversible response are presented: i) a similar numerical construction where particle rotations are also constrained, and ii) an analytical homogenization-based approach. These methods are shown to provide lower bounds for the reversible response, and are not pursued further.

3.3.4 Hardening and stored plastic work

In order to shed light on hardening processes, we discuss here the thermodynamics of deformation during a closed cycle. To do so, we compute the change in the stored elastic energy $\mathcal{A} = \sum_c \mathcal{A}^c$ and the dissipation increment as $d\mathcal{D} = \sum_c d\mathcal{D}^c$, where the summation takes place over all contacts. Fig. 3.13 a) shows the frictional dissipation in the sample, normalized with the initial stored elastic energy $\mathcal{A}_0$, against the Rendulic angle during loading and unloading probes from the isotropic state A. We observe that dissipation is present throughout all angles, yet attains its maximum in the (DC) and (DE) directions at both loading and unloading. Fig. 3.13 b) shows the corresponding normalized change of the elastic energy stored in the contacts at the end of the loading-unloading cycle, and shows similar angle dependence as the dissipation. This change in stored energy reflects the arrangement of contacts and corresponds to the stored plastic work (hardening) in the system. The same quantities are plotted for the anisotropic state B in Fig. 3.14. At this state, maximum dissipation occurs near (DC), while almost no dissipation occurs at (DE). During unloading, the situation is reversed, i.e. we observe most dissipation near (DE). Finally, the distribution of stored plastic work reflects processes occurring during both loading and unloading.

3.3.5 Micromechanics

Fluctuation-dissipation observations

The goal of this section is to shed light on the nature of dissipation, and reveal its relation to contact fluctuations. Radjai et al. [283] established that, in idealized two-dimensional assemblies, full mobilization of friction predominantly occurs in the so-called weak network. Fig. 3.15 a) verifies this observation in our 3D granular assembly by plotting, for various probes, the rate of dissipation at each contact against the associated interparticle force. For large enough contact force magnitudes, we observe an exponential decay of dissipation with increasing contact force for all probes originating from all three initial states.

On the contrary, the relation of dissipation to contact fluctuations has not been properly investigated, despite its importance. Fig. 3.15 b) shows the rate of

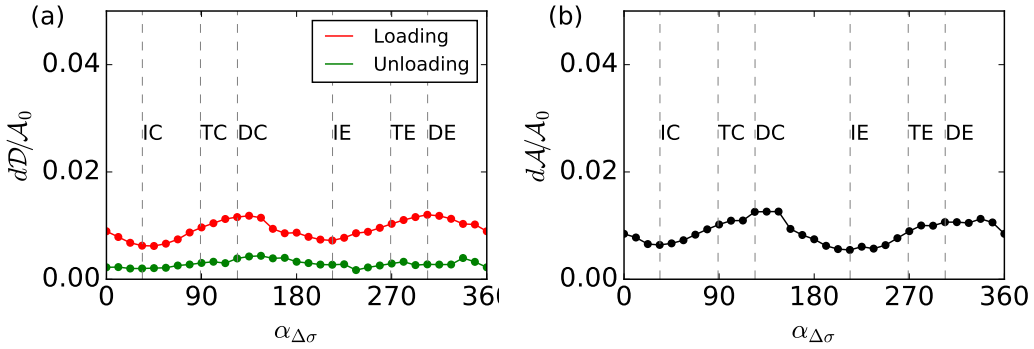

Figure 3.13: Dissipation and hardening during probing from the *isotropic state A*: a) Frictional dissipation during loading-unloading, and b) stored plastic work in a cycle, both normalized with the initial stored elastic energy, and plotted against the Rendulic angle.

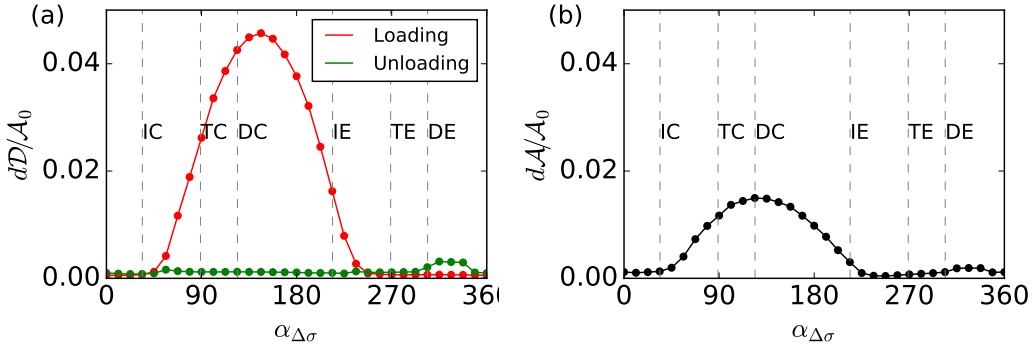

Figure 3.14: Dissipation and hardening during probing from the *anisotropic state B*: a) Frictional dissipation during loading-unloading, and b) stored plastic work in a cycle, both normalized with the initial stored elastic energy, and plotted against the Rendulic angle.

dissipation at each contact against the associated magnitude of the fluctuation in the deformation of the contact (see Eq. 3.17), which is related to the force fluctuation via the interparticle contact law. We observe a substantial increase in the rate of dissipation with increasing fluctuation magnitude. In fact, fluctuations that are lower than a threshold — dependent on the contact scale parameters that govern the frictional limit — exhibit almost no dissipation which lends credibility to the notion of elastic fluctuations (Appendix 3.E). This observation may be verified pictorially by inspecting Figs. 3.16 a) and b). Fig. 3.16 a) shows, for a two-dimensional cross-section of the dense specimen, the contact deformation fluctuation vectors during probing (computed via Eq. 3.17), while Fig. 3.16 b) shows the corresponding contours of frictional dissipation rate at the same instant. One can observe active regions with both pronounced frictional dissipation and large fluctuation magnitudes.

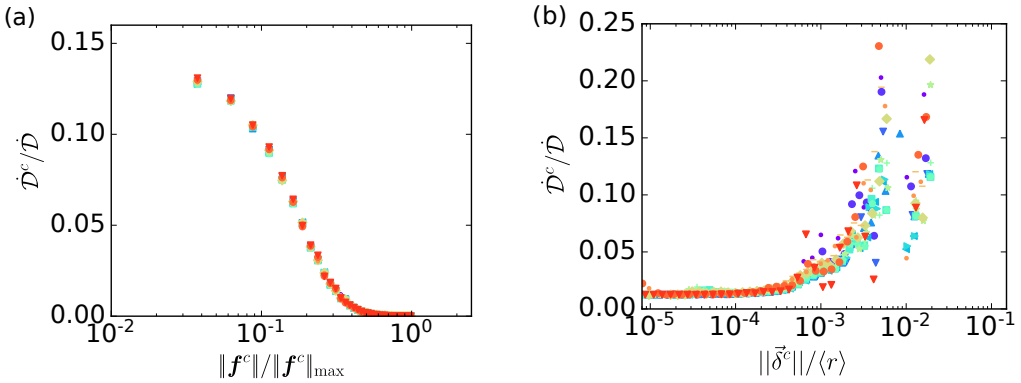

Figure 3.15: Normalized dissipation versus a) normalized force magnitude, and b) normalized contact fluctuation magnitude. Colors represent different probes originating at state A.

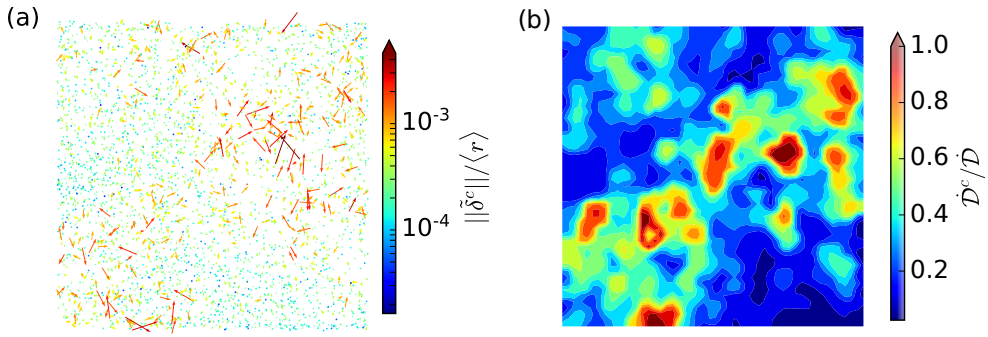

Figure 3.16: Two-dimensional slices of a) contact deformation fluctuations, b) normalized rate of dissipation for the dense specimen.

Mobilized friction and plastic debt

The focus of this section is to describe the evolution of the micromechanical state of the sample in terms of mobilized friction at the contact scale. Fig. 3.17 shows the relationship between the magnitude of the tangential (f_t) and normal (f_n) contact force for all contacts in the three considered states. Their ratio represents the contact-scale mobilized friction $\eta = f_t/f_n$, bounded by the Coulomb limit, while dashed lines represent the system average. Interestingly, we identify a substantial percentage of contacts at the Coulomb limit at the isotropic state — a departure from previous observations on spheres [49]. Not surprisingly, the amount of sliding contacts increases in the anisotropic state B, to accommodate the increasing level of macroscopic shear. This is also evident by the increase in the average mobilized friction. At the preloaded state B', the magnitude of forces increases, while the mobilized friction decreases, in accordance with previous observations in spheres [49].

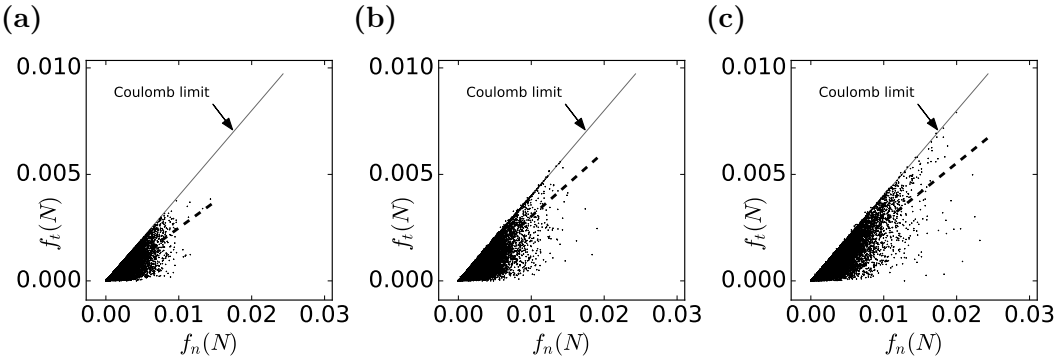

Figure 3.17: Tangential vs normal contact forces for the dense granular assembly at states a) A, b) B, and c) B'.

Further information about the micromechanical state of the system can be obtained by adopting the machinery of Calvetti, Viggiani, and Tamagnini [49]. To this end, we introduce the scaled mobilized interparticle friction $\eta_\mu = f_t/(\mu f_n)$, noting that $\eta_\mu \leq 1$ for conventional probes, while $\eta_\mu > 1$ is possible for reversible (inhibited-dissipation) probes. In the latter, the quantity $\Delta f^p = f_t - \mu f_n$ is interpreted as a plastic "debt" (as defined in [49]), that would be required to bring sliding contacts back to the Coulomb limit. For conciseness, we only present such measurements for two characteristic directions (DC and DE), at state B. In particular, Figure 3.18 shows the mobilized interparticle friction as a function of the magnitude of normal contact force, for both conventional and reversible probes. Substantial irreversible behavior

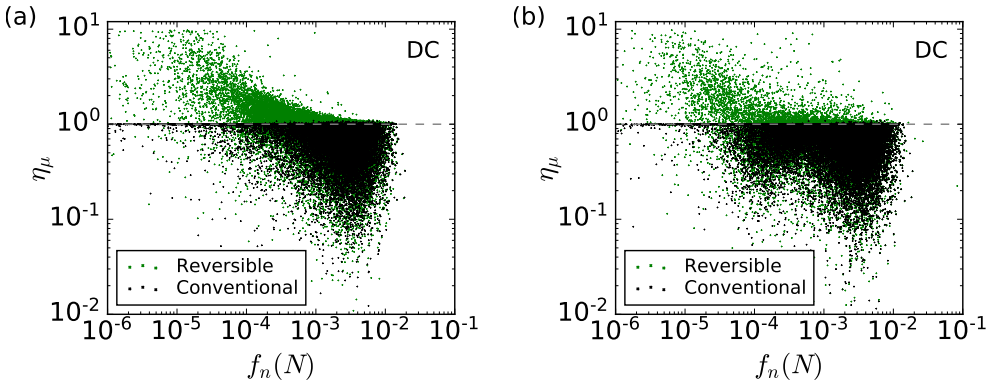

Figure 3.18: Mobilized friction versus normal force for the dense granular assembly during stress probing along a) deviatoric compression (DC), and b) deviatoric extension (DE) at state B.

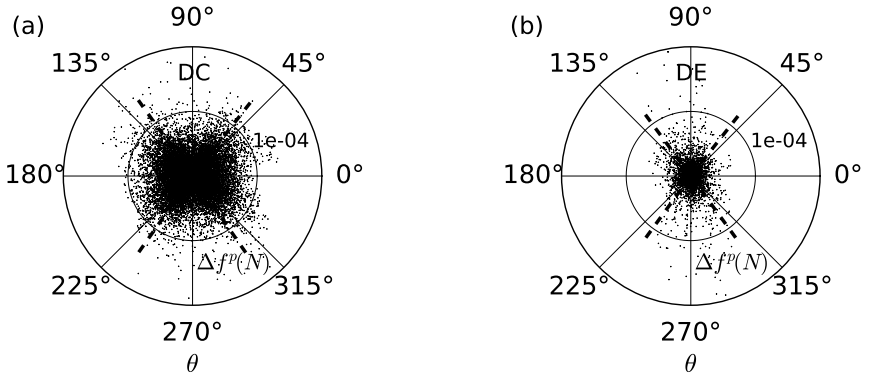

Figure 3.19: Plastic debt vs contact orientation angle for the dense granular assembly during probing along a) deviatoric compression (DC), and b) deviatoric extension (DE) at state B. Dashed lines represent the weighted average orientation of plastic debt at each quadrant.

emerges during the (DC) probe, which is evident by the development, in the case of the reversible probes, of shear forces larger than those allowed by the Coulomb condition. On the contrary, during the (DE) probe, only few contacts experience shear forces above the frictional limit. For the same probes, Figure 3.19 reports the plastic debt against the contact orientation angle projected in the $x-z$ plane (θ), indicating some degree of preferred orientation albeit with significant scatter. This is more clearly seen by the misalignment of the weighted average orientation of plastic debt at each quadrant — represented by dashed lines — with the diagonal directions. A perfect alignment would indicate a uniform (isotropic) orientational distribution.

3.3.6 Fabric evolution

The change in structure revealed partially in Sections 3.3.4 using the isotropic measure of stored energy, and in Section 3.3.5 using the concept of plastic debt, is now further illuminated by investigating the evolution of fabric. Figure 3.21 shows the evolution of different measures of fabric, during probing for the two characteristic probes (DE) and (DC) at state B. In particular, (a1-a2) and (b1-b2) show the change in orientational distribution of contact normals that belong to the strong and weak network, respectively, along a slice in the x-z plane. Green and red colors are used to mark a positive (gain) and negative (loss) change in the contact density, respectively. Further, (c1-c2) show the orientational distribution of the magnitude of contact displacement fluctuations. For both states and both probes, we observe that strong network contacts are consistently gained in the direction of compressive loading. On the other hand, the density of sliding contacts increases roughly in the perpendicular direction, and decreases in a direction almost parallel to the plastic strain direction. Interestingly, at the isotropic state A while probing along (DC), the sliding contact density gain is unimodal in nature, as opposed to the bimodal gain in the case of the same probe at the anisotropic state B. The same modality difference is observed when comparing the sliding contact density loss for the (DE) probe at states A and B. For a related discussion on the anisotropy of the weak network in biaxial experiments, we refer to [10]. Finally, the orientation of maximum contact fluctuations appears to be correlated with the direction of maximum loss of sliding contacts.

3.3.7 Effect of interparticle friction

In this section, we briefly investigate the effect of interparticle friction μ in the incremental response. Fig. 3.22 compares the total, elastic, and plastic strain response envelopes obtained during stress probing at state B for a range of values $\mu \in [0.2, 1]$. We identify an anticlockwise rotation and contraction of the total and plastic strain response envelope with increasing interparticle friction. Once the latter increases beyond a critical value $\mu_{cr} \approx 0.8$, the envelopes converge to a well-defined shape, and the macroscopic response is completely dictated, at that point, by particle morphology. These observations are in line with studies showing that the macroscopic friction plateaus with increasing interparticle friction [215]. The elastic envelopes remain essentially unaffected.

3.3.8 Effect of particle shape

In this section, we focus on investigating the effect of particle shape on mapping the grain-scale behavior to the incremental continuum response. In particular, we choose to address the effect of the common spherical idealization (e.g. [28, 48, 49, 332, 115, 366]), by comparing the granular sample to an equivalent spherical one; the investigation presented in this work could serve as the backbone for a systematic study of particle morphology on the incremental continuum response of granular media. Via the same dry pluviation procedure (Section 3.3.1), we construct an idealized spherical counterpart of the dense granular assembly. To this end, each grain is substituted by a sphere of equal volume, while keeping particle material properties the same. Further, in order to achieve a fair comparison between the spherical and granular assembly, the same relative density ($D_r = 85\%$) is imposed[3]. Note that this consideration compensates partly for shape since it accounts for its effect on

[3]Experiments were also conducted for granular and spherical samples created at the same void ratio rather than the same relative density, during which qualitatively similar differences were observed.

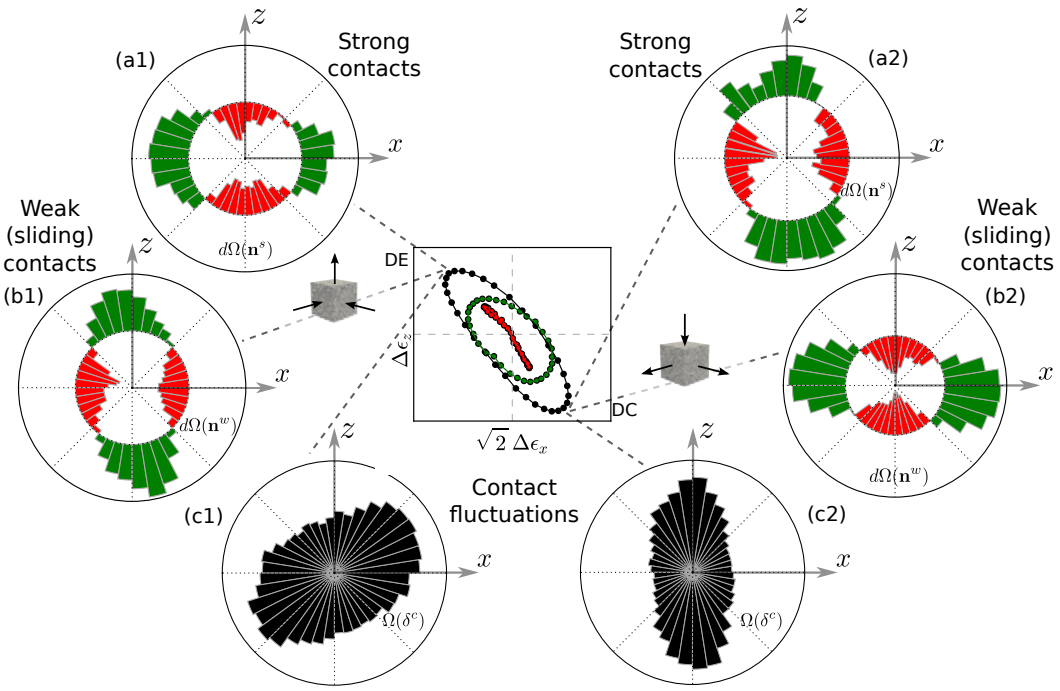

Figure 3.20: Incremental change in the fabric of contact normals in a) the strong force network, and b) weak force network, and c) orientational distribution of contact displacement fluctuations for probing at *state A*. Numbers denote loading path (1: DE, 2: DC).

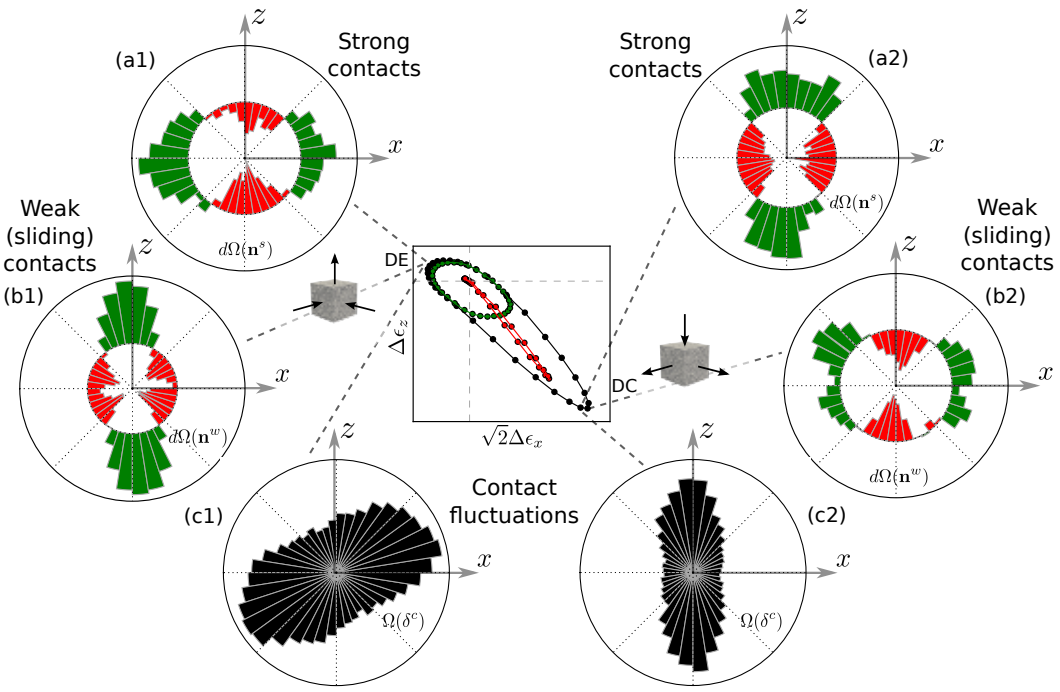

Figure 3.21: Incremental change in the fabric of contact normals in a) the strong force network, and b) weak force network, and c) orientational distribution of contact displacement fluctuations for probing at *state B*. Numbers denote loading path (1: DE, 2: DC).

e_{min}, e_{max} [309]. The latter were estimated as $e_{min} = 0.61$ and $e_{max} = 0.75$, respectively, following the same protocol described in Section 3.3.1. The granular sample and its idealized spherical counterpart are depicted in Fig. 3.23. The spherical specimen undergoes the same isotropic-triaxial compression history in order to achieve states A, B, and B', which, then, serve as initial conditions to the same stress probing protocols. Fig. 3.24 compares the strain response envelopes (total, elastic, plastic, reversible, and irreversible) of the idealized and granular assembly at state A, while Figs. 3.25 and 3.26 show the same comparison at states B and B', respectively. The following observations ensue:

- The spherical assembly exhibits a similar strain response to the granular one at the isotropic state. Yet, at the anisotropic and preloaded states, the response deviates significantly.
- The spherical assembly undergoes larger plastic strains, which is consistent with observations of increasing mobilized macroscopic friction angle with increasing angularity [57].

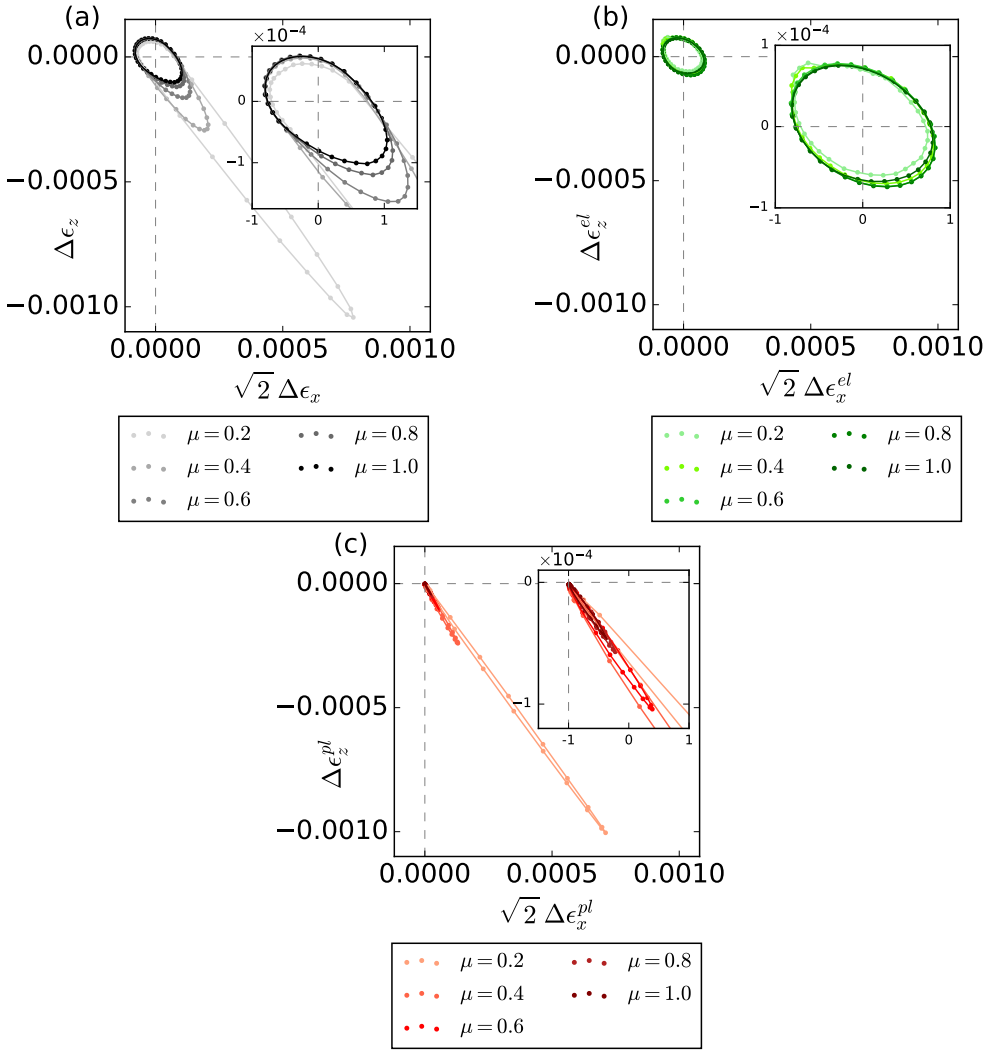

Figure 3.22: Effect of interparticle friction on the incremental response: a) Total, b) elastic, and c) plastic strain response envelope for the dense *granular* assembly at the anisotropic state B for varying interparticle friction.

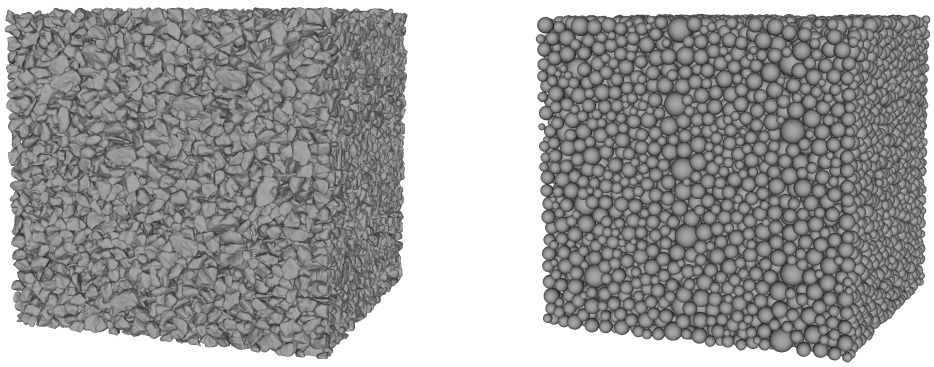

Figure 3.23: Granular assembly and its idealized spherical counterpart.

- At the isotropic state A, the difference in strain response due to particle shape is small, which indicates reduced interlocking and mobilization of friction at that state.
- At the virgin state B, we observe a substantial increase in magnitude ($\sim 35\%$), and a shift in the direction of plastic flow in the case of the spherical assembly.
- Differences in macroscopic strain response are most pronounced at state B'. Plastic strains for the spherical specimen are 6 times larger than the granular specimen, while the asymmetry of the irreversible envelope of the granular assembly is also more pronounced.

For completeness, Appendix 3.F extends these macroscopic observations of shape to the grain scale, by comparing the statistics of micromechanical attributes of the two assemblies.

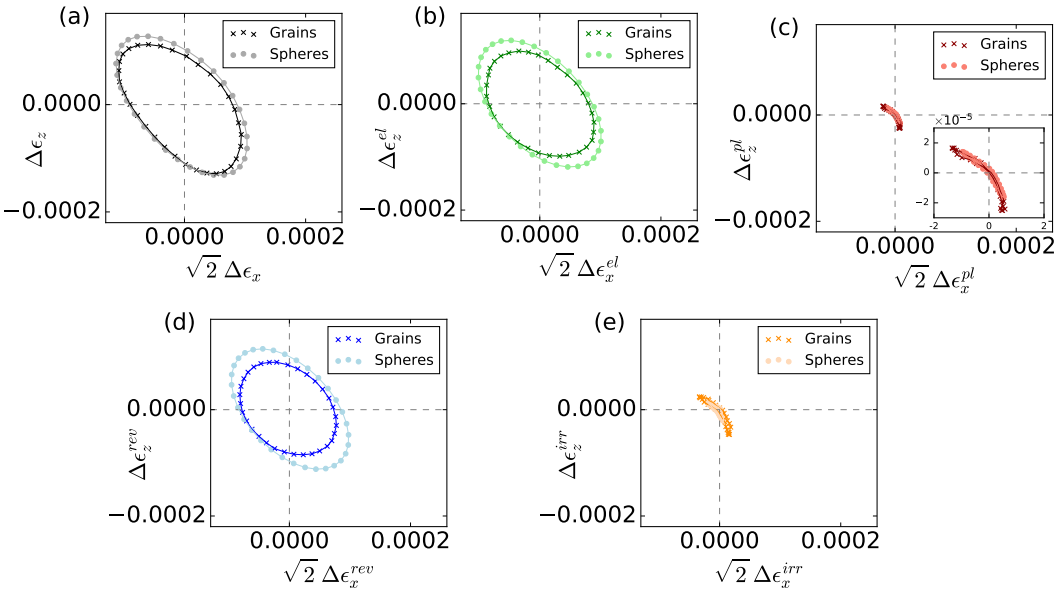

Figure 3.24: Effect of particle shape on the material response during probing from the *isotropic* state A: a) Total, b) elastic, c) plastic, d) reversible, and e) irreversible strain response envelope for the spherical and granular assembly.

Remark: Note that the above differences in the incremental response due to particle morphology may be partially alleviated by incorporating rolling friction into the interaction between spheres, which, however, requires laborious calibration (e.g. [48, 271]) and does not guarantee realistic behavior beyond the calibrated stress paths.

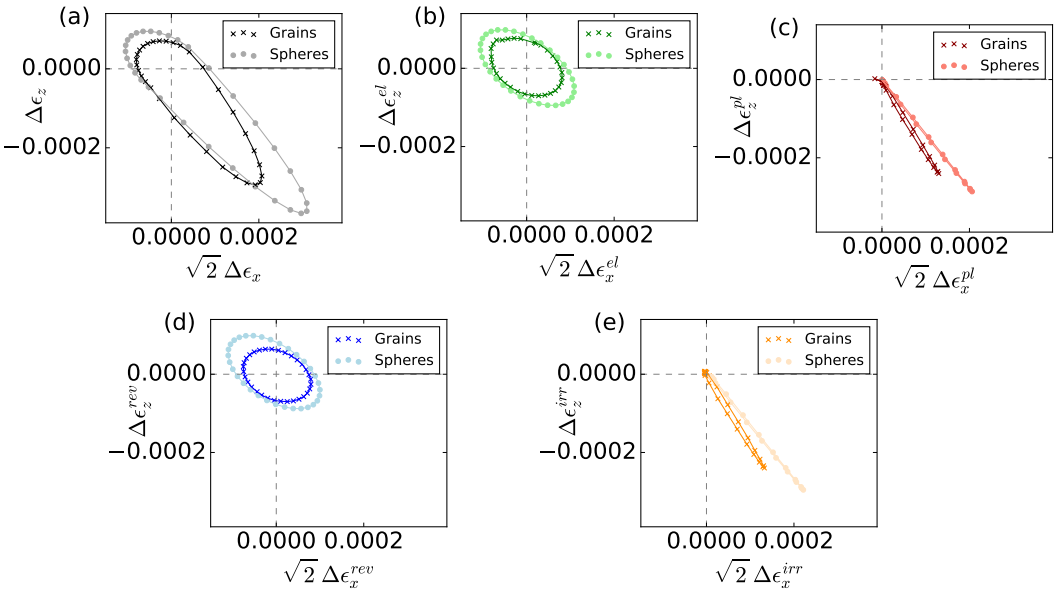

Figure 3.25: Effect of particle shape on the material response during probing from the *virgin* state B: a) Total, b) elastic, c) plastic, d) reversible, and e) irreversible strain response envelope for the spherical and granular assembly.

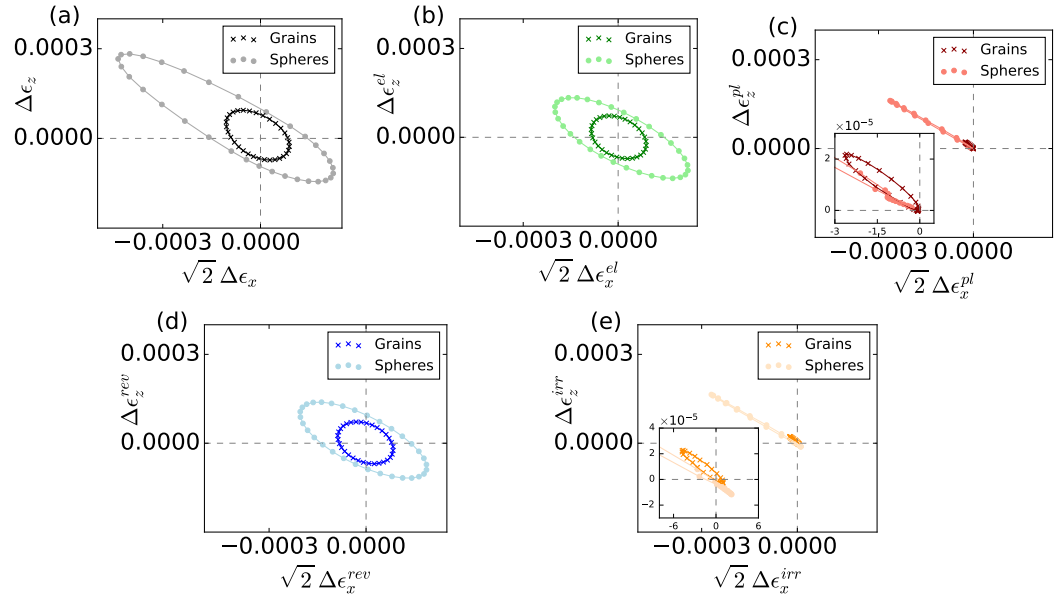

Figure 3.26: Effect of particle shape on the material response during probing from the *preloaded* state B': a) Total, b) elastic, c) plastic, d) reversible, and e) irreversible strain response envelope for the spherical and granular assembly.

3.3.9 Yield surface and flow rule

The final section of this work focuses on quantifying yield and plastic flow in 3D principal stress space, which has only been investigated through physical experiments or, computationally, for idealized assemblies [338]. To this end, the specimen described in Section 3.3.1 is first subjected to isotropic compression followed by rectilinear deviatoric stress probes with uniformly distributed Lode angle. The process is repeated for deviatoric planes corresponding to multiple pressure levels, until a cone is covered in the principal stress space

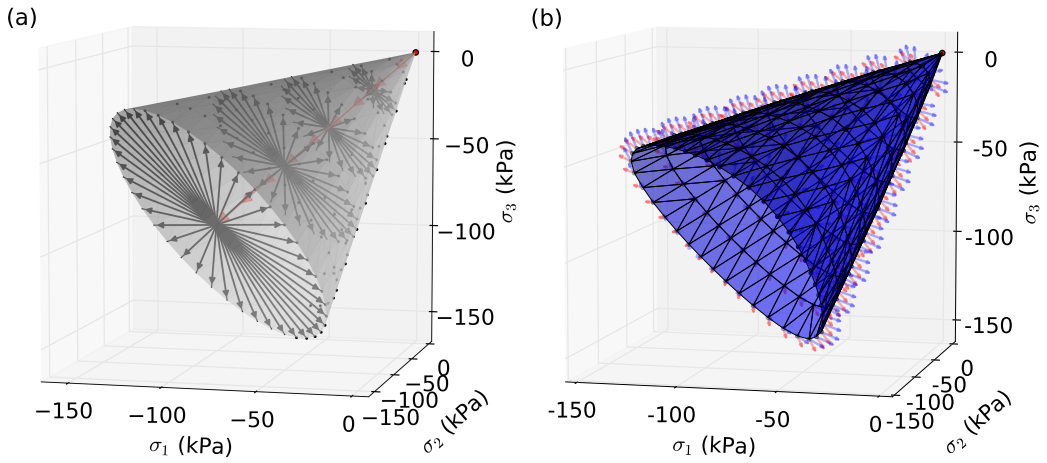

Figure 3.27: Quantifying yielding in 3D principal stress space: a) Rectilinear deviatoric probes, and b) yield surface in principal stress space with surface normals (blue arrows) and incremental plastic strain vectors (red arrows).

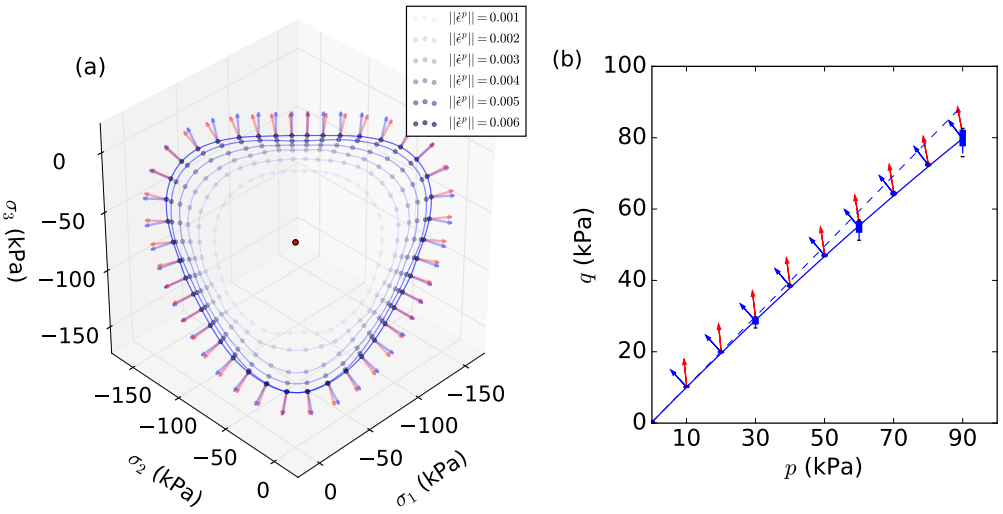

Figure 3.28: Yielding and plastic flow in two planes: a) Deviatoric plane ($p = 90$ kPa), and b) meridian plane ($\theta = 0°$).

(Fig. 3.27 a)). As opposed to previous studies [338, 48] who only considered a sextant section of a deviatoric plane, here each plane is completely covered to account for potential fabric effects. Throughout each probe, the evolution of plastic strain rate is monitored. We interpret the yield surface as the locus of stress states corresponding to the same value of the norm of plastic strain rate. We find that beyond a value of $||\dot{\boldsymbol{\epsilon}}^p|| = 5{\cdot}10^{-3}$, the surfaces essentially converge to an ultimate yield surface, which is shown in 3D in Fig. 3.27 b). Fig. 3.28 a) shows in more detail a particular deviatoric plane ($p = 90$ kPa), where the convergence of the sequence of yield surfaces is evident. In the same figure, the plastic strain increments are compared to the yield surface normals, exhibiting only minor nonassociativity (in regions of pronounced shear), verifying previous experimental and numerical observations [192, 13, 366]. Further, we find that this minor degree of associativity is independent of pressure. Fig. 3.28 b) shows a characteristic meridian plane corresponding to Lode angle $\theta = 30°$. In this plane, we observe prominent nonassociativity in accordance with previous experimental evidence that normality tends to overpredict the volumetric plastic strain. Upon closer observation, we can identify a small decrease in the degree of associativity with increasing pressure. This is related to the curved nature of the yield surface, highlighted in the same figure.

Naturally, the next step is to compare these high fidelity results with common analytical yield loci. Fig. 3.29 compares the yield locus obtained by the experiments against the Lade-Duncan [193] ($I_1^3 - bI_3 = 0$), Mohr-Coulomb ($|\sigma_i - \sigma_j|/(2\sqrt{\sigma_i\sigma_j}) - \tan\phi = 0$), Drucker-Prager [90] ($I_1 - aJ_2 = 0$) and Matsuoka-Nakai [225] ($I_1 I_2 - cI_3 = 0$) loci, where I_1, I_2, I_3 are the first, second, and third stress invariants, and J_2 is the second deviatoric stress invariant. The macroscopic friction angle under compression was calibrated for the Mohr-Coulomb criterion at $\phi \approx 51°$. Then the following expressions produce the parameters that are consistent with the Mohr-Coulomb

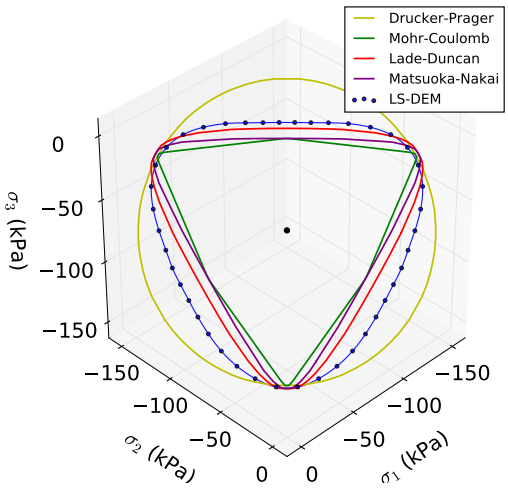

Figure 3.29: Comparison of analytical yield loci with virtual experiment data.

criterion:

$$a = \frac{2\sin\phi}{\sqrt{3}(3-\sin\phi)} \quad b = \frac{(3-\sin\phi)^3}{\cos^2\phi(1-\sin\phi)} \quad c = \frac{9-\sin^2\phi}{1-\sin^2\phi}.$$

For each of the criteria, we calculate the average pressure-normalized ℓ_2 error measure, given by $e = 1/(pN)\sum_{i=1}^{N}\|\boldsymbol{\sigma}_i^{\text{LS-DEM}} - \boldsymbol{\sigma}_i^{\text{Model}}\|_2$, where $\boldsymbol{\sigma}_i^{\text{LS-DEM}}, \boldsymbol{\sigma}_i^{\text{Model}}$ are the stress states corresponding to the virtual experiment and particular model, respectively, at the i^{th} point of the discretized yield surface comprised of a total of N points. We obtain:

Model	Drucker-Prager	Mohr-Coulomb	Lade-Duncan	Matsuoka-Nakai
e	0.137	0.095	0.040	0.076

Among the available loci, the ultimate yield surface is best described by the Lade-Duncan one.

3.4 Conclusions

We have presented an *in-silico* experimentation framework for granular materials, enabled by the accurate mathematical representation of the morphology and interaction of particles, as well as the control of their collective state, far beyond what has been accessible with preexisting techniques. Naturally arising, within this new paradigm, is the concept of a granular 'DNA' and its expression to an emergent macroscopic behavior that is largely free from idealizations. The remainder of the paper focused on utilizing virtual stress probing experiments towards a systematic investigation of the incremental behavior of sand.

In a first set of axisymmetric experiments, we quantified the reversible (i.e. those due to dissipation-free grain-scale mechanisms) and the elastic strains (i.e. those recovered upon unloading) in the granular assembly due to axisymmetric probing. We found that the reversible strain envelopes are slightly smaller (and, hence, contained within) the elastic ones, and quantified the anisotropy in the elastic response. In accordance with previous works, we identified evidence of a nonassociative and slightly nonregular flow rule. Next, we provided quantitative measurements of energy dissipation and contact fluctuations, the decoding of which remains the cornerstone of granular mechanics, and exhibited a threshold 'elastic' fluctuation above which the onset of yielding

occurs. Finally, hardening processes were examined from the perspective of the evolution of stored plastic work and fabric in the strong and weak contact networks.

Subsequent experiments focused on quantifying the effect of particle friction and morphology on the macroscopic response. Regarding the former, a combined effect of rotation and contraction of the strain response envelopes was identified upon increase of the interparticle friction. Beyond a critical value, the envelopes converge to a stationary envelope dictated by particle morphology. Remarkably, the idealized spherical counterpart of a granular assembly could qualitatively capture almost all aspects of its incremental behavior. Yet, from a quantitative perspective, we identified an important signature of morphology at anisotropic and, in particular, preloaded states. More specifically, experiments revealed a larger magnitude of plastic strain and a less pronounced stiffness increase due to preloading in the spherical specimen compared to the actual granular specimen.

A last set of deviatoric stress probing experiments furnished an important application of the proposed framework, where the entire yield surface and plastic potential was mapped in 3D principal stress space. We investigated the influence of pressure and Lode angle on the nonassociativity of the plastic flow, and found that, among the common analytical criteria, the failure surface was best described by the Lade-Duncan criterion.

The evidence from this study highlights the importance of high fidelity characterization and virtual testing for sands and potentially many other particulate materials. We are confident that such findings will help expand our understanding of the behavior of granular materials, and eventually guide the development of a new generation of constitutive theories. Interesting future avenues involve more in-depth investigation of granular fabric as well as the incorporation of grain fracture and multiphysics coupling. Finally, we see great potential in using virtual experiments to create a high-fidelity database for different families of granular materials, to be leveraged by Data-Driven and machine learning techniques.

Appendices

Appendix 3.A

Presented here is a standard thermodynamic formalism of the discrete contact interaction problem. In analogy to continuum thermodynamics [381, 260], consider the Gibbs energy G^c at a contact:

$$G^c = G^c(\mathbf{f}^c, \mathbf{q}^c, \theta) \tag{3.3}$$

as a function of the contact force $\mathbf{f}^c$, the temperature θ, and an internal variable $\mathbf{q}^c$ related to dissipative events (e.g. sliding). Neglecting thermal effects, the free energy vanishes at zero interparticle force. A convenient way to formulate the energy is through the local compliance $\mathbf{C}^c$ at the contact:

$$G^c = \frac{1}{2}\mathbf{f}^c \cdot \mathbf{C}^c\mathbf{f}^c + \mathbf{f}^c \cdot \mathbf{q}^c. \tag{3.4}$$

By construction, the internal variable $\mathbf{q}^c$ represents the plastic deformation $\boldsymbol{\delta}^{c,\mathrm{p}}$ that remains at the contact upon unloading to zero force,

$$\mathbf{q}^c = \left.\frac{\partial G^c}{\partial \mathbf{f}^c}\right|_{\mathbf{f}^c=\mathbf{0}} =: \boldsymbol{\delta}^{c,\mathrm{p}}. \tag{3.5}$$

The decomposition of the contact deformation into an elastic and plastic part follows by duality:

$$\boldsymbol{\delta}^c = \frac{\partial G^c}{\partial \mathbf{f}^c} = \boldsymbol{\delta}^{c,\mathrm{e}} + \boldsymbol{\delta}^{c,\mathrm{p}} \tag{3.6}$$

where:

$$\boldsymbol{\delta}^{c,\mathrm{e}} = \mathbf{C}^c\mathbf{f}^c \quad \text{or} \quad \mathbf{f}^c = \mathbf{C}^{c^{-1}}\boldsymbol{\delta}^{c,\mathrm{e}} = \mathbf{K}^c\boldsymbol{\delta}^{c,\mathrm{e}} \tag{3.7}$$

where $\mathbf{K}^c$ is the inverse compliance (stiffness) at the contact.
Assuming Ziegler's orthogonality condition, the dissipative force conjugate to the internal variable is given by:

$$\boldsymbol{\chi}^c = \frac{\partial G^c}{\partial \boldsymbol{\delta}^{c,\mathrm{p}}} = \mathbf{f}^c. \tag{3.8}$$

Note in passing that the contact compliance is assumed to be independent of internal processes ($\mathbf{q}^c$), for the sake of simplicity. Generalization towards contact damage or aging [308] is easily achieved by dropping this assumption. In order to obtain a closed set of equations, the above equilibrium relations need

to be combined with appropriate kinetic relations [260]. Indeed, the existence of a kinetic (dissipation) potential ψ^c follows from standard thermodynamic arguments [259] such that:

$$\dot{\boldsymbol{\delta}}^{c,p} \in \partial_{\boldsymbol{\chi}^c} \psi^c. \tag{3.9}$$

In an algorithmic (incremental) setting, we obtain the equivalent relations:

$$d\boldsymbol{\delta}^c = d\boldsymbol{\delta}^{c,\mathrm{e}} + d\boldsymbol{\delta}^{c,\mathrm{p}} \tag{3.10}$$

$$d\mathbf{f}^c = \mathbf{K}^c d\boldsymbol{\delta}^{c,\mathrm{e}} \tag{3.11}$$

$$d\boldsymbol{\delta}^{c,p} \in \partial_{\boldsymbol{\chi}^c} \psi^c. \tag{3.12}$$

Finally, to fully determine the contact law, a specific form of the contact stiffness and the kinetic potential needs to be identified. The prototypical example, used in the stress probing experiments of Section 3.3, is that of a Hookean stiffness with Coulomb friction. In this case, the contact stiffness is given by:

$$\mathbf{K}^c = \mathbf{C}^{-1} = k_n^c \, \mathbf{n}^c \otimes \mathbf{n}^c + k_t^c \, (\mathbf{s}^c \otimes \mathbf{s}^c + \mathbf{t}^c \otimes \mathbf{t}^c) \tag{3.13}$$

where $(\mathbf{n}^c, \mathbf{s}^c, \mathbf{t}^c)$ form a local cartesian system at the contact c, and k_n^c, k_t^c are the normal and tangential stiffness respectively [4], while the kinetic potential is given by the indicator function $I_{\mathcal{C}}(\mathbf{f}^c)$ of the Coulomb cone $\mathcal{C}$:

$$\mathcal{C} = \{\mathbf{f}^c \,|\, \|\mathbf{f}^c - (\mathbf{f}^c \cdot \mathbf{n}^c)\mathbf{n}^c\| - \mu(\mathbf{f}^c \cdot \mathbf{n}^c) \leq 0\} \tag{3.14}$$

where $\mathbf{n}^c$ denotes the contact normal, and μ the interparticle friction.

Remark: The thermodynamic description provided herein is far from general. Instead, the contact scale interaction is treated as 'standard' material behavior, which includes a specific form of the Gibbs free energy and the restrictive statement of Ziegler's orthogonality. This description can be appropriately extended to allow for more complex interaction laws, by adapting relevant developments in the continuum thermodynamic modeling of frictional materials [74] to our discrete system.

Appendix 3.B

We verify the representativeness of the granular assembly through a simple investigation of the effect of sample size. Four samples of the same relative density ($D_r = 85\%$) were constructed, that comprised of an increasing number of grains (4913, 9261, 15625, and 19683, respectively). The samples were subjected to drained triaxial compression to the anisotropic state B, followed by an axisymmetric stress probing protocol (Section 3.3.1). We observe satisfactory convergence of the strain response to a well defined envelope for sample sizes above 15625 grains.

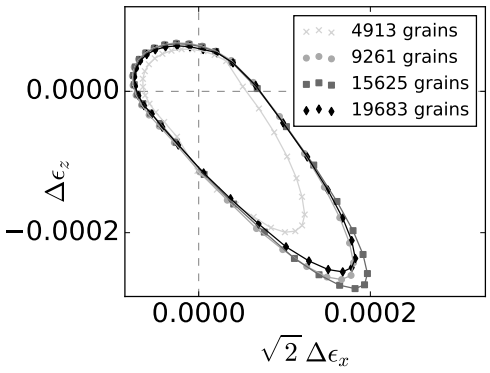

Figure 3.B.1: Effect of sample size on the strain response envelope.

Appendix 3.C

We provide evidence of the irreversibility of contact deformation upon unloading, similarly to a recent investigation by Kuhn and Daouadji [190]. To do so, we track the contacts that were sliding during loading for a probing experiment at state B. In particular, Fig. 3.C.1 shows the transition of the number of such sliding contacts N^c, normalized by the number of particles N^p, upon unloading for various probing directions. We observe that a significant proportion of sliding contacts continue to slide during unloading, regardless of the direction of probing. This evidence suggests that contact deformations are not reversed during unloading.

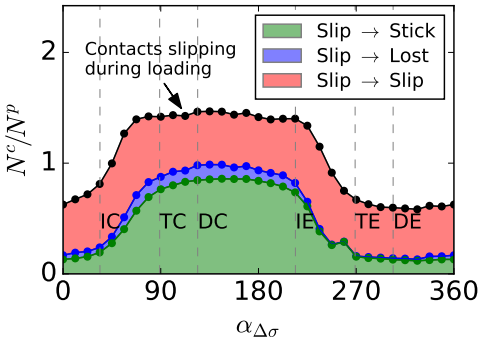

Figure 3.C.1: Transition of number of contacts, normalized by number of particles, that were sliding during loading, plotted as a function of the probing angle.

Appendix 3.D

We address the calculation of elasticity parameters in Table 3.2. First, a least-squares fit is applied to solve for the components of the elastic stiffness tensor $\mathbf{C}$ (in the principal plane) below:

$$\begin{bmatrix} \Delta\sigma_x \\ \Delta\sigma_y \\ \Delta\sigma_z \end{bmatrix} = \begin{bmatrix} C_{11} & C_{12} & C_{13} \\ C_{21} & C_{22} & C_{23} \\ C_{31} & C_{32} & C_{33} \end{bmatrix} \begin{bmatrix} \Delta\epsilon_x \\ \Delta\epsilon_y \\ \Delta\epsilon_z \end{bmatrix} \tag{3.15}$$

given the data pairs $(\Delta\boldsymbol{\sigma}, \Delta\boldsymbol{\epsilon})$ for all probes at a specific state. By comparing the fitted stiffness tensor $\mathbf{C}$ to the isotropic and transversely isotropic elasticity tensors:

$$\mathbf{C}^{iso} = \begin{bmatrix} 1/E & -\nu/E & -\nu/E \\ -\nu/E & 1/E & -\nu/E \\ -\nu/E & -\nu/E & 1/E \end{bmatrix} \quad \mathbf{C}^{tra} = \begin{bmatrix} 1/E_x & -\nu_x/E_x & -\nu_{zx}/E_z \\ -\nu_x/E_x & 1/E_x & -\nu_{zx}/E_z \\ -\nu_{zx}/E_z & -\nu_{zx}/E_z & 1/E_z \end{bmatrix}. \tag{3.16}$$

we obtain the Young's modulus E and Poisson's ratio ν, in the case of isotropy, as well as the transverse and longitudinal moduli E_x, E_z, and the associated Poisson's ratios $\nu_x (= \nu_{xy} = \nu_{yx}), \nu_{zx} (= \nu_{xz})$, in the case of transverse isotropy.

Appendix 3.E

We discuss alternative strategies for extracting the reversible strain response of an assembly. As outlined in Section 3.3.3, by carrying out probes where frictional dissipation has been inhibited, we obtain slightly overestimated reversible strain envelopes, due to the relaxation of the contact topology. Here we compare these envelopes to those produced by two alternative strategies: i) the inhibited-dissipation/rotation approach of Calvetti, Viggiani, and Tamagnini [48], and ii) an analytical homogenization-based approach.

The first method delivers the reversible response through a set of probes where we inhibit not only frictional dissipation but also grain rotation [48]. This additional constraint is introduced in order to preserve the contact topology, yielding a purely reversible process. However, constraining rotations has the undesired side-effect of stiffening (underestimating) the reversible response, producing a loose lower bound for the true reversible strain response. Further, rotational constraints induce external moments on the particles, which lead to the development of couple stress. The latter is known to affect the development of RVE-scale and meso-scale instabilities [253], and, hence, the determination of the true material response. The second method, detailed in the next section, extracts the reversible strain component by relying on an analytical homogenization technique and a new closure relation, that extend previous results on idealized elastic assemblies.

Fig. 3.E.1 compares the reversible response furnished by the inhibited dissipation approach (Section 3.3.3) to that of the inhibited dissipation/rotation approach, as well as the homogenization-based method, for all states considered in this study. The last two methods give very similar results, and tend to equally underestimate the response, particularly in the (DC) and (DE) directions.

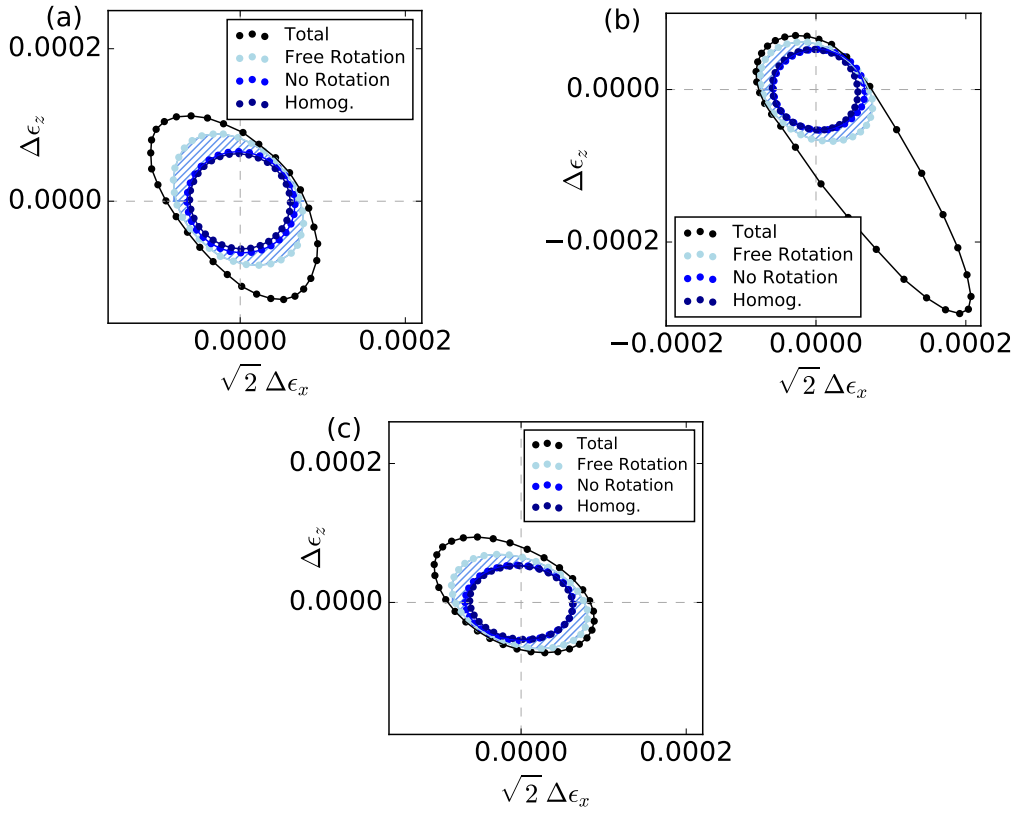

Figure 3.E.1: Comparison between reversible envelopes generated via free-rotation (light blue) and constrained-rotation (blue) simulations, as well as via homogenization-based approach (dark blue) for a) the isotropic state A, b) the anisotropic state B, and c) the preloaded state B'.

Homogenization-based approach

We derive a micromechanical expression for the decomposed reversible and irreversible strains in an assembly. To this end, consider an RVE of arbitrarily shaped particles, which is subject to an average strain increment $d\bar{\boldsymbol{\varepsilon}}$ and, thus, develops a stress increment $d\bar{\boldsymbol{\sigma}}$. At any contact c within the assembly (Fig. 3.E.2) (between particles p, q), the displacement $d\boldsymbol{\delta}^c$ can be described [206] by a projection of the average displacement gradient $d\bar{\boldsymbol{\varepsilon}}$ to the branch vector $\mathbf{l}^c$, corrected by a nonaffine displacement fluctuation. In all generality :

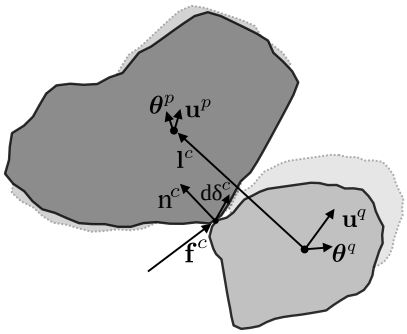

Figure 3.E.2: 2D schematic of deformed particle contact.

$$d\boldsymbol{\delta}^c = d\bar{\boldsymbol{\varepsilon}} \cdot \mathbf{l}^c + d\tilde{\boldsymbol{\delta}}^c \tag{3.17}$$

where $\mathbf{l}^c$ is the contact branch vector, and $d\tilde{\boldsymbol{\delta}}^c$ is the fluctuation of the incremental contact deformation. Invoking the decomposition of the contact deformation (Eq. 3.10), we obtain:

$$d\boldsymbol{\delta}^{c,\mathrm{e}} + d\boldsymbol{\delta}^{c,\mathrm{p}} = d\bar{\boldsymbol{\varepsilon}} \cdot \mathbf{l}^c + d\tilde{\boldsymbol{\delta}}^c. \tag{3.18}$$

We shall decompose the strain into a reversible and an irreversible part:

$$d\bar{\boldsymbol{\varepsilon}} = d\bar{\boldsymbol{\varepsilon}}^{\mathrm{rev}} + d\bar{\boldsymbol{\varepsilon}}^{\mathrm{irr}}. \tag{3.19}$$

Remark: The total strain may be directly computed based on particle kinematics [25], but this is not true for its decomposition. By construction, the reversible component represents the strain derived from reversible grain-scale processes, which coincide with elastic processes at that scale.

The reversible strain will be used to define elastic contact displacement fluctuations $d\tilde{\boldsymbol{\delta}}^{c,\mathrm{e}}$ below:

$$d\boldsymbol{\delta}^{c,\mathrm{e}} = d\bar{\boldsymbol{\varepsilon}}^{\mathrm{rev}} \cdot \mathbf{l}^c + d\tilde{\boldsymbol{\delta}}^{c,\mathrm{e}}. \tag{3.20}$$

In analogy with previous analytical studies of purely elastic assemblies (e.g. [234]), the elastic fluctuations in Eq. 3.20 are unknown, which calls for a closure relation, relating those to the average strain. This relation is furnished in this study by the incremental force balance of all particles in the assembly. For a particle p sharing contacts $\mathcal{C}^p$ with its neighbors, we can write:

$$\sum_{c \in \mathcal{C}^p} d\mathbf{f}^c = 0 \tag{3.21}$$

$$\sum_{c \in \mathcal{C}^p} \mathbf{K}^c d\boldsymbol{\delta}^{c,\mathrm{e}} = 0 \qquad \text{(via Eq. 3.11)} \tag{3.22}$$

$$\sum_{c \in \mathcal{C}^p} \mathbf{K}^c (d\bar{\boldsymbol{\varepsilon}}^{\mathrm{rev}} \mathbf{l}^c + d\tilde{\boldsymbol{\delta}}^{c,\mathrm{e}}) = 0 \qquad \text{(via Eq. 3.20)} \tag{3.23}$$

where $\mathbf{K}^c$ is the contact stiffness given by Eq. 3.13.
The linear system obtained by collecting the equilibrium equations for all particles is generally underdetermined (depending on the coordination number)

and, therefore, needs to be supplemented by appropriate boundary conditions. Consider the equilibrium of each of the two participating particles (p, q), assuming that i) contact c experiences an unknown fluctuation $d\tilde{\boldsymbol{\delta}}^{\mathrm{c,e}}$, and ii) the first shell of contacts (i.e contacts between any of the participating particles (p, q) and their neighbours ($\mathcal{C}^p$ and $\mathcal{C}^q$, respectively)) undergo a different unknown fluctuation $d\hat{\tilde{\boldsymbol{\delta}}}^{\mathrm{c,e}}$. This simplifies the equilibrium equation of the two participating particles to a solvable system:

$$\sum_{c'\in\mathcal{C}^p\setminus c}\mathbf{K}^{c'}(d\bar{\boldsymbol{\varepsilon}}^{\mathrm{rev}}\mathbf{l}^{c'}+d\hat{\tilde{\boldsymbol{\delta}}}^{\mathrm{c,e}})+\mathbf{K}^{c}(d\bar{\boldsymbol{\varepsilon}}^{\mathrm{rev}}\mathbf{l}^{c}+d\tilde{\boldsymbol{\delta}}^{\mathrm{c,e}})=0 \tag{3.24}$$

$$\sum_{c'\in\mathcal{C}^q\setminus c}\mathbf{K}^{c'}(d\bar{\boldsymbol{\varepsilon}}^{\mathrm{rev}}\mathbf{l}^{c'}+d\hat{\tilde{\boldsymbol{\delta}}}^{\mathrm{c,e}})+\mathbf{K}^{c}(-d\bar{\boldsymbol{\varepsilon}}^{\mathrm{rev}}\mathbf{l}^{c}-d\tilde{\boldsymbol{\delta}}^{\mathrm{c,e}})=0 \tag{3.25}$$

where the sign change is due to change of reference ($\mathbf{l}^{pq}=\mathbf{l}^{c}=-\mathbf{l}^{qp}$). Solving Eq. 3.24 for $d\hat{\tilde{\boldsymbol{\delta}}}^{\mathrm{c,e}}$ and substituting into Eq. 3.25, we finally obtain, after algebraic manipulations:

$$d\tilde{\boldsymbol{\delta}}^{\mathrm{c,e}}=-\boldsymbol{\Gamma}^{c}\cdot d\bar{\boldsymbol{\varepsilon}}^{\mathrm{rev}} \tag{3.26}$$

in terms of the fluctuation tensor:

$$\boldsymbol{\Gamma}^{c}=\Big[\big(\mathbf{I}+\boldsymbol{\Delta}\big)\cdot\mathbf{K}^{c}\Big]^{-1}\cdot\Big[\sum_{c'\in\mathcal{C}^p}\mathbf{K}^{c'}\otimes\mathbf{l}^{c'}-\boldsymbol{\Delta}\cdot\sum_{c'\in\mathcal{C}^q}\mathbf{K}^{c'}\otimes\mathbf{l}^{c'}\Big] \tag{3.27}$$

and where:

$$\boldsymbol{\Delta}=\big(\sum_{c'\in\mathcal{C}^p\setminus c}\mathbf{K}^{c'}\big)\big(\sum_{c'\in\mathcal{C}^q\setminus c}\mathbf{K}^{c'}\big)^{-1}. \tag{3.28}$$

Combining Eqs. 3.26 and 3.20, we can solve for the elastic contact displacement:

$$d\boldsymbol{\delta}^{\mathrm{c,e}}=d\bar{\boldsymbol{\varepsilon}}^{\mathrm{rev}}\cdot\mathbf{l}^{c}-\boldsymbol{\Gamma}^{c}:d\bar{\boldsymbol{\varepsilon}}^{\mathrm{rev}}. \tag{3.29}$$

The final ingredient required here is the incremental version of the well-established virial stress relation [68, 26]:

$$d\bar{\boldsymbol{\sigma}}=\frac{1}{V}\sum_{c\in\mathcal{C}}(d\mathbf{f}^{c}\otimes\mathbf{l}^{c}+\mathbf{f}^{c}\otimes d\mathbf{l}^{c}). \tag{3.30}$$

Rearranging Eq. 3.30, and using Eq. 3.11:

$$\frac{1}{V}\sum_{c\in\mathcal{C}}\mathbf{K}^c d\boldsymbol{\delta}^{c,\mathrm{e}}\otimes\mathbf{l}^c = d\bar{\boldsymbol{\sigma}} - \frac{1}{V}\sum_{c\in\mathcal{C}}\mathbf{f}^c\otimes d\mathbf{l}^c =: d\bar{\boldsymbol{\sigma}}^{\mathrm{kt}} \tag{3.31}$$

where the RHS represents the readily computable kinetic contribution to the stress increment.
The extraction of the reversible strain is concluded by substituting for Eq.3.29 above, to obtain:

$$\frac{1}{V}\sum_{c\in\mathcal{C}}\mathbf{K}^c(d\bar{\boldsymbol{\varepsilon}}^{\mathrm{rev}}\cdot\mathbf{l}^c - \boldsymbol{\Gamma}^c : d\bar{\boldsymbol{\varepsilon}}^{\mathrm{rev}})\otimes\mathbf{l}^c = d\bar{\boldsymbol{\sigma}}^{\mathrm{kt}} \tag{3.32}$$

or:

$$d\bar{\boldsymbol{\varepsilon}}^{\mathrm{rev}} = \left[\frac{1}{V}\sum_{c\in\mathcal{C}}\left(\mathbf{l}^c\otimes\mathbf{K}^c\otimes\mathbf{l}^c - \mathbf{l}^c\otimes\mathbf{K}^c\cdot\boldsymbol{\Gamma}^c\right)\right]^{-1} d\bar{\boldsymbol{\sigma}}^{\mathrm{kt}}. \tag{3.33}$$

Note that the RHS solely involves micromechanical quantities readily available in a virtual experiment. Finally, the irreversible strain follows from Eq. 3.19 as $d\bar{\boldsymbol{\varepsilon}}^{\mathrm{irr}} = d\bar{\boldsymbol{\varepsilon}} - d\bar{\boldsymbol{\varepsilon}}^{\mathrm{rev}}$.

Remark: Not surprisingly, this approach leads to the development of a non-affine stiffness tensor (Eq. 3.33). It is similar in nature to the approach of Froiio and Roux [115] who explicitly construct the stiffness of a disk assembly by adopting [4], and also intimately related to previous studies, outside the context of stress probing, that deal with the analytical determination of the stiffness of an assembly of particles [58, 234, 206, 151, 150, 3, 4, 5, 340, 62, 64, 96, 248, 365, 284], most prominently the approach of Misra and Chang [234], in the idealized setting and with a different closure relation.

Appendix 3.F

We extend here the macroscopic investigation of the influence of shape, given in Section 3.3.8, to the grain scale. This is achieved by comparing micromechanical attributes of the granular assembly to those of its idealized spherical counterpart. In particular, Fig. 3.F.1 plots the tangential contact force f_t as a function of the normal force f_n for the three investigated states (A,B,B'), with the dashed lines representing the average mobilized friction angles. Interestingly, the granular assembly consistently exhibits a higher mobilization

of interparticle friction at any given state, while the distribution of forces of the two samples is qualitatively similar. Analogous observations can be made by inspecting Fig. 3.F.2 which compares the mobilized friction angle of the two assemblies plotted against the magnitude of normal force for the conventional and reversible (DC) probes at state B. Beyond the clear qualitative agreement, we verify the emergence of a higher mobilized interparticle friction for the granular assembly in the conventional probes. Measurements taken at different states and stress paths led to the same conclusions, and were thus omitted in this comparison.

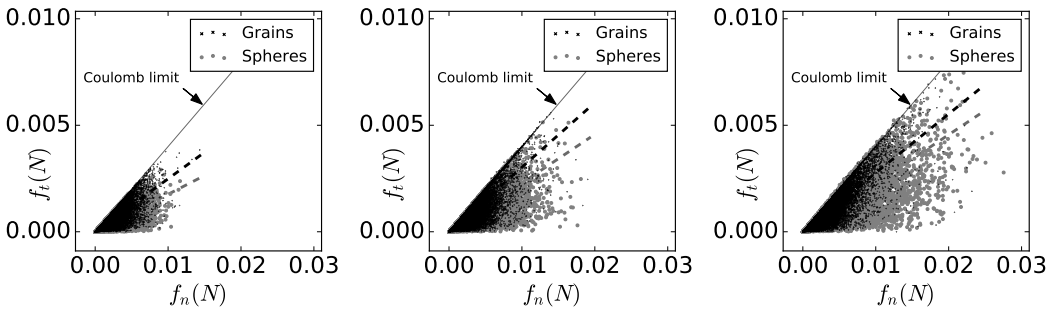

Figure 3.F.1: Tangential vs normal contact forces at states a) A, b) B, and c) B' for the granular and spherical assembly.

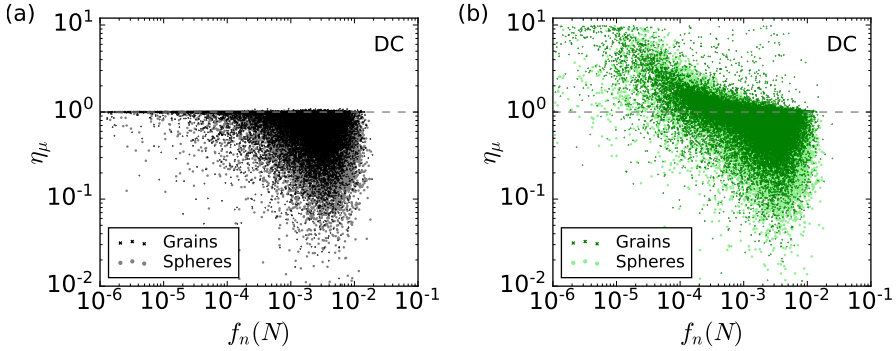

Figure 3.F.2: Mobilized friction vs magnitude of normal contact force for the granular and spherical assembly at the (DC) direction at state B for a) the conventional, and b) the reversible (inhibited dissipation) simulation.

Chapter 4

DATA-DRIVEN MULTISCALE MODELING IN MECHANICS

K. Karapiperis, L. Stainier, M. Ortiz, and J. E. Andrade. "Data-Driven multiscale modeling in mechanics". In: *Journal of the Mechanics and Physics of Solids* (2020), p. 104239.

Abstract

We present a Data-Driven framework for multiscale mechanical analysis of materials. The proposed framework relies on the Data-Driven formulation in mechanics [172], with the material data being directly extracted from lower-scale computations. Particular emphasis is placed on two key elements: the parametrization of material history, and the optimal sampling of the mechanical state space. We demonstrate an application of the framework in the prediction of the behavior of sand, a prototypical complex history-dependent material. In particular, the model is able to predict the material response under complex nonmonotonic loading paths, and compares well against plane strain and triaxial compression shear banding experiments.

4.1 Introduction

Traditionally, the mechanical behavior of history-dependent materials has been described by empirical constitutive laws formulated within the framework of continuum thermodynamics and plasticity theory [72, 291, 214]. In that context, the material state is described by internal variables that are often phenomenological and are subject to *ad-hoc* evolution laws (kinetic relations). Advancements in atomistic [2, 45] and micromechanical [78, 376] simulation have inspired physics-based internal variables that encapsulate the microstructure (e.g. density of defects/dislocations for heterogeneous solids [218, 325], fabric tensors for granular materials [204], etc). Naturally, these developments also gave rise to multiscale methods, which attempt to either pass information from the fine to the coarse scale (hierarchical) [383, 108, 18, 249] or seamlessly connect the two scales by modeling their interaction (concurrent/semi-concurrent) [176, 331, 41, 360, 288].

Despite the relative success of these conventional paradigms, further progress

has been hindered by many challenges. In the case of conventional constitutive modeling, the process inherently induces uncertainty due to the imperfect knowledge of the functional form of the constitutive laws [172] and their extrapolative properties beyond the finite data set used for calibration. Moreover, the process of calibration itself can be challenging due to the continuously increasing model complexity (e.g. [298, 79]). On the other hand, conventional multiscale methods can be notoriously demanding in computational time and memory. The data obtained from lower-scale simulations, carried out concurrently or on-the-fly, are never reused, rendering the conventional paradigm inherently inefficient.

In light of the aforementioned challenges, and driven by the progress in data science, promising alternatives have surfaced in the form of machine learning and Data-Driven techniques. The first machine learning studies relied on neural networks (NN) trained with experimental data in order to predict mechanical behavior [121]. With the increase in computation, deep learning has found multiple applications in behavior prediction with tensor basis- [157], hybrid graph- [357], and recurrent-NN [367, 237], used as surrogates for constitutive laws or lower-scale simulations. Despite their efficiency and, in some cases, their desired built-in invariance properties, the above machine learning techniques leave a lot to be desired. They rely on a (hidden) mathematical representation of constitutive relations, therefore leading to extrapolation from the training material data set, and often depend on application-specific network architectures.

The Data-Driven paradigm for computational mechanics [172, 174] bypasses any modeling step by formulating the problem directly on a given material data set, while enforcing pertinent constraints and conservation laws. More specifically, by defining a phase space of stress-strain field pairs, this approach leads to a distance minimization problem between a given material data set and the subset of field pairs that satisfy the conservation laws. Recently, the Data-Driven paradigm was extended to dynamics [173] and inelasticity [92]. Also, variations of the Data-Driven framework have been proposed that consider locally linear [143] or locally convex embeddings [136].

In this study, we present a new multiscale Data-Driven paradigm as a complement to conventional multiscale modeling. The framework departs from previous developments in Data-Driven computing in that i) material data are

directly extracted from lower-scale computations (e.g. molecular dynamics (MD), discrete element method (DEM) and finite element method (FEM)), ii) it enables optimal phase space sampling, offline or on-the-fly, and iii) it is thermodynamically consistent without imposing any constraints on the nature of history-dependence.

The paper is organized as follows. In Section 4.2 we review the general framework of Data-Driven Inelasticity, which represents our study's point of departure. Section 4.3 addresses phase space sampling from lower-scale computations, and briefly introduces optimal strategies. Next, in Section 4.4, we discuss pertinent general representations of the material history that ensure the consistency of the multiscale computation. Finally, Section 4.5 presents a detailed application of the method in multiscale modeling of granular materials. We conclude with a discussion of the proposed framework in Section 4.6.

4.2 Data-Driven inelasticity

Consider the purely mechanical problem of a body that is discretized in N nodes and M material points (Fig 4.1 a)). The body is subject to applied forces $\mathbf{f} = \{\mathbf{f}_\alpha\}_{\alpha=1}^N$, and undergoes displacements $\mathbf{u} = \{\mathbf{u}_\alpha\}_{\alpha=1}^N$ at its nodes. The internal state is characterized by local stress and strain pairs $\{(\boldsymbol{\varepsilon}_e, \boldsymbol{\sigma}_e)\}_{e=1}^M$. We consider the pair $\mathbf{z}_e = (\boldsymbol{\varepsilon}_e, \boldsymbol{\sigma}_e)$ as a point in a local phase space Z_e, and $\mathbf{z} = \{\mathbf{z}_e\}_{e=1}^M$ as a point in the global phase space Z. Within a time-discrete formulation, the internal state of the system is subject to the following compatibility and equilibrium constraints:

$$\boldsymbol{\varepsilon}_{e,k} = \mathbf{B}_e u_k, \quad e = 1, \dots, M \tag{4.1}$$

$$\sum_{e=1}^{M} w_e \mathbf{B}_e^T \boldsymbol{\sigma}_{e,k} = \mathbf{f}_k \tag{4.2}$$

where $\mathbf{u}_k, \mathbf{f}_k, \boldsymbol{\varepsilon}_k, \boldsymbol{\sigma}_k$ denote the displacements, forces, strains, and stresses at time t_k, respectively, while $\{w_e\}_{e=1}^M$ are elements of volume, and $\mathbf{B}_e$ is a discrete strain operator for material point e. A constraint set E_k may be defined as:

$$E_k = \{\mathbf{z} \in \mathbf{Z} \,|\, (4.1) \text{ and } (4.2)\} \tag{4.3}$$

and consists of all the compatible and equilibrated internal states, due to the applied loads and displacements at time t_k.

Instead of providing closure to Equations 4.1 and 4.2 by postulating a constitutive relation $\boldsymbol{\sigma} = \boldsymbol{\sigma}(\boldsymbol{\varepsilon})$, the Data-Driven formulation of the mechanical problem relies directly on the material data. More specifically, the material behavior is described by a material data set $D_{e,k}$ of points $\mathbf{z}_{e,k} \in Z_{e,k}$, that is attainable at a material point given its past local history of deformation:

$$D_{e,k} = \{(\boldsymbol{\varepsilon}_{e,k}, \boldsymbol{\sigma}_{e,k}) \,|\, (\text{past local history}) \,\}. \tag{4.4}$$

Accordingly, a global material data set may be defined as:

$$D_k = D_{1,k} \times \ldots \times D_{M,k}.$$

The history-dependent Data-Driven problem consists of finding the compatible and equilibrated internal state $\mathbf{z}_k \in E_k$ that minimizes the distance to the global material data set D_k at time t_k. Equivalently, the problem consists of finding the point $\mathbf{y}_k$ in the material data at time that is closest to the constraint set E_{k+1} at time t_k. To this end, the local phase spaces Z_e are equipped with the following metric:

$$|\mathbf{z}_e|_e = \left(\mathbb{C}_e \boldsymbol{\varepsilon}_e \cdot \boldsymbol{\varepsilon}_e + \mathbb{C}_e^{-1} \boldsymbol{\sigma}_e \cdot \boldsymbol{\sigma}_e\right)^{1/2} \tag{4.5}$$

where $\mathbb{C}_e$ are symmetric positive definite matrices, that are only introduced as a numerical scheme, and do not represent actual material behavior. The above norm induces a metrization of the global phase space Z, by means of the norm:

$$|\mathbf{z}| = \big(\sum_{e=1}^{M} w_e |\mathbf{z}_e|_e^2 \big)^{1/2} \tag{4.6}$$

with corresponding global distance:

$$d(\mathbf{z}, \mathbf{y}) = |\mathbf{z} - \mathbf{y}|. \tag{4.7}$$

Consisely, the time discrete Data-Driven problem may be formulated as:

$$\min_{\mathbf{y} \in D_k} \min_{\mathbf{z} \in E_k} d(\mathbf{z}_k, \mathbf{y}_k) = \min_{\mathbf{z} \in E_k} \min_{\mathbf{y} \in D_k} d(\mathbf{z}_k, \mathbf{y}_k). \tag{4.8}$$

For fixed $\mathbf{y}_k \in D_k$, the closest point projection $\mathbf{z}_k = P_{E_k}\mathbf{y}_k$ involves minimizing the quadratic function $d^2(\cdot, \mathbf{y}_k)$ subject to the compatibility and equilibrium constraints (Eqs 4.1-4.2). The former may be enforced directly, while the latter may be enforced by means of Lagrange multipliers $\boldsymbol{\eta}_k$, which represent virtual displacements of the system. The resulting Euler-Lagrange equations read:

$$\big(\sum_{e=1}^{M} w_e \mathbf{B}_e^T \mathbb{C}_e \mathbf{B}_e\big)\mathbf{u}_k = \sum_{e=1}^{M} w_e \mathbf{B}_e^T \mathbb{C}_e \boldsymbol{\varepsilon}_{e,k}^* \tag{4.9}$$

$$\big(\sum_{e=1}^{M} w_e \mathbf{B}_e^T \mathbb{C}_e \mathbf{B}_e\big)\boldsymbol{\eta}_k = \mathbf{f}_{k+1} - \sum_{e=1}^{M} w_e \mathbf{B}_e^T \boldsymbol{\sigma}_{e,k}^* \tag{4.10}$$

$$\boldsymbol{\sigma}_{e,k} = \boldsymbol{\sigma}_{e,k}^* + \mathbb{C}_e \sum_{\alpha=1}^{N} \mathbf{B}_{e\alpha} \boldsymbol{\eta}_{\alpha,k} \tag{4.11}$$

where $(\boldsymbol{\varepsilon}_{e,k}^*, \boldsymbol{\sigma}_{e,k}^*)$ is the unknown optimal local state in the material data set for material point e.

4.2.1 Solution algorithm

The simplest Data-Driven solver involves the fixed point iteration:

$$\mathbf{z}_k^{(j+1)} = P_{E_k} P_{D_k} \mathbf{z}_k^{(j)} \tag{4.12}$$

where j is the iteration number, $P_{D_k}\mathbf{z}_k^{(j)}$ denotes the closest point projection onto D (i.e. finding the point in the material data set that is closest to $\mathbf{z}_k^{(j)}$), and $P_{E_k}\mathbf{y}_k^{(j)}$ denotes the projection of a fixed $\mathbf{y}_k \in D_k$ onto E_k. The algorithm converges when the local states remain unchanged under the closest point projection to the material data set [172], as shown in Algorithm 1.

Two key questions arise in a multiscale interpretation of the Data-Driven framework: i) How can we efficiently sample the phase space, offline and on-the-fly, using lower-scale computations? ii) How we can parametrize the material history given the available data from these computations? We address these questions in the following sections.

Algorithm 1 Fixed-point solver

Require: Data sets $D_{e,1}$ (via offline phase space sampling: **Algorithms** 2, 3),
Strain operators $\mathbf{B}_e$ ($e=1, ..., M$), Applied forces $\mathbf{f}_1$
for all time steps $k = 1, ..., N_k$ **do**
i) Set iteration $j = 0$. Initial local data assignment:
for all $e = 1, ..., M$ **do**
if k = 0 **then**
Choose $(\boldsymbol{\varepsilon}^{*,(0)}_{e,1}, \boldsymbol{\sigma}^{*,(0)}_{e,1})$ randomly from $D_{e,1}$
else
Set $(\boldsymbol{\varepsilon}^{*,(0)}_{e,k}, \boldsymbol{\sigma}^{*,(0)}_{e,k}) = (\boldsymbol{\varepsilon}^{*}_{e,k-1}, \boldsymbol{\sigma}^{*}_{e,k-1})$
end if
end for
ii) Solve Equations (4.9), (4.10) for $\mathbf{u}^{(j)}_k$ and $\boldsymbol{\eta}^{(j)}_k$
iii) Compute local mechanical states:
for all $e = 1, ..., M$ **do**
Solve Equations (4.1), (4.11) for $\boldsymbol{\varepsilon}^{(j)}_{e,k}$ and $\boldsymbol{\sigma}^{(j)}_{e,k}$
end for
iv) Assign local material states:
for all $e = 1, ..., M$ **do**
Choose $(\boldsymbol{\varepsilon}^{*,(j+1)}_{e,k}, \boldsymbol{\sigma}^{*,(j+1)}_{e,k})$ in $D_{e,k}$ closest to $(\boldsymbol{\varepsilon}^{(j)}_{e,k}, \boldsymbol{\sigma}^{(j)}_{e,k})$
end for
v) Compute global distance d via Eq. (4.7)
if $d >$ tol **then**
Augment $D_{e,k}$ via on-the-fly sampling: **Algorithm** 4
end if
vi) Test for convergence
if $(\boldsymbol{\varepsilon}^{*,(j+1)}_{e,k}, \boldsymbol{\sigma}^{*,(j+1)}_{e,k}) = (\boldsymbol{\varepsilon}^{*,(j)}_{e,k}, \boldsymbol{\sigma}^{*,(j)}_{e,k})$ **then**
Set $\mathbf{u}_k = \mathbf{u}^{(j)}_k$, $(\boldsymbol{\varepsilon}_{e,k}, \boldsymbol{\sigma}_{e,k}) = (\boldsymbol{\varepsilon}^{(j)}_{e,k}, \boldsymbol{\sigma}^{(j)}_{e,k})$
else
$j \leftarrow j + 1$, **goto** ii)
end if
vi) Compute $D_{e,k+1}$ using Equations (4.16), (4.17)
end for

4.3 Phase space sampling

The reliability of a multiscale Data-Driven prediction of mechanical behavior is contingent upon the quality of the material data sets compiled from lower-scale computations. The process of generating these data sets is termed phase space sampling. We discuss here two types of methods: 'offline' sampling, which relies on preexisting experimental data or the identification of a target

subset of the phase space, and 'on-the-fly' sampling, which does not require any prior information. Regardless of the method of sampling, a model for micromechanical unit-cell calculations is required, which can be furnished for example by Molecular Dynamics (MD), Discrete Element (DEM), or lower-scale Finite Element (FEM) simulation, depending on the material at hand (Fig. 4.1 b)). The generation of unit cells at a given initial state of a given material has been addressed in multiple studies (e.g. [168] for athermal granular materials or [109] for thermalized MD systems in various ensembles.) The micromechanical model $\mathcal{M}$ takes as input components of a local state (e.g. $\boldsymbol{\epsilon}$ for a purely strain-driven calculation), and returns the remaining components of the state (e.g. $\boldsymbol{\sigma} = \mathcal{M}(\boldsymbol{\epsilon})$).

4.3.1 Offline sampling

Within offline sampling, we propose two methods, goal-oriented sampling and minimax sampling, and provide simple algorithms for both. Goal-oriented sampling takes advantage of experimental field data to generate the input to the micromechanical calculations (Fig. 4.1 c)). In its simplest form, the input is the strain measured (e.g. using DIC) on different parts of a discretized deforming body. Algorithm 2 presents the simple steps involved.

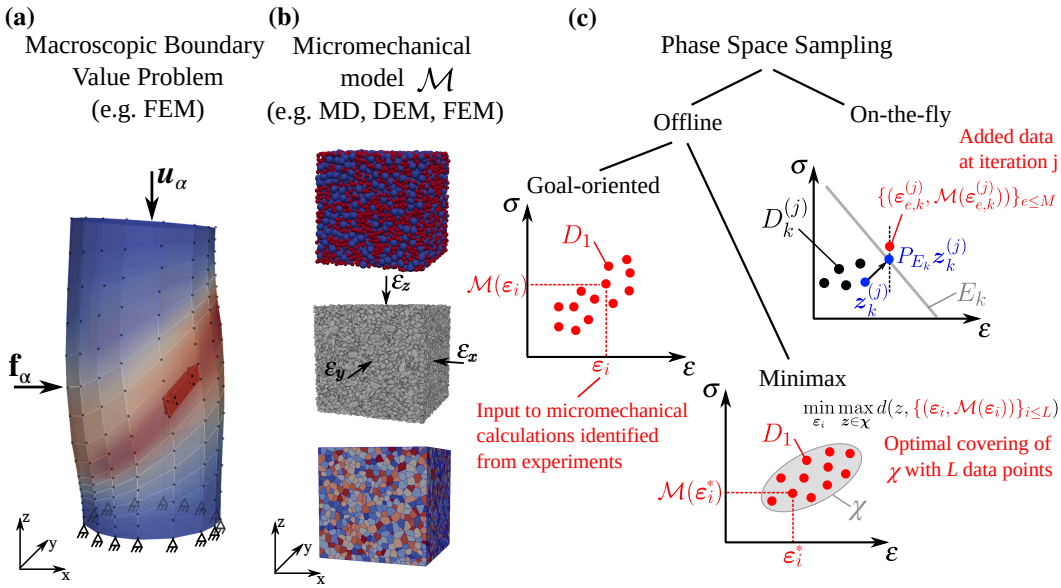

Figure 4.1: Overview of Data-Driven Multiscale Modeling: a) Discretized macroscopic boundary value problem. b) Micromechanical model for unit-cell calculations during sampling. c) Proposed phase space sampling methods within the multiscale Data-Driven framework.

Algorithm 2 Offline goal-oriented phase space sampling

Require: Micromechanical model $\mathcal{M}$, Experimental data
Calculate strains $\boldsymbol{\varepsilon}_i$ on L discrete points of the experimental deformed configuration
for $i = 1, ..., L$ **do**
Carry out unit-cell calculations with imposed $\boldsymbol{\varepsilon}_i$
end for
Set $D_{e,1} = \{(\boldsymbol{\varepsilon}_i, \mathcal{M}(\boldsymbol{\varepsilon}_i))\}_{i \leq L}, e = 1, ..., M$

In the absence of experimental field data, one must resort to alternative sampling techniques. Fortunately, the Data-Driven framework naturally lends itself to optimal minimax sampling [156], due to its formulation in terms of distances in phase space. In this case, we identify a target subset $\boldsymbol{\chi}$ of the phase space (heuristically or using expert knowledge), and seek the optimal input to unit-cell calculations, under computational constraints (number of calculations L), so as to cover $\boldsymbol{\chi}$. Without loss of generality, this input is considered to be the strain (strain-driven calculations), and is determined by the solution of the following problem:

$$\min_{\boldsymbol{\varepsilon}_i} \max_{\mathbf{z} \in \boldsymbol{\chi}} d(\mathbf{z}, \{(\boldsymbol{\varepsilon}_i, \mathcal{M}(\boldsymbol{\varepsilon}_i))\}_{i \leq L}). \tag{4.13}$$

At the minimizers $\boldsymbol{\varepsilon}_i^*$, we obtain an optimal covering $\{(\boldsymbol{\varepsilon}_i^*, \mathcal{M}(\boldsymbol{\varepsilon}_i^*))\}_{i \leq L}$ of $\boldsymbol{\chi}$, as shown in Fig. 4.1 c).

Algorithm 3 Offline minimax phase space sampling

Require: Micromechanical model $\mathcal{M}$, Target phase subspace $\boldsymbol{\chi}$
Solve (13) for the minimizers $\{\boldsymbol{\epsilon}_i\}_{i \leq L}$
Set $D_{e,1} = \{(\boldsymbol{\varepsilon}_i, \mathcal{M}(\boldsymbol{\varepsilon}_i))\}_{i \leq L}, e = 1, ..., M$

Remark: This process may involve computationally expensive evaluations of $\mathcal{M}(\varepsilon)$. Therefore, these may be replaced with $\hat{\mathcal{M}}(\varepsilon)$, where $\hat{\mathcal{M}}$ is an appropriate surrogate model or meta-model [322]. We require that the model be simple to evaluate and able to capture essential aspects of material behavior (e.g. simple plasticity models [90] or machine learning models such as Gaussian Process regression [307] and Neural Networks), and that sufficient preexisting data exist to train the meta-model.

4.3.2 On-the-fly sampling

It is possible that no experimental data are available, and that we also cannot easily identify the subset of interest in phase space. In this case, we introduce a simple 'on-the-fly' sampling approach, that requires no prior information. The basic principle is the utilization of the Data-Driven solution itself to inform new unit-cell calculations, whenever the distance to the material data set surpasses a chosen threshold. This indicates that the particular region of phase space is not well covered by data and should be targeted by additional calculations. The steps involved are shown in Algorithm 4. As before, without loss of generality, we assume purely strain-driven calculations.

Algorithm 4 On-the-fly phase space sampling

Require: Micromechanical model $\mathcal{M}$, Time step k, Iteration j, Data sets $D_{e,k}^{(j)}$, $e=1,\ldots,M$
  for all $e = 1, ..., M$ **do**
    Carry out unit-cell calculation imposing $\boldsymbol{\varepsilon}_{e,k}^{(j)}$ (obtained in Algorithm 1 - iii))
    Augment local material data set: $D_{e,k}^{(j+1)} \leftarrow D_{e,k}^{(j)} + \{(\boldsymbol{\varepsilon}_{e,k}^{(j)}, \mathcal{M}(\boldsymbol{\varepsilon}_{e,k}^{(j)}))\}$
  end for

Note that, in the applications presented later in this study, and given the presence of experimental data, we shall restrict our attention to offline goal-oriented sampling. The analysis and implementation of the remaining phase space sampling methods will be the subject of a future study.

4.4 History parametrization

The efficient and compact history parametrization is a major challenge for materials with an extended memory of their deformation. The first discussion on history parametrization within the Data-Driven formulation is due to Eggersmann et al. [92], where various representational paradigms are explored, including the hereditary/history functional and the internal variable formalism. Alternatively, a thermodynamically-motivated energy based representation, where the local phase space is augmented with the free energy and the dissipation, can be considered. These two parametrizations are particularly appealing within this multiscale paradigm: the energy-based, which is material independent and universal, and the internal variable-based, which must be tailored to a particular material.

4.4.1 Energy-based parametrization

The energy-based approach effects a parametrization of history by enhancing the state space with the free energy $\mathcal{A}$ and dissipation $\mathcal{D}$, and considering their implicit relation with the remaining state variables $\boldsymbol{\sigma}$ and $\boldsymbol{\epsilon}$. This relation is furnished by the principle of conservation of energy and the second principle (Clausius-Plank inequality):

$$\dot{\mathcal{D}} = \boldsymbol{\sigma} : \dot{\boldsymbol{\epsilon}} - \dot{\mathcal{A}} \geq 0 \tag{4.14}$$

or, in a time discrete setting and for material point e:

$$\mathcal{D}_{e,k+1} - \mathcal{D}_{e,k} = \frac{\boldsymbol{\sigma}_{e,k} + \boldsymbol{\sigma}_{e,k+1}}{2} : (\boldsymbol{\varepsilon}_{e,k+1} - \boldsymbol{\varepsilon}_{e,k}) - (\mathcal{A}_{e,k+1} - \mathcal{A}_{e,k}) \geq 0. \tag{4.15}$$

We can, then, represent the local material data set at time t_{k+1} as:

$$D_{e,k+1} = \{(\boldsymbol{\varepsilon}_{e,k+1}, \boldsymbol{\sigma}_{e,k+1}) \,|\, (\boldsymbol{\varepsilon}_{e,k}, \boldsymbol{\sigma}_{e,k}), (4.15)\}. \tag{4.16}$$

The above expression implies that the admissible stress-strain pairs at time t_{k+1} (i.e. the pairs looked up by the Data-Driven solver to find the closest point projection to the material data set) are those that are thermodynamically consistent with the previously converged state at time t_k. The special case where $\mathcal{D}_{e,k+1} - \mathcal{D}_{e,k} = 0$ defines a bounded equilibrium set (or elastic domain) on the enhanced phase space. Note that, when dealing with experimental data, the equality above will never be satisfied exactly, which calls for an appropriately defined numerical threshold. As long as the state variables above are easily computable from lower-scale simulations, this parametrization can be readily obtained.

This is the first data-driven formulation where thermodynamic constraints are explicitly imposed, as opposed to earlier models where these constraints are implicitly imposed, for example using the internal variable formalism [92] or the GENERIC formalism [129].

4.4.2 Internal-variable based parametrization

The second parametrization under investigation relies on enhancing the state space with a set of internal variables tailored to the material at hand. In this case, the local material data set admits the following representation [92]:

$$D_{e,k+1} = \{(\boldsymbol{\varepsilon}_{e,k+1}, \boldsymbol{\sigma}_{e,k+1}) \,|\, (\boldsymbol{\varepsilon}_{e,k}, \boldsymbol{\sigma}_{e,k}, \boldsymbol{q}_{e,k})\} \tag{4.17}$$

where $\mathbf{q}_{e,k}$ defines an internal variable — or a collection thereof — encapsulating the material history. In other words, $D_{e,k+1}$ consists of stress-strain pairs in phase space that are attainable from the initial state $(\boldsymbol{\epsilon}_{e,k}, \boldsymbol{\sigma}_{e,k}, \boldsymbol{q}_{e,k})$ or any other sufficiently neighboring state, with respect to an appropriately defined metric. Implicit here is the assumption that neighboring states have undergone equivalent history.

Internal variables typically encode information about the microstructure of the material. In several occasions, pertinent internal variables may be known and directly computable from lower-scale simulation data. In the general case, they may be derived through a statistical analysis of the microstructure followed by appropriate dimensionality reduction [299, 43]. The objective is to optimally encode the microstructural information in an internal variable of the lowest possible order, thereby resulting in the lowest-dimensional state space. Most importantly, the Data-Driven paradigm relies only on identifying the relevant variables, while bypassing any need for definining analytical evolution laws.

4.5 Application to granular materials

Granular materials constitute an excellent candidate for exploring the performance of the proposed framework, since they are known to exhibit complex history-dependent continuum behavior [277]. Traditionally, the quasistatic behavior of granular materials has been described by empirical constitutive laws that are formulated within the framework of plasticity [297, 318, 34, 239, 79, 261, 17], and are constrained by a set of principles known as the Critical State Theory [297, 204]. Despite progress in their constitutive description, which was inspired by the recently-enhanced access to grain-scale information (XRCT [87], DEM [78], etc.), this conventional modeling approach breaks down during the transition between different regimes, and often relies on prohibitively many parameters [79].

In the remainder of the paper, we will systematically investigate the proposed Data-Driven framework in the modeling of an angular sand. First, we will briefly review the recently developed Level-Set Discrete Element Method

which will serve as the machinery for phase space sampling. Then we will explore the performance of the two history parametrizations, within material point simulations involving nonmonotonic loading paths. Finally, we will demonstrate the prediction of granular material behavior against experiments in two boundary value problems.

4.5.1 *In-silico* experiments using LS-DEM

We rely on the recently developed Level-Set Discrete Element Method (LS-DEM) [170] to generate granular material data sets. Similarly to the original formulation of DEM [78], LS-DEM resolves the kinematics of athermal rigid particles interacting through frictional contacts (Fig. 4.2), but also accounts for accurate particle morphology, described by level set functions. For the purpose of this study, we will assume a linear (Hookean) elastic contact law capped by Coulomb friction, which has been shown to capture all essential aspects of material behavior in sand [169]. Under these assumptions, the interparticle force $\mathbf{f}^c$ associated with a contact c (Fig. 4.2 c)) is given by:

$$\mathbf{f}^c = \mathbf{f}_n^c + \mathbf{f}_t^c \tag{4.18}$$

$$\mathbf{f}_n^c = k_n \delta_n \mathbf{n} \tag{4.19}$$

$$\mathbf{f}_t^c = -\frac{\Delta \mathbf{s}}{\|\Delta \mathbf{s}\|} \min(k_t \|\Delta \mathbf{s}\|, \mu \|f_n\|) \tag{4.20}$$

where $k_n(k_t)$ is the normal (tangential) Hookean stiffness, related to the elastic properties of the individual particles, δ_n is the interparticle penetration (local contact deformation), $\mathbf{n}$ is the contact normal, $\Delta \mathbf{s}$ the accumulated tangential contact displacement, and μ is the friction coefficient. Note that this contact

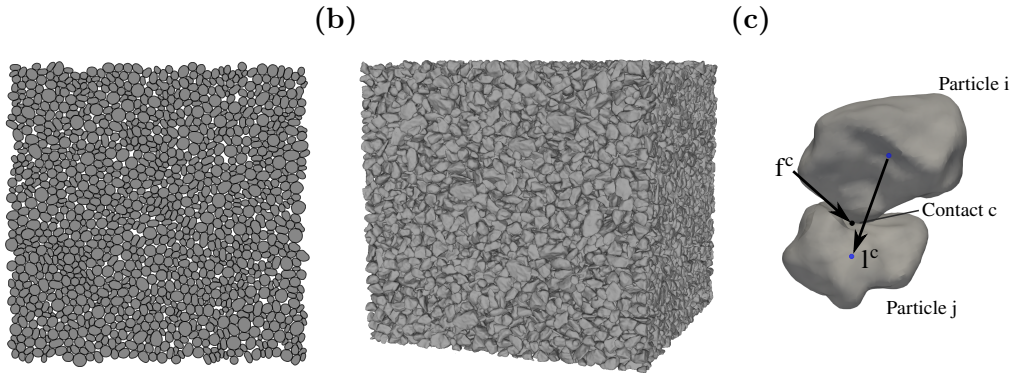

Figure 4.2: LS-DEM for granular material simulation: a) 2D and b) 3D granular assembly in LS-DEM. c) Frictional particle contact.

law (and other more complex laws) may be described in terms of a free energy $\mathcal{A}^c$ and kinetic potential ψ^c (or its associated dissipation function $\mathcal{D}^c$) [168]. This consideration will help us seamlessly describe the energy-based history parametrization. Finally, once all forces acting at a particle $\mathbf{f} = \sum_{c \in \mathcal{C}^p} \mathbf{f}^c$ and resulting moments $\mathbf{m}$ are known, then the particle's dynamics are updated by integrating Newton's equations of motion, given its inertial properties.

4.5.2 Exploring history parametrizations via material point simulations

In this section, we specify the two parametrizations of Section 4.4 for the case of granular materials, and assess their performance in material point simulations. In the interest of carefully assessing these parametrizations, we will restrict ourselves to previously studied stress paths instead of using the optimal phase space sampling strategy. Fig. 4.3 shows the three considered loading-unloading paths, namely isotropic compression, simple shear, and constant-volume biaxial compression. For each of these paths, we perform LS-DEM experiments[1] at regularly spaced levels of pressure $p = -1/3 \text{ tr}(\sigma)$ or deviatoric stress $q = \sqrt{3/2 \boldsymbol{s} : \boldsymbol{s}}$, where $\boldsymbol{s} = \boldsymbol{\sigma} + p\boldsymbol{I}$. At each level, experiments are repeated for multiple samples prepared at the same initial isotropic state. This allows us to generate the data sets that will be used for the subsequent Data-Driven material point predictions. Note that all simulations are nonmonotonic, in order to assess the method's ability to distinguish between loading and unloading paths.

We restrict our investigation to quasistatic deformation in these and all subsequent experiments of this study. This is achieved by ensuring that the dimensionless inertial number $I = \dot{\gamma} d \sqrt{\rho / p}$ is kept below a value of 10^{-4} [229]. Further, in order to avoid boundary effects and satisfy the Hill-Mandel condition, we enforce periodic boundary conditions [263]. The 2D specimens used for these experiments are comprised of Caicos sand particles characterized during an earlier study [224] with elastic parameters $E = 63.5$ MPa, $\nu = 0.5$, and a friction coefficient of $\mu = 0.5$. An example specimen is shown in Fig. 4.2 a).

The objective of the Data-Driven material point simulation is to determine the path that minimizes the distance to an applied strain trajectory by navigating

[1] The term 'experiments' will be used throughout this section to refer to LS-DEM numerical experiments.

through the available data sets in a thermodynamically consistent manner. This translates to a simplification of the Data-Driven problem of Eq. 4.8 to:

$$\min_{\mathbf{y}\in D_{k+1}} d(\mathbf{z}_{k+1}, \mathbf{y}_{k+1}) \tag{4.21}$$

where $\mathbf{z}_{k+1}$ is imposed[2], rather than sought from a constraint set, and D_{k+1} is given by Eq. 4.16 or Eq. 4.17, depending on the parametrization.

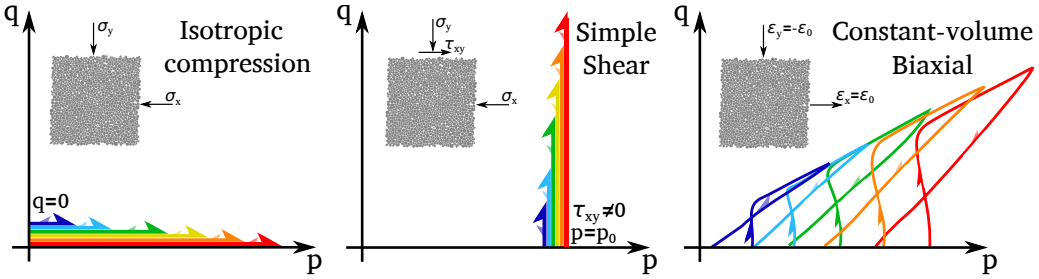

Figure 4.3: Stress paths for the investigated material point simulations.

Energy-based parametrization

Adopting the energy-based representation requires access to each of the state variables in Eq. 4.15. For this granular system, assuming quasistatic conditions, the average stress is given by the Love-Christoffersen expression [68]:

$$\bar{\boldsymbol{\sigma}} = \frac{1}{V}\sum_{c} \mathbf{f}^c \otimes \mathbf{l}^c \tag{4.22}$$

where the summation runs over each contact c in the assembly. Similarly, the average strain $\bar{\boldsymbol{\epsilon}}$ may be similarly obtained through homogenization [25] or directly from the boundary deformation of the unit cell. Assuming periodic boundary conditions, the Hill-Mandel macrohomogeneity condition [139] is satisfied, allowing us to write:

$$d\mathcal{D} = \bar{\boldsymbol{\sigma}} : d\bar{\boldsymbol{\varepsilon}} - d\mathcal{A} \tag{4.23}$$

where $d\mathcal{D}$ derives from frictional contact dissipation:

$$d\mathcal{D} = \sum_{c} d\mathcal{D}^c = \frac{1}{V}\sum_{c} \mathbf{f}_t^c \cdot d\mathbf{u}^{c,slip} \tag{4.24}$$

[2]In fact, only the strain or stress is imposed, depending on whether it is a strain- or stress-driven calculation.

where $d\mathbf{u}^{c,slip} = (\mathbf{f}_t^{c,t} - \mathbf{f}_t^{c,t+dt})/k_t$.

Finally, the free energy is due to the deformation of contacts under normal and tangential loading:

$$\mathcal{A} = \sum_c \mathcal{A}^c = \frac{1}{2V} \sum_c \left(\frac{\|\mathbf{f_n^c}\|^2}{k_n} + \frac{\|\mathbf{f_t^c}\|^2}{k_t} \right). \tag{4.25}$$

Let us now explore the performace of this parametrization in material point simulations. Fig. 4.4 shows the data collected from the isotropic compression experiments up to a pressure of 100 kPa. Different colors represent different sets of simulations, each carried out at a particular value of pressure or deviatoric stress. These represent the data points available to the Data-Driven solver, and are termed 'Data' in the plot legend. The initial compression of the samples is accompanied by a small increase in pressure and a large increase in dissipation, until the jamming transition [220] occurs at $\epsilon_{vol} \approx -0.015$. Compressing beyond that point leads to a significant increase in pressure but only a small increase in dissipation. Similarly, unloading induces negligible change in volumetric strain or dissipation, therefore producing several equilibrium sets (notice the almost horizontal segments in Fig. 4.4 b)). The same figure shows the sequence of data points determined by the Data-Driven (DD) algorithm for a strain-driven compression cycle at a peak pressure of 50 kPa, that lies in-between the peak pressures of the available data sets. The success of the data driven simulation is immediately verified upon comparison with a validation experiment at the same peak pressure ('Validation' in the plot legends). Both loading and unloading branches and well captured. Note, in passing, that the difference in terms of dissipation-free energy between different data sets and, hence, between validation and Data-Driven simulation is larger than the same difference in terms of stress-strain. In particular, dissipation is much more sensitive to the initial contact arrangement and leads to larger deviations due to its incremental calculation.

Similarly, Fig. 4.5 shows the data collected from the simple shear experiments up to 2% shear strain starting from a compressed state of $p_0 = 100$ kPa. Until the samples experience yielding at approximately $\tau = 25$ kPa, the response is largely free of dissipation (Fig. 4.5 b)) producing once again equilibrium sets. All subsequent loading and unloading branches are tied to significant dissipation. Shown in the same figure is the Data-Driven simulation carried

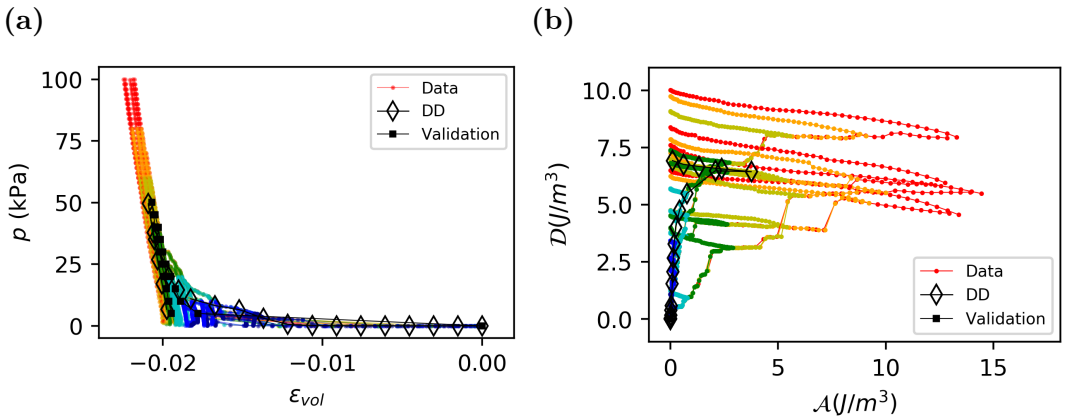

Figure 4.4: Material data sets (colored), Data-Driven simulation (♢), and validation experiment (■) in isotropic compression: a) Volumetric strain vs Pressure. b) Free energy vs Dissipation.

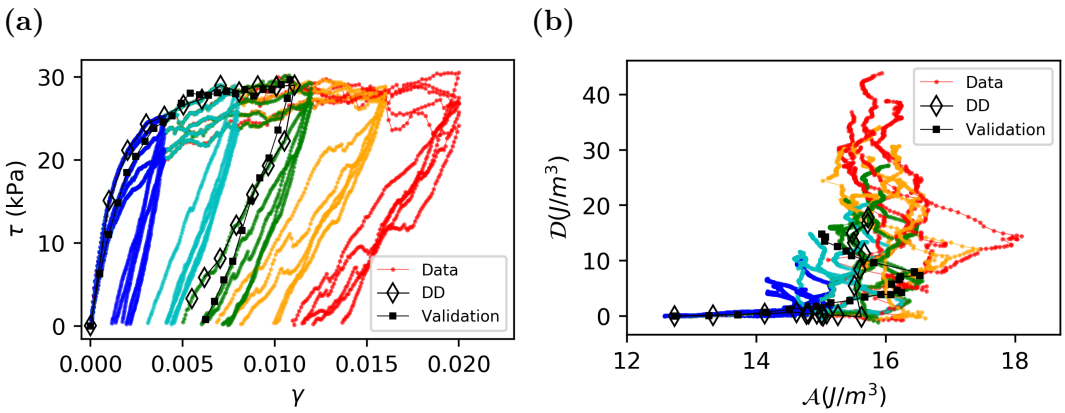

Figure 4.5: Material data sets (colored), Data-Driven simulation (♢), and validation experiment (■) in simple shear: a) Shear strain vs Shear stress. b) Internal energy vs Dissipation.

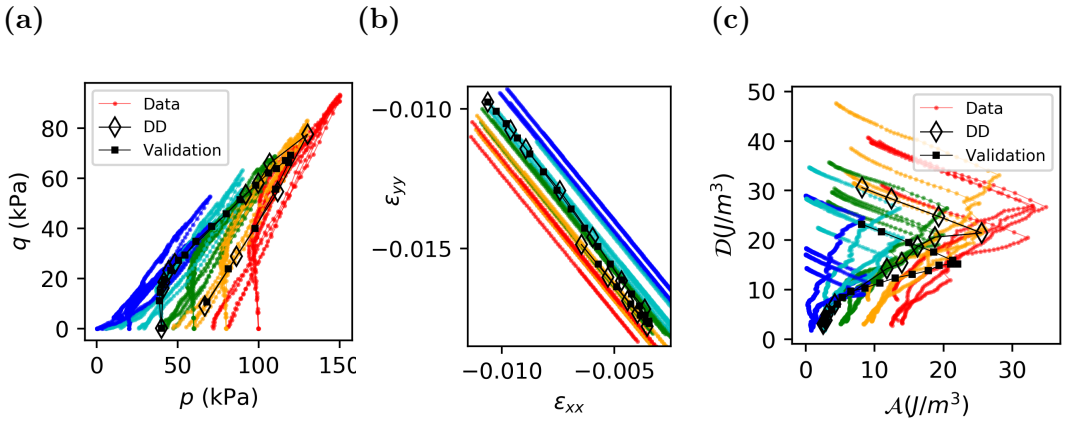

Figure 4.6: Material data sets (colored), Data-Driven simulation (♢), and validation experiment (■) in constant-volume biaxial compression : a) Pressure vs Stress Deviator. b) Strain components ϵ_{xx} vs ϵ_{yy}. c) Internal energy vs Dissipation.

out to an intermediate peak shear strain $\gamma = 0.01$ and followed by unloading to zero shear stress. Once again, by comparison with a validation experiment based on the same shear strain history, it is clear that the algorithm is able to distinguish the best available data set at any point throughout both the loading and unloading branches.

Finally, Fig. 4.6 shows the material data generated by the biaxial compression experiments at various initial isotropic states. The samples initially experience a decrease in pressure followed by a phase transition [79] to a critical state, and later unload to zero deviator stress. Fig. 4.6 b) shows the applied strain trajectory which is the input to the Data-Driven simulation, and is designed to slightly depart from the constant volume strain trajectories readily available in the data (shown as straight lines). The algorithm is able to transition between sets, to produce a final trajectory in state space that compares well with the validation simulation (Fig. 4.6 a)).

Internal variable-based parametrization

We now turn to the internal variable-based representation of material history. A long history of studying and modeling granular matter has identified several relevant internal variables such as the packing fraction and fabric tensor [79, 281, 277]. Here, following the discussion in Section 4.4.2, we derive the internal variables by analyzing the statistics of the internal microstructure, and performing appropriate dimensionality reductions. In this system, the microstructure may be described by the joint probability density of contact normals and forces, $\mathbf{q} = P_{\mathbf{nf}}(\mathbf{n}, \mathbf{f})$[3]. The former relates to the arrangement of the contact structure, while the combination of normals and forces provides the frictional history. Tractable low-order representations may be achieved through a finite-dimensional approximation of the density. First, restricting our attention to the marginal density $P_{\mathbf{n}}(\mathbf{n})$ and exploiting its symmetry, we can accurately represent it by a second order Fourier expansion [299]:

$$P_{\mathbf{n}}(\mathbf{n}) = \frac{1}{4\pi}(1 + \mathbf{n} \cdot \boldsymbol{\alpha}^n \mathbf{n}) \tag{4.26}$$

[3] A more general representation is given by the joint probability density of contact normals, branch vectors, and contact forces, $\mathbf{q} = P_{\mathbf{nlf}}(\mathbf{n}, \mathbf{l}, \mathbf{f})$. The combination of contact normals and branch vectors encapsulates additional information about particle shape, and becomes redundant for monodisperse spherical assemblies where $\mathbf{n} \equiv \mathbf{l}$.

which reduces the problem to the determination of the 6 components of a symmetric contact anisotropy tensor $\boldsymbol{\alpha}^n$. The trace of the tensor $\mathrm{tr}(\boldsymbol{\alpha}^n)$ represents the most important and lowest order description of state which is the packing fraction ϕ, or equivalently the void ratio e [217, 281], followed by the remaining 5 components describing the contact anisotropy [313, 164, 299]. Once $P_{\mathbf{n}}(\mathbf{n})$ is characterized, the description of the internal state is completed by describing the conditional density $P_{\mathbf{f}|\mathbf{n}}(\mathbf{f}|\mathbf{n})$. The simplest way to proceed is through a first-order (mean) description of this density, as $\langle \mathbf{f}(\mathbf{n}) \rangle = \langle f_n(\mathbf{n}) \rangle \, \mathbf{n} + \langle \mathbf{f}_t(\mathbf{n}) \rangle$, where f_n and $\mathbf{f}_t$ are the normal and tangential force components. For the latter, accurate Fourier expansions are, once again, available [31, 326]:

$$\langle f_n(\mathbf{n}) \rangle = \langle f \rangle (1 + \mathbf{n} \cdot \boldsymbol{\alpha}^{f_n} \mathbf{n}) \qquad \langle \mathbf{f}_t(\mathbf{n}) \rangle = \langle f \rangle (\boldsymbol{\alpha}^{f_t} \mathbf{n} - (\mathbf{n} \cdot \boldsymbol{\alpha}^{f_t} \mathbf{n}) \mathbf{n}) \tag{4.27}$$

where $\boldsymbol{\alpha}^{f_n}$ and $\boldsymbol{\alpha}^{f_t}$ are the normal and tangential force anisotropy tensors, respectively.
Based on the above, we obtain the following set of relevant internal variables:

$$\mathbf{q} = \{ \boldsymbol{\alpha}^n, \boldsymbol{\alpha}^{f_n}, \boldsymbol{\alpha}^{f_t} \}. \tag{4.28}$$

Similarly to the energy-based representation (Section 4.5.2), these state variables $(\boldsymbol{\sigma}, \boldsymbol{\epsilon}, \mathbf{q})$ are directly accessible from the micromechanics. While a notion of hierarchy of these variables was discussed above, a systematic investigation of their relative importance for the macroscopic response is required in order to potentially further reduce the dimensionality of the representation.

Let us now explore the performance of the internal variable-based parametrization in the same material point simulations as before. In each of the three cases (isotropic compression, simple shear, biaxial compression), the corresponding precompiled material data sets are now parametrized by the contact fabric, normal force fabric, and tangential force fabric anisotropy tensors (Eqs. 4.17 and 4.28). The sum of Euclidean (Frobenius) norms of each of the three tensors provides a simple metric for this set of internal variables. Finally, a Data-Driven simulation is carried out and compared to a validation experiment. Finally, a Data-Driven simulation is carried out and compared to a validation experiment.

Fig. 4.7 a) compares the Data-Driven simulation of isotropic compression to the corresponding validation experiment. As in the case of the energy-based parametrization, the algorithm is able to predict the pressure response of the isotropically strained sample during both loading and unloading. Fig. 4.7 b) shows the evolution of the internal variables in a low-dimensional subspace spanned by the void ratio e and the second invariant of the contact fabric anisotropy tensor α^n. The latter represents the intensity of developing fabric, which remains approximately zero during isotropic compression.

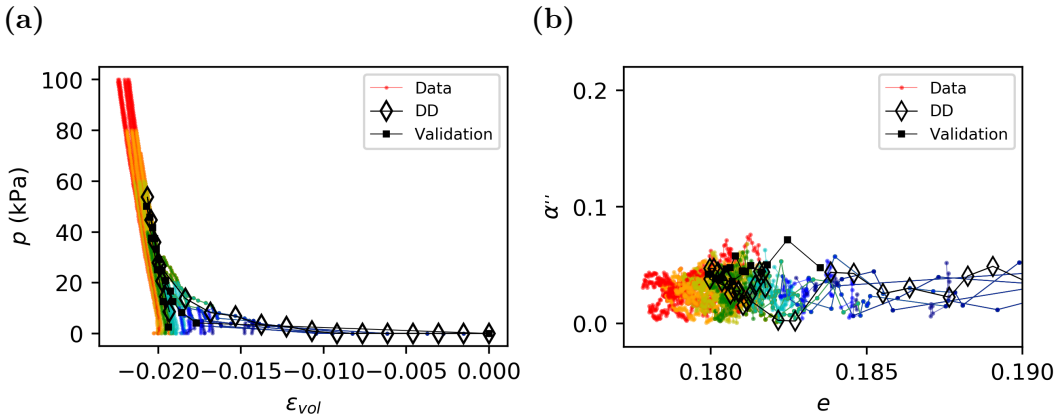

Figure 4.7: Material data sets (colored), Data-Driven simulation (♢), and validation experiment (■) in isotropic compression: a) Volumetric strain vs Pressure. b) Void ratio vs Contact fabric anisotropy invariant.

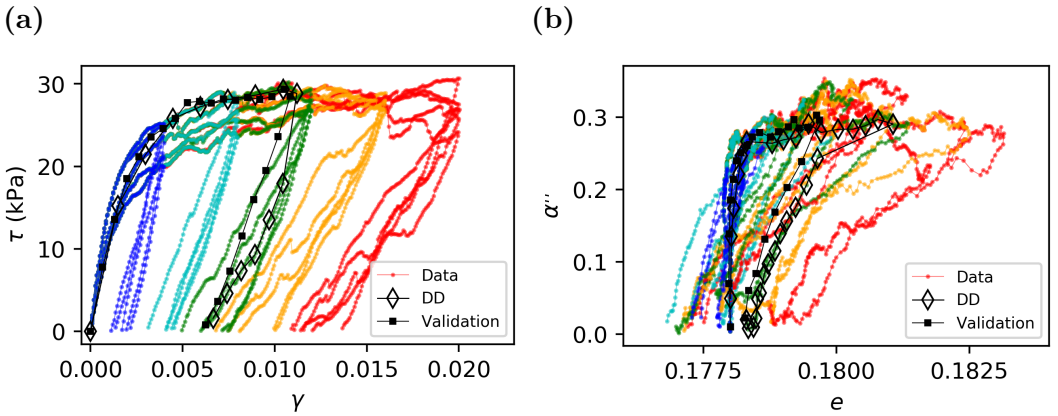

Figure 4.8: Material data sets (colored), Data-Driven simulation (♢), and validation experiment (■) in simple shear: a) Shear strain vs Shear stress. b) Void ratio vs Contact fabric anisotropy invariant.

Analogously, Fig. 4.8 a) compares the Data-Driven simulation of cyclic simple shear to the corresponding validation experiment, exhibiting once again a good agreement. Equally satisfactory agreement is obtained in the internal variable

space. Given the size of the space, we choose again to plot only a subspace spanned by e and α_n (Fig. 4.8 b)). Upon loading, we observe a sharp increase in the contact fabric anisotropy, followed by a smaller increase in the void ratio upon yielding. During unloading, both variables decay to produce an almost isotropic but looser state.

Finally, we assess the performance of the parametrization in the undrained biaxial compression experiments. Fig. 4.9 a) shows the simulated pressure-stress deviator response to the same strain trajectory as Fig. 4.6 b), showing excellent agreement with the validation experiment. In terms of internal variables, Fig. 4.9 b) shows the evolution of the invariants of the contact and force normal fabric anisotropy tensors. Despite the departure of the simulated trajectory from the available individual data sets, the algorithm is able to produce consistent transitions between the data sets towards an overall good prediction of the response. This illustrates the interpolating properties of the framework.

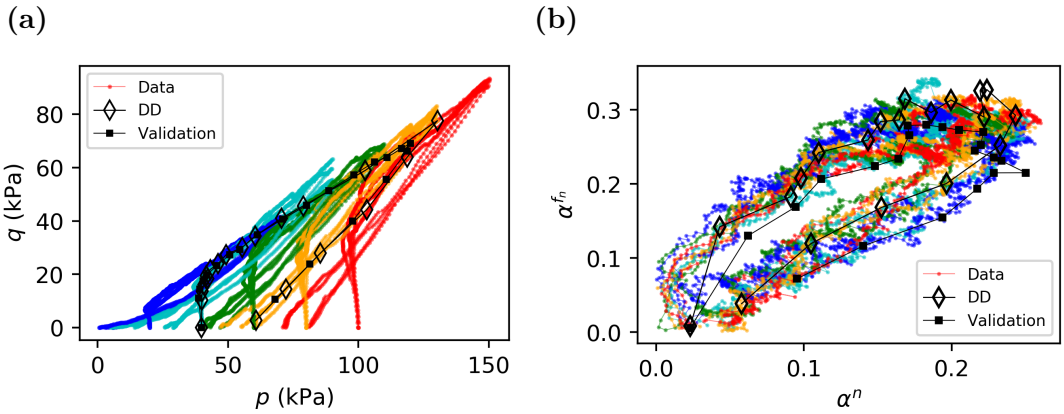

Figure 4.9: Material data sets (colored), Data-Driven simulation (♢), and validation experiment (■) in biaxial compression: a) Pressure vs Stress Deviator. b) Contact fabric anisotropy invariant vs Normal force fabric anisotropy invariant.

To summarize, it was shown that both the energy-based and the internal variable-based parametrization perform well in two-dimensional material point simulations of both simple and more complex nonmonotonic stress paths. The first parametrization, furnished by thermodynamics, is universal and material independent. On the other hand, the second parametrization was tailored to granular materials by mathematically describing the microstructure and performing appropriate reductions.

4.5.3 Boundary value problems

We now investigate the performance of the multiscale Data-Driven paradigm, in conjunction with the energy-based history parametrization, in predicting the mechanical response in two boundary value problems: a) plane-strain fault rupture through a dense granular layer, and b) shear banding in three-dimensional triaxial compression. In the first problem, material data sets will be obtained from the experiment itself, in a demonstration of 'self-consistent', phase space sampling. On the other hand, in the second problem, material data sets will be independently generated through unit cell simulations, in a demonstration of the general phase space sampling approach.

Plane strain fault rupture

We consider a sandbox experiment inspired by the fault rupture study of Anastasopoulos et al. [14]. In the latter, sand is pluviated into a rectangular container to form a specimen of a 10m width and 30m height at prototype scale. A piston underneath the sandbox forces the right part of the specimen to quasistatically subside, inducing a fault rupture through the body of sand at a 30° angle to the horizontal (Fig. 4.10 b)).

We employ LS-DEM to simulate the experiment by replicating the boundary conditions and using the model granular material described in [166]. A snapshot of the LS-DEM simulation along with the resulting contours of dissipation is shown in Fig. 4.10 b). In accordance with similar observations in the physical experiment, both a primary rupture and an antithetic secondary rupture are identified at angles 125° and 52° to the horizontal, respectively.

The virtual specimen is spatiotemporally sampled to produce material data sets — including stress, strain, internal energy, and dissipation — in accordance with the energy-based parametrization (Section 4.4.1). This is achieved by superimposing a finite element mesh on the discrete element assembly to associate subassemblies to their nearest material point (Gauss integration point). This results in a number of material data sets equal to the number of material points. We refer to this type of phase space sampling as self-consistent since it is in some sense equivalent to the self-consistent Data-Driven identification from field data [199]. In contrast to the goal-oriented sampling discussed in Section 4.3.1 and implemented in the next application, all components of the

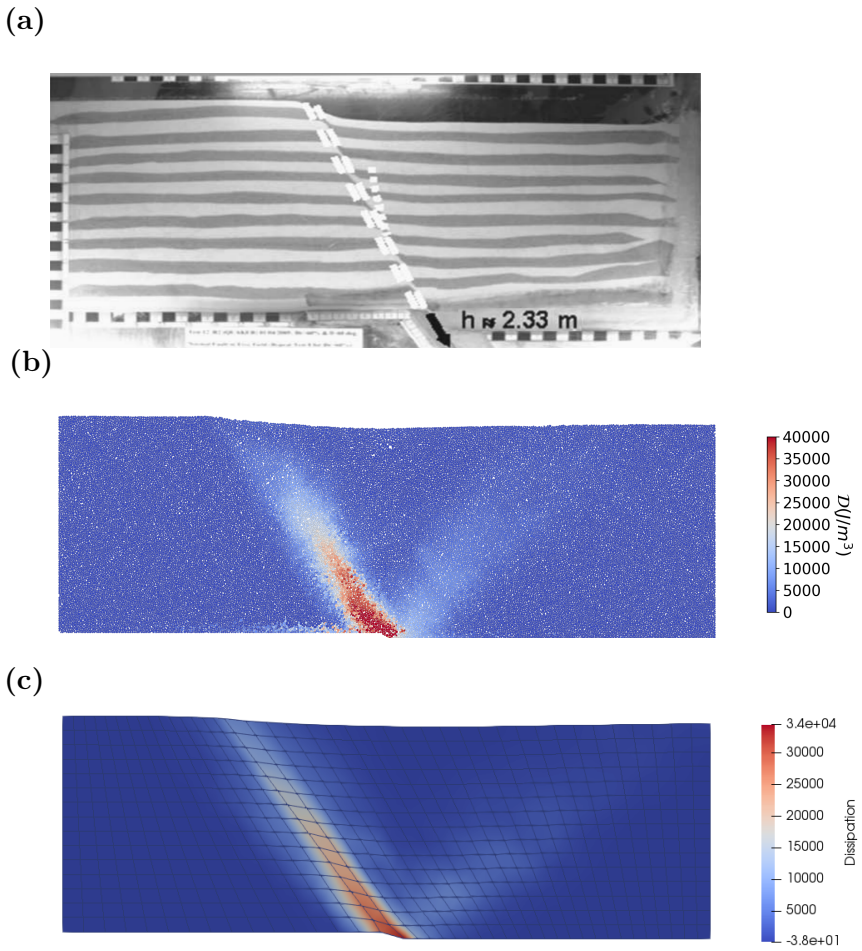

Figure 4.10: Plane strain fault rupture: a) Experimental setup adopted from Anastasopoulos et al. [14]. b) LS-DEM simulation. c) Data-Driven simulation and resulting shear bands.

local state are readily available, hence, no unit cell calculations are carried out. The data sets are initially randomly assigned to each material point in the discretized (FEM) model used for the Data-Driven simulation. Informed by the evolving boundary constraint set, the algorithm is able to make correct associations and transitions between the available data sets, and, thus, capture the mechanical response. Fig. 4.10 c) shows the resulting contours of dissipation in the Data-Driven simulation, which compare well with those of the LS-DEM experiment. In particular, both ruptures are predicted, albeit with angles 122° and 47°, respectively. Finally, Fig. 4.11 compares the evolution of surface settlement in the LS-DEM and Data-Driven simulation verifying the good quantitative agreement.

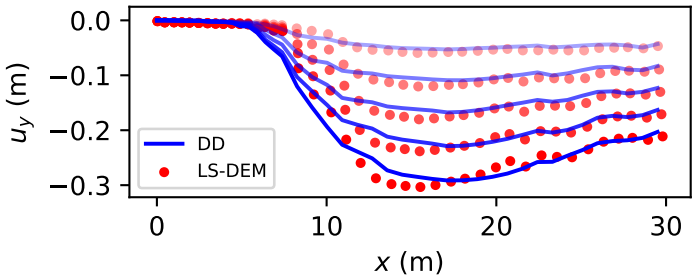

Figure 4.11: Evolution of surface settlement profile in LS-DEM and Data-Driven simulations.

Shearing banding in triaxial compression

We now consider an *in-situ* triaxial compression experiment on a specimen of angular (Hostun) sand, performed within an XRCT scanner, as described in [16]. Fig. 4.12 a) shows a 2-dimensional slice of the scanned specimen, which measures 11 mm in diameter and 22 mm in height, and is comprised of 53,939 angular grains. An encasing flexible latex membrane allows the sample to be subjected to radial cell pressure, while a freely rotating platen in contact with the top part of the sample can enforce a vertical compression. The specimen is first compressed isotropically to 100 kPa, and then compressed triaxially by keeping the cell pressure constant while prescribing a vertical displacement to the platen under quasistatic conditions. Eventually, failure occurs through the formation of a persistent shear band.

Recently, the experiment has been modelled using LS-DEM, where, for each physical grain in the sample, an equivalent virtual grain is generated through a level set imaging algorithm [169]. The resulting virtual specimen is then subjected to the same boundary conditions, by modeling the membrane as well as the kinematics of the platen. The deformed specimen at critical state is shown in Fig. 4.12 b). LS-DEM is able to capture both the onset and spatiotemporal evolution of the shear band, as reported in detail in a recent publication [169].

We now simulate the experiment using the Data-Driven framework. In a first simulation, the material data are directly gleaned from the LS-DEM calculation (Fig. 4.12 b)) in a self-consistent manner, as in Section 4.5.3. In a second simulation, we choose instead to compile new material data sets by means of periodic unit cell calculations, using goal-oriented sampling (Section 4.3.1). To this end, we need to generate cells (Fig. 4.13 a)) that are representative of the initial local states in the heterogeneous cylindrical specimen, and use

them to sample the phase space. First, we compute the void ratio distribution in the specimen, which is enough to fully characterize its heterogeneity given the predominantly isotropic fabric. We then generate cells with void ratios sampled from that distribution (Fig. 4.13 b)).

Finally, we need to identify the subset of the phase space that needs to be sampled, i.e. the predominant loading paths to which we shall subject the representative unit cells. We expect that, after triaxial compression to a peak state and the associated onset of shear banding, a bifurcation of the response occurs, with the exterior of the band unloading along the same stress path, and the interior of the band undergoing locally approximately simple shear.

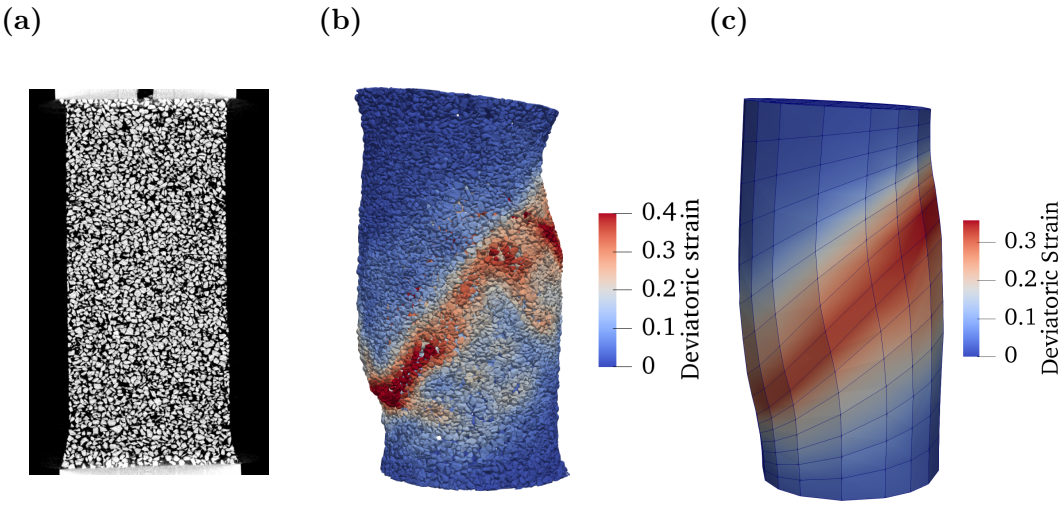

Figure 4.12: Sand specimen subjected to triaxial compression: a) XRCT at the end of isotropic compression. b) LS-DEM simulation, and c) self-consistent Data-Driven simulation of triaxial compression, both at critical state.

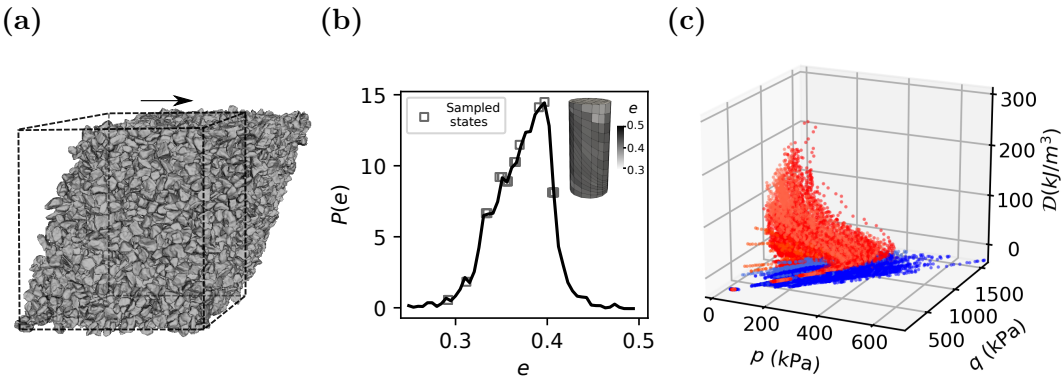

Figure 4.13: Goal-oriented sampling: a) Example periodic cell used for sampling. b) Initial heterogeneous local void ratio distribution in the cylindrical specimen. c) Data clustering in $p - q - \mathcal{D}$ space.

Indeed, we can identify these paths via a simple clustering analysis of the experimental data. In particular, we employ the DB-SCAN algorithm [103] equipped with the following distance:

$$d(\mathbf{z}, \mathbf{y}) = |\{\mathbf{z}_k - \mathbf{y}_k\}_{k=1}^{N}| \tag{4.29}$$

arising from the history-matching metric:

$$|\{\mathbf{z}_k\}_{k=1}^{N}| = \big(\sum_{k=1}^{n} |\mathbf{z}_k|^2\big)^{1/2} \tag{4.30}$$

where $|\mathbf{z}_n|$ is given by Eq. 4.5). The above metric induces trajectory clustering on the data, which are plotted in terms of isotropic and deviatoric invariants in Fig. 4.13 c). Two major clusters are obtained, one inside the shear band (red), characterized by pronounced dissipation, and one outside the shear band (blue), where the response remains almost 'elastic'. Sampling 10 paths within each cluster for a total of 20 unit cell calculations is enough to produce the required data sets. In case we encounter a solution that lies unacceptably far from the data set at any point, then additional sampling can be carried out.

In both types of simulations discussed above, the material data sets are parametrized following the energy-based approach, while FEM is used for the discretization of the macroscopic boundary value problem. Note that, in this application, localization arises from the heterogeneity of the sample rather than by a prescribed discontinuous boundary displacement (as in the fault rupture experiment). Hence, we need to provide partial information about the heterogeneous structure, in order to aid the convergence of the algorithm and the onset of localization. This is achieved by attaching to a given material point, an initial material data set that corresponds to a void ratio similar to the initial void ratio of that material point in the experiment. This simply serves as a starting point for the fixed point iterations of the solver. Upon this initialization, all material data sets are available to each material point subject to thermodynamic constraints.

Fig. 4.12 c) shows the deformed specimen obtained from the self-consistent as well as the goal-oriented Data-Driven simulation at critical state. Upon comparison with the deformed LS-DEM specimen (Fig. 4.12 b)), it is clear that the localized response is well captured. Finally, Fig. 4.14 compares the macroscopic response in terms of axial strain, principal stress ratio, and volumetric

strain of the sample, as obtained from the experiment, LS-DEM, and the two Data-Driven simulations, all showing good agreement.

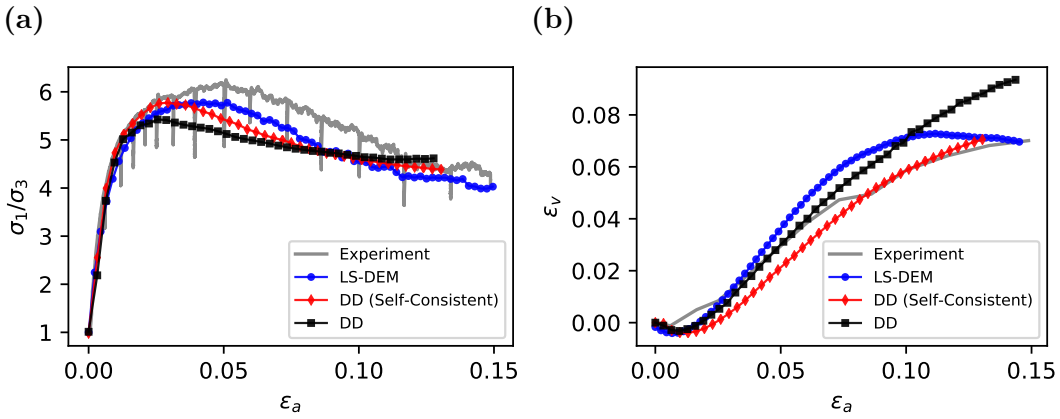

Figure 4.14: Comparison between physical experiment, LS-DEM simulation and Data-Driven prediction (self-consistent and goal-oriented) in terms of a) axial strain vs principal stress ratio and b) axial strain vs volumetric strain.

4.6 Conclusions

We have presented a new multiscale paradigm for the prediction of material behavior. The proposed framework relies on the general inelastic formulation of Data-Driven Mechanics, where the sampling of the phase space is achieved through lower-scale computations, carried out offline or on-the-fly. The resulting material data-sets are appropriately parametrized to account for history-dependence. We have demonstrated an application of the framework to granular materials, where grain-scale computations with the Level-Set Discrete Element Method were used to generate the required data sets. Within this application, we investigated the performance of two history parametrizations: one thermodynamics-motivated and material-independent, and one internal variable-based and tailored to granular materials. The framework was able to capture the nonmonotonic and localized response in both plane-strain rupture and triaxial compression boundary value problems.

It is worth briefly contrasting Data-Driven computing to machine learning-based methods and conventional multiscale methods. Machine learning almost always requires specifying ad hoc effective coordinates, or 'features', which carry most of the information in the data. The identification of these features is also often ad hoc, and reduces the overall modeling process to old-fashioned

fitting or regression. In addition, the internal representation of the machine-learned model is often hidden and devoid of physical meaning. By contrast, Data-Driven methods use the data, all the data, and nothing but the data in making predictions. In particular, no empirical or subscale information is lost or manipulated in any way. The physical interpretation of the Data-Driven solutions (that the admissible equilibrium and compatible states should be as close to the data as possible) makes eminent physical sense, and the process of solution is transparent with no hidden representations or manipulations. The proposed Data-Driven multiscale paradigm is also superior to conventional multiscale methods since the data are readily reusable for future predictions involving the same material. Since searching a material database is typically much faster than a new unit-cell calculation, as more and more data relevant to a particular application are present in the dataset, the framework becomes increasingly superior to conventional techniques.

To conclude, Data-Driven techniques will likely continue to gain popularity in an era when data from high-fidelity simulations and high-resolution experiments are becoming increasingly abundant, as long as these methods serve the long-standing objective of minimizing uncertainty and improving predictive capability. However, techniques such as the proposed framework should not be viewed as a replacement for classical constitutive modeling paradigms that have matured over the years, but rather as a complement in an emerging era of Data-Driven computing. Uncovering and mathematically describing the laws that emerge from the collective behavior of complex micromechanical systems remains a fundamental research goal, and Data-Driven techniques can only help towards that goal, by revealing how much of the rich micromechanical data is relevant to the macroscopic behavior.

Chapter 5

NONLOCALITY IN GRANULAR COMPLEX NETWORKS: LINKING TOPOLOGY, KINEMATICS, AND FORCES

K. Karapiperis and J. E. Andrade. "Nonlocality in granular complex networks: Linking topology, kinematics and forces". In: *Extreme Mechanics Letters* 42 (2020), p. 101041.

Abstract

Dry granular systems respond to shear by a process of self-organization that is nonlocal in nature. This study reveals the interplay between the topological, kinematical, and force signature of this process during shear banding in a sample of angular sand. Using Level-Set Discrete Element simulations of an in-situ triaxial compression experiment and complex networks techniques, we identify communities of similar topology (cycles), kinematics (vortex clusters), and kinetics (force chains), and study their cooperative evolution. We conclude by discussing the implications of our observations for continuum modeling, including the identification of mesoscale order parameters, and the development of nonaffine kinematics models.

5.1 Introduction

The study of nonlocality in granular materials can be traced back to the pioneering experiments of Roscoe [296] and, later, Mühlhaus and Vardoulakis [239], establishing the characteristic width of a shear band in sand at 8-10 particle diameters. Further evidence of nonlocality has been identified in the dynamic flow regime [229] for example in the form of nozzle jamming in silos [384] and thickness-dependent repose angles in surface flows [273, 320]. Later, advances in experimental techniques [87, 254, 355] as well as discrete element (DEM) [78] and contact dynamics (CD) [235] simulations inspired grain-scale studies in an effort to explain these emergent phenomena. Most notably, photoelastic experiments and particle simulations helped identify the heterogeneous nature of force transmission in an assembly in the form of force chains [209, 282, 283]. Subsequent experiments conjectured force chain buckling [254] as a mechanism for shear localization, which was later investigated

through structural stability analyses enabled by DEM [345, 339]. Measurements of force correlations were used in [219] to quantify the heterogeneous nature of force networks under shear, yielding a consistent correlation length of about 10 particle diameters. Similarly, the study of velocity correlations has revealed the nonaffine nature of granular kinematics, termed granulence [278, 274]. As a signature of these correlations, vortices of characteristic sizes emerge [269, 162, 293], accompanied by intense particle rotations [255, 253, 28, 191, 9], eventually leading to the development of a shear band [188, 285, 1, 343]. Finally, the use of complex networks techniques [314, 188, 323, 22, 342, 361, 363, 364] has contributed to the identification of stable [342] and unstable [54] mesoscale features and communities [122] and their topological transformations.

Alongside these micromechanical studies, it was recognized that standard continuum theories failed to capture nonlocal effects [146, 275]. As a result, two major families of theories have emerged: enhanced continua [99] and nonlocal theories [163]. Enhanced (or weakly nonlocal [294]) continua depart from the standard Cauchy assumption of affine deformation, by introducing higher-order kinematics and their conjugate kinetics. Most notably, the micropolar theory [75, 100], which equips the material point with rotational degrees of freedom, has succesfully captured several aspects of shear bands in sands [239, 336]. On the other hand, (strongly) nonlocal theories introduce an additional field that represents the (solid-like or fluid-like) state of the material locally [21, 163]. Characteristic examples include the Landau-type [196] order parameter formulation termed partial fluidization theory [21], gradient plasticity [353, 351], and the nonlocal granular fluidity model [161]. In this family, the length scale is typically identified as the characteristic length scale of the diffusion process of a local microstructural event, such as a shear transformation [106], due to the correlated motion of its neighbors. Recently, the hypotheses inherent to some of these formulations have been supported by micromechanics, through advanced homogenization techniques [94, 93, 29, 340, 210], kinematic models [343], and direct micromechanical descriptions of order parameters [374]. Yet, the micromechanical description of nonlocality within a sound theoretical framework still remains largely an open question.

In this Letter, we investigate the emergent length scale in the quasistatic flow of sand. To this end, we rely on three-dimensional Level-Set Discrete Element

Method (LS-DEM) simulations of triaxial compression [169] of a sample of angular sand characterized by X-ray computed tomography [15]. We utilize complex network techniques, which have not received proper attention in 3D systems, to reveal stable and unstable mesoscale topological structures, vortex clusters, and force chains, which depart from earlier observations in idealized and predominantly two-dimensional systems. Particular emphasis is placed on the cooperative evolution of these features through distinct stages of the experiment.

This Letter is organized as follows: Section 5.2 details the experiments and simulations furnishing the micromechanical data to be subsequently analyzed. In Sections 5.3-5.5, we present the methods used to analyze the topology, kinematics, and forces in the system, respectively, and discuss the outcome of each analysis. We conclude by summarizing our main findings, and discussing their implications for continuum theory in Section 5.6.

5.2 Triaxial compression experiments and simulations

The data analyzed in this work are obtained from a high-fidelity discrete element simulation of a quasi-static *in-situ* triaxial compression experiment reported in an earlier publication [169]. In the experiment, a cylindrical specimen of angular Hostun sand, encased in a flexible latex membrane, is subjected to a triaxial loading protocol [15]. Fig. 5.1 a) shows a 2-dimensional slice of the XRCT scanned specimen, which measures 11 mm in diameter and 22 mm in height, and is comprised of 53,939 angular grains. The specimen is first compressed isotropically to 100 kPa. Next, keeping the radial pressure constant, a freely rotating platen in contact with the top part of the sample enforces a vertical compression until failure. Air can escape through a hole in the loading platen, giving rise to drained conditions.

The experiment is computationally replicated using a variant of DEM [78] termed LS-DEM [170]. Similarly to the original formulation, LS-DEM resolves the kinematics of particles interacting through frictional contacts, but also accounts for accurate particle morphology. In particular, for each physical grain in the triaxial sample, a virtual grain is generated through a level set imaging algorithm (Fig. 5.1 a)). The resulting virtual specimen is subjected to identical boundary conditions, by modeling the membrane as well as the kinematics of the platen. The deformed virtual specimen is shown in Fig. 5.1

a), where the formation of a shear band can be identified. Note that the friction coefficient ($\mu = 0.55$) was calibrated against the experiment, but falls within the range of experimental values [310]. For more details regarding the LS-DEM simulation, the interested reader is referred to [169].

Figures 5.1 b) and c) compare the macroscopic response of the sample in experiment and simulation, in terms of ratio of major to minor principal stress σ_1/σ_3 and volumetric strain ε_v respectively. The sample exhibits a peak in the macroscopic stress ratio (equivalently, friction angle), only to decay later to a constant critical state value. In accordance with earlier experiments and theory [318, 37], the peak state coincides with the maximal rate of dilation of the shear band, while the volume remains constant at critical state. Note that the volumetric strain in the simulation plateaus slightly earlier than in the experiment, which can be attributed to the slightly premature attainment of the peak state in the simulation, and to the different method of measuring the volumetric strain in the experiment (3D DIC) and the simulation (change of volume enclosed by the membrane). The peak and critical state regimes are of particular interest to this study, and are highlighted in the figures.

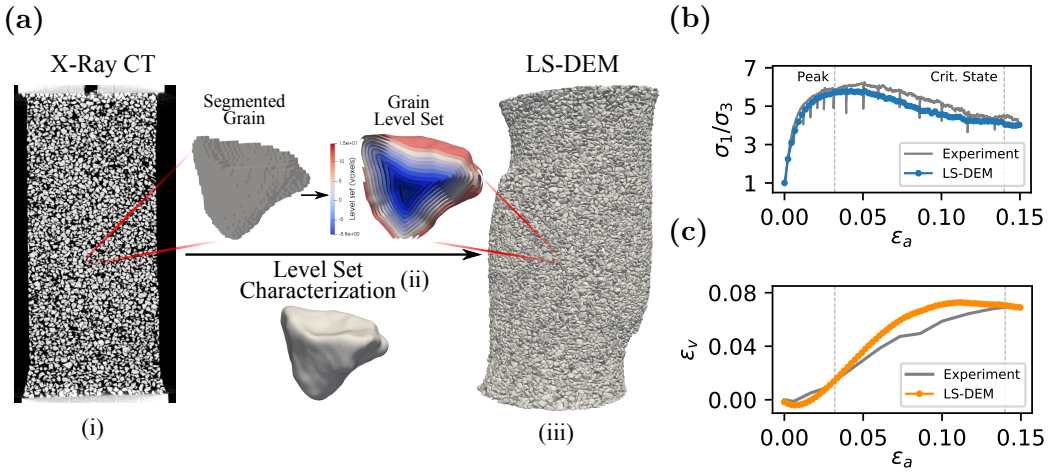

Figure 5.1: Triaxial compression problem analyzed in this study: a) LS-DEM simulation of a sample of Hostun sand characterized by XRCT. b) Principal stress ratio plotted against axial strain. The peak and critical state are indicated with dashed lines. c) Volumetric strain plotted against axial strain.

5.3 Mesoscale topological evolution

5.3.1 Complex networks

The nonlocal response of the granular assembly to externally applied loads is encoded in its evolving contact network structure. Motivated by the success of complex network analysis in identifying the nonlocal topological evolution of idealized two-dimensional systems [342], we proceed by considering the assembly as a graph, where particles serve as nodes, and contacts or contact forces serve as edges connecting the nodes (Fig. 5.2 a)). In particular, we study two types of networks that are defined as follows. In the unweighted or binary network $\mathbf{B}$, edge weights B_{ij} are zero-valued if no contact exists between particles i and j, and unit-valued if the particles interact through at least one contact. On the other hand, in the weighted network $\mathbf{W}$, edge weights are given by the normalized interparticle force $W_{ij} = f_{ij}/\langle f \rangle$, where f_{ij} is the total force arising from potentially multiple contact points. The unweighted and weighted contact networks have been recently used to extract interesting features [265] such as cycles [323, 22, 342] and communities [122], and to pinpoint shear band nucleation [361, 363] and force chain development [178].

In this section, we restrict our attention to the unweighted network, while the weighted network will be considered later in Section 5.5. In particular, we focus on identifying and characterizing the evolution of mesoscale structures during the shear-banding or unjamming transition. This is achieved through a minimal cycle analysis of the network [86]. A cycle is a closed walk along the graph edges, i.e. one that starts and ends at the same node. A cycle basis is a set of simple (non-intersecting) cycles that forms a basis of the cycle space of the graph. A minimum cycle basis is a basis with minimal total length of cycles. Fig. 5.2 b) shows examples of minimal 3-, 4-, 5-, and 6-cycles that pass through a given particle in the system. In a two-dimensional system, the minimal cycles would simply correspond to the faces of the contact graph, i.e. the regions formed by drawing the graph.

5.3.2 Results

The size of our network allows us to study the statistics of cycle sizes, since even rare occasions of long minimal cycles can be accounted for. Fig. 5.2 c) shows the probability density function (PDF) of cycle sizes N_c in the whole sample

at peak and critical state. Interestingly, the density appears to decay super-exponentially with cycle size and may be well approximated by $P(N_c) \sim e^{-\alpha N_c^3}$, as shown in the same figure. In accordance with previous observations [342, 363], the density of longer cycles increases at critical state, which could be a manifestation of dilatation.

We now turn our attention to the density of individual cycles inside the shear band, where significant topological changes occur. Fig. 5.2 d) shows the evolution of the density of 3-, 4-, 5-, and 6-cycles (constituting ∼80% of the total number of cycles) as a function of the shear strain ϵ_s in the localized band. We observe that 3-, 4-, and 5-cycles are almost equally populous in the initially jammed configuration, hinting on their importance as stabilizing mesoscale features. This lies in contrast to previous studies on idealized two-dimensional [342] and three-dimensional [363] assemblies which showed that 3-cycles constitute the clear majority in a jammed state, due to their high rotational frustration. We conjecture that this is due to the pronounced asphericity and irregularity of the sand grains, that enhance stability, in line with recent evidence of the effect of particle morphology on the mechanical response [168]. Upon further deformation, 3-, 4-, and 5-cycles exhibit a power-law decay to a common critical state density, also shared by 6-cycles, hinting on the existence of a common steady state in cycle birth-and-death dynamics.

Inspired by the apparent importance of several classes of cycles in our system, and in order to describe the ensuing phase transition, we introduce the *average cycle membership* of a particle i, given by $\bar{N}_c(i) = \sum_j j c_j(i) / \sum_j c_j(i)$, where $j \in [3, \infty)$ is the cycle size and $c_j(i)$ is the number of minimal cycles of size j that pass through node i. This measure in turn gives rise to the *minimal cycle coefficient* $D(i) = 3/\bar{N}_c(i)$. A highly stable particle entirely surrounded by 3-cycles will have $D = 1$, while a highly unstable particle will be surrounded by long cycles such that $D \to 0$. The proposed coefficient is a generalization of the local clustering coefficient $C(i)$, which measures the density of 3-cycles surrounding a particle, and similar higher order coefficients for longer cycles [46].

We note that the minimal cycle coefficient D also bears resemblance to two other measures in the complex networks literature: the *loop coefficient* [359, 358] and the *subgraph centrality* [104]. The former is given by $L(i) = 1/(k_i(k_i - 1)) \sum_{j,k \in \Gamma_i} 1/d_{jk/i}$, where Γ_i is the local subgraph of neighbors of i where node

i has been excluded, and $d_{jk/i}$ is the shortest path length between particles j and k within Γ_i. The second relevant measure is the subgraph centrality $SC(i) = \sum_{k=0}^{\infty} B_{ii}^k/k!$, which measures the number of closed walks starting and ending in node i. The difference with D is that SC includes trivial even-sized walks and cycles that are not simple. It has been successfully used as a proxy for fluctuating kinetic energy during failure of a granular assembly [362].

Fig. 5.2 e) shows the evolution of the average minimal cycle coefficient $\langle D \rangle$ within the shear band, and compares it to that of the average coordination number $\langle Z \rangle$, the prototypical order parameter for the jamming transition [208]. In both cases, we observe a similar decay to a critical state value. The large Pearson's correlation coefficient ($\sim$0.6) between the particle-scale D and Z implies that the minimal-cycle coefficient could serve as an equivalent mesoscale

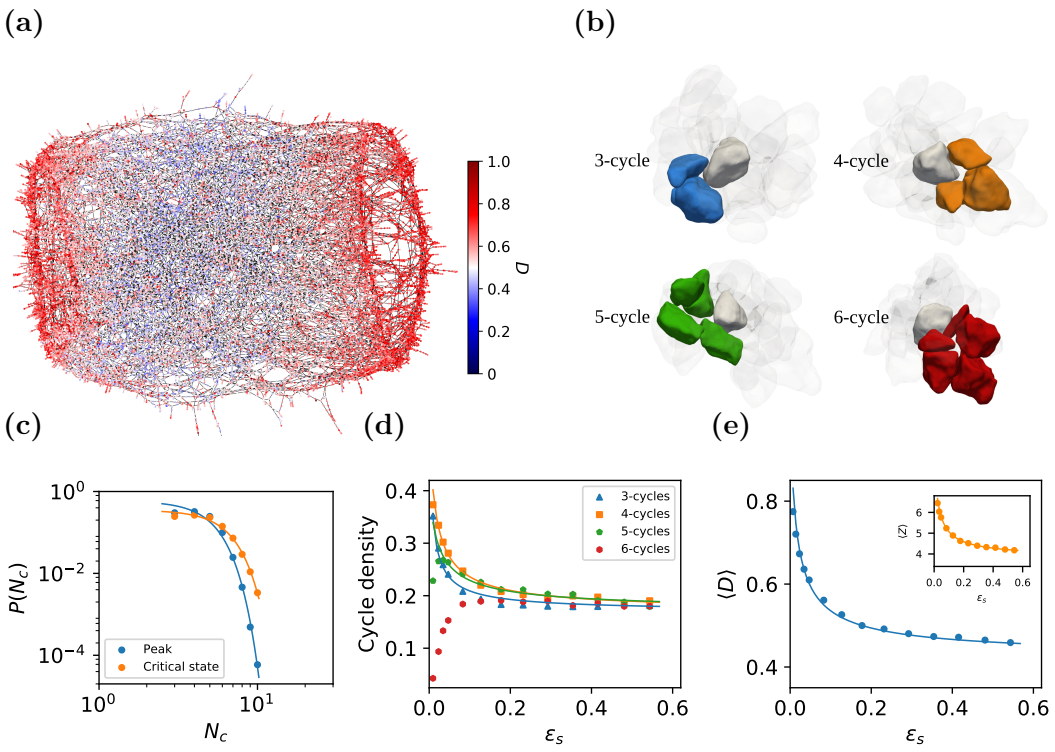

Figure 5.2: Evolution of topology: a) Graph representation of the sample at critical state, with nodes colored by their minimal cycle coefficient. b) Example minimal 3-,4-,5-, and 6-cycles passing through a given center node. c) PDF of cycle size N_c in the sample, and fitted distribution. d) Evolution of density of 3-, 4-, 5-, and 6-cycles inside the shear band. e) Evolution of the average minimal cycle coefficient inside the shear band. Inset: Evolution of the average coordination number.

order parameter for this transition. In the next sections, we will address its relevance to the kinematics and kinetics of the system.

5.4 Nonaffine kinematics

In this section, we characterize for the first time the kinematics that accompany the topological changes within a three-dimensional shear band by studying the formation and evolution of vortex clusters. Earlier kinematics studies have either focused on two-dimensional systems [9, 1, 343], have relied on simplified scalar measures of nonaffine deformation [105, 341, 54] or have not addressed shear bands [264].

5.4.1 Vortex identification

We analyze the nonaffine particle displacements $\delta\mathbf{u}_i \equiv \mathbf{u}_i - \boldsymbol{\epsilon} \cdot \tilde{\mathbf{x}}_i$, where $\mathbf{u}_i$ is the displacement, and $\tilde{\mathbf{x}}_i$ is the position of particle i with respect to a local coordinate system aligned with the shear band. The affine (approximately simple-shear) strain $\boldsymbol{\epsilon}$ dominating the band's deformation is found in a least-squares sense [105] as:

$$\min_{\boldsymbol{\epsilon}} \sum_{i \in \mathcal{S}} ||\mathbf{u}_i - \boldsymbol{\epsilon} \cdot \tilde{\mathbf{x}}_i||^2 \tag{5.1}$$

where the summation takes place among the set of particles $\mathcal{S}$ within the band. We proceed to identify mesoscale vortex structures formed by the nonaffine displacements. As opposed to two-dimensional systems [269, 293], where vorticity is parallel to the out-of-plane axis, vortices can freely rotate in 3D systems and form clusters [264]. To identify those clusters, we employ the methodology of [264], by first computing the vorticity field:

$$\boldsymbol{\omega}(\mathbf{x}) = \rho(\mathbf{x})^{-2} \sum_{i \in \mathcal{S}} \sum_{j \in \mathcal{S}} \phi_i(\mathbf{x}) \left[\nabla \phi_j(\mathbf{x}) \times \delta\mathbf{u}_{ij}\right] \tag{5.2}$$

where $\phi(\mathbf{x}) = e^{-||\mathbf{x}-\mathbf{x}_i||^2/\bar{d}^2}$ is the coarse-graining kernel [372], $\rho(\mathbf{x})$ is the coarse-grained number density field, and $\delta\mathbf{u}_{ij} = \delta\mathbf{u}_i - \delta\mathbf{u}_j$ is the relative nonaffine displacement between particles i and j. To identify a cluster, we choose a particle within the shear band at random and traverse its contact network using a breadth-first search algorithm. For contacting particles i, j, their normalized vorticities, $\tilde{\boldsymbol{\omega}}_i$, $\tilde{\boldsymbol{\omega}}_j$, respectively, are compared by computing the angle of their cosine similarity $\theta_{ij} = \cos^{-1}(\tilde{\boldsymbol{\omega}}_i \cdot \tilde{\boldsymbol{\omega}}_j)$. The particles are included in the same

cluster if $\theta_{ij} < \theta_c = \pi/6$, and the search continues until no more particles are included in the cluster[1].

5.4.2 Results

The nonaffine displacement field along with the identified vortex clusters are shown in Fig. 5.3 a). In contrast to two-dimensional systems where there is a clear geometrically defined length scale in the form of a vortex radius [293, 343], here the complex shape of vortices requires an alternative definition of length scale. To this end, we compute the distribution of vortex cluster size N_v throughout the stages of the experiment, and find, in accordance with [264], that it is well described by a power law with exponential cutoff, $P(N_v) \sim N_v^{-\alpha} e^{-N_v/\nu_v}$, as shown in Fig. 5.3 b). By analyzing the exponential tails, a characteristic vortex length scale $\ell_v \equiv \nu_v^{1/3}$ of about 4 grain diameters is obtained. Its evolution throughout the experiment is shown in the inset Fig. 5.3 b), where a slight increase with shear strain is identified.

Next, we characterize the vortex strength ω_v, which we define as the average vorticity in each cluster. As shown in Fig. 5.3 c), the average vortex strength increases to a steady state value, while its density is well approximated by the Boltzmann-Maxwell distribution $P(\omega_v) \sim \omega_v^2 e^{-\omega_v^2/2}$. Finally, we characterize the directionality of these vortex clusters. This is achieved by computing the average normalized vorticity of each cluster $\tilde{\boldsymbol{\omega}}_c$, and comparing it to a macroscopic director $\boldsymbol{\Omega}$ that is orthogonal to both the direction of shear and the normal to the shear band plane, as shown in Fig. 5.3 a). The distribution of their cosine similarity $\cos\bar{\chi} = \tilde{\boldsymbol{\omega}}_c \cdot \boldsymbol{\Omega}$ is plotted is Fig. 5.3 d). We observe a slightly anisotropic distribution with some degree of preferential alignment of the vorticity with $\pm\boldsymbol{\Omega}$, which would correspond to the primary (homothetic) and secondary (antithetic) vortices observed in 2D systems [9, 1, 343]. Most vortices appear to be arbitrarily oriented in space.

5.5 Forces

To shed light on the kinetics that accompany the kinematical (Section 5.4) and topological (Section 5.3) transition, we will now characterize the evolving

[1]The critical angle is chosen as $\theta_c = \pi/6$, following [264]. A sensitivity analysis showed that cluster sizes decrease with increasing θ_c, yet their distribution consistently follows a power law with exponential cutoff.

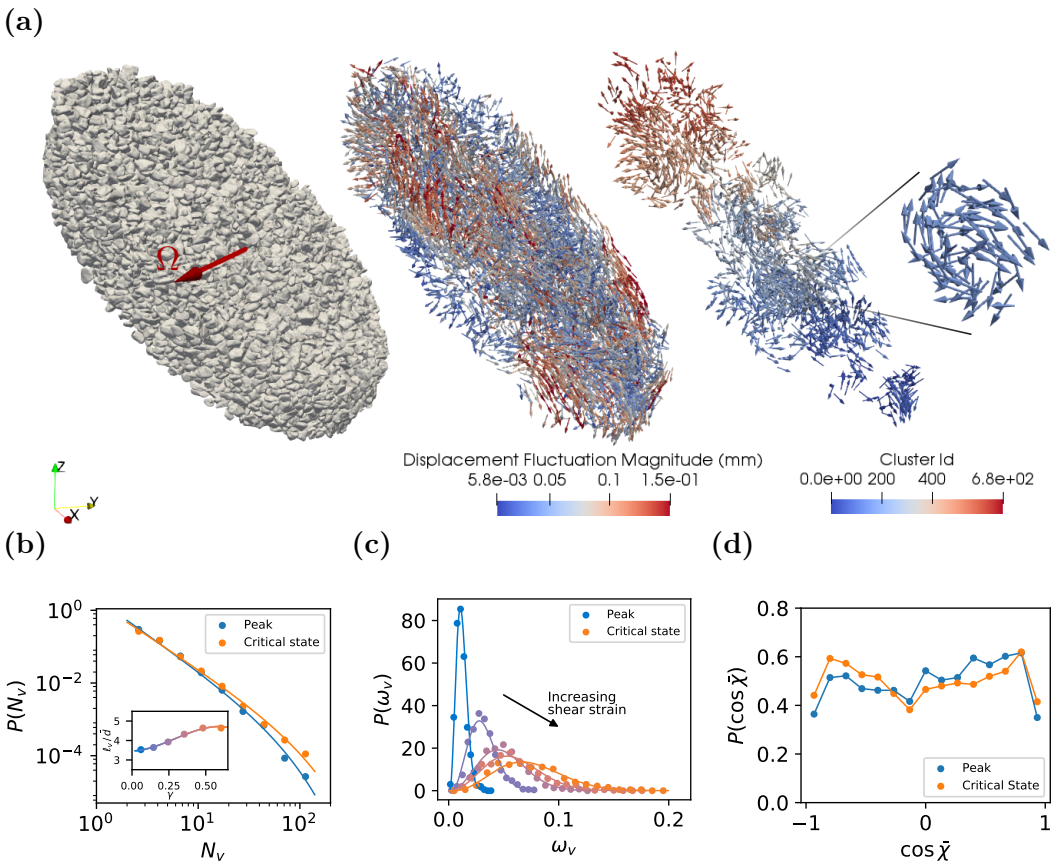

Figure 5.3: Evolution of kinematics: a) Nonaffine displacement field and identified vortex clusters within the shear band. b) PDF of cluster size N_v and fitted power laws with exponential cutoff. Inset: Evolution of characteristic length ℓ_v as a function of the shear strain within the band. c) PDF of the vortex strengths and fitted Maxwell-Botzmann distribution. d) PDF of the orientational order parameter $\cos\bar{\chi}$.

force chain architecture. Driven by the lack of general agreement on what constitutes a force chain, we first reconcile the two major identification techniques in the literature: network community detection [30] and 'direct' identification [270]. We then proceed with observations on chain stability and establish direct links with topology and kinematics.

5.5.1 Force chain extraction via community detection

Our point of departure is the characterization of the weighted and unweighted contact networks outlined in Section 5.3. Following [30], we seek communities $\{s_i\}$ of grains strongly connected via intergranular forces of similar magnitude,

by maximizing the modularity function:

$$Q = \sum_{i,j} (W_{ij} - \gamma P_{ij}) \delta(s_i, s_j) \tag{5.3}$$

where W_{ij} is the weighted adjacency matrix, γ is the resolution parameter controlling the size of communities, P_{ij} is the so-called null model representing the expected weight of the edge connecting nodes i and j, and $\delta(s_i, s_j)$ is the Kronecker delta. We adopt the geographical null model [30], given by the unweighted adjacency matrix, $P_{ij} = B_{ij}$, in order to respect the spatial connectivity constraints in the granular system.

5.5.2 Direct force chain identification

For the 'direct' extraction of force chains, we employ a three-dimensional extension of the detection algorithm described in [270]. Hereby, chains are identified as quasilinear sequences of particles that reside in the strong-force network [282]. More specifically, let $\sigma_3, \mathbf{n}_3$ denote the minor (most compressive) principal stress and its direction, respectively, obtained from a spectral decomposition of the particle stress. The latter is given by $\boldsymbol{\sigma} = 1./V^p \sum_c \mathbf{f}^c \otimes \mathbf{x}^c$, where V^p is the particle volume, and $\mathbf{x}^c$ is the location of the contact force $\mathbf{f}^c$ with respect to the particle centroid. For a sequence of particles to constitute a force chain $\mathcal{S}$, its members must i) exhibit a compressive stress that is higher than the sample average:

$$|\sigma_3^i| > \frac{1}{N} \sum_{j=1}^{N} |\sigma_3^j|, \quad \forall i \in \mathcal{S} \tag{5.4}$$

where N is the number of particles in the sample, and ii) be sufficiently colinear:

$$\frac{\mathbf{l}_{ij} \cdot \mathbf{n}_3^i}{||\mathbf{l}_{ij}|| \cdot ||\mathbf{n}_3^i||} > \cos \alpha, \quad \forall i, j \in \mathcal{S} \tag{5.5}$$

where $\mathbf{l}_{ij}$ is the branch vector connecting consecutive particles i, j in the chain. The angle α represents the maximum allowable angle between chain segments which we take as $\alpha = 45°$.

5.5.3 Results

Fig. 5.4 a) shows the contact force network at critical state, along with the resulting force chains obtained via direct identification and community detection, respectively. The latter is based on a resolution parameter $\gamma^* = 3.0$

(recall its definition in Section 5.5.1), optimized to generate chains maximally similar to those identified 'directly'. Similarity is assessed based on the coincidence of member particles of chains determined by the two methods. We find that, for $\gamma = \gamma^*$, the chains determined by the two methods share the majority ($\sim 60\%$) of their participating members.

Fig. 5.4 c) shows the PDF of community sizes N_{com} for varying resolution parameter γ. The sizes are found to follow a power law distribution $P(N_{com}) \sim N_{com}^{-\alpha}$, where α is almost linearly correlated with γ. On the other hand, in accordance with earlier studies [270], the size of chains obtained by direct identification follows an exponential distribution, as shown in Fig. 5.4 d). This is further evidence that for large enough γ, the two identification methods are reconciled.

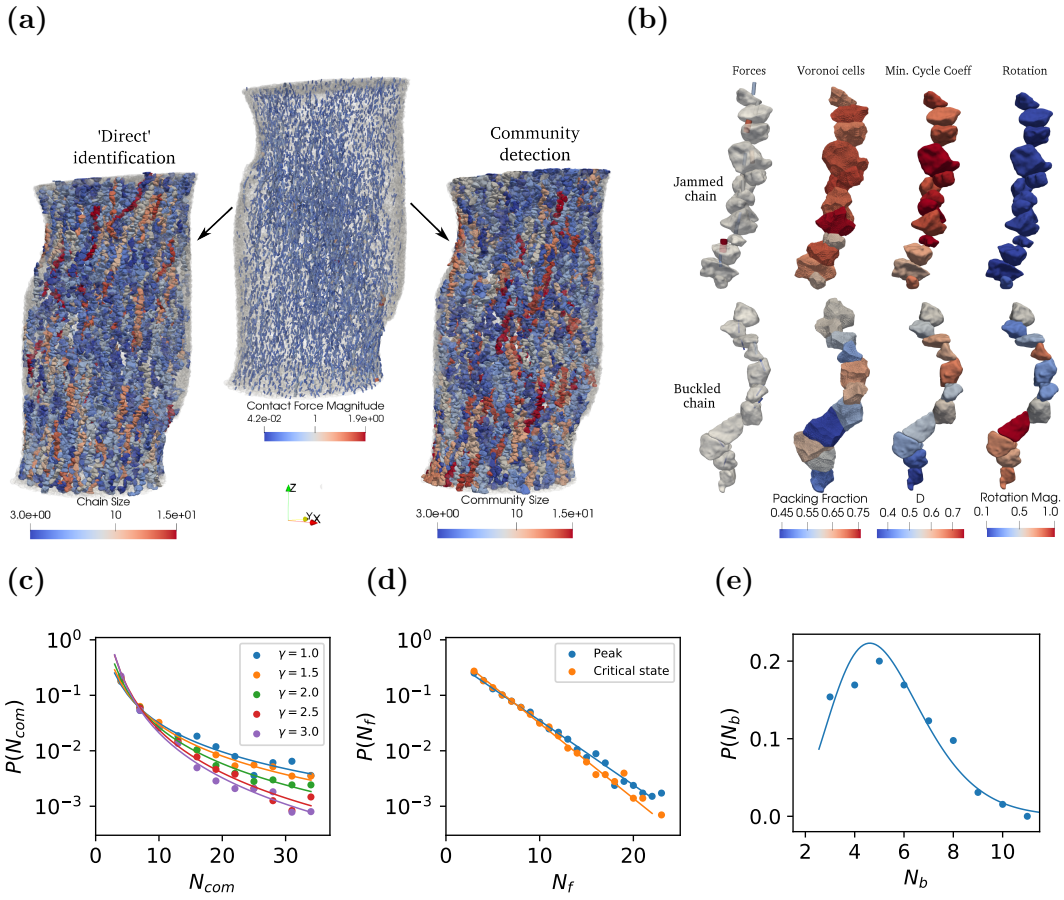

Figure 5.4: Evolution of forces: a) Force network, directly identified chains and detection of communities at critical state. b) Characterization of a jammed and a buckled chain using various descriptors. c) PDF of community size N_{com} and fitted power law distribution for different values of the resolution parameter γ. d) PDF of force chain size N_f and fitted exponential distribution. e) PDF of buckled force chain size N_b and fitted distribution.

Of particular importance to force transmission is the structural characterization of force chains. Fig. 5.4 b) shows examples of a jammed (stable) and a buckled force chain, along with several of their topological and kinematical attributes. A chain is assumed to have buckled when two criteria are met [345]: i) an increase in local chain curvature beyond a critical threshold, identified via sensitivity analysis, and ii) a reduction of the potential energy $\mathcal{A}$ stored in the deformed chain contacts. The latter is given by:

$$\mathcal{A} = \frac{1}{2} \sum_{c} \left(\frac{\|\mathbf{f}_n^c\|^2}{k_n} + \frac{\|\mathbf{f}_t^c\|^2}{k_t} \right) \tag{5.6}$$

where $\mathbf{f}_n^c$ and $\mathbf{f}_t^c$ are the resolved normal and tangential forces at a contact c, while k_n and k_t are the normal and tangential contact stiffness, respectively. A jammed chain is one that persists through loading without buckling. Fig. 5.4 e) shows the PDF of buckled chain segment sizes N_b throughout the experiment, where we can also identify the longest segment that is prone to buckling ($N_b = 10$). It appears that longer buckling wavelengths are not energetically favorable. Note that, in contrast to earlier studies, the stability of force chains is assessed here with no recourse to numerical proxies such as rolling friction, but rather as an immediate consequence of morphology and interlocking.

Finally, we address the stability of chains in relation to the measures of topology and kinematics investigated in Sections 5.3 and 5.4. To do so, we compare these measures for buckled chains (occurring almost exclusively within the band) and persistent stable chains. Under an increase in the stored elastic energy and a loss of lateral support due to dilatation, a chain becomes increasingly susceptible to buckling. With the help of nonconvex Voronoi tesselations (Appendix 5.A), we can identify the critical local chain packing fraction ϕ_c that induces instability in a chain, as shown in Fig. 5.5 a). Similarly, Fig. 5.5 b) compares the average minimal cycle coefficient D_c, in stable and buckled chains, showing that buckling is associated with a significant increase in D_c. Finally, Fig. 5.5 c) shows the minimum distance (in grain diameters) of stable and buckled chains to the surface of the nearest vortex cluster. Interestingly, all chains avoid forming in the interior of vortices, and most buckling events happen on the surface of vortices. This is because the kinematics in the interior of vortex clusters are unfavorable for force chain stability. At the same time, there is no space for force chains to form further away from the surface of clusters, since the latter densely occupy the shear band (Fig. 3 a)). Overall, this confirms that, along with topology, vortices also govern the formation

of chains, in accordance with recent observations in two-dimensional systems [343].

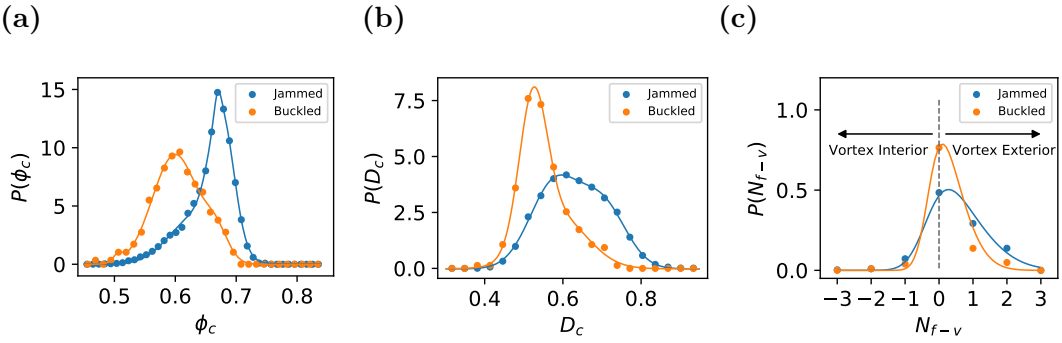

Figure 5.5: PDFs of a) packing fraction, b) minimal cycle coefficients and c) minimal topological distance to the surface of the nearest vortex cluster, for jammed and buckled chains.

5.6 Conclusions

Nonlocality is inherently linked to pattern formation such as shear banding. The objective of this study is to reveal the topological, kinematical, and force signature of shear banding of a sample of angular sand. We based our investigation on high-fidelity three-dimensional simulations using the Level-Set Discrete Element Method and relied on complex network techniques to characterize the emergent length scale. Several implications for improved predictive capabilities arise from this investigation.

Regarding topology, we found that 4- and 5-cycles emerge as equally stabilizing mesoscale structures alongside the shorter well-documented 3-cycles [363]. We conjecture that this is due to particle asphericity and angularity, which enhances topological interlocking, reduces rotations, and thus increases structural stability. By uncovering the evolution of the density of minimal cycles, the prediction of shear banding becomes possible given information about the current density and its rate of decay. We presented the first evidence of a characteristic signature of cycle evolution that is determined by particle morphology. Such a quantitative analysis has not been possible with methods available so far. We also introduced the minimal cycle coefficient D, in order to collectively account for the apparent importance of several families of cycles.

With regard to kinematics, we have provided evidence that dilatancy is the result of the attrition of shorter (3-,4-,5-) cycles and the associated build up of

longer cycles. Furthermore, we have revealed the nonaffine nature of mesoscale kinematics by characterizing, for the first time, the strength and orientational order of vortex clusters within the shear band, while extending previous findings regarding their size distribution. Interestingly, the vortex strength of these arbitrarily shaped clusters follows a Maxwell-Boltzmann distribution, that converges to a well-defined critical state. In terms of their orientational order, we identified a significant departure from the primary and secondary vortices observed in earlier two-dimensional studies. These are all essential descriptors of nonlocal kinematics in enhanced continuum theories.

To delineate the conjugate kinetics, we relied once again on complex networks. First, we reconciled the definition of force chains as fundamental units of force transmission, by comparing the two major identification techniques. We characterized for the first time the distribution of the critical buckling wavelength of force chains, which emerged from a high-fidelity representation of particle morphology, and without recourse to proxies such as rolling friction. The width of a shear band naturally arises as the maximum such wavelength. We also found that buckling chains were characterized by significantly lower average minimal cycle coefficient compared to stable chains, which confirms the high relevance of this new coefficient.

There are several ways to incorporate these new observations into improved predictive nonlocal continuum descriptions. The coarsest description would rely on a mesoscale order parameter that collectively accounts for topological rearrangements within a Landau-type framework [21]. The proposed minimal cycle coefficient appears to be a promising candidate. Work towards this direction would require systematically investigating its diffusive spatial coupling and its relation to the local rheology. Perhaps a more detailed description would rely on modeling, and subsequently coarse-graining, the coupled birth-and-death dynamics of force chains, cycles, and vortices. We identified several constraints that these dynamics must satisfy, such as their critical state densities and rates of decay. Additional work is required in order to understand the dissipation that accompanies these birth-and-death processes. A final avenue would be to explicitly model the nonaffine kinematic field within the shear band [343]. Our characterization of the size, strength, and orientation of vortices can form the basis for constructing admissible nonaffine fields. Which theoretical framework can provide a consistent closure of these kinematics

in terms of their conjugate kinetics remains an open question. Could this be a modified micropolar framework or, perhaps, a gradient theory of self-organization [352]? The road to a unified nonlocal continuum theory remains long and challenging.

Appendix 5.A

To calculate the local packing fraction in Section 5.5.3, we need to compute the volume of the cell associated to each particle. To do so, we employ a generalization of the standard Voronoi tesselation [306] for the case of arbitrarily-shaped and nonconvex particles. This involves a standard Voronoi tesselation of the particles' discretized surface points. In other words, the points at the surface mesh of all particles are used as the input of a standard Voronoi computation [306], generating the example subcells shown in Fig. 5.A.1. Then, all subcells belonging to the same particle are conglomerated into the nonconvex Voronoi super-cell attached to that particle. The accuracy of the scheme depends on the density of the surface discretization of each particle.

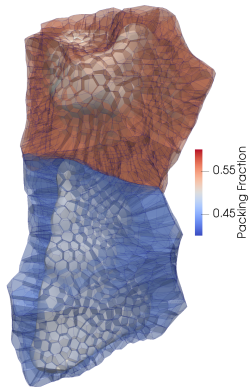

Figure 5.A.1: Two nonconvex Voronoi cells each comprised of multiple convex subcells.

Chapter 6

DATA-DRIVEN NONLOCAL MECHANICS

K. Karapiperis, M. Ortiz, and J. E. Andrade. "Data-Driven nonlocal mechanics" (in preparation)

Abstract

Nonlocal effects permeate most microstructured materials, including granular materials, metals, and foams. The quest for predictive nonlocal mechanical theories with well-defined internal length scales has been ongoing for more than a century since the seminal work of the Cosserat's. We present here a novel framework for the nonlocal analysis of material behavior that completely bypasses the need to define such length scales. The proposed framework extends the Data-Driven paradigm, originally introduced for simple continua, into generalized continua. The case of micropolar media is used as a vehicle to introduce this paradigm, which can also be adapted to strain-gradient and micromorphic media. The Data-Driven problem is formulated directly on a material data set, comprised of higher-order kinematics and their conjugate kinetics, which are identified from experiments or inferred from lower scale computations. Two applications are presented: a micropolar elastic plate with a hole, which is used to demonstrate the convergence properties of the method, and the shear banding problem of a triaxially compressed sample of quartz sand, which is used to demonstrate the applicability of the method on a complex problem involving history-dependent and noisy data.

6.1 Introduction

In the standard (Cauchy) continuum description, a solid body is decomposed into a set of infinitesimal material points, whose constitutive behavior is independent from one another except via the exchange of linear momentum, energy, and entropy. As a result, the material response is invariant with respect to spatial scaling. Any deviation from this behavior is termed nonlocality, and is a manifestation of the material microstructure spanning a characteristic length scale. Indeed, many natural and man-made materials exhibit nonlocal behavior. Dense granular materials fail by forming localized shear bands of a

characteristic width [239], marked by intense nonaffine deformation (grain rotation, vortex formation) [269, 165]. Due to the presence of dislocations, thin metal wires exhibit characteristic strain gradient hardening when subjected to torsion [111]. A similar size effect of stiffening of slender specimens is reported in many other materials including foams [194] and bones [195].

Continuum theories for the nonlocal mechanical analysis of materials are categorized into strongly nonlocal and weakly nonlocal [294]. Strongly nonlocal theories typically rely on an integral formulation [182, 33] or a constitutive equation that is itself a PDE [7, 353, 161]. On the other hand, weakly nonlocal theories, also known as gradient or generalized continuum theories, enrich the constitutive description with gradients of local kinematic variables. Due to the presence of these gradients, the response at a material point depends on the response at a neighborhood of that point. We will henceforth restrict our attention to weakly nonlocal theories. The most general description of weak nonlocality is furnished by the micromorphic continuum [99], according to which the material points composing a macroscopic body are themselves considered a continuum at an appropriate scale of observation, and are subject to their own microdeformation. This mathematical assumption endows the material point with additional degrees of freedom beyond the translational ones present in the Cauchy continuum. The number of additional degrees of freedom induces a hierarchy in the class of generalized continua [120, 113]. For example, by restricting the microdeformation to a rigid rotation, one obtains the micropolar continuum [75, 101] and its constrained version termed couple-stress continuum [111]. Analogously, prescribing the microdeformation to be the same as the deformation gradient gives rise to strain-gradient theory [347, 232, 110].

Traditionally, weakly nonlocal modeling has relied on empirical constitutive laws formulated within continuum thermodynamics [72, 291]. Despite their success in regularizing the ill-posed local problem [239, 111], such formulations rarely have a sound micromechanical basis, and are notoriously hard to calibrate. Specifically, establishing a bridge between micromechanics and the internal length scales required by those theories is very challenging, which is why these length scales are typically defined in an ad-hoc manner [11, 375]. Similar challenges arise in choosing appropriate internal variables and their evolution laws, in an effort to capture history dependence and other aspects

of material behavior beyond nonlocality. Overall, the conventional modeling process inherently induces uncertainty due to the imperfect knowledge of the functional form of the constitutive laws [172], and their extrapolative properties beyond the finite data set used for calibration.

To overcome these long-standing challenges, we hereby propose a reformulation of generalized continuum mechanics by extending the Data-Driven paradigm originally introduced for local mechanics [172, 92, 167]. We specifically focus on the micropolar continuum as the prototypical example of generalized continua. All other types of continua in this taxonomy can be addressed in a similar fashion. The proposed framework bypasses any modeling step, by formulating the problem directly on a given material data set, identified from experiments or micromechanical simulations, while enforcing pertinent constraints and conservation laws. Being entirely parameter-free, the framework avoids the need to define any constitutive relation, and hence, any internal length scale, which is instead implicitly determined from the material data set. The framework is capable of capturing any history-dependent but rate-independent behavior in a thermodynamically consistent manner.

The paper is organized as follows. In Section 6.2, we briefly review the fundamentals of micropolar continua and the family of materials amenable to this description. Next, in Section 6.3, we present the Data-Driven micropolar formulation along with a numerical solution algorithm. Its convergence properties are studied based on a simple boundary value problem of an elastic micropolar plate with a hole. Section 6.4 addresses the extension to inelastic and history-dependent problems. In Section 6.5, we apply the extended framework to the problem of shear banding of a cylindrical sample of quartz sand, where the material database is compiled from discrete element computations. We conclude with an overview and discussion in Section 6.6.

6.2 Fundamentals of micropolar theory

The micropolar continuum is a collection of infinitesimal point particles, each of which is described by a position vector $\mathbf{X}$ in an appropriate reference configuration, and a rigid director triad $\boldsymbol{\Xi}$ representing the material microstructure (Fig. 6.1). Similarly to the Cauchy continuum, a deformation mapping φ maps each particle to its deformed configuration $\mathbf{x} = \varphi(\mathbf{X})$. Additionally, a microrotation $\mathbf{R}(\mathbf{X}) \in SO(3)$ maps $\boldsymbol{\Xi}$ to its rotated configuration $\boldsymbol{\xi}$. The

microrotation tensor may be conveniently parametrized by a microrotation vector $\boldsymbol{\theta}$. This description introduces three additional rotational degrees of freedom $(\theta_i, i = 1, 2, 3)$ to each material point beyond the conventional three translational ones $(u_i, i = 1, 2, 3)$ of the standard Cauchy continuum. In the geometrically linear regime, the following measures of strain and curvature are adopted [98, 100]:

$$\varepsilon_{ij} = u_{i,j} + \epsilon_{ijk}\theta_k \tag{6.1}$$

$$\kappa_{ij} = \theta_{i,j}. \tag{6.2}$$

The balance equations are furnished by the conservation of linear and angular momentum:

$$\sigma_{ij,j} + \rho b_i = 0 \tag{6.3}$$

$$\mu_{ij,j} + \epsilon_{ijk}\sigma_{jk} + \rho c_i = 0 \tag{6.4}$$

where $\boldsymbol{\sigma}$ is the Cauchy stress, $\boldsymbol{\mu}$ is the couple stress, $\boldsymbol{\epsilon}$ is the third-order permutation tensor, ρ is the density, $\mathbf{b}$ is the body force, and $\mathbf{c}$ is the body couple.

The kinematic assumption discussed above is valid for several natural and man-made materials. In the case of granular materials, the micropolar kinematics succesfully separate the grains' rotations from their translations. The rotational motion of the grains determines the nonaffine kinematics that dominate the material behavior within a shear band, and significantly affects dilatancy [239, 252]. Chiral metamaterials [324, 212] are also conveniently described by

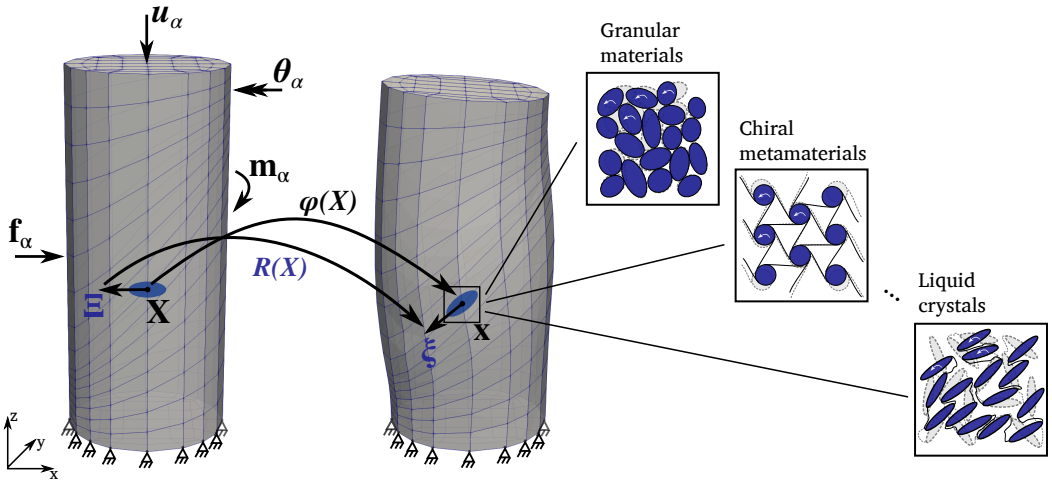

Figure 6.1: Deformation of a discretized micropolar continuum body, and types of microstructures amenable to the micropolar description.

micropolar kinematics. This family of materials features internal rotational units connected by ligaments to generate an auxetic lattice. Finally, the micropolar assumption has also been applied to the modeling of liquid crystals [102], which are comprised of rod-like molecules embedded in a polymer network, and interacting through short-range forces and couples.

6.3 Data-Driven micropolar elasticity

We consider the geometrically linear mechanical problem of an elastic micropolar body that is discretized into N nodes and M material points (Fig 6.1). The body is subject to applied forces $\mathbf{f} = \{\mathbf{f}^\alpha\}_{\alpha=1}^N$ and moments $\mathbf{m} = \{\mathbf{m}^\alpha\}_{\alpha=1}^N$, and undergoes displacements $\mathbf{u} = \{\mathbf{u}^\alpha\}_{\alpha=1}^N$ and microrotations $\boldsymbol{\theta} = \{\theta^\alpha\}_{\alpha=1}^N$ at its nodes. The internal state of the system is characterized by two conjugate pairs, stress-strain $\{(\boldsymbol{\varepsilon}^e, \boldsymbol{\sigma}^e)\}_{e=1}^M$ and couple stress-curvature $\{(\boldsymbol{\kappa}^e, \boldsymbol{\mu}^e)\}_{e=1}^M$. Collectively, we consider $\mathbf{z}^e = (\boldsymbol{\varepsilon}^e, \boldsymbol{\kappa}^e, \boldsymbol{\sigma}^e, \boldsymbol{\mu}^e)$ as a point in the local phase space Z^e, and $\mathbf{z} = \{\mathbf{z}^e\}_{e=1}^M$ as a point in the global phase space Z. The system is subject to the following discretized compatibility and equilibrium constraints (Equations 6.1-6.4):

$$\varepsilon_{ij}^e = \sum_\alpha \left(N_{,j}^{e\alpha} u_i^\alpha + \epsilon_{ijk} N^{e\alpha} \theta_k^\alpha\right), \qquad e = 1, \dots, M \tag{6.5}$$

$$\kappa_{ij}^e = \sum_\alpha N_{,j}^{e\alpha} \theta_i^\alpha, \qquad e = 1, \dots, M \tag{6.6}$$

$$\sum_{e=1}^M w_e \sigma_{ij}^e N_{,j}^{e\alpha} = f_i^\alpha, \qquad \alpha = 1, \dots, N \tag{6.7}$$

$$\sum_{e=1}^M w_e \left(\mu_{ij}^e N_{,j}^{e\alpha} + \epsilon_{ijk} \sigma_{jk}^e N^{e\alpha}\right) = m_i^\alpha, \qquad \alpha = 1, \dots, N \tag{6.8}$$

where N^{ea} is the shape function of node α evaluated at the material point e within an appropriate numerical approximation scheme (e.g. FEM), ϵ_{ijk} is the third-order permutation tensor, and $\{w_e\}_{e=1}^M$ are elements of volume. The set of global states satisfying the above constraints define the equilibrium set E.

The classical formulation of micropolar mechanics provides closure to the above equations by postulating constitutive relations of the form $\boldsymbol{\sigma}^e = \boldsymbol{\sigma}^e(\boldsymbol{\varepsilon}^e)$ and $\boldsymbol{\mu}^e = \boldsymbol{\mu}^e(\boldsymbol{\kappa}^e)$. On the contrary, the Data-Driven formulation of the problem consists of finding the global state $\mathbf{z}$ that satisfies the compatibility and equilibrium constraints and, at the same time, minimizes the distance to a given

material data set D. To this end, the local phase spaces Z_e are equipped with the following metric:

$$|\mathbf{z}^e| = \min_{\substack{\kappa,\lambda,\mu>0 \\ \alpha,\beta,\gamma>0}} \mathbb{C}^e(\kappa,\lambda,\mu)\,\boldsymbol{\varepsilon}^e\cdot\boldsymbol{\varepsilon}^e + \mathbb{D}^e(\alpha,\beta,\gamma)\,\boldsymbol{\kappa}^e\cdot\boldsymbol{\kappa}^e + \mathbb{C}^{e^{-1}}(\kappa,\lambda,\mu)\boldsymbol{\sigma}^e\cdot\boldsymbol{\sigma}^e + \mathbb{D}^{e^{-1}}(\alpha,\beta,\gamma)\,\boldsymbol{\mu}^e\cdot\boldsymbol{\mu}^e \tag{6.9}$$

where $\mathbb{C}e$, $\mathbb{D}^e$ are symmetric positive definite matrices, that are only introduced as a numerical scheme, and do not represent actual material behavior. We adopt here the isotropic micropolar elasticity tensors:

$$\mathbb{C}_{ijkl} = \lambda\delta_{ij}\delta_{kl} + (\mu+\kappa)\delta_{ik}\delta_{jl} + (\mu-\kappa)\delta_{il}\delta_{jk} \tag{6.10}$$

$$\mathbb{D}_{ijkl} = \alpha\delta_{ij}\delta_{kl} + (\gamma+\beta)\delta_{ik}\delta_{jl} + (\gamma-\beta)\delta_{il}\delta_{jk}. \tag{6.11}$$

By minimizing with respect to the coefficients defining the metric, then any nonlocal effects are optimally determined by the data. Under appropriate constraints on the material parameters ($\kappa,\mu,\beta,\gamma>0, \lambda>-2\mu/3, \alpha>-2\gamma/3$), it is straightforward to verify that the minimization problem of Eq. 6.9 is convex.

The above norm induces a metrization of the global phase space Z by means of the norm:

$$|\mathbf{z}| = \sum_{e=1}^{N} w_e|\mathbf{z}^e|.$$

The Data-Driven problem is then mathematically formulated as:

$$\begin{aligned} \min_{\mathbf{y}\in D} |\mathbf{z}-\mathbf{y}| \;\equiv\; \min_{\mathbf{z}\in D} |\mathbf{z}-\mathbf{y}| \\ \text{s.t. } \mathbf{z}\in E \qquad \text{s.t. } \mathbf{y}\in E. \end{aligned} \tag{6.12}$$

The compatibility constraints can be enforced by direct substitution, while the equilibrium constraints can be enforced by means of Lagrange multipliers, resulting in the stationary problem:

$$\begin{aligned} \delta\Bigg(&\sum_e w^e|z^e|\big(\sum_\alpha N^{e\alpha}_{,j}u^\alpha_i + \sum_\alpha \epsilon_{ijk}N^{e\alpha}\theta^\alpha_k, \sum_\alpha N^{e\alpha}_{,j}\theta^\alpha_i, \sigma^e_{ij}, \mu^e_{ij}\big) \\ &- \sum_\alpha\big(\sum_e w_e\sigma^e_{ij}N^{e\alpha}_{,j} - f^\alpha_i\big)\eta^\alpha_i \\ &- \sum_\alpha\big(\sum_e w_e(\mu^e_{ij}N^{e\alpha}_{,j} + \epsilon_{ijk}\sigma^e_{jk}N^{e\alpha} - m^\alpha_i\big)\zeta^\alpha_i\Bigg) = 0. \end{aligned} \tag{6.13}$$

Taking all possible variations, we obtain the following system of coupled Euler-Lagrange equations:

$$\delta u_i^\alpha \Rightarrow \sum_b \sum_e w_e \big(C^{e^*}_{ijkl} N^{e\alpha}_{,j} N^{eb}_{,l} u^b_k + C^{e^*}_{ijkl} N^{e\alpha}_{,j} N^{eb} \epsilon_{klm} \theta^b_m\big) = \sum_e w_e C^{e^*}_{ijkl} N^{e\alpha}_{,j} \varepsilon^{e^*}_{kl} \tag{6.14}$$

$$\delta \theta_i^\alpha \Rightarrow \sum_b \sum_e w_e \big(C^{e^*}_{ijkl} N^{e\alpha} N^{eb}_{,l} \epsilon_{ijm} u^b_k + \big(C^{e^*}_{ijkl} \epsilon_{ijm} \epsilon_{kln} N^{e\alpha} N^{eb} + D^{e^*}_{mjnl} N^{e\alpha}_{,j} N^{eb}_{,l}\big)\theta^b_n\big) = \sum_e w_e \big(C^{e^*}_{ijkl} \epsilon_{ijm} N^{e\alpha} \epsilon^{e^*}_{kl} + D^{e^*}_{mjkl} N^{e\alpha}_{,j} \kappa^{e^*}_{kl}\big) \tag{6.15}$$

$$\delta \sigma^e_{ij} \Rightarrow \big(C^{e*^{-1}}\big)_{ijkl} \big(\sigma^e_{kl} - \sigma^{e^*}_{kl}\big) = \sum_\alpha N^{e\alpha}_{,j} \eta^\alpha_i + \sum_\alpha \epsilon_{nij} N^{e\alpha} \zeta^\alpha_n \tag{6.16}$$

$$\delta \mu^e_{ij} \Rightarrow \big(D^{e*^{-1}}\big)_{ijkl} \big(\mu^e_{kl} - \mu^{e^*}_{kl}\big) = \sum_\alpha N^{e\alpha}_{,j} \zeta^\alpha_i \tag{6.17}$$

$$\delta \eta^a_i \Rightarrow \sum_e w_e N^{e\alpha}_{,j} \sigma^e_{ij} = f^\alpha_i \tag{6.18}$$

$$\delta \zeta^a_i \Rightarrow \sum_e w_e \big(\mu^e_{ij} N^{e\alpha}_{,j} + \epsilon_{ijk} \sigma^e_{jk} N^{e\alpha}\big) = m^\alpha_i \tag{6.19}$$

where $C^{e^*}_{ijkl} = C^e_{ijkl}(\kappa^*, \lambda^*, \mu^*)$ and $D^{e^*}_{ijkl} = D^e_{ijkl}(\kappa^*, \lambda^*, \mu^*)$ are the optimal metric tensors, and similarly, $\mathbf{z}^{e^*} = (\boldsymbol{\varepsilon}^{e^*}, \boldsymbol{\kappa}^{e^*}, \boldsymbol{\sigma}^{e^*}, \boldsymbol{\mu}^{e^*})$ are the optimal local data points in the data set D^e that result in the closest possible satisfaction of the constraints.

Eqs. (6.16)-(6.19) may be manipulated to yield two coupled equations for the Lagrange multipliers:

$$\sum_b \sum_e w_e \big(C^{e^*}_{ijkl} N^{eb}_{,j} N^{e\alpha}_{,l} \eta^b_i + C^{e^*}_{ijkl} \epsilon_{kij} N^{eb} N^{e\alpha}_{,l} \zeta^b_k\big) = f^\alpha_k - \sum_e w_e N^{e\alpha}_{,l} \sigma^{e^*}_{kl} \tag{6.20}$$

$$\sum_b \sum_e w_e D^{e^*}_{ijkl} N^{eb}_{,j} N^{e\alpha}_{,l} \zeta^b_i = m^\alpha_k - \sum_e w_e N^{e\alpha}_{,l} \mu^{e^*}_{kl} - \sum_e w_e \epsilon_{klm} \sigma_{lm} N^{e\alpha} \tag{6.21}$$

Further, Eqs. (6.16) and (6.21) can be combined to yield:

$$\sum_b \sum_e w_e \big(C^{e^*}_{ijkl} N^{e\alpha} N^{eb}_{,l} \epsilon_{ijm} \eta^b_k + \big(C^{e^*}_{ijkl} \epsilon_{ijm} \epsilon_{kln} N^{e\alpha} N^{eb} + D^{e^*}_{mjnl} N^{e\alpha}_{,j} N^{eb}_{,l}\big)\zeta^b_n\big) = m^\alpha_m - \sum_e w_e \big(N^{e\alpha}_{,l} \mu^{e^*}_{ml} + \epsilon_{mkl} N^{e\alpha} \sigma^{e^*}_{kl}\big). \tag{6.22}$$

Upon inspection, we obtain two standard micropolar elasticity problems: one in terms of $\mathbf{u}, \boldsymbol{\theta}$ as defined by Eqs. (6.14) and (6.15), and one in terms of $\boldsymbol{\eta}, \boldsymbol{\zeta}$ as defined by Eqs. (6.20) and (6.22).

6.3.1 Solution algorithm

The simplest Data-Driven solver involves the fixed point iteration:

$$\mathbf{z}^{(j+1)} = P_E P_D \mathbf{z}^{(j)} \tag{6.23}$$

where j is the iteration number, $P_D\mathbf{z}^{(j)}$ denotes the closest point projection onto D (i.e. finding the point in the material data set that is closest to $\mathbf{z}^{(j)}$), and $P_E\mathbf{y}^{(j)}$ denotes the projection of a fixed $\mathbf{y} \in D$ onto E. The algorithm converges when the local states remain unchanged under the closest point projection to the material data set. The solution algorithm is shown below.

Algorithm 5 Fixed-point solver

Require: Data sets D^e, Shape functions $N^{e\alpha}$, Applied forces f_i^α, Applied moments m_i^α

where $e=1,...,M$, $\alpha=1,...,N$, $i=1,2,3$

i) Set $j=0$. Initial local data assignment:

for all $e=1,...,M$ **do**

Choose $(\boldsymbol{\varepsilon}^{e^*,(0)}, \boldsymbol{\kappa}^{e^*,(0)}, \boldsymbol{\sigma}^{e^*,(0)}, \boldsymbol{\mu}^{e^*,(0)})$ randomly from D^e

Initialize metric tensors $\mathbb{C}^{e^*,(0)}, \mathbb{D}^{e^*,(0)}$

end for

ii) Solve coupled Equations (6.14), (6.15) for $u_i^{\alpha,(k)}$ and $\theta_i^{\alpha,(k)}$

Solve coupled Equations (6.20), (6.22) for $\eta_i^{\alpha,(k)}$ and $\zeta_i^{\alpha,(k)}$

iii) Compute local mechanical states:

for all $e=1,...,M$ **do**

Solve Equations (6.5), (6.6) for $\boldsymbol{\varepsilon}^{e,(j)}, \boldsymbol{\kappa}^{e,(j)}$

Solve Equations (6.16), (6.17) for $\boldsymbol{\sigma}^{e,(j)}, \boldsymbol{\mu}^{e,(j)}$

end for

iv) Assign local material states:

for all $e=1,...,M$ **do**

Choose $(\boldsymbol{\varepsilon}^{e^*,(j+1)}, \boldsymbol{\kappa}^{e^*,(j+1)}, \boldsymbol{\sigma}^{e^*,(j+1)}, \boldsymbol{\mu}^{e^*,(j+1)})$

closest to $(\boldsymbol{\varepsilon}^{e,(j)}, \boldsymbol{\kappa}^{e,(j)}, \boldsymbol{\sigma}^{e,(j)}, \boldsymbol{\mu}^{e,(j)})$ in D^e

Solve for optimal metric tensors $\mathbb{C}^{e^*,(j+1)}, \mathbb{D}^{e^*,(j+1)}$

end for

v) Test for convergence

if $(\boldsymbol{\varepsilon}^{e^*,(j+1)}, \boldsymbol{\kappa}^{e^*,(j+1)}, \boldsymbol{\sigma}^{e^*,(j+1)}, \boldsymbol{\mu}^{e^*,(j+1)}) = (\boldsymbol{\varepsilon}^{e^*,(j)}, \boldsymbol{\kappa}^{e^*,(j)}, \boldsymbol{\sigma}^{e^*,(j)}, \boldsymbol{\mu}^{e^*,(j)})$ **then**

Set $u_i^\alpha = u_i^{\alpha,(j)}$, $\theta_i^\alpha = \theta_i^{\alpha,(j)}$, $(\boldsymbol{\varepsilon}^e, \boldsymbol{\kappa}^e, \boldsymbol{\sigma}^e, \boldsymbol{\mu}^e) = (\boldsymbol{\varepsilon}^{e,(j)}, \boldsymbol{\kappa}^{e,(j)}, \boldsymbol{\sigma}^{e,(j)}, \boldsymbol{\mu}^{e,(j)})$

else

$j \leftarrow j+1$, **goto** ii)

end if

6.3.2 Numerical analysis of convergence

To study the convergence of the Data-Driven solver with respect to the size of the data set, we shall consider the problem of an isotropically stressed micropolar plate with a hole, as shown in Fig. 6.2 a). We will assume that the material behavior obeys an isotropic micropolar linear elastic law. Due to plane stress conditions, only a neighborhood of the subspace $\sigma_{13} = \sigma_{31} = \sigma_{23} = \sigma_{32} = \sigma_{33} = \mu_{11} = \mu_{12} = \mu_{21} = \mu_{22} = \mu_{31} = \mu_{32} = \mu_{33} = 0$ needs to be covered by the data [97]. Hence, we sample the 6-dimensional hypercube covering an appropriate region $(\sigma_{11}, \sigma_{12}, \sigma_{21}, \sigma_{22}, \mu_{31}, \mu_{32})$ in phase space with a uniform grid. The corresponding strains and curvatures follow from isotropic linear elasticity. We first solve the problem classically and, then, also solve the problem using the Data-Driven solver with different discretizations along each dimension of the hypercube, corresponding to different data set cardinalities $|D| \in [1, 10^7]$. With finer data sets, we visually inspect the convergence the Data-Driven solution to the classical solution, for example in the case of rotations (cf. Fig. 6.2 b), c)).

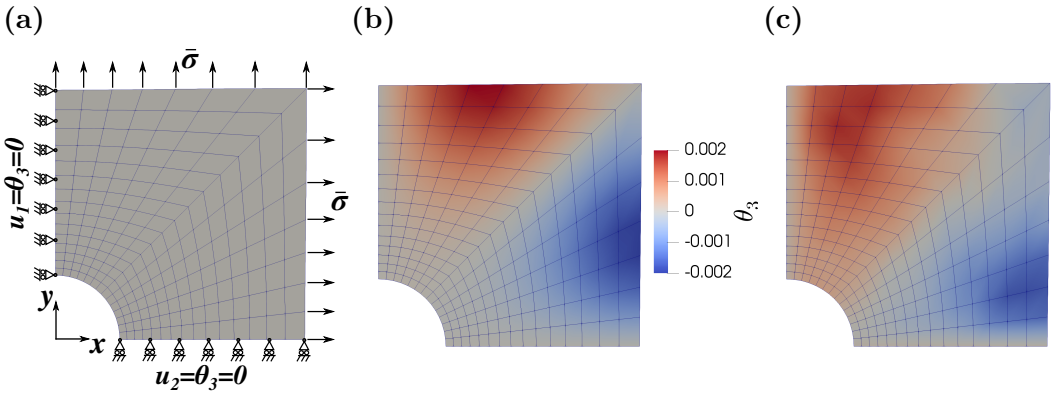

Figure 6.2: Micropolar plate with a hole: a) Simulation setup. b) Reference rotation field corresponding to the classical solution (FEM). c) Rotation field corresponding to the Data-Driven solution with a data set size $|D| = 10^6$.

Fig. 6.3 a) shows the reduction of the global distance between equilibrium set and the material data set as a function of the size of the data set. We find that the global distance decreases in the form of a power law with an exponent of 2.45. The convergence of the Data-Driven solution to the reference (classical) solution is shown Fig. 6.3 b), where we plot two root mean square (RMS) error

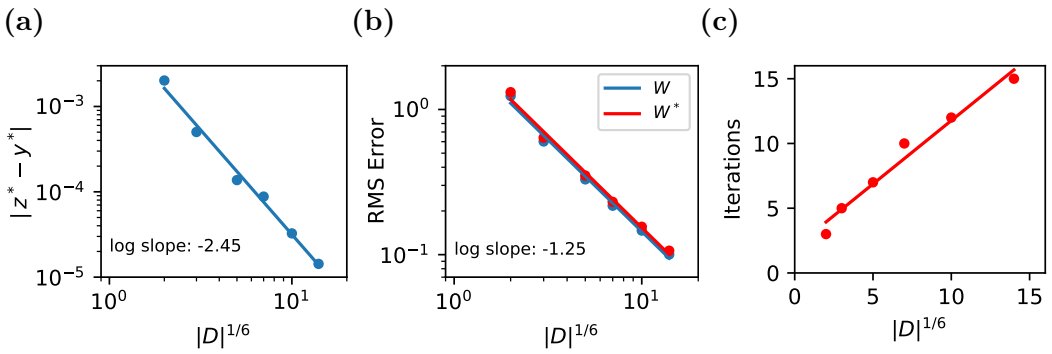

Figure 6.3: Results of convergence analysis: a) Global distance between constraint manifold and material data set plotted as a function of the number of data points in each dimension. b) Number of iterations until convergence plotted as a function of the number of data points in each dimension.

metrics defined as [172]:

$$RMS_W = \left(\frac{\sum_e w_e W(\boldsymbol{\varepsilon} - \boldsymbol{\varepsilon}^{\text{ref}}, \boldsymbol{\kappa} - \boldsymbol{\kappa}^{\text{ref}})}{\sum_e w_e W(\boldsymbol{\varepsilon}^{\text{ref}}, \boldsymbol{\kappa}^{\text{ref}})} \right)^{1/2} \tag{6.24}$$

$$RMS_{W^*} = \left(\frac{\sum_e w_e W^*(\boldsymbol{\sigma} - \boldsymbol{\sigma}^{\text{ref}}, \boldsymbol{\mu} - \boldsymbol{\mu}^{\text{ref}})}{\sum_e w_e W^*(\boldsymbol{\sigma}^{\text{ref}}, \boldsymbol{\mu}^{\text{ref}})} \right)^{1/2} \tag{6.25}$$

where W is the energy density and W^* is the complementary energy. We observe that the convergence is superlinear and, most importantly, the error is equally split between kinematics (W) and their conjugate kinetics (W^*), as a result of the novel distance measure of Eq. 6.9. Finally, Fig. 6.3 c) shows that the number of fixed point iterations required until convergence approximately coincides with the number of data points along each dimension of the uniformly sampled data set.

6.4 Extension to inelasticity

Practical applications of Data-Driven computing often concern inelastic materials, whose behavior is history dependent and irreversible. To extend the Data-Driven micropolar framework to inelasticity, we shall restrict our attention to a time-discrete formulation. Following [167], the Data-Driven problem of at time t_{k+1} transforms to:

$$\min_{\mathbf{y}_{k+1} \in D_{k+1}} |\mathbf{z}_{k+1} - \mathbf{y}_{k+1}| \equiv \min_{\mathbf{z}_{k+1} \in D_{k+1}} |\mathbf{z}_{k+1} - \mathbf{y}_{k+1}| \tag{6.26}$$

$$\text{s.t. } \mathbf{z}_{k+1} \in E_{k+1} \qquad \text{s.t. } \mathbf{y}_{k+1} \in E_{k+1}$$

where $\mathbf{z}_{k+1} = \{\mathbf{z}^e_{k+1}\}^M_{e=1} \in Z$ and $\mathbf{z}^e_{k+1} = (\boldsymbol{\varepsilon}^e_{k+1}, \boldsymbol{\kappa}^e_{k+1}, \boldsymbol{\sigma}^e_{k+1}, \boldsymbol{\mu}^e_{k+1})$. The time-dependent constraint set E_{k+1} arises from the time-dependent applied forces $\mathbf{f}_{k+1}$ and moments $\mathbf{m}_{k+1}$. Accordingly, the behavior at a material point is described by a material data set D^e_{k+1} of points that is attainable at time t_{k+1} given its past local history of deformation:

$$D^e_{k+1} = \{(\boldsymbol{\varepsilon}^e_{k+1}, \boldsymbol{\sigma}^e_{k+1}, \boldsymbol{\kappa}^e_{k+1}, \boldsymbol{\mu}^e_{k+1}) \,|\, \text{past history}\}. \tag{6.27}$$

The global material data set then follows as:

$$D_{k+1} = D^1_{k+1} \times \ldots \times D^M_{k+1}. \tag{6.28}$$

The fixed point Data-Driven solver now takes the form:

$$\mathbf{z}^{(j+1)}_{k+1} = P_{E_{k+1}} P_{D_{k+1}} \mathbf{z}^{(j)}_{k+1} \tag{6.29}$$

representing a time-dependent extension of Eq. 6.23. From the solution of the Euler-Lagrange equations (Eqs (6.14),(6.15), 6.20,6.22), now arise the time-discrete field variables $\mathbf{u}_{k+1}, \boldsymbol{\theta}_{k+1}$ and Lagrange mutipliers $\boldsymbol{\eta}_{k+1}, \boldsymbol{\zeta}_{k+1}$.

It becomes clear that the main challenge is the parametrization of material history, as we deal with evolving material data sets. In previous works, various representational paradigms have been explored including the hereditary/history functional and the internal variable formalism [92], as well as the thermodynamically-motivated energy-based representation [167]. Adopted in this work is the latter which is material-independent and universal.

To effect the energy-based history parametrization, we augment the phase space with the free energy $\mathcal{A}$ and dissipation $\mathcal{D}$, and consider their implicit relation with the remaining state variables $\boldsymbol{\epsilon}, \boldsymbol{\sigma}, \boldsymbol{\kappa}, \boldsymbol{\mu}$. This relation is furnished by the principle of conservation of energy and the second principle (Clausius-Plank inequality):

$$\dot{\mathcal{D}} = \boldsymbol{\sigma} : \dot{\boldsymbol{\epsilon}} + \boldsymbol{\mu} : \dot{\boldsymbol{\kappa}} - \dot{\mathcal{A}} \geq 0 \tag{6.30}$$

or in a local, time-discrete setting:

$$\mathcal{D}^e_{k+1} - \mathcal{D}^e_k = \frac{\boldsymbol{\sigma}^e_k + \boldsymbol{\sigma}^e_{k+1}}{2} : (\boldsymbol{\epsilon}^e_{k+1} - \boldsymbol{\epsilon}^e_k) + \frac{\boldsymbol{\mu}^e_k + \boldsymbol{\mu}^e_{k+1}}{2} : (\boldsymbol{\kappa}^e_{k+1} - \boldsymbol{\kappa}^e_k) - (\mathcal{A}^e_{k+1} - \mathcal{A}^e_k) \geq 0. \tag{6.31}$$

The local material data set at time t_{k+1} is then formalized as:

$$D^e_{k+1} = \{(\boldsymbol{\epsilon}^e_{k+1}, \boldsymbol{\sigma}^e_{k+1}, \boldsymbol{\kappa}^e_{k+1}, \boldsymbol{\mu}^e_{k+1}) \,|\, (\boldsymbol{\epsilon}^e_k, \boldsymbol{\sigma}^e_k, \boldsymbol{\kappa}^e_k, \boldsymbol{\mu}^e_k), (6.30)\}. \tag{6.32}$$

The above relation states that the admissible stress-strain pairs at time t_{k+1} are those that are thermodynamically consistent with the material state at time t_k. The special case where $\mathcal{D}^e_{k+1} - \mathcal{D}^e_k = 0$ defines a bounded equilibrium set (or elastic domain) on the augmented phase space.

6.5 Application to granular materials

6.5.1 Micropolar homogenization

Granular materials are excellent candidates for exploring the performance of the Data-Driven framework given their nonlocal and history-dependent behavior [168, 165]. Adopting the thermodynamics-based history representation requires access to the generalized state variables in Eq. 6.31. Indeed, each of these variables are micromechanically accessible. Assuming quasistatic conditions, the average stress is given by the well-established Love-Christoffersen expression [68]:

$$\bar{\boldsymbol{\sigma}} = \frac{1}{V} \sum_{c \in \mathcal{R}^c} \mathbf{f}^c \otimes \mathbf{l}^c \tag{6.33}$$

where the summation runs over the set of contacts $\mathcal{R}^c$ in a granular assembly or representative volume element (RVE), $\mathbf{f}^c$ is the contact force, and $\mathbf{l}^c$ is the contact branch vector (Fig 6.4).

On the other hand, the homogenized couple stress may be obtained in a body-integral form through coarse graining [128], or in a more computationally tractable manner through a surface integral form utilizing Hashin's homogenization principle [94]:

$$\bar{\boldsymbol{\mu}} = \frac{1}{V} \sum_{c \in \partial\mathcal{R}^c} (\mathbf{l}^c \times \mathbf{f}^c) \otimes \mathbf{x}^{p(c)} \tag{6.34}$$

where $\mathbf{x}^{p(c)}$ denotes the position of the center of the particle of the RVE boundary corresponding to contact c with respect to the RVE centroid, and $\partial\mathcal{R}^c$ denotes the set of contacts of the RVE boundary particles with exterior particles. Note that couple stresses naturally arise from the eccentricity of contact

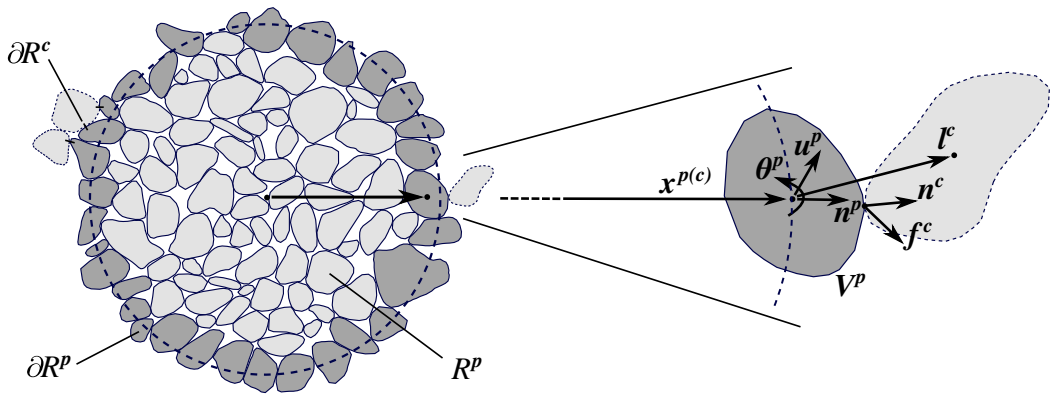

Figure 6.4: Representative volume element for a granular assembly.

forces. The average strain $\bar{\boldsymbol{\epsilon}}$ may be obtained through the homogenization of the displacement gradient and microrotation [94]:

$$\bar{\varepsilon} = \overline{\nabla \mathbf{u}} + \boldsymbol{\epsilon} \cdot \bar{\boldsymbol{\theta}} = \frac{1}{V}\Big(\sum_{p \in \partial \mathcal{R}^p} \mathbf{u}^p \otimes \mathbf{n}^p + \boldsymbol{\epsilon} \cdot \sum_{p \in \mathcal{R}^p} \boldsymbol{\theta}^p V^p \Big) \tag{6.35}$$

where $\mathcal{R}^p$, $\partial \mathcal{R}^p$ represent the set of RVE interior and boundary particles, respectively.

Analogously, the homogenized curvature is given by:

$$\bar{\kappa} = \overline{\nabla \boldsymbol{\theta}} = \frac{1}{V} \sum_{p \in \partial \mathcal{R}^p} \boldsymbol{\theta}^p \otimes \boldsymbol{n}^p \tag{6.36}$$

where $\mathbf{n}^p$ is the outward oriented normal vector on the RVE at the center of bounding particle p.

Assuming kinematically and statically admissible boundary conditions for the RVE, the micropolar Hill-Mandel macrohomogeneity condition [202] is satisfied, allowing us to write:

$$\overline{d\mathcal{D}} = \bar{\boldsymbol{\sigma}} : d\bar{\boldsymbol{\epsilon}} + \bar{\boldsymbol{\mu}} : d\bar{\boldsymbol{\kappa}} - \overline{d\mathcal{A}} \tag{6.37}$$

where $\overline{d\mathcal{D}}$ derives from frictional contact dissipation [167]:

$$\overline{d\mathcal{D}} = \frac{1}{V} \sum_c \mathbf{f}_t^c \cdot d\mathbf{u}^{c,slip} \tag{6.38}$$

where $d\mathbf{u}^{c,slip} = (\mathbf{f}_t^{c,t} - \mathbf{f}_t^{c,t+dt})/k_t$.

Finally, the free energy is due to the deformation of contacts under normal and tangential loading:

$$\bar{\mathcal{A}} = \frac{1}{2V} \sum_c \left(\frac{\|\mathbf{f_n^c}\|^2}{k_n} + \frac{\|\mathbf{f_t^c}\|^2}{k_t} \right) \tag{6.39}$$

where $\mathbf{f}_n^c = (\mathbf{f}^c \cdot \mathbf{n}^c)\,\mathbf{n}^c$ is the normal component of the contact force, $\mathbf{f}_t^c = \mathbf{f}^c - \mathbf{f}_n^c$ is the tangential component, and k_n, k_t are the normal and tangential contact stiffness, respectively. It is implied that particle morphology is fully resolved such that the contact interaction occurs through distributed contact forces and in the absence of contact moments.

6.5.2 Shear banding in triaxial compression of sand

One of the most studied aspects of nonlocality in granular materials is shear banding. Perhaps the most important breakthrough in understanding and modeling shear bands was the observation that rotational motion governs the bands' formation and dissipative properties [255, 253]. This, in turn, inspired the development of micropolar constitutive models typically within the framework of plasticity [239, 336]. While these models have been relatively successful in regularizing the shear banding problem, they are also subject to significant limitations. These relate more generally to the issue of defining and calibrating appropriate length scales and internal variables, but also to more specific challenges such as capturing the mechanisms of both homothetic and antithetic rotations governing the nonaffine kinematics within a localized band [9].

In this section, we utilize the history-dependent version of the micropolar Data-Driven framework to model shear banding of a triaxially compressed cylindrical specimen of Hostun sand. In a previous study, an in-situ triaxial experiment was carried out on such a specimen within an XRCT scanner [16]. The specimen is encased in a flexible membrane allowing it to be subjected to radial cell pressure, while a platen in contact with the top part of the specimen enforces a vertical compression. The specimen is first compressed isotropically to 100 kPa, and then compressed triaxially by keeping the cell pressure constant while prescribing a vertical displacement to the platen under quasistatic conditions. Failure eventually occurs through the formation of a shear band. The experiment was later modelled in a one-to-one fashion using the Level-Set Discrete Element Method (LS-DEM) [169]. For each physical grain in the sample, an equivalent virtual grain was generated through a level set imaging algorithm. The resulting virtual specimen was, then, subjected to the same boundary conditions by modeling the membrane as well as the kinematics of the platen. LS-DEM was able to capture both the onset and spatiotemporal evolution of the shear band [169]. We refer to [16, 169] for

details on the experiments and simulations, respectively.

We now simulate the experiment using the Data-Driven framework, where spatial discretization of the problem is achieved with a finite element mesh (Fig. 6.5). The required material data are directly gleaned from the LS-DEM calculation in a self-consistent manner. More specifically, the LS-DEM specimen is spatiotemporally sampled to produce data sets of stress, strain, couple stress, curvature, internal energy, and dissipation, in accordance with Section 6.5.1. This is achieved by superimposing the finite element mesh on the discrete element assembly, to associate subassemblies (RVEs) to their nearest material point (Gauss integration point). The data sets are initially assigned to each material point in the Data-Driven model by randomly sampling from the available data sets of similar initial packing fraction to the true material data set sampled from that material point. This sampling procedure informs the model about the initial heterogeneous structure (to aid the onset of localization in a comparable pattern), but also introduces some randomness in the initial assignment. The Data-Driven calculation is carried out for both a coarse and a fine mesh, composed of 6144 and 14784 material points, respectively. We find that the algorithm is able to make correct associations and transitions between the available data sets, informed by the evolving boundary conditions and the evolving thermodynamically-constrained local material data sets. Fig. 6.5 shows the resulting rotation fields in the LS-DEM and fine-mesh Data-Driven calculation, showing good agreement.

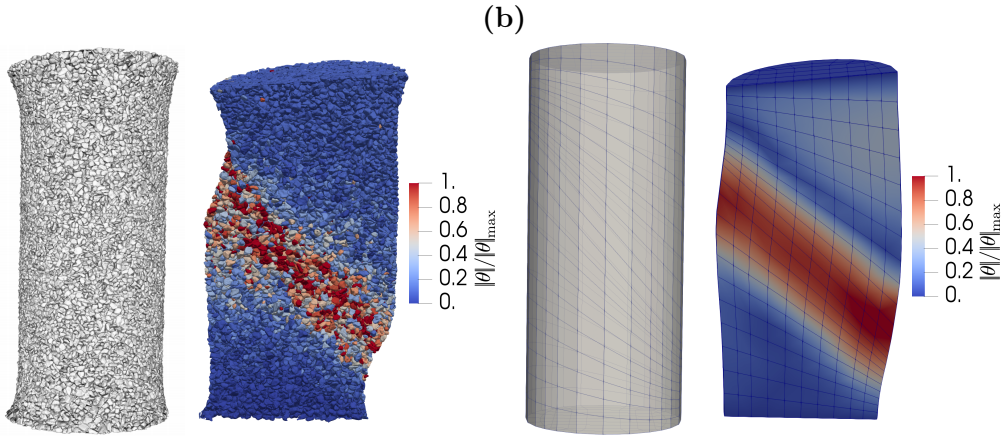

Figure 6.5: Undeformed cylindrical specimen and its deformed localized cross-section in the case of a) LS-DEM simulation, and b) Data-Driven FEM calculation. Colors indicate contours of normalized rotation magnitude.

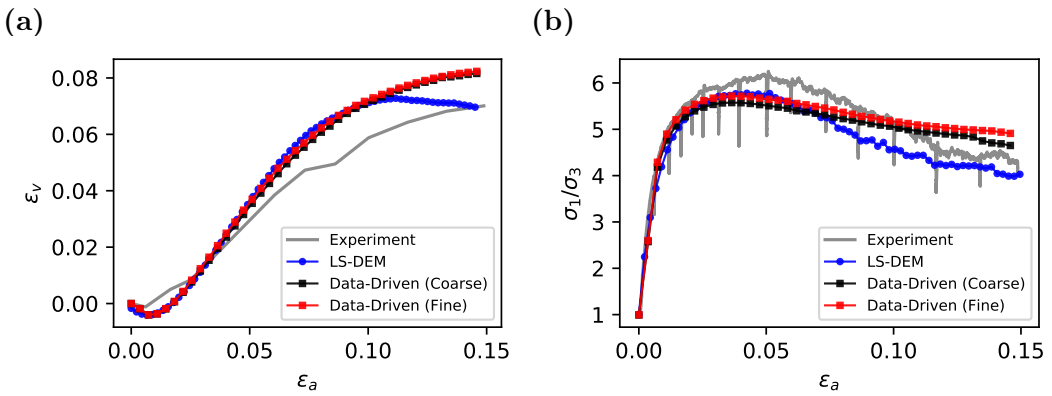

Figure 6.6: Comparison between experiment, LS-DEM simulation, and Data-Driven prediction in terms of a) axial strain vs volumetric strain, and b) axial strain vs principal stress ratio.

Figures 6.6 a) and b) compare the volumetric response and principal stress ratio, respectively, obtained in the experiment, LS-DEM simulation, and Data-Driven computation, all showing reasonably good agreement. In particular, the coincidence of the coarse- and fine-mesh Data-Driven solutions verifies the mesh-insensitivity of the approach in the post-localized regime. Finally, Fig. 6.7 shows the normalized rotation magnitude as a function of the distance from the shear band (in multiples of median particle diameter), as measured in the LS-DEM and Data-Driven computations. An excellent fit is obtained, indicating that this characteristic length scale is correctly encoded in the material data sets.

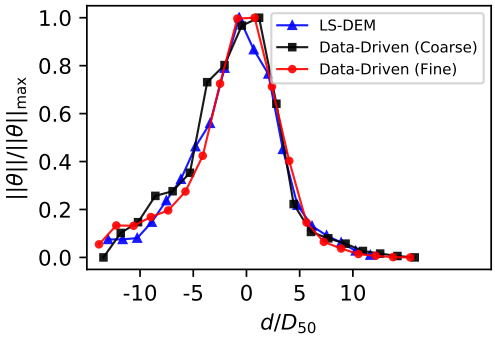

Figure 6.7: Rotation magnitude plotted against the distance from the shear band center d normalized by the median particle diameter D_{50}.

Remark:

We refer to [167] for an example of Data-Driven phase space sampling for simple continua where material data sets are obtained from independent unit cell calculations instead of the target boundary value problem itself. Such an approach can also be extended to micropolar continua by introducing appropriate generalized boundary conditions on the unit cell, which satisfy the micropolar Hill-Mandel conditions [202].

6.6 Conclusions

We presented a Data-Driven paradigm for the mechanical analysis of generalized continua that accounts for nonlocality arising from the material microstructure. We focused on the micropolar continuum; yet, any other formulation within the taxonomy of weakly nonlocal continua (e.g. second-gradient, micromorphic) is readily addressable. By formulating the problem on a phase space augmented by higher-order kinematics and their conjugate kinetics, we bypass the need to define an internal length scale, in stark contrast with the conventional approach based on constitutive modeling. In fact, the framework is entirely parameter-free owing to the introduction of a novel distance measure in phase space. The framework's extension to history-dependent behavior was achieved in a thermodynamically consistent manner by further augmenting the phase space with the free energy and dissipation. In terms of applications, we first considered the problem of a micropolar plate with a hole, which we used as a benchmark to verify the framework's improved convergence properties due to the incorporation of this new distance measure and despite the involvement of higher order gradients. A second application featured the shear banding problem of a specimen of sand subjected to triaxial compression. The material database was populated through micropolar homogenization of micromechanical LS-DEM calculations, which provides an example of application of the Data-Driven approach in a multiscale analysis mode. Evidently, the data set can also comprise experimental data in addition to micromechanical data. We emphasize that strict reliance on fundamental data (stress and strain) makes it possible to merge data sets from various provenances, which facilitates building up and disseminating data repositories.

Chapter 7

CONCLUSIONS AND OUTLOOK

7.1 Main findings

In this thesis, we have introduced novel theoretical and computational approaches for predicting the history-dependent — local and nonlocal — behavior of granular solids. Naturally arising in this study is the concept of a granular genome, which incorporates grain-scale properties, and expresses itself to an assembly-scale state. The latter is, in turn, mapped to an attainable continuum behavior. To enable this mapping, a number of complementary methodologies are developed, including homogenization methods, data-driven computing, and complex network analysis. After a meticulous review of the state-of-the-art, we embark on a four-pronged research approach.

In Chapter 3, we present a framework for *in-silico* stress probing experiments, designed to reveal the nature of incremental constitutive equations, formulated within plasticity theory. By relying on the Level-Set Discrete Element Method, we systematically probe different directions in stress space originating from the same initial state. We specifically study assemblies of sand particles, characterized by X-ray computed tomography, as well as morphologically simpler counterparts of the same systems. We extract and analyze the anisotropic elasticity, elastic-reversible coupling, yielding, plastic flow, and the evolution of internal variables as a function of genome and state. More specifically, in the context of classical plasticity, we find that the yield surface departs from the best available description in terms of the Lade-Duncan locus, and we accurately quantify the nonassociativity and irregularity of the flow rule. Within hyperplasticity, we characterize the change in internal energy and dissipation as a function of probing direction and state. Finally, we quantify the incremental evolution of several novel descriptors of fabric, including the weak force, strong force, and fluctuation fabric. All the above are essential ingredients of a new generation of constitutive theories.

In Chapter 4, we depart from the conventional modeling approach, and introduce a multiscale Data-Driven paradigm that completely bypasses the need to define a constitutive law. The problem is formulated as a distance minimiza-

tion between a material data set and an equilibrium manifold. Two major challenges are identified and addressed: phase space sampling and history parametrization. Optimal phase space sampling is achieved through grain-scale computations, which are carried out either offline or on-the-fly. We also develop two history parametrizations, one thermodynamics-based and material-independent, and one statistically-informed and tailored to granular materials. We find that both parametrizations perform well both in nonmonotonic material point simulations and complex boundary value problems, such as the rupture through a dense layer of sand.

In Chapter 5, we turn our attention to understanding and modeling nonlocal aspects of granular material behavior. Using complex networks, we analyze a sample of angular sand undergoing shear banding, a prototypical failure mode governed by nonlocal effects. We particularly focus on revealing the cooperative evolution of topology, nonaffine kinematics and their conjugate kinetics. Regarding topology, we find that force cycles, up to 6 particles long, govern the onset and evolution of shear banding. This finding contradicts earlier topological studies on spherical assemblies, hinting on the importance of the granular genome. A new topological measure, termed minimal cycle coefficient, is introduced, which serves as an order parameter for the system. In terms of kinematics, we analyze the size, strength, and orientation of vortex clusters within the shear band. This vorticity, which is accompanied with intense particle rotation, furnishes a complete model of nonaffine kinematics. Finally, we study the stability of force chains as a function of neighborhood topology and kinematics. We find that buckling force chains arise at regions of low average minimal cycle coefficient and high average rotation, and at the edge of vortices.

Finally, in Chapter 6, driven by our observations of the importance of higher-order kinematics, we extend the Data-Driven paradigm to the class of weakly nonlocal continua. In particular, we focus on the micropolar continuum, in which the material point is endowed with rotational degrees of freedom beyond the translational ones of the standard Cauchy continuum. This leads to a coupled Data-Driven formulation on a phase space augmented with curvature and couple stress. The extension also features a new distance measure that improves the convergence properties of the original scheme, and renders it entirely parameter-free. We show that, in this extended framework, the internal

length scale of a shear banding problem is successfully encoded in the material data set. This is verified by accurately capturing the post-localized softening response of an *in-situ* triaxial experiment in a mesh-insensitive manner.

7.2 Outlook

A number of possibilities for future work arise as a result of this work. Regarding the first part of the thesis, the constitutive behavior can be probed within a wider range of states than those investigated, for instance under rotated principal stress states, which is important in many applications. Another obvious way forward is the incorporation of the acquired information about elasticity, coupling, flow, and hardening into a complete theory of plasticity. Within the multiscale Data-Driven approach, it is worthwhile addressing the dynamic (rate-dependent) and finite deformation regime, which would allow us to tackle a wider range of interesting problems involving granular materials. Addiitionally, the potential for using machine learning techniques to improve the convergence properties of the method while relying on smaller data sets is very promising. Similarly, the consideration of noisy history-dependent data sets, merged from various provenances, would help improve the accuracy of the approach.

Moving to the nonlocal part of the thesis, several questions remain with respect to incorporating our complex network-derived observations to a complete nonlocal continuum theory. For instance, the proposed minimal cycle coefficient can be used as an order parameter within a Landau-type theory. This would require additional analysis to study its diffusive spatial coupling and relation to local rheology. In the last part of the study, regarding the extended Data-Driven framework, the obvious way forward is to develop the theory for other types of media beyond micropolar, such as strain gradient and micromorphic media. This would open up many opportunities for modeling a wider range of microstructured materials.

To conclude, the methodologies developed here are not tied to granular materials, but can also be used for other families of materials that exhibit a regime of rate-independent behavior, and for which lower-scale simulation is possible and efficient. This includes glass, foams, gels, and other materials. Moreover, the capability to understand and predict material behavior naturally paves the way to engineer a desired behavior. For example, our study enables the design

of granular shape and mechanical properties (granular genome) to target a desired stress-strain response. In this pursuit, machine learning and data-driven methods such as those developed herein will likely prove very useful.

BIBLIOGRAPHY

[1] S. Abedi, A.L. Rechenmacher, and A.D. Orlando. "Vortex formation and dissolution in sheared sands". In: *Granular Matter* 14.6 (2012), pp. 695–705.

[2] Farid F. Abraham et al. "Instability dynamics in three-dimensional fracture: An atomistic simulation". In: *Journal of the Mechanics and Physics of Solids* 45.9 (1997), pp. 1461–1471.

[3] I. Agnolin and J.-N. Roux. "Internal states of model isotropic granular packings. I. Assembling process, geometry, and contact networks". In: *Physical Review E* 76 (2007), p. 061302.

[4] I. Agnolin and J.-N. Roux. "Internal states of model isotropic granular packings. III. Elastic properties". In: *Physical Review E* 76 (2007), p. 061304.

[5] I. Agnolin and J.-N. Roux. "On the elastic moduli of three-dimensional assemblies of spheres: Characterization and modeling of fluctuations in the particle displacement and rotation". In: *International Journal of Solids and Structures* 45.3 (2008), pp. 1101–1123.

[6] Jun Ai et al. "Assessment of rolling resistance models in discrete element simulations". In: *Powder Technology* 206.3 (2011), pp. 269–282.

[7] E.C. Aifantis. "On the microstructural origin of certain inelastic models". In: *Journal of Engineering Materials and Technology* 106.4 (1984), pp. 326–330.

[8] E.C. Aifantis. "On the role of gradients in the localization of deformation and fracture". In: *International Journal of Engineering Science* 30.10 (1992), pp. 1279–1299.

[9] F. Alonso-Marroquín et al. "Effect of rolling on dissipation in fault gouges". In: *Physical Review E* 74 (2006), p. 031306.

[10] F. Alonso-Marroquín et al. "Role of anisotropy in the elastoplastic response of a polygonal packing". In: *Physical Review E* 71 (2005), p. 051304.

[11] M.I. Alsaleh, G.Z. Voyiadjis, and K.A. Alshibli. "Modelling strain localization in granular materials using micropolar theory: mathematical formulations". In: *International Journal for Numerical and Analytical Methods in Geomechanics* 30.15 (2006), pp. 1501–1524.

[12] K.A. Alshibli, M.I. Alsaleh, and G.Z. Voyiadjis. "Modelling strain localization in granular materials using micropolar theory: Numerical implementation and verification". In: *International Journal for Numerical and Analytical Methods in Geomechanics* 30.15 (2006), pp. 1525–1544.

[13] A. Anandarajah, K. Sobhan, and N. Kuganenthira. "Incremental stress-strain behavior of granular soil". In: *Journal of Geotechnical Engineering* 121.1 (1995), pp. 57–68.

[14] I. Anastasopoulos et al. "Fault rupture propagation through sand: Finite-element analysis and validation through centrifuge experiments". In: *Journal of Geotechnical and Geoenvironmental Engineering* 133.8 (2007), pp. 943–958.

[15] E. Andò et al. "Experimental micro-mechanics of granular media studied by x-ray tomography: Recent results and challenges". In: *Géotechnique Letters* 3.3 (2013), pp. 142–146.

[16] E. Andò et al. "Grain-scale experimental investigation of localised deformation in sand: a discrete particle tracking approach". In: *Acta Geotechnica* 7.1 (2012), pp. 1–13.

[17] J. E. Andrade and R. I. Borja. "Capturing strain localization in dense sands with random density". In: *International Journal for Numerical Methods in Engineering* 67.11 (2006), pp. 1531–1564.

[18] J. E. Andrade and X. Tu. "Multiscale framework for behavior prediction in granular media". In: *Mechanics of Materials* 41.6 (2009). Advances in the Dynamics of Granular Materials, pp. 652–669.

[19] J. E. Andrade et al. "On the rheology of dilative granular media: Bridging solid- and fluid-like behavior". In: *Journal of the Mechanics and Physics of Solids* 60.6 (2012), pp. 1122–1136.

[20] José E. Andrade and Carlos F. Avila. "Granular Element Method (GEM): Linking inter-particle forces with macroscopic loading". In: *Granular Matter* 14.1 (2012), pp. 51–61.

[21] I.S. Aranson and L.S. Tsimring. "Continuum description of avalanches in granular media". In: *Physical Review E* 64 (2001), p. 020301.

[22] Roberto Arévalo, Iker Zuriguel, and Diego Maza. "Topology of the force network in the jamming transition of an isotropically compressed granular packing". In: *Physical Review E* 81 (2010), p. 041302.

[23] ASTM International. "ASTM D4254-16, Standard Test Methods for Minimum Index Density and Unit Weight of Soils and Calculation of Relative Density". In: *West Conshohocken, PA* (2016).

[24] ASTM International. "Standard test methods for maximum index density and unit weight of soils using a vibratory table". In: *West Conshohocken, PA* (2006).

[25] K. Bagi. "Analysis of microstructural strain tensors for granular assemblies". In: *International Journal of Solids and Structures* 43.10 (2006), pp. 3166–3184.

[26] K. Bagi. “Stress and strain in granular assemblies”. In: *Mechanics of Materials* 22.3 (1996), pp. 165–177.

[27] J. P. Bardet and J. Proubet. “A numerical investigation of the structure of persistent shear bands in granular media”. In: *Géotechnique* 41.4 (1991), pp. 599–613.

[28] J.P. Bardet. “Numerical simulations of the incremental responses of idealized granular materials”. In: *International Journal of Plasticity* 10.8 (1994), pp. 879–908.

[29] J.P. Bardet and I. Vardoulakis. “The asymmetry of stress in granular media”. In: *International Journal of Solids and Structures* 38.2 (2001), pp. 353–367.

[30] Danielle S. Bassett et al. “Extraction of force-chain network architecture in granular materials using community detection”. In: *Soft Matter* 11 (2015), pp. 2731–2744.

[31] Richard J. Bathurst and Leo Rothenburg. “Observations on stress-force-fabric relationships in idealized granular materials”. In: *Mechanics of Materials* 9.1 (1990), pp. 65–80.

[32] Paul T. Bauman et al. “On the application of the Arlequin method to the coupling of particle and continuum models”. In: *Computational Mechanics* 42.4 (2008), pp. 511–530.

[33] Z. Bazant, T. Belytschko, and T. Chang. “Continuum theory for strain–softening”. In: *Journal of Engineering Mechanics* 100.12 (1984), pp. 1666–1692.

[34] K. Been and M. G. Jefferies. “A state parameter for sands”. In: *Géotechnique* 35.2 (1985), pp. 99–112.

[35] Robert P Behringer and Bulbul Chakraborty. “The physics of jamming for granular materials: A review”. In: *Reports on Progress in Physics* 82.1 (2018), p. 012601.

[36] D. Bigoni and T. Hueckel. “Uniqueness and localization: I. Associative and non-associative elastoplasticity”. In: *International Journal of Solids and Structures* 28.2 (1991), pp. 197–213.

[37] M. D. Bolton. “The strength and dilatancy of sands”. In: *Géotechnique* 36.1 (1986), pp. 65–78.

[38] T. Börzsönyi et al. “Shear-induced alignment and dynamics of elongated granular particles”. In: *Physical Review E* 86 (2012), p. 051304.

[39] J.-P. Bouchaud et al. “Force chain splitting in granular materials: A mechanism for large-scale pseudo-elastic behaviour”. In: *European Physical Journal E* 4.4 (2001), pp. 451–457.

[40] M. Bouzid et al. “Non-local rheology in dense granular flows”. In: *The European Physical Journal E* 38.11 (2015), pp. 1–15.

[41] Jeremy Q. Broughton et al. “Concurrent coupling of length scales: Methodology and application”. In: *Phys. Rev. B* 60 (1999), pp. 2391–2403.

[42] Eric Brown et al. “Universal robotic gripper based on the jamming of granular material”. In: *Proceedings of the National Academy of Sciences* 107.44 (2010), pp. 18809–18814.

[43] W. Michael Brown et al. “Algorithmic dimensionality reduction for molecular structure analysis.” In: *Journal of Chemical Physics* 129.6 (2008), p. 064118.

[44] R. Buarque de Macedo, J. P. Marshall, and J. E. Andrade. “Granular object morphological generation with genetic algorithms for discrete element simulations”. In: *Granular Matter* 20.4 (2018), p. 73.

[45] V. Bulatov et al. “Connecting atomistic and mesoscale simulations of crystal plasticity”. In: *Nature* 391.6668 (1998), pp. 669–672.

[46] Caldarelli, G., Pastor-Satorras, R., and Vespignani, A. “Structure of cycles and local ordering in complex networks”. In: *European Physical Journal B* 38.2 (2004), pp. 183–186.

[47] F. Calvetti, G. Combe, and J. Lanier. “Experimental micromechanical analysis of a 2D granular material: relation between structure evolution and loading path”. In: *Mechanics of Cohesive-frictional Materials* 2.2 (1997), pp. 121–163.

[48] F. Calvetti, G. Viggiani, and C. Tamagnini. “A numerical investigation of the incremental behavior of granular soils”. In: *Rivista Italiana di Geotecnica* 37 (2003), pp. 11–29.

[49] F. Calvetti, G. Viggiani, and C. Tamagnini. “Micromechanical inspection of constitutive modelling”. In: *Constitutive Modelling and Analysis of Boundary Value Problems in Geotechnical Engineering. Napoli, Italy* (2003), pp. 187–216.

[50] B. Cambou. “From global to local variables in granular materials”. In: *Powders and grains* 93 (1993), pp. 73–86.

[51] B. Cambou, H. Magoariec, and E. Vincens. “State internal variables at different scales for the modeling of the behavior of granular materials”. In: *Continuum Mechanics and Thermodynamics* 27.1 (2015), pp. 223–241.

[52] C. S. Campbell. “Granular material flows - An overview”. In: *Powder Technology* 162.3 (2006), pp. 208–229.

[53] C. S. Campbell. "Rapid granular flows". In: *Annual Review of Fluid Mechanics* 22.1 (1990), pp. 57–90.

[54] Yixin Cao et al. "Structural and topological nature of plasticity in sheared granular materials". In: *Nature Communications* 9 (2018).

[55] M. E. Cates et al. "Jamming, force chains, and fragile matter". In: *Physical Review Letters* 81 (1998), pp. 1841–1844.

[56] I. Cavarretta, M. Coop, and C. O'Sullivan. "The influence of particle characteristics on the behaviour of coarse grained soils". In: *Géotechnique* 60.6 (2010), pp. 413–423.

[57] CEGEO et al. "Particle shape dependence in 2D granular media". In: *EPL (Europhysics Letters)* 98.4 (2012), p. 44008.

[58] C. S. Chang, Y. Chang, and M. G. Kabir. "Micromechanics modeling for stress-strain behavior of granular soils. I: Theory". In: *Journal of Geotechnical Engineering* 118.12 (1992), pp. 1959–1974.

[59] C. S. Chang and J. Gao. "Second-gradient constitutive theory for granular material with random packing structure". In: *International Journal of Solids and Structures* 32.16 (1995), pp. 2279–2293.

[60] C. S. Chang and M. R. Kuhn. "On virtual work and stress in granular media". In: *International Journal of Solids and Structures* 42.13 (2005), pp. 3773–3793.

[61] C. S. Chang and C. L. Liao. "Constitutive relation for a particulate medium with the effect of particle rotation". In: *International Journal of Solids and Structures* 26.4 (1990), pp. 437–453.

[62] C. S. Chang, A. Misra, and K. Acheampong. "Elastoplastic Deformation for Particulates with Frictional Contacts". In: *Journal of Engineering Mechanics* 118.8 (1992).

[63] Ching S. Chang, Yibing Deng, and Zhenning Yang. "Modeling of minimum void ratio for granular soil with effect of particle size distribution". In: *Journal of Engineering Mechanics* 143.9 (2017), p. 04017060.

[64] C.S. Chang and P.-Y. Hicher. "An elasto-plastic model for granular materials with microstructural consideration". In: *International Journal of Solids and Structures* 42.14 (2005), pp. 4258–4277.

[65] S. Chapman and T.G. Cowling. *The mathematical theory of nonuniform gases*. Cambridge University Press, 1970.

[66] Y. P. Cheng, Y. Nakata, and M. D. Bolton. "Discrete element simulation of crushable soil". In: *Géotechnique* 53.7 (2003), pp. 633–641.

[67] J. Christoffersen and J.W. Hutchinson. "A class of phenomenological corner theories of plasticity". In: *Journal of the Mechanics and Physics of Solids* 27.5 (1979), pp. 465–487.

[68] J. Christoffersen, M. M. Mehrabadi, and S. Nemat-Nasser. "A micromechanical description of granular material behavior". In: *Journal of Applied Mechanics* 48.2 (1981), pp. 339–344.

[69] M.B. Cil, K.A. Alshibli, and P. Kenesei. "3D Experimental measurement of lattice strain and fracture behavior of sand particles using synchrotron x-Ray diffraction and tomography". In: *Journal of Geotechnical and Geoenvironmental Engineering* 143.9 (2017), p. 04017048.

[70] E.W.C. Coenen, V.G. Kouznetsova, and M.G.D. Geers. "Novel boundary conditions for strain localization analyses in microstructural volume elements". In: *International Journal for Numerical Methods in Engineering* 90.1 (2012), pp. 1–21.

[71] D. M. Cole and J. F. Peters. "A physically based approach to granular media mechanics: grain-scale experiments, initial results and implications to numerical modeling". In: *Granular Matter* 9.5 (2007), p. 309.

[72] Bernard D. Coleman and Morton E. Gurtin. "Thermodynamics with internal state variables". In: *The Journal of Chemical Physics* 47.2 (1967), pp. 597–613.

[73] I. F. Collins and I. Einav. "On the validity of elastic/plastic decompositions in soil mechanics". In: *Proceedings of Symposium on Elastoplasticity for Prof. K. Hashiguchi Retirement Anniversary, Kyushu University, JAPAN* (2005).

[74] I. F. Collins and G. T. Houlsby. "Application of thermomechanical principles to the modelling of geotechnical materials". In: *Proceedings of the Royal Society of London. Series A: Mathematical, Physical and Engineering Sciences* 453.1964 (1997), pp. 1975–2001.

[75] E. Cosserat and F. Cosserat. *Theorie des corps deformables*. Paris: Herman, 1909.

[76] F. da Cruz et al. "Rheophysics of dense granular materials: Discrete simulation of plane shear flows". In: *Physical Review E* 72 (2005), p. 021309.

[77] P. A. Cundall. "Numerical experiments on localization in frictional materials". In: *Ingenieur-Archiv* 59.2 (1989), pp. 148–159.

[78] P. A. Cundall and O. D. L. Strack. "A discrete numerical model for granular assemblies". In: *Géotechnique* 29.1 (1979), pp. 47–65.

[79] Y. F. Dafalias and M. T. Manzari. "Simple plasticity sand model accounting for fabric change effects". In: *Journal of Engineering Mechanics* 130.6 (2004), pp. 622–634.

[80] A. Daouadji et al. "Diffuse failure in geomaterials: Experiments, theory and modelling". In: *International Journal for Numerical and Analytical Methods in Geomechanics* 35.16 (2011), pp. 1731–1773.

[81] F. Darve, E. Flavigny, and M. Meghachou. “Yield surfaces and principle of superposition: Revisit through incrementally non-linear constitutive relations”. In: *International Journal of Plasticity* 11.8 (1995), pp. 927–948.

[82] F. Darve and S. Labanieh. “Incremental constitutive law for sands and clays: Simulations of monotonic and cyclic tests”. In: *International Journal for Numerical and Analytical Methods in Geomechanics* 6.2 (1982), pp. 243–275.

[83] F. Darve and F. Laouafa. “Instabilities in granular materials and application to landslides”. In: *Mechanics of Cohesive-frictional Materials* 5.8 (2000), pp. 627–652.

[84] F. Darve and F. Nicot. “On incremental non-linearity in granular media: Phenomenological and multi-scale views (Part I)”. In: *International Journal for Numerical and Analytical Methods in Geomechanics* 29.14 (2005), pp. 1387–1409.

[85] F. Darve et al. “Failure in geomaterials: Continuous and discrete analyses”. In: *Computer Methods in Applied Mechanics and Engineering* 193.27âĂŞ29 (2004). Computational Failure Mechanics for Geomaterials, pp. 3057–3085.

[86] Narsingh Deo, G. Prabhu, and M. S. Krishnamoorthy. “Algorithms for generating fundamental cycles in a graph”. In: *ACM Transactions on Mathematical Software* 8.1 (Mar. 1982), 26âĂŞ42.

[87] J. Desrues et al. “Void ratio evolution inside shear bands in triaxial sand specimens studied by computed tomography”. In: *Géotechnique* 46.3 (1996), pp. 529–546.

[88] A. Donev et al. “Jamming in hard sphere and disk packings”. In: *Journal of Applied Physics* 95.3 (2004), pp. 989–999.

[89] A. Drescher and G. de Josselin de Jong. “Photoelastic verification of a mechanical model for the flow of a granular material”. In: *Journal of the Mechanics and Physics of Solids* 20.5 (1972), pp. 337–340.

[90] D. C. Drucker and W. Prager. “Soil mechanics and plastic analysis or limit design”. In: *Quarterly of Applied Mathematics* 10.2 (1952), pp. 157–165.

[91] O. DurÃąn, N.P. Kruyt, and S. Luding. “Analysis of three-dimensional micro-mechanical strain formulations for granular materials: Evaluation of accuracy”. In: *International Journal of Solids and Structures* 47.2 (2010), pp. 251–260.

[92] R. Eggersmann et al. “Model-free Data-Driven inelasticity”. In: *Computer Methods in Applied Mechanics and Engineering* 350 (2019), pp. 81–99.

[93] W. Ehlers. "Homogenisation of discrete media towards micropolar continua: A computational approach". In: *AIP Conference Proceedings* 1227.1 (2010), pp. 306–313.

[94] W. Ehlers et al. "From particle ensembles to Cosserat continua: Homogenization of contact forces towards stresses and couple stresses". In: *International Journal of Solids and Structures* 40.24 (2003), pp. 6681–6702.

[95] F. Emeriault and B. Cambou. "Micromechanical modelling of anisotropic non-linear elasticity of granular medium". In: *International Journal of Solids and Structures* 33.18 (1996), pp. 2591–2607.

[96] F. Emeriault, B. Cambou, and A. Mahboubi. "Homogenization for granular materials: Non-reversible behaviour". In: *Mechanics of Cohesive-frictional Materials* 1.2 (1996), pp. 199–218.

[97] A. Cemal Eringen. "Theory of micropolar plates". In: *Zeitschrift für angewandte Mathematik und Physik ZAMP* 18.1 (1967), pp. 12–30.

[98] A.C. Eringen. "Linear theory of micropolar elasticity". In: *Journal of Mathematics and Mechanics.* 15 (1966), 909âĂŞ–924.

[99] A.C. Eringen. *Microcontinuum Field Theories: I. Foundations and Solids*. Springer New York, 1999.

[100] A.C. Eringen. "Theory of Micropolar Elasticity". In: *Microcontinuum Field Theories: I. Foundations and Solids*. New York, NY: Springer New York, 1999, pp. 101–248.

[101] A.C. Eringen and E.S. Suhubi. "Nonlinear theory of simple micro-elastic solids-I". In: *International Journal of Engineering Science* 2.2 (1964), pp. 189–203.

[102] A.Cemal Eringen. "An assessment of director and micropolar theories of liquid crystals". In: *International Journal of Engineering Science* 31.4 (1993), pp. 605–616.

[103] Martin Ester et al. "A Density-Based Algorithm for Discovering Clusters a Density-Based Algorithm for Discovering Clusters in Large Spatial Databases with Noise". In: *Proceedings of the Second International Conference on Knowledge Discovery and Data Mining*. KDDâĂŹ96. AAAI Press, 1996, pp. 226–231.

[104] Ernesto Estrada and Juan A. RodrÃŋguez-Velazquez. "Subgraph centrality in complex networks". In: *Physical Review E* 71.5 (2005).

[105] M. L. Falk and J. S. Langer. "Dynamics of viscoplastic deformation in amorphous solids". In: *Physical Review E* 57 (1998), pp. 7192–7205.

[106] M. L. Falk, M. Toiya, and W. Losert. "Shear transformation zone analysis of shear reversal during granular flow". In: *ArXiv e-prints* (2008).

[107] M.L. Falk and J.S. Langer. “Deformation and failure of amorphous, solidlike materials”. In: *Annual Review of Condensed Matter Physics* 2.1 (2011), pp. 353–373.

[108] FrÃľdÃľric Feyel and Jean-Louis Chaboche. “FE2 multiscale approach for modelling the elastoviscoplastic behaviour of long fibre SiC/Ti composite materials”. In: *Computer Methods in Applied Mechanics and Engineering* 183.3 (2000), pp. 309–330.

[109] Giacomo Fiorin, Michael L. Klein, and JÃľrÃťme HÃľnin. “Using collective variables to drive molecular dynamics simulations”. In: *Molecular Physics* 111.22-23 (2013), pp. 3345–3362.

[110] N.A. Fleck and J.W. Hutchinson. “Strain gradient plasticity”. In: *Advances in Applied Mechanics* 33 (1997), pp. 295–361.

[111] N.A. Fleck et al. “Strain gradient plasticity: Theory and experiment”. In: *Acta Metallurgica et Materialia* 42.2 (1994), pp. 475–487.

[112] S. Forest, R. Dendievel, and G. R. Canova. “Estimating the overall properties of heterogeneous Cosserat materials”. In: *Modelling and Simulation in Materials Science and Engineering* 7.5 (1999), p. 829.

[113] S. Forest and R. Sievert. “Elastoviscoplastic constitutive frameworks for generalized continua”. In: *Acta Mechanica* 160.1 (2003), pp. 71–111.

[114] Y. Forterre and O. Pouliquen. “Flows of dense granular media”. In: *Annual Review of Fluid Mechanics* 40.1 (2008), pp. 1–24.

[115] F. Froiio and J.âĂŘN. Roux. “Incremental response of a model granular material by stress probing with DEM simulations”. In: *AIP Conference Proceedings* 1227.1 (2010), pp. 183–197.

[116] Kangjia Fu, Zhihua Zhao, and Lihua Jin. “Programmable granular metamaterials for reusable energy absorption”. In: *Advanced Functional Materials* 29.32 (2019), p. 1901258.

[117] P. Fu and Y.F. Dafalias. “Fabric evolution within shear bands of granular materials and its relation to critical state theory”. In: *International Journal for Numerical and Analytical Methods in Geomechanics* 35.18 (2011), pp. 1918–1948.

[118] Z. Gao et al. “A critical state sand plasticity model accounting for fabric evolution”. In: *International Journal for Numerical and Analytical Methods in Geomechanics* 38.4 (2014), pp. 370–390.

[119] B. S. Gardiner and A. Tordesillas. “Micromechanical constitutive modelling of granular media: Evolution and loss of contact in particle clusters”. In: *Journal of Engineering Mathematics* 52.1 (2005), p. 93.

[120] P. Germain. "The method of virtual power in continuum mechanics. Part 2: microstructure". In: *SIAM Journal on Applied Mathematics* 25.3 (1973), pp. 556–575.

[121] J. Ghaboussi, J. H. Garrett, and X. Wu. "Knowledge-based modeling of material behavior with neural networks". In: *Journal of Engineering Mechanics* 117.1 (1991), pp. 132–153.

[122] Chad Giusti et al. "Topological and geometric measurements of force-chain structure". In: *Physical Review E* 94 (2016), p. 032909.

[123] B. J. Glasser and I. Goldhirsch. "Scale dependence, correlations, and fluctuations of stresses in rapid granular flows". In: *Physics of Fluids* 13.2 (2001), pp. 407–420.

[124] J. D. Goddard. "Continuum modeling of granular media". In: *Applied Mechanics Reviews* 66.5 (2014), p. 050801.

[125] J.D. Goddard and A.K. Didwania. "Computations of dilatancy and yield surfaces for assemblies of rigid frictional spheres". In: *The Quarterly Journal of Mechanics and Applied Mathematics* 51.1 (1998), pp. 15–44.

[126] C. Goldenberg et al. "Scale separation in granular packings: Stress plateaus and fluctuations". In: *Physical Review Letters* 96 (2006), p. 168001.

[127] I. Goldhirsch. "Rapid granular flows". In: *Annual Review of Fluid Mechanics* 35.1 (2003), pp. 267–293.

[128] I. Goldhirsch. "Stress, stress asymmetry and couple stress: From discrete particles to continuous fields". In: *Granular Matter* 12.3 (2010), pp. 239–252.

[129] David González, Francisco Chinesta, and Elías Cueto. "Thermodynamically consistent data-driven computational mechanics". In: *Continuum Mechanics and Thermodynamics* 31.1 (2019), pp. 239–253.

[130] G. Gudehus. "A comparison of some constitutive laws for soils under radially symmetric loading and unloading". In: *3rd International Conference of Numerical Methods in Geomechanics* 4 (1979), pp. 1309–1324.

[131] N. Guo and J. Zhao. "A coupled FEM/DEM approach for hierarchical multiscale modelling of granular media". In: *International Journal for Numerical Methods in Engineering* 99.11 (2014), pp. 789–818.

[132] N. Guo and J. Zhao. "The signature of shear-induced anisotropy in granular media". In: *Computers and Geotechnics* 47 (2013), pp. 1–15.

[133] John M. Harmon et al. "Modeling connected granular media: Particle bonding within the level set discrete element method". In: *Computer Methods in Applied Mechanics and Engineering* 373 (2021), p. 113486.

[134] Matt Harrington, Andrea J. Liu, and Douglas J. Durian. "Machine learning characterization of structural defects in amorphous packings of dimers and ellipses". In: *Physical Review E* 99 (2019), p. 022903.

[135] Q.-C. He. "On the micromechanical definition of macroscopic strain and strain-rate tensors for granular materials". In: *Computational Materials Science* 94 (2014). IWCMM23 Special Issue, pp. 51–57.

[136] Qizhi He and Jiun-Shyan Chen. "A physics-constrained data-driven approach based on locally convex reconstruction for noisy database". In: *Computer Methods in Applied Mechanics and Engineering* 363 (2020), p. 112791.

[137] M. van Hecke. "Jamming of soft particles: Geometry, mechanics, scaling and isostaticity". In: *Journal of Physics: Condensed Matter* 22.3 (2010), p. 033101.

[138] R. Hill. "A general theory of uniqueness and stability in elastic-plastic solids". In: *Journal of the Mechanics and Physics of Solids* 6.3 (1958), pp. 236–249.

[139] R. Hill. "The essential structure of constitutive laws for metal composites and polycrystals". In: *Journal of the Mechanics and Physics of Solids* 15.2 (1967), pp. 79–95.

[140] G. T. Houlsby and A. M Puzrin. *Principles of Hyperplasticity*. Springer, 2006.

[141] Tomasz Hueckel. "Coupling of elastic and plastic deformations of bulk solids". In: *Meccanica* 11.4 (1976), pp. 227–235.

[142] R. Hurley et al. "Extracting inter-particle forces in opaque granular materials: Beyond photoelasticity". In: *Journal of the Mechanics and Physics of Solids* 63 (2014), pp. 154–166.

[143] Ruben Ibanez et al. "A manifold learning approach to Data-Driven computational elasticity and inelasticity". In: *Archives of Computational Methods in Engineering* 25 (2018), pp. 47–57.

[144] H.M. Inglis, P.H. Geubelle, and K. Matous. "Boundary condition effects on multiscale analysis of damage localization". In: *Philosophical Magazine* 88.16 (2008), pp. 2373–2397.

[145] K. Ishihara, F. Tatsuoka, and S. Yasuda. "Undrained deformation and liquefaction of sand under cyclic stresses". In: *Soils and Foundations* 15.1 (1975), pp. 29–44.

[146] I.G. Vardoulakis J. Sulem. *Bifurcation analysis in geomechanics*. 1st ed. Blackie Academic & Professional, 1995.

[147] H. M. Jaeger, S. R. Nagel, and R. P. Behringer. "Granular solids, liquids, and gases". In: *Review of Modern Physics* 68 (1996), pp. 1259–1273.

[148] M. Jean. “The non-smooth contact dynamics method”. In: *Computer Methods in Applied Mechanics and Engineering* 177.3 (1999), pp. 235–257.

[149] M. G. Jefferies. “Nor-Sand: A simple critical state model for sand”. In: *Géotechnique* 43.1 (1993), pp. 91–103.

[150] J. Jenkins et al. “Fluctuations and the effective moduli of an isotropic, random aggregate of identical, frictionless spheres”. In: *Journal of Mechanics Physics of Solids* 53 (2005), pp. 197–225.

[151] J. T. Jenkins and M.A. Koenders. “The incremental response of random aggregates of identical round particles”. In: *The European Physical Journal E* 13.2 (2004), pp. 113–123.

[152] J.T. Jenkins and S.B. Savage. “A theory for the rapid flow of identical, smooth, nearly elastic, spherical particles”. In: *Journal of Fluid Mechanics* 130 (May 1983), pp. 187–202.

[153] J.T. Jenkins and O.D.L. Strack. “Mean-field inelastic behavior of random arrays of identical spheres”. In: *Mechanics of Materials* 16.1âĂŞ2 (1993). Special Issue on Mechanics of Granular Materials, pp. 25–33.

[154] M. Jirasek and S. Rolshoven. “Localization properties of strain-softening gradient plasticity models. Part I: Strain-gradient theories”. In: *International Journal of Solids and Structures* 46.11 (2009), pp. 2225–2238.

[155] M. Jirasek and S. Rolshoven. “Localization properties of strain-softening gradient plasticity models. Part II: Theories with gradients of internal variables”. In: *International Journal of Solids and Structures* 46.11 (2009), pp. 2239–2254.

[156] M.E. Johnson, L.M. Moore, and D. Ylvisaker. “Minimax and maximin distance designs”. In: *Journal of Statistical Planning and Inference* 26.2 (1990), pp. 131–148.

[157] R. E. Jones et al. “Machine learning models of plastic flow based on representation theory”. In: *Computer Modeling in Engineering & Sciences* 117.3 (2018), pp. 309–342.

[158] G. De Josselin de Jong. “The double sliding, free rotating model for granular assemblies”. In: *Géotechnique* 21 (1971), pp. 155–163.

[159] P. Jop. “Rheological properties of dense granular flows”. In: *Comptes Rendus Physique* 16.1 (2015). Granular physics / Physique des milieux granulaires, pp. 62–72.

[160] P. Jop, Y. Forterre, and O. Pouliquen. “A constitutive law for dense granular flows”. In: *Nature* 441.7094 (2006), pp. 727–730.

[161] K. Kamrin and G. Koval. “Nonlocal constitutive relation for steady granular flow”. In: *Physical Review Letters* 108 (2012), p. 178301.

[162] K. Kamrin, C.H. Rycroft, and M. Z. Bazant. "The stochastic flow rule: A multi-scale model for granular plasticity". In: *Modelling and Simulation in Materials Science and Engineering* 15.4 (2007), S449.

[163] Ken Kamrin. "Non-locality in granular flow: Phenomenology and modeling approaches". In: *Frontiers in Physics* 7 (2019), p. 116.

[164] Ken-Ichi Kanatani. "Distribution of directional data and fabric tensors". In: *International Journal of Engineering Science* 22.2 (1984), pp. 149–164.

[165] K. Karapiperis and J.E. Andrade. "Nonlocality in granular complex networks: Linking topology, kinematics and forces". In: *Extreme Mechanics Letters* 42 (2021), p. 101041.

[166] K. Karapiperis, J.P. Marshall, and J.E. Andrade. "Reduced gravity effects on the strength of granular matter: DEM simulations versus experiments". In: *Journal of Geotechnical and Geoenvironmental Engineering* 146.5 (2020), p. 06020005.

[167] K. Karapiperis et al. "Data-Driven multiscale modeling in mechanics". In: *Journal of the Mechanics and Physics of Solids* (2020), p. 104239.

[168] Konstantinos Karapiperis et al. "Investigating the incremental behavior of granular materials with the level-set discrete element method". In: *Journal of the Mechanics and Physics of Solids* 144 (2020), p. 104103.

[169] R. Kawamoto et al. "All you need is shape: Predicting shear banding in sand with LS-DEM". In: *Journal of the Mechanics and Physics of Solids* 111 (2018), pp. 375–392.

[170] R. Kawamoto et al. "Level set discrete element method for three-dimensional computations with triaxial case study". In: *Journal of the Mechanics and Physics of Solids* 91 (2016), pp. 1–13.

[171] Sean Keller and Heinrich M. Jaeger. "Aleatory architectures". In: *Granular Matter* 18.2 (2016), p. 29.

[172] T. Kirchdoerfer and M. Ortiz. "Data-Driven computational mechanics". In: *Computer Methods in Applied Mechanics and Engineering* 304 (2016), pp. 81–101.

[173] T. Kirchdoerfer and M. Ortiz. "Data-Driven computing in dynamics". In: *International Journal for Numerical Methods in Engineering* 113.11 (2018), pp. 1697–1710.

[174] T. Kirchdoerfer and M. Ortiz. "Data-Driven Computing with noisy material data sets". In: *Computer Methods in Applied Mechanics and Engineering* 326 (2017), pp. 622–641.

[175] V. R. Kohestani and M. Hassanlourad. "Modeling the mechanical behavior of carbonate sands using artificial neural networks and support vector machines". In: *International Journal of Geomechanics* 16.1 (2016), p. 04015038.

[176] S. Kohlhoff, P. Gumbsch, and H. F. Fischmeister. "Crack propagation in b.c.c. crystals studied with a combined finite-element and atomistic model". In: *Philosophical Magazine A* 64.4 (1991), pp. 851–878.

[177] W. T. Koiter. *Couple-stresses in the theory of elasticity.* 1964.

[178] Jonathan E. Kollmer and Karen E. Daniels. "Betweenness centrality as predictor for forces in granular packings". In: *Soft Matter* 15 (2019), pp. 1793–1798.

[179] D. Kolymbas. "An outline of hypoplasticity". In: *Archive of Applied Mechanics* 61.3 (1991), pp. 143–151.

[180] V. Kouznetsova, W. A. M. Brekelmans, and F. P. T. Baaijens. "An approach to micro-macro modeling of heterogeneous materials". In: *Computational Mechanics* 27.1 (2001), pp. 37–48.

[181] V. Kouznetsova, M. G. D. Geers, and W. A. M. Brekelmans. "Multi-scale constitutive modelling of heterogeneous materials with a gradient-enhanced computational homogenization scheme". In: *International Journal for Numerical Methods in Engineering* 54.8 (2002), pp. 1235–1260.

[182] E. Kröner. "Elasticity theory of materials with long range cohesive forces". In: *International Journal of Solids and Structures* 3.5 (1967), pp. 731–742.

[183] N. P. Kruyt. "Micromechanical study of plasticity of granular materials". In: *Comptes Rendus Mecanique* 338.10 (2010). Micromechanics of granular materials, pp. 596–603.

[184] N. P. Kruyt and L. Rothenburg. "On micromechanical characteristics of the critical state of two-dimensional granular materials". In: *Acta Mechanica* 225.8 (2014), pp. 2301–2318.

[185] N.P. Kruyt and L. Rothenburg. "Micromechanical definition of the strain tensor for granular materials". In: *Journal of Applied Mechanics* 63.3 (1996), pp. 706 –711.

[186] E. Kuhl et al. "A comparison of discrete granular material models with continuous microplane formulations". In: *Granular Matter* 2.3 (2000), pp. 113–121.

[187] M. R. Kuhn. "Are granular materials simple? An experimental study of strain gradient effects and localization". In: *Mechanics of Materials* 37.5 (2005), pp. 607–627.

[188] M. R. Kuhn. "Structured deformation in granular materials". In: *Mechanics of Materials* 31.6 (1999), pp. 407–429.

[189] M. R. Kuhn and A. Daouadji. "Multi-directional behavior of granular materials and its relation to incremental elasto-plasticity". In: *International Journal of Solids and Structures* 152-153 (2018), pp. 305–323.

[190] M. R. Kuhn and A. Daouadji. "Quasi-static incremental behavior of granular materials: Elastic-plastic coupling and micro-scale dissipation". In: *Journal of the Mechanics and Physics of Solids* 114 (2018), pp. 219–237.

[191] Matthew R Kuhn and Katalin Bagi. "Contact rolling and deformation in granular media". In: *International Journal of Solids and Structures* 41.21 (2004). Granular Mechanics, pp. 5793–5820.

[192] P. V. Lade. "Elasto-plastic stress-strain theory for cohesionless soil with curved yield surfaces". In: *International Journal of Solids and Structures* 13.11 (1977), pp. 1019–1035.

[193] P.V. Lade and J.M. Duncan. "Cubical triaxial tests on cohesionless soil". In: *Journal of Geotechnical and Geoenvironmental Engineering* 101 (1973), pp. 491–493.

[194] Roderic S. Lakes. "Size effects and micromechanics of a porous solid". In: *Journal of Materials Science* 18.9 (1983), pp. 2572–2580.

[195] R.S. Lakes. "Dynamical study of couple stress effects in human compact bone". In: *Journal of Biomechanical Engineering* 104.1 (1982).

[196] L.D Landau and E.M Lifshitz. *Statistical Physics*. Pergamon, New York, 1980.

[197] F. Larsson et al. "Computational homogenization based on a weak format of micro-periodicity for RVE-problems". In: *Computer Methods in Applied Mechanics and Engineering* 200.1 (2011), pp. 11–26.

[198] R. Larsson and S. Diebels. "A second-order homogenization procedure for multi-scale analysis based on micropolar kinematics". In: *International Journal for Numerical Methods in Engineering* 69.12 (2007), pp. 2485–2512.

[199] Adrien Leygue et al. "Data-based derivation of material response". In: *Computer Methods in Applied Mechanics and Engineering* 331 (2018), pp. 184–196.

[200] L. Li, E. Marteau, and J.E. Andrade. "Capturing the inter-particle force distribution in granular material using LS-DEM". In: *Granular Matter* 21.3 (2019), p. 43.

[201] X. Li and X.S. Li. “Micro-macro quantification of the internal structure of granular materials”. In: *Journal of Engineering Mechanics* 135.7 (2009), pp. 641–656.

[202] X. Li, Q. Liu, and J. Zhang. “A micro-macro homogenization approach for discrete particle assembly: Cosserat continuum modeling of granular materials”. In: *International Journal of Solids and Structures* 47.2 (2010), pp. 291–303.

[203] X. Li et al. “A mixed finite element procedure of gradient Cosserat continuum for second-order computational homogenisation of granular materials”. In: *Computational Mechanics* 54.5 (2014), pp. 1331–1356.

[204] X. S. Li and Y. F. Dafalias. “Anisotropic critical state theory: Role of fabric”. In: *Journal of Engineering Mechanics* 138.3 (2012), pp. 263–275.

[205] X. S. Li and Y. F. Dafalias. “Dilatancy for cohesionless soils”. In: *Géotechnique* 50.4 (2000), pp. 449–460.

[206] C.-L. Liao et al. “Stress-strain relationship for granular materials based on the hypothesis of best fit”. In: *International Journal of Solids and Structures* 34.31 (1997), pp. 4087–4100.

[207] A.J. Liu and S.R. Nagel. “Nonlinear dynamics: Jamming is not just cool any more”. In: *Nature* 396 (1998), pp. 21–22.

[208] Andrea J. Liu and Sidney R. Nagel. “The jamming transition and the marginally jammed solid”. In: *Annual Review of Condensed Matter Physics* 1.1 (2010), pp. 347–369.

[209] C. h. Liu et al. “Force fluctuations in bead packs”. In: *Science* 269.5223 (1995), pp. 513–515.

[210] Q. Liu. “A new version of Hill’s lemma for Cosserat continuum”. In: *Archive of Applied Mechanics* 85.6 (2015), pp. 761–773.

[211] W.K. Liu, S. Jun, and Y.F. Zhang. “Reproducing kernel particle methods”. In: *International Journal for Numerical Methods in Fluids* 20.8-9 (1995), pp. 1081–1106.

[212] Xiaoning Liu and Gengkai Hu. “Elastic metamaterials making use of chirality: A review”. In: *StrojniÅąki vestnik - Journal of Mechanical Engineering* 62.7-8 (2016), pp. 403–418.

[213] G. Lois, A. LemaÃőtre, and J. M. Carlson. “Emergence of multi-contact interactions in contact dynamics simulations of granular shear flows”. In: *EPL (Europhysics Letters)* 76.2 (2006), p. 318.

[214] J. Lubliner. *Plasticity theory*. Dover, 1990.

[215] Stefan Luding. “Anisotropy in cohesive, frictional granular media”. In: *Journal of Physics: Condensed Matter* 17.24 (2005), S2623–S2640.

[216] C.K. Lun et al. "Kinetic theories for granular flow: Inelastic particles in Couette flow and slightly inelastic particles in a general flowfield". In: *Journal of Fluid Mechanics* 140 (Mar. 1984), pp. 223–256.

[217] Mahyar Madadi et al. "On the fabric tensor of polydisperse granular materials in 2D". In: *International Journal of Solids and Structures* 41.9 (2004), pp. 2563–2580.

[218] R. Madec, B. Devincre, and L. P. Kubin. "From dislocation junctions to forest hardening". In: *Physical Review Letters* 89 (2002), p. 255508.

[219] T.S. Majmudar and R.P. Behringer. "Contact force measurements and stress-induced anisotropy in granular materials". In: *Nature* 435 (2005), pp. 1079–1082.

[220] T.S. Majmudar, M. Sperl, and R.P. Behringer. "Jamming transition in granular systems". In: *Physical Review Letters* 98 (2007).

[221] J. Mandel. "Conditions de Stabilité et Postulat de Drucker". In: *Rheology and Soil Mechanics / Rhéologie et Mécanique des Sols: Symposium Grenoble, April 1–8, 1964 / Symposium Grenoble, 1Er–8 Avril 1964*. Ed. by J. Kravtchenko and P.M. Sirieys. Berlin, Heidelberg: Springer Berlin Heidelberg, 1966, pp. 58–68.

[222] M. L. Manning, J. S. Langer, and J. M. Carlson. "Strain localization in a shear transformation zone model for amorphous solids". In: *Physical Review E* 76 (2007), p. 056106.

[223] M. T. Manzari and Y. F. Dafalias. "A critical state two-surface plasticity model for sands". In: *Géotechnique* 47.2 (1997), pp. 255–272.

[224] Eloïse Marteau and José E. Andrade. "A novel experimental device for investigating the multiscale behavior of granular materials under shear". In: *Granular Matter* 19.4 (2017), p. 77.

[225] H. Matsuoka and T. Nakai. "Stress-deformation and strength characteristics of soil under three different principal stresses". In: *Proceedings of the Japan Society of Civil Engineers* 1974.232 (1974), pp. 59–70.

[226] M. M. Mehrabadi, B. Loret, and S. Nemat-Nasser. "Incremental constitutive relations for granular materials based on micromechanics". In: *Proceedings of the Royal Society of London A: Mathematical, Physical and Engineering Sciences* 441.1913 (1993), pp. 433–463.

[227] M.M. Mehrabadi, S. Nemat-Nasser, and M. Oda. "On statistical description of stress and fabric in granular materials". In: *International Journal for Numerical and Analytical Methods in Geomechanics* 6.1 (1982), pp. 95–108.

[228] S.D. Mesarovic and J. Padbidri. "Minimal kinematic boundary conditions for simulations of disordered microstructures". In: *Philosophical Magazine* 85.1 (2005), pp. 65–78.

[229] GDR MiDi. "On dense granular flows". In: *The European Physical Journal E* 14.4 (2004), pp. 341–365.

[230] C. Miehe, J. Dettmar, and D. Zah. "Homogenization and two-scale simulations of granular materials for different microstructural constraints". In: *International Journal for Numerical Methods in Engineering* 83.8-9 (2010), pp. 1206–1236.

[231] C. Miehe, J. Schroeder, and J. Schotte. "Computational homogenization analysis in finite plasticity: Simulation of texture development in polycrystalline materials". In: *Computer Methods in Applied Mechanics and Engineering* 171.3 (1999), pp. 387–418.

[232] R. D. Mindlin. "Micro-structure in linear elasticity". In: *Archive for Rational Mechanics and Analysis* 16.1 (1964), pp. 51–78.

[233] R.D. Mindlin. "Second gradient of strain and surface-tension in linear elasticity". In: *International Journal of Solids and Structures* 1.4 (1965), pp. 417–438.

[234] A. Misra and C. S. Chang. "Effective elastic moduli of heterogeneous granular solids". In: *International Journal of Solids and Structures* 30.18 (1993), pp. 2547–2566.

[235] J. J. Moreau. "Unilateral Contact and Dry Friction in Finite Freedom Dynamics". In: *Nonsmooth Mechanics and Applications*. Ed. by J. J. Moreau and P. D. Panagiotopoulos. Springer Vienna, 1988, pp. 1–82.

[236] C.F. Moukarzel. "Granular Matter Instability: A Structural Rigidity Point of View". In: *Rigidity Theory and Applications*. Ed. by M. F. Thorpe and P. M. Duxbury. Boston, MA: Springer US, 2002, pp. 125–142.

[237] M. Mozaffar et al. "Deep learning predicts path-dependent plasticity". In: *Proceedings of the National Academy of Sciences* 116.52 (2019), pp. 26414–26420.

[238] D.M. Mueth, H.M. Jaeger, and S.R. Nagel. "Force distribution in a granular medium". In: *Physical Review E* 57 (1998), pp. 3164–3169.

[239] H. B. Mühlhaus and I. Vardoulakis. "The thickness of shear bands in granular materials". In: *Géotechnique* 37.3 (1987), pp. 271–283.

[240] Kieran A. Murphy et al. "Freestanding loadbearing structures with Z-shaped particles". In: *Granular Matter* 18 (2016).

[241] V. Nardelli and M. R. Coop. "The experimental contact behaviour of natural sands: normal and tangential loading". In: *Géotechnique* 0.0 (2018), pp. 1–15.

[242] Benjamin Nassauer, Thomas Liedke, and Meinhard Kuna. "Polyhedral particles for the discrete element method". In: *Granular Matter* 15.1 (2013), pp. 85–93.

[243] S. Nemat-Nasser. "A micromechanically-based constitutive model for frictional deformation of granular materials". In: *Journal of the Mechanics and Physics of Solids* 48.6âĂŞ7 (2000), pp. 1541–1563.

[244] S. Nemat-Nasser and J. Zhang. "Constitutive relations for cohesionles frictional granular materials". In: *International Journal of Plasticity* 18 (2002), pp. 531–547.

[245] N.-S. Nguyen, H. Magoariec, and B. Cambou. "Local stress analysis in granular materials at a mesoscale". In: *International Journal for Numerical and Analytical Methods in Geomechanics* 36.14 (), pp. 1609–1635.

[246] N.S. Nguyen et al. "Analysis of structure and strain at the meso-scale in 2D granular materials". In: *International Journal of Solids and Structures* 46.17 (2009), pp. 3257–3271.

[247] F. Nicot, F. Darve, and H. Dat Vu Khoa. "Bifurcation and second-order work in geomaterials". In: *International Journal for Numerical and Analytical Methods in Geomechanics* 31.8 (2007), pp. 1007–1032.

[248] F. Nicot, F. Darve, and RNVO Group: Natural Hazards and Vulnerability of Structures. "A multi-scale approach to granular materials". In: *Mechanics of Materials* 37.9 (2005), pp. 980–1006.

[249] M. Nitka et al. "Two-scale modeling of granular materials: a DEM-FEM approach". In: *Granular Matter* 13.3 (2011), pp. 277–281.

[250] G.T. Nolan and P.E. Kavanagh. "Random packing of nonspherical particles". In: *Powder Technology* 84.3 (1995), pp. 199–205.

[251] M. Oda. "Initial fabrics and their relation to mechanical properties of granular materials". In: *Soils and Foundations* 12.1 (1972), pp. 17–36.

[252] M. Oda and K. Iwashita. *Mechanics of granular materials: An introduction*. A.A. Balkena, Rotterdam, The Netherlands, 1999.

[253] M. Oda and K. Iwashita. "Study on couple stress and shear band development in granular media based on numerical simulation analyses". In: *International Journal of Engineering Science* 38.15 (2000), pp. 1713–1740.

[254] M. Oda, H. Kazama, and J. Konishi. "Effects of induced anisotropy on the development of shear bands in granular materials". In: *Mechanics of Materials* 28.1 (1998), pp. 103–111.

[255] M. Oda, J. Konishi, and S. Nemat-Nasser. "Experimental micromechanical evaluation of strength of granular materials: Effects of particle rolling". In: *Mechanics of Materials* 1.4 (1982), pp. 269–283.

[256] M. Oda, J. Konishi, and S. Nemat-Nasser. "Some experimentally based fundamental results on the mechanical behaviour of granular materials". In: *Géotechnique* 30.4 (1980), pp. 479–495.

[257] M. Oda, S. Nemat-Nasser, and J. Konishi. "Stress induced anisotropy in granular masses". In: *Soils and Foundations* 25.3 (1985).

[258] Corey S. O'Hern et al. "Force distributions near jamming and glass transitions". In: *Physical Review Letters* 86 (2001), pp. 111–114.

[259] Lars Onsager. "Reciprocal Relations in Irreversible Processes. I." In: *Phys. Rev.* 37 (1931), pp. 405–426.

[260] M. Ortiz. *Continuum Mechanics Lecture Notes*. California Institute of Technology, 2012.

[261] M Ortiz and A Pandolfi. "A variational Cam-clay theory of plasticity". In: *Computer Methods in Applied Mechanics and Engineering* 193.27 (2004). Computational Failure Mechanics for Geomaterials, pp. 2645–2666.

[262] S. Osher and R. Fedkiw. *Level Set Methods and Dynamic Implicit Surfaces*. Springer Verlag, 2003.

[263] C. O'Sullivan. *Particulate discrete element modelling: A geomechanics perspective*. CRC Press: New York, 2011.

[264] Norihiro Oyama, Hideyuki Mizuno, and Kuniyasu Saitoh. "Avalanche interpretation of the power-law energy spectrum in three-dimensional dense granular flow". In: *Physical Review Letters* 122 (2019), p. 188004.

[265] L. Papadopoulos et al. "Network Analysis of Particles and Grains". In: *ArXiv e-prints* (Aug. 2017).

[266] E. Pasternak and H.-B. Mühlhaus. "Generalised homogenisation procedures for granular materials". In: *Journal of Engineering Mathematics* 52.1 (2005), pp. 199–229.

[267] M. Pastor, O. C. Zienkiewicz, and A. H. C. Chan. "Generalized plasticity and the modelling of soil behaviour". In: *International Journal for Numerical and Analytical Methods in Geomechanics* 14.3 (1990), pp. 151–190.

[268] Dayakar Penumadu and Rongda Zhao. "Triaxial compression behavior of sand and gravel using artificial neural networks (ANN)". In: *Computers and Geotechnics* 24.3 (1999), pp. 207–230.

[269] J.F. Peters and L.E. Walizer. "Patterned nonaffine motion in granular media". In: *Journal of Engineering Mechanics* 139.10 (2013).

[270] J.F. Peters et al. "Characterization of force chains in granular material". In: *Physical Review E* 72 (2005), p. 041307.

[271] J.-P. Plassiard, N. Belheine, and F.-V. Donzé. "A spherical discrete element model: calibration procedure and incremental response". In: *Granular Matter* 11.5 (2009), pp. 293–306.

[272] Alexander Podlozhnyuk, Stefan Pirker, and Christoph Kloss. "Efficient implementation of superquadric particles in Discrete Element Method within an open-source framework". In: *Computational Particle Mechanics* 4.1 (2017), pp. 101–118.

[273] O. Pouliquen. "Scaling laws in granular flows down rough inclined planes". In: *Physics of Fluids* 11.3 (1999), pp. 542–548.

[274] O. Pouliquen. "Velocity correlations in dense granular flows". In: *Physical Review Letters* 93 (2004), p. 248001.

[275] O. Pouliquen and Y. Forterre. "A non-local rheology for dense granular flows". In: *Philosophical Transactions of the Royal Society of London A: Mathematical, Physical and Engineering Sciences* 367.1909 (2009), pp. 5091–5107.

[276] F. Radjai. "Force transmission in cohesive granular media". In: *Joint IUTAM-ISIMM Symposium on Mathematical Modeling and Physical Instances of Granular Flows (MPGF09), Reggio Calabria, Italy.* (2009).

[277] F. Radjai, J. Roux, and A. Daouadji. "Modeling granular materials: Century-long research across scales". In: *Journal of Engineering Mechanics* 143.4 (2017), p. 04017002.

[278] F. Radjai and S. Roux. "Turbulentlike fluctuations in quasistatic flow of granular media". In: *Physical Review Letters* 89 (2002), p. 064302.

[279] F. Radjai, S. Roux, and J.J. Moreau. "Contact forces in a granular packing". In: *Chaos* 9.3 (1999), pp. 544–550.

[280] F. Radjai, H. Troadec, and S. Roux. "Key features of granular plasticity". In: *Granular Materials: Fundamentals and Applications*. Ed. by S.J. Antony et al. The Royal Society of Chemistry, 2004, pp. 157–184.

[281] F. Radjai et al. "Fabric evolution and accessible geometrical states in granular materials". In: *Granular Matter* 14.2 (2012), pp. 259–264.

[282] F. Radjai et al. "Force distributions in dense two-dimensional granular systems". In: *Physical Review Letters* 77 (1996), pp. 274–277.

[283] Farhang Radjai et al. "Bimodal character of stress transmission in granular packings". In: *Physical Review Letters* 80 (1998), pp. 61–64.

[284] L. La Ragione. "The incremental response of a stressed, anisotropic granular material: loading and unloading". In: *Journal of the Mechanics and Physics of Solids* 95 (2016), pp. 147–168.

[285] A. L. Rechenmacher. "Grain-scale processes governing shear band initiation and evolution in sands". In: *Journal of the Mechanics and Physics of Solids* 54.1 (2006), pp. 22–45.

[286] K. R. Reddy, S. K. Saxena, and J. S. Budiman. "Development of a true triaxial testing apparatus". In: *Geotechnical Testing Journal (ASTM)* 15.2 (1992), pp. 89–105.

[287] R. A. Regueiro. "On finite strain micromorphic elastoplasticity". In: *International Journal of Solids and Structures* 47.6 (2010), pp. 786–800.

[288] Richard A. Regueiro and Beichuan Yan. "Concurrent Multiscale Computational Modeling for Dense Dry Granular Materials Interfacing Deformable Solid Bodies". In: *Bifurcations, Instabilities and Degradations in Geomaterials*. Ed. by Richard Wan, Mustafa Alsaleh, and Joe Labuz. Berlin, Heidelberg: Springer Berlin Heidelberg, 2011, pp. 251–273.

[289] C. X. Ren et al. "Machine learning reveals the state of intermittent frictional dynamics in a sheared granular fault". In: *Geophysical Research Letters* 46.13 (2019), pp. 7395–7403.

[290] J. R. Rice. "The localization of plastic deformation". In: *in: W.T. Koiter (Ed.), Theoretical and Applied Mechanics*. North-Holland Publishing Company, 1976, pp. 207–220.

[291] J.R. Rice. *Continuum mechanics and thermodynamics of plasticity in relation to microscale deformation mechanisms*. Brown University, 1974.

[292] V. Richefeu, G. Combe, and G. Viggiani. "An experimental assessment of displacement fluctuations in a 2D granular material subjected to shear". In: *Géotechnique Letters* 2.3 (2012), pp. 113–118.

[293] Pierre Rognon, Thomas Miller, and Itai Einav. "A circulation-based method for detecting vortices in granular materials". In: *Granular Matter* 17 (2015), pp. 177–188.

[294] D. Rogula. "Introduction to Nonlocal Theory of Material Media". In: *Nonlocal Theory of Material Media*. Springer Vienna, 1982, pp. 123–222.

[295] Miguel P. Romo et al. "Recurrent and constructive: Algorithm networks for sand behavior modeling". In: *International Journal of Geomechanics* 1.4 (2001), pp. 371–387.

[296] K. H. Roscoe. "The Influence of Strains in Soil Mechanics". In: *Géotechnique* 20.2 (1970), pp. 129–170.

[297] K. H. Roscoe, A. N. Schofield, and C. P. Wroth. "On the yielding of soils". In: *Géotechnique* 8.1 (1958), pp. 22–53.

[298] F. Roters et al. "Overview of constitutive laws, kinematics, homogenization and multiscale methods in crystal plasticity finite-element modeling: Theory, experiments, applications". In: *Acta Materialia* 58.4 (2010), pp. 1152–1211.

[299] L. Rothenburg and R. J. Bathurst. "Analytical study of induced anisotropy in idealized granular materials". In: *Géotechnique* 39.4 (1989), pp. 601–614.

[300] L. Rothenburg and N.P. Kruyt. "Critical state and evolution of coordination number in simulated granular materials". In: *International Journal of Solids and Structures* 41.21 (2004). Granular Mechanics, pp. 5763–5774.

[301] S. Roux and F. Radjai. "Texture-Dependent Rigid-Plastic Behavior". In: *Physics of Dry Granular Media*. Ed. by H.J. Herrmann, J.-P. Hovi, and S. Luding. Dordrecht: Springer Netherlands, 1998, pp. 229–236.

[302] P. W. Rowe. "The stress-dilatancy relation for static equilibrium of an assembly of particles in contact". In: *Proceedings of the Royal Society of London A: Mathematical, Physical and Engineering Sciences* 269.1339 (1962), pp. 500–527.

[303] P. Royis and T. Doanh. "Theoretical analysis of strain response envelopes using incrementally non-linear constitutive equations". In: *International Journal for Numerical and Analytical Methods in Geomechanics* 22.2 (1998), pp. 97–132.

[304] J.W. Rudnicki and J.R. Rice. "Conditions for the localization of deformation in pressure-sensitive dilatant materials". In: *Journal of the Mechanics and Physics of Solids* 23.6 (1975), pp. 371–394.

[305] C. H. Rycroft, K. Kamrin, and M. Z. Bazant. "Assessing continuum postulates in simulations of granular flow". In: *Journal of the Mechanics and Physics of Solids* 57.5 (2009), pp. 828–839.

[306] C.H. Rycroft. "Multiscale modeling in granular flow". Doctoral Dissertation. Massachusetts Institute of Technology, 2007.

[307] Jerome Sacks et al. "Design and analysis of computer experiments". In: *Statistical Science* 4.4 (Nov. 1989), pp. 409–423.

[308] Abouzar Sadrekarimi and Scott M. Olson. "Particle damage observed in ring shear tests on sands". In: *Canadian Geotechnical Journal* 47.5 (2010), pp. 497–515.

[309] Christophe Salot, Philippe Gotteland, and Pascal Villard. "Influence of relative density on granular materials behavior: DEM simulations of triaxial tests". In: *Granular Matter* 11.4 (2009), pp. 221–236.

[310] C. S. Sandeep and K. Senetakis. "Exploring the micromechanical sliding behavior of typical quartz grains and completely decomposed volcanic granules subjected to repeating shearing". In: *Energies* 10 (2017), pp. 1–16.

[311] J. C. Santamarina and G. Cascante. "Stress anisotropy and wave propagation: A micromechanical view". In: *Canadian Geotechnical Journal* 33.5 (1996), pp. 770–782.

[312] M. Satake. *Cosntitution of mechanics of granular materials through graph representation*. Tokyo University Press, Tokyo, 1978.

[313] M. Satake. "Fabric tensor in granular materials". In: *Proceedings of the IUTAM Symposium on Deformation and Failure of Granular Materials*. Ed. by P. A. Vermeer and H. J. Luger. Amsterdam: A.A. Balkem, 1982, pp. 63–68.

[314] M. Satake. "New formulation of graph-theoretical approach in the mechanics of granular materials". In: *Mechanics of Materials* 16.1 (1993), pp. 65–72.

[315] S. B. Savage. "Analyses of slow high-concentration flows of granular materials". In: *Journal of Fluid Mechanics* 377 (Dec. 1998), pp. 1–26.

[316] S. B. Savage. "Instability of unbounded uniform granular shear flow". In: *Journal of Fluid Mechanics* 241 (Aug. 1992), pp. 109–123.

[317] S.B. Savage and D.J. Jeffrey. "The stress tensor in a granular flow at high shear rates". In: *Journal of Fluid Mechanics* 110 (1981), pp. 255–272.

[318] M.A. Schofield and C.P. Wroth. *Critical State of Soil Mechanics*. McGraw-Hill: London, 1968.

[319] K. Senetakis, M. R. Coop, and M. C. Todisco. "The inter-particle coefficient of friction at the contacts of Leighton Buzzard sand quartz minerals". In: *Soils and Foundations* 53.5 (2013), pp. 746–755.

[320] L.E. Silbert, J. W. Landry, and G. S. Grest. "Granular flow down a rough inclined plane: Transition between thin and thick piles". In: *Physics of Fluids* 15.1 (2003), pp. 1–10.

[321] Leonardo E. Silbert et al. "Rheology and contact lifetimes in dense granular flows." In: *Physical Review Letters* 99 (2007), p. 068002.

[322] T.W. Simpson, J.D. Poplinski, and J.K. Allen. "Metamodels for computer-based engineering design: Survey and recommendations". In: *Engineering with Computers* 17.2 (2001), pp. 129–150.

[323] A.G. Smart and J. M. Ottino. "Evolving loop structure in gradually tilted two-dimensional granular packings". In: *Physical Review E* 77 (2008), p. 041307.

[324] A. Spadoni and M. Ruzzene. "Elasto-static micropolar behavior of a chiral auxetic lattice". In: *Journal of the Mechanics and Physics of Solids* 60.1 (2012), pp. 156–171.

[325] Douglas E. Spearot, Karl I. Jacob, and David L. McDowell. "Nonlocal separation constitutive laws for interfaces and their relation to nanoscale simulations". In: *Mechanics of Materials* 36.9 (2004), pp. 825–847.

[326] Ishan Srivastava et al. "Flow-arrest transitions in frictional granular matter". In: *Physical Review Letters* 122 (2019), p. 048003.

[327] L. Staron. "Correlated motion in the bulk of dense granular flows". In: *Physical Review E* 77 (2008), p. 051304.

[328] L. Staron and F. Radjai. "Friction versus texture at the approach of a granular avalanche". In: *Physical Review E* 72 (2005), p. 041308.

[329] A. S. J. Suiker, R. de Borst, and C.S. Chang. "Micro-mechanical modelling of granular material. Part 1: Derivation of a second-gradient micro-polar constitutive theory". In: *Acta Mechanica* 149.1 (2001), pp. 161–180.

[330] A. S. J. Suiker and N. A. Fleck. "Frictional collapse of granular assemblies". In: *Journal of Applied Mechanics* 71.3 (2004), pp. 350–358.

[331] E. B. Tadmor, M. Ortiz, and R. Phillips. "Quasicontinuum analysis of defects in solids". In: *Philosophical Magazine A* 73.6 (1996), pp. 1529–1563.

[332] C. Tamagnini, X. Calvetti, and G. Viggiani. "An assessment of plasticity theories for modeling the incrementally nonlinear behavior of granular soils". In: *Journal of Engineering Mathematics* 52 (2005), pp. 265–291.

[333] C. Tamagnini and G. Viggiani. "On the incremental nonlinearity of soils. Part I: Theoretical aspects". In: *Rivista Italiana di Geotecnica* 36.1 (2002), pp. 44–61.

[334] D.W. Taylor. *Fundamentals of Soil Mechanics*. John Wiley & Sons, Inc. New York, N.Y., 1948.

[335] J. Tejchman and G. Gudehus. "Shearing of a narrow granular layer with polar quantities". In: *International Journal for Numerical and Analytical Methods in Geomechanics* 25.1 (2001), pp. 1–28.

[336] J. Tejchman and W. Wu. "Numerical study on patterning of shear bands in a Cosserat continuum". In: *Acta Mechanica* 99.1 (1993), pp. 61–74.

[337] K. Terada and N. Kikuchi. *Nonlinear homogenization method for practical applications*. Computational Methods in Micromechanics, 1995.

[338] C. Thornton. "Numerical simulations of deviatoric shear deformation of granular media". In: *Géotechnique* 50.1 (2000), pp. 43–53.

[339] A. Tordesillas, G. Hunt, and J. Shi. "A characteristic length scale in confined elastic buckling of a force chain". In: *Granular Matter* 13.3 (2011), pp. 215–218.

[340] A. Tordesillas and M. Muthuswamy. "A thermomicromechanical approach to multiscale continuum modeling of dense granular materials". In: *Acta Geotechnica* 3.3 (2008), pp. 225–240.

[341] A. Tordesillas, M. Muthuswamy, and S.D. Walsh. "Mesoscale measures of nonaffine deformation in dense granular assemblies". In: *Journal of Engineering Mechanics* 134.12 (2008).

[342] A. Tordesillas, D.M. Walker, and Q. Lin. "Force cycles and force chains". In: *Physical Review E* 81 (2010), p. 011302.

[343] A. Tordesillas et al. "Granular vortices: Identification, characterization and conditions for the localization of deformation". In: *Journal of the Mechanics and Physics of Solids* 90.Supplement C (2016), pp. 215–241.

[344] A. Tordesillas et al. "Structural stability and jamming of self-organized cluster conformations in dense granular materials". In: *Journal of the Mechanics and Physics of Solids* 59.2 (2011), pp. 265–296.

[345] Antoinette Tordesillas and Maya Muthuswamy. "On the modeling of confined buckling of force chains". In: *Journal of the Mechanics and Physics of Solids* 57.4 (2009), pp. 706–727.

[346] Antoinette Tordesillas et al. "Multiscale characterisation of diffuse granular failure". In: *Philosophical Magazine* 92.36 (2012), pp. 4547–4587.

[347] R. A. Toupin. "Elastic materials with couple-stresses". In: *Archive for Rational Mechanics and Analysis* 11.1 (1962), pp. 385–414.

[348] Fubin Tu et al. "Generalized bridging domain method for coupling finite elements with discrete elements". In: *Computer Methods in Applied Mechanics and Engineering* 276 (2014), pp. 509–533.

[349] B. Utter and R.P. Behringer. "Transients in sheared granular matter". In: *European Physical Journal E* 14.4 (2004), pp. 373–380.

[350] Y. P. Vaid and D. Negussey. "Relative density of pluviated sand samples". In: *Soils and Foundations* 24.2 (1984), pp. 101–105.

[351] K. C. Valanis. "A gradient theory of internal variables". In: *Acta Mechanica* 116.1 (1996), pp. 1–14.

[352] K. C. Valanis. "A gradient thermodynamic theory of self-organization". In: *Acta Mechanica* 127.1 (1998), pp. 1–23.

[353] I. Vardoulakis and E.C. Aifantis. "A gradient flow theory of plasticity for granular materials". In: *Acta Mechanica* 87.3 (1991), pp. 197–217.

[354] I. Vardoulakis, M. Goldscheider, and G. Gudehus. "Formation of shear bands in sand bodies as a bifurcation problem". In: *International Journal for Numerical and Analytical Methods in Geomechanics* 2.2 (1978), pp. 99–128.

[355] G. Viggiani, M. M. Küntz, and J. Desrues. "An experimental investigation of the relationships between grain size distribution and shear banding in sand". In: *Continuous and Discontinuous Modelling of Cohesive-Frictional Materials*. Berlin, Heidelberg: Springer Berlin Heidelberg, 2001, pp. 111–127.

[356] I. Vlahinić et al. "Towards a more accurate characterization of granular media: extracting quantitative descriptors from tomographic images". In: *Granular Matter* 16.1 (2014), pp. 9–21.

[357] Nikolaos Vlassis, Ran Ma, and WaiChing Sun. *Geometric deep learning for computational mechanics Part I: Anisotropic Hyperelasticity*. 2020.

[358] I. Vragovic and E. Louis. "Network community structure and loop coefficient method". In: *Physical Review E* 74 (2006), p. 016105.

[359] I. Vragovic, E. Louis, and A. Diaz-Guilera. "Efficiency of informational transfer in regular and complex networks". In: *Physical Review E* 71 (2005), p. 036122.

[360] Gregory J. Wagner and Wing Kam Liu. "Coupling of atomistic and continuum simulations using a bridging scale decomposition". In: *Journal of Computational Physics* 190.1 (2003), pp. 249–274.

[361] D. M. Walker and A. Tordesillas. "Topological evolution in dense granular materials: A complex networks perspective". In: *International Journal of Solids and Structures* 47.5 (2010), pp. 624–639.

[362] David M. Walker, Antoinette Tordesillas, and Gary Froyland. "Mesoscale and macroscale kinetic energy fluxes from granular fabric evolution". In: *Physical Review E* 89 (2014), p. 032205.

[363] David M. Walker et al. "A complex network analysis of granular fabric evolution in three-dimensions". English. In: *Dynamics of Continuous, Discrete and Impulsive Systems, Series B: Applications and Algorithums* 19.4-5 (2012), pp. 471–495.

[364] David M. Walker et al. "Structural templates of disordered granular media". In: *International Journal of Solids and Structures* 54 (2015), pp. 20–30.

[365] S.D.C. Walsh, A. Tordesillas, and J.F. Peters. "Development of micromechanical models for granular media". In: *Granular Matter* 9.5 (2007), p. 337.

[366] R. Wan and M. Pinheiro. "On the validity of the flow rule postulate for geomaterials". In: *International Journal for Numerical and Analytical Methods in Geomechanics* 38.8 (2013), pp. 863–880.

[367] Kun Wang and WaiChing Sun. "A multiscale multi-permeability poroplasticity model linked by recursive homogenizations and deep learning". In: *Computer Methods in Applied Mechanics and Engineering* 334 (2018), pp. 337–380.

[368] Y. Wang and K. Hutter. "Granular Material Theories Revisited". In: *Geomorphological Fluid Mechanics*. Ed. by N.J. Balmforth. Berlin, Heidelberg: Springer Berlin Heidelberg, 2001, pp. 79–107.

[369] C. Wellmann and P. Wriggers. "A two-scale model of granular materials". In: *Computer Methods in Applied Mechanics and Engineering* 205–208 (2012). Special Issue on Advances in Computational Methods in Contact Mechanics dedicated to the memory of Professor J.A.C. Martins, pp. 46–58.

[370] W. Wu and D. Kolymbas. "Hypoplasticity Then and Now". In: *Constitutive Modelling of Granular Materials*. Ed. by D. Kolymbas. Springer Berlin, 2000, pp. 57–101.

[371] Yonghao Yue et al. "Hybrid grains: Adaptive coupling of discrete and continuum simulations of granular media". In: *ACM Transactions on Graphics.* 37.6 (2018).

[372] Jie Zhang, Robert P. Behringer, and Isaac Goldhirsch. "Coarse-graining of a physical granular system". In: *Progress of Theoretical Physics Supplement* 184 (Mar. 2010), pp. 16–30.

[373] Pin Zhang et al. "An AI-based model for describing cyclic characteristics of granular materials". In: *International Journal for Numerical and Analytical Methods in Geomechanics* 44.9 (2020), pp. 1315–1335.

[374] Qiong Zhang and Ken Kamrin. "Microscopic description of the granular fluidity field in nonlocal flow modeling". In: *Physical Review Letters* 118 (2017), p. 058001.

[375] Xu Zhang and Katerina Aifantis. "Interpreting the internal length scale in strain gradient plasticity". In: *Reviews on Advanced Materials Science* 41 (Jan. 2015), pp. 72–83.

[376] Caizhi Zhou, S. Bulent Biner, and Richard LeSar. "Discrete dislocation dynamics simulations of plasticity at small scales". In: *Acta Materialia* 58.5 (2010), pp. 1565–1577.

[377] H. Zhu, M. M. Mehrabadi, and M. Massoudi. "Incorporating the effects of fabric in the dilatant double shearing model for planar deformation of granular materials". In: *International Journal of Plasticity* 22.4 (2006), pp. 628–653.

[378] H. Zhu, M. M. Mehrabadi, and M. Massoudi. "The frictional flow of a dense granular material based on the dilatant double shearing model". In: *Computers & Mathematics with Applications* 53.2 (2007). Recent Advances in Non-Linear Mechanics, pp. 244–259.

[379] H. Zhu, F. Nicot, and F. Darve. "Meso-structure evolution in a 2D granular material during biaxial loading". In: *Granular Matter* 18.1 (2016), p. 3.

[380] Jian-Hua Zhu, Musharraf M Zaman, and Scott A Anderson. "Modeling of soil behavior with a recurrent neural network". In: *Canadian Geotechnical Journal* 35.5 (1998), pp. 858–872.

[381] H. Ziegler. "An introduction to thermomechanics". In: *Applied Mathematics and Mechanics* 21 (1977).

[382] O.C. Zienkiewicz and G.N. Pande. "Time-dependent multilaminate model of rocks: A numerical study of deformation and failure of rock masses". In: *International Journal for Numerical and Analytical Methods in Geomechanics* 1.3 (1977), pp. 219–247.

[383] Tarek I. Zohdi, J.Tinsley Oden, and Gregory J. Rodin. "Hierarchical modeling of heterogeneous bodies". In: *Computer Methods in Applied Mechanics and Engineering* 138.1 (1996), pp. 273–298.

[384] Iker Zuriguel et al. "Clogging transition of many-particle systems flowing through bottlenecks". In: *Scientific Reports* 4 (2014), p. 7324.